

https://dspace.org/

Microwave-assisted synthesis of palladium-based ferroalloy electrocatalysts for application in alkaline direct alcohol fuel cells

Ramashala, Kanyane Nonhlanhla Eugenia

2024-11

University of the Witwatersrand, Johannesburg

https://hdl.handle.net/10539/45179

Ramashala, Kanyane Nonhlanhla Eugenia. (2024). Microwave-assisted synthesis of palladium-based ferroalloy electrocatalysts for application in alkaline direct alcohol fuel cells. [PhD thesis, University of the Witwatersrand, Johannesburg]. WIReDSpace. https://hdl.handle.net/10539/45179

Downloaded from a DSpace repository. https://dspace.org/

Microwave-assisted synthesis of palladium-based ferroalloy electrocatalysts for application in alkaline direct alcohol fuel cells



UNIVERSITY OF THE
WITWATERSRAND,
JOHANNESBURG

Kanyane Nonhlanhla Eugenia Ramashala

(Nee' Mphahlele)

A thesis submitted to the Faculty of Science, University of the Witwatersrand, Johannesburg, in the fulfilment for the degree of

Doctor of Philosophy in Chemistry

Supervisor: Prof. Kenneth I. Ozoemena

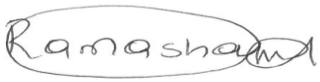
Co-Supervisor: Prof. Caren Billing

Co-Supervisor: Dr. R. Mmalewane Modibedi

Johannesburg, October 2024

DECLARATION

I declare that this thesis is my own unaided work. It is being submitted for the degree of Doctor of Philosophy in the University of the Witwatersrand, Johannesburg. It has not been submitted before any degree or examination.

Signature  Date 07 October 2024

DEDICATION

This research work is a heartfelt dedication to my late father (Masetloe Mphahlele), my mother (Semangele Mphahlele), my beloved husband (Steve Ramashala), my grandmother (Elizabeth Ntemane), my little brother (Mampuru Mphahlele) and lastly to my two beautiful children (Oletilwe and Orearabile Ramashala). Their unwavering support and love have been my inspiration throughout this journey.

ACKNOWLEDGEMENTS

First and foremost, I would like to thank God Almighty for the gift of life. He gave me strength and courage when I felt ineffective and demotivated. “Your love is truly deeper than the ocean.”

Secondly, a special thank you to my supervisor, Prof. K. Ozoemena. He stood by me from the inception until completion. His guidance, motivation, patience, and support were constant during this challenging journey.

Additionally, I wish to express my appreciation to Prof. C. Billing for her contribution and encouragement throughout this journey.

Likewise, I am immensely grateful to Dr. M. Modibedi for being a beacon of consistency, inspiration, and guidance throughout my studies.

Also, my sincere gratitude to Dr. A. K. Ipadeola, Dr. A. B. Haruna, Dr. P. V. Mwonga, and Dr. N. Palaniyandy. What an amazing team that contributed to ensuring I completed this thesis with accuracy and validity.

I deeply extend my gratitude to my colleagues and close friends within the CSIR’s Electrochemical Energy Technologies (EET) research group: Dr. T Munonde, Thandiwe Maumau, Thembelihle Mehlo, Christina Mathebula, and Nomthandazo Mabena. It would've been nearly impossible to complete this thesis without your expertise and knowledge in electrochemistry and energy storage, which have been imperative in providing exactitude work.

To Dr. L. Mabena, thank you for your partial financial contribution, which assisted me during the characterisation experiments. I appreciate your earnest friendship. Moreover, to close friends and family who stood by me throughout this demanding journey, thank you for the motivation that kept me hopeful and focused.

Moreover, thank you so much to my beautiful children (Oletilwe and Orearabile). You were constant emotional anchors that energised me and ensured I remained positive. I am truly blessed to be your mother. Throughout this life journey, I hope that you will have confidence

and courage in knowing that sowing seeds of hard work equates to reaping a bountiful harvest, just as I have tried to lead you by example as your mother.

To my grandmother (Mrs. Elizabeth Ntemane), thank you for your abundant love and endless sacrifices. I am proud to say that I come from a lineage of strong, hard-working black women. I'm fortunate and honored to have you in my life, and I hope to continue to make you proud.

The success of this project wouldn't have been possible without my beautiful, loving and supportive mother (Mrs. Semangele Mphahlele). All the phone calls and prayers helped me to soldier on. Thank you for your unconditional love and for always being on my side.

Lastly, my heartfelt gratitude goes to my beloved husband (Mr. Steve Ramashala). This journey has been undeniably challenging, but you were by my side every step of the way. I appreciate your love and unwavering support. "I love you, Mr. Rams"!

RESEARCH OUTPUTS

Publications

1. N.E Mphahlele, A.K Ipadeola, A.B Haruna, P.V Mwonga, R.M Modibedi, N. Palaniyandy, C. Billing, K.I Ozoemena, Microwave-induced defective PdFe/C nano-electrocatalyst for highly efficient alkaline glycerol oxidation reactions, Electrochimica Acta, 409(2022) 139977 – **Published.**

2. N.E Mphahlele, A.K Ipadeola, A.B Haruna, P.V Mwonga, R.M Modibedi, K.I Ozoemena, Electrochemical activity of Palladium-based bi-metallic nano-electrocatalysts towards ethylene glycol, ethanol and glycerol oxidation in alkaline medium, **To be published.**

3. N.E Mphahlele, A.K Ipadeola, A.B Haruna, P.V Mwonga, R.M Modibedi, K.I Ozoemena, Electrochemical performance of Palladium-based tri-metallic nano- electrocatalysts towards the oxidation of alcohols in basic medium, **To be published.**

4. N.E Mphahlele, A.K Ipadeola, A.B Haruna, P.V Mwonga, R.M Modibedi, K.I Ozoemena, Facile synthesis of Palladium Ferromanganese alloy supported on carbon as an excellent anode for Direct Ethylene Glycol Fuel Cell, **To be published.**

Conference and Workshop

1. N.E. Mphahlele, N. Palaniyandy, K. Raju, M. Modibedi, C. Billing and K. Ozoemena, Interrogating the effects of microwave-induced nano-sizing of physiochemistries Pd-decorated Ferroalloy nanostructures for alkaline fuel cells, poster presentation at Faraday Discussion Meeting, hosted at Cape Town, Lagoon beach – 24 January 2017.

2. Nonhlanhla Mphahlele, Mmalewane Modibedi and Kenneth I. Ozoemena. The synthesis of carbon supported Pd-based ferroalloy electrocatalysts towards oxidation of glycerol in basic medium, 43rd National Convention of the SACI hosted at the CSIR International Convention Center - 04 December 2018 (the talk was oral).

3. Nonhlanhla Mphahlele, Mmalewane Modibedi and Kenneth I. Ozoemena. A facile Microwave synthesised Pd-based PdFeMn/C as a highly active nano-catalyst for

ADAFCs, poster presentation at 9th SANI workshop (NYRS) Future Africa Campus at the UP – 12 November 2019.

4. Nonhlanhla Mphahlele, Caren Billing and Kenneth I. Ozoemena. The performance of Fe-Mn based alloy electrocatalyst decorated with Pd as anode towards DEGFCs, oral presentation: 3rd International workshop on Porous Materials and their Applications (IWMPA-2021) – Virtual event – 27 – 28 July 2021.

NRF – SAASTA Programme

1. Webinar workshop (Exploring the energy security grand challenge and the promise of a hydrogen economy) organized by the National Research Foundation and the South African Agency for Science and Technology (NRF-SAASTA). Nonhlanhla Ramashala gave a presentation about the role and importance of advanced energy materials for energy storage and conversion – on 25 August 2022.

2. The National Research Foundation and the South African Agency for Science and Technology (NRF-SAASTA) organized a hydrogen fuel cell shoot as part of a learner-teacher program. We hosted learners from the Ntsako secondary school, and Nonhlanhla Ramashala and Nomthandazo Mabena facilitated the visit. The shoot was performed at the CSIR Laboratory on June 15, 2022.

Workshop/Training

1. Res4Africa training: Virtual event was facilitated by various expect at various energy spaces including:

- Renewable energy transition in South Africa
- Renewable energy transition in North Africa
- Renewable energy transition in the Sahel region
- Energy Innovation and Digitalization
- Energy management
- Bankability and Project Finance

ABSTRACT

This research work describes the study of Pd-based ferro-electrocatalysts for application towards direct ethanol fuel cells (DEFCs), direct ethylene glycol fuel cells (DEGFCs), direct glycerol fuel cells (DGFCs) and oxygen reduction reaction (ORR) operated in a basic environment. The initial part of the research was to explore the Pd-based monometallic and bimetallic (Pd/C and PdFe/C) by utilising varied methods such as the conventional sodium borohydride ($NaBH_4$) and microwave-assisted technique (MW) towards the oxidation of glycerol (gly), intending to choose the best method viable for these catalysts. This study revealed that MW techniques tuned the physicochemical properties of Pd/C and PdFe/C by augmenting their crystallinity and defect. These led to improved electrocatalytic activities towards glycerol oxidation reaction (GOR) over $NaBH_4$ technique.

MW process as a powerful tool was further used in the entire study to synthesise bimetallic and trimetallic electrocatalysts in ethanol (EtOH), ethylene glycol (EG) and glycerol (Gly) oxidation reaction in an alkaline environment. The synthesised bimetallic catalysts studied in this research work were (PdFe/C, PdCo/C, and PdMn/C) at varied ratios of Pd: M (Pd_2M/C (2:1) and PdM/C (1:1)). Amongst them all, Pd_2Fe/C and PdFe/C were observed to be the most favourable catalysts towards all the alcohols, with the excellent specific activity of about, for EtOH (11.59 and 4.15 mA cm^{-2}), EG (9.82 and 5.51 mA cm^{-2}) and Gly (8.94 and 4.73 mA cm^{-2}), respectively.

The satisfactory performance exhibited by the PdFe/C electrocatalyst prompted the exploration of the second 3d transition metal (PdFeMn/C and PdFeCo/C), intending to investigate the synergistic behaviour between the non-noble metals and Pd. The XRD confirmed that these electrocatalysts are in a crystalline nature with a decrease in d spacing (from 0.2247 nm, PdFe/C to 0.2236 nm (PdFeMn/C)) after the insertion of Mn into PdFe/C. This was supported by the TEM images obtained for the PdFeMn/C catalyst with a particle size of sub 10 nm. The comparison studies towards EtOH, EG and Gly were investigated for all the electrocatalysts and there was a remarkable observation, which is dissimilar from the theoretical studies (DFT). Density Functional Theory (DFT) revealed that PdFeCo performed better in terms of Gibbs free energy, binding energy, and energy band gap than PdFeMn; however, the experimental

studies favoring the performance of PdFeMn. The PdFeMn/C delivered the best electrochemical activities, including a superior electrochemical active surface area (ECSA), larger current densities and mass activity response, and less susceptibility to poisoning and high conductivity as compared to PdFe/C and PdFeCo/C electrocatalysts.

Furthermore, the PdFeMn/C electrocatalyst exhibited remarkable electrochemical properties during the ORR (basic medium). Ultimately, the best two anode electrocatalysts (PdFe/C & PdFeMn/C) were explored and tested for the proof-of-concept in the two-electrode configuration with the micro-3D printed cell. The PdFeMn/C delivered improved µ-ethylene glycol fuel cell, µ-glycerol fuel cell, and µ-ethanol fuel cell activities with respective to high voltage and power density of 33.27 mW cm^{-2}, 11.00 mW cm^{-2} and 45,80 mW cm^{-2} respectively, operated at 100 mV / s. These electrocatalysts have demonstrated promising results in advancing ADAFCs.

TABLE OF CONTENTS

Section ***Page***

Declaration i

Dedication ii

Acknowledgments iv

Research outputs vi

Abstract viii

Table of contents xiv

List of figures xx

List of tables xxii

List of abbreviations xxiv

CHAPTER 1 INTRODUCTION 1

1.1 Motivation and Rationale 1

1.2 Study objectives 4

1.3 Thesis outline 4

1.4 References 6

CHAPTER 2 LITERATURE REVIEW 7

2.1 Batteries, Heat engine, and Fuel cell comparison 7

2.2 Operating Principles of FCs 9

2.3 Types and Classifications of Fuel Cells. 10

2.4 An overview of DAFCs in alkaline environments 11

2.5 Operating principles of DAFCs in alkaline medium 13

2.6 Electrocatalysts in DAFCs 13

2.7 Pd catalysts for the oxidation of alcohol in an alkaline environment. 14

2.7.1 Single Components Catalysts 14

2.7.2 Bimetallic and Trimetallic Electrocatalyst 15

2.7.3 The role of electrocatalysts in ethanol electrooxidation reactions. 16

2.7.4 The role of electrocatalysts in ethylene glycol electrooxidation reactions. 17

2.7.5 The role of electrocatalysts in glycerol electrooxidation reactions. 18

2.7.6 Pd-based ferroalloy nanostructures 18
2.8 Reaction Mechanism 20
2.9 Cathode material 22
2.9.1 ORR in the alkaline environment 22
2.9.2 Operating principles of ORR in alkaline medium 23
2.9.3 Kinetics of ORR 23
2.9.4 Electrocatalyst For ORR Application 24
2.10 Preparation and methodology of electrocatalysts 25
2.10.1 Microwave assisted technique. 25
2.11 Electrochemical characterisation of Anodic and cathodic Catalysts 27
2.11.1 The Study of Cyclic Voltammetry 27
2.11.2 Reversible reactions 30
2.11.3 Irreversible Process 31
2.11.4 Quasi-reversible process 32
2.11.5 Study of Linear Sweep Voltammetry 32
2.11.6 The Study of Chronoamperometry 33
2.11.7 The study of Electrochemical Impedance spectroscopy 34
2.12 References 36
CHAPTER 3 EXPERIMENTAL PROCEDURE 42
3.1 Materials and Reagents 42
3.1.1 Preparation procedure of Pd-based electrocatalysts. 43
3.1.1.1 Synthesis of bimetallic electrocatalysts utilising the NaBH4 method 43
3.1.1.2 Synthesis of bimetallic nano-electrocatalysts using MW technique 43
3.1.1.3 Synthesis of trimetallic electrocatalysts utilising MW method 44
3.2 Physical characterisation conditions 45
3.2.1 XRD 45
3.2.2 SEM 46
3.2.3 TEM 46
3.2.4 BET 46
3.2.5 Raman Spectroscopy 46
3.2.6 XPS 47
3.2.7 Density Functional Theory (DFT) Simulation 47
3.3 The electrochemical characterisation conditions. 48

3.3.1 Electrochemical characterisation of electrocatalysts 48
3.3.2 Modification of the AOR electrode 48
3.3.3 Modification of the ORR electrode 48
CHAPTER 4 Microwave-induced defective PdFe/C nano-electrocatalyst for highly efficient alkaline glycerol oxidation reactions 49
4.1 Introduction 49
4.2 Results and Discussion 51
4.2.1 Computational Studies 51
4.2.2 Physico-chemical Characterisation 54
4.2.2.1 TEM analysis 54
4.2.2.2 XRD Analysis 55
4.2.2.3 Nitrogen Desorption-Adsorption (Surface Area) Analysis 56
4.2.2.4 Raman Spectroscopic Analysis 58
4.2.2.5 XPS Analysis 59
4.2.3 Electrochemical and Electrocatalytic Properties 62
4.2.3.1 Cyclic voltammetry in 0.5 M KOH in the absence and presence of glycerol 62
4.2.3.2 Chronoamperometry and Electrochemical Impedance Spectroscopy 64
4.3 Conclusions 66
4.4 References 68
CHAPTER 5 Interrogating the effect of microwave irradiation on bimetallic electrocatalysts toward ethanol oxidation reaction 70
5.1 Introduction 70
5.2 Results and Discussion 72
5.2.1 Computational work on the development of bimetallics. 72
5.2.1 Physico-chemical Characterisation 72
5.2.1.1 X-Ray Diffraction Measurements 72
5.2.1.2 TEM analysis 74
5.2.2 Electrochemical characterisation 76
5.2.2.1 Chronoamperometric analysis 79
5.2.2.2 The of EIS on various bimetallics. 79
5.3 Conclusions 81
5.4 References 83

CHAPTER 6 Electrochemical activities of Palladium-based bi-metallic nano-electrocatalysts towards ethylene glycol oxidation in alkaline medium 85
6.1 Introduction 85
6.2 Results and Discussion 86
6.2.1 Computational work 86
6.2.2 Physico-chemical Characterisation 87
6.2.3 X-Ray Diffraction Measurements 87
6.2.3.1 TEM analysis 88
6.2.4 Electrochemical characterisation 90
6.2.4.1 Cyclic Voltammetry of bimetallics. 90
6.2.4.2 Chronoamperometry study 93
6.3 Conclusions 94
6.4 References 95
CHAPTER 7 Electrochemical activities of Palladium-based bi-metallic nano-electrocatalysts towards the oxidation of Gly in an alkaline environment 97
7.1 Introduction 97
7.2 Results and Discussion 99
7.2.1 Computational evaluation 99
7.2.2 Physico-chemical Characterisation 99
7.2.2.1 XRD analysis 99
7.2.3 Electrochemical characterisation 103
7.2.3.1 Cyclic Voltammetry of bimetallic. 103
7.2.3.2 Chronoamperometry study 106
7.3 Conclusions 107
7.4 References 108
CHAPTER 8 Electrochemical activities of Palladium-based tri-metallic nano-electrocatalysts towards the oxidation of alcohols in basic medium 110
8.1 Introduction 110
8.2 Results and Discussion 111
8.2.1 Computational Description Work 111
8.2.2 Physico-chemical characterisation 114
8.2.2.1 XRD of trimetallic electrocatalysts 114
8.2.2.2 X-ray Photoelectron Spectroscopy Characterisation (XPS) 115

8.2.2.3 SEM images 117
8.2.2.4 TEM images 118
8.2.3 Electrochemical characterisation 120
8.2.3.1 CV Test 120
8.2.3.2 CV of monometallic, bimetallic and tri-metallic electrocatalysts for EGOR 121
8.2.3.3 Chronoamperometric evaluation 124
8.2.3.4 CV of monometallic, bimetallic, and tri-metallic electrocatalysts for EOR 125
8.2.3.5 Chronoamperometry Test 127
8.2.3.6 CV of monometallic, bimetallic, and trimetallic electrocatalysts for GOR 128
8.2.3.7 Chronoamperometric analysis 131
8.2.3.8 Comparison of alcohol electro-oxidation for the various electrocatalysts 132
8.2.3.9 Electrochemical impedimetric analysis of alcohol electro-oxidations on electrocatalysts. 133
8.2.3.10 Proof-of-concept of the DEFCs 135
8.2.3.11 Proof-of-concept of the DEGFCs 137
8.2.3.12 Proof-of-concept of the DGFCs 138
8.3 Conclusions 140
8.4 References 142
CHAPTER 9 Facile synthesis of Palladium Ferromanganese alloy supported on carbon as an excellent anode for Direct Ethylene Glycol Fuel Cell 144
9.1 Introduction 144
9.2 Results and discussion: Ethylene glycol oxidation reaction 146
9.2.1 Computational studies 146
9.2.2 Physicochemical Characterisations 147
9.2.2.1 XRD analysis 147
9.2.2.2 X-Ray Photoelectron Spectroscopy 149
9.2.3 Electrochemical measurements 152
9.2.3.1 CV studies in KOH electrolyte 152
9.2.3.2 Cyclic Voltammetry in ethylene glycol 153
9.2.3.3 The EG concentration on ethylene glycol oxidation 157
9.2.3.4 The effect of KOH concentration on ethylene glycol oxidation 159
9.2.3.5 Reaction pathways for EGOR over the PdFeMn/C 159
9.2.3.6 Chronoamperometric analysis 161

9.2.3.7 Electrochemical Impedance Measurements 162
9.2.3.8 Linear sweep voltammograms: oxygen reduction reaction 164
9.3 Conclusions 166
9.4 References 168
CHAPTER 10 CONCLUSIONS AND RECOMMENDATIONS 171
10.1 Introduction 171
10.2 Conclusions 171
10.3 Recommendations 174

LIST OF FIGURES

Figure ***Description*** ***Page***

Figure 1.1 A schematic diagram describing the sustainable landscape [8] 2

Figure 2.1: a) Electrolysis setup b) An Alkaline fuel cells used on space flight [103, 104] 7

Figure 2.3: A schematic diagram displaying the A, Batteries and B Fuel cells. The picture shows how the fuel cells are supplied with fuel. [105] 8

Figure 2.4: a) Typical gasoline car using a spark-ignited internal combustion engine, and b, Typical diagram showing a hydrogen-powered fuel cell [106, 107]..... 9

Figure 2.5: Operating principles of Polymer exchange membrane Fuel Cells (PEMFCs) [20 10

Scheme 2.1: Schematic diagram representing the ethylene glycol pathways indicating the poisoning and non-poisoning paths [72] 22

Figure 2.6: A schematic diagram representing microwave vs conventional heating [110] 27

Figure 2.7: a) Typical three-electrode system [91] and b) The excitation signal of CV via a triangular potential waveform with switching potentials at (0.8, -0.2 V) vs SCE [92] 28

Figure 2.8: A typical CV curve representing an electrochemical of reversible one and electron redox process [93]. 29

Figure 2.11: Linear sweep voltammogram [97]. 33

Figure 2.12: a). The Randles equivalent circuit and b). Nyquist plot obtained from the Randles circuit [101] 35

Figure 4.1: Glycerol molecule adsorption sites for Pd- and Pd/Fe-based electrodes. The dark blue dots (shades) show the possible site where glycerol is adsorbed. 52

Figure 4.2: a,c,e,g) Band structure and b,d,f,h) partial density of states (PDOS) of the a,b,e,f) Pd and c,d,g,h) PdFe. The dotted lines represent the Fermi energy level, the PDOS shows that the electrons in the conduction band are mainly from the 3d orbital of the 3d orbital of the Pd and Fe..... 53

Figure 4.3: TEM images of Pd-based catalysts obtained from the conventional $NaBH_4$ method: a) Pd/C and c) PdFe/C; and microwave-assisted method: b) Pd/C and d) PdFe/C. 55

Figure 4.4: Comparison of the XRD patterns of the various Pd-based nano-electrocatalysts supported on carbon synthesised using a) the $NaBH_4$ and b) the microwave-assisted methods..... 56

Figure 4.5: N_2 adsorption and desorption isotherms of Pd-based catalysts obtained from the conventional $NaBH_4$ method: a) Pd/C and b) PdFe/C; and microwave-assisted method: c) Pd/C and d) PdFe/C. 57

Figure 4.6: Raman spectra of $NaBH_4$ a) Pd/C, and b) PdFe/C and MW c) Pd/C, and d) PdFe/C 58

Figure 4.7: a,b) Wide survey, deconvoluted elementals scans c,d) Pd 3d, e,f) Fe 2p, g,h) C 1s, i,j) O 1s and k,l) Pd 4d and Fe 3d valences of PdFe/C ($NaBH_4$) and PdFe/C (MW) electrocatalysts. 61

Figure 4.8: Cyclic voltammograms of Pd-based nano-electrocatalysts from conventional $NaBH_4$ method: a) Pd/C and PdFe/C, and microwave-assisted synthesis b) Pd/C(MW) and PdFe/C(MW) in 0.5 M KOH solution under N_2 atmosphere at a sweep rate of 50 mV / s. 62

Figure 4.9: Chronoamperometric measurements of the Pd-based nano-electrocatalysts from conventional $NaBH_4$ method: a) Pd/C and PdFe/C, and microwave-assisted synthesis b) Pd/C (MW) and PdFe/C (MW) in 0.5 M KOH/0.5 M glycerol solution under N_2 atmosphere at -0.2 V and their corresponding Nyquist plots curves of the Pd-based nano-electrocatalysts obtained from the c) $NaBH_4$ method and d) microwave-assisted method, respectively. All data were obtained at a fixed potential of -0.2 V in glycerol electrooxidation. The electrical equivalent circuit (EEC) was used to fit e) monometallic while f) bimetallic. 65

Figure 5.1: XRDs patterns of bimetallic electrocatalysts (at varied Pd_2M/C and PdM/C). 73

Figure 5.4: CV of Pd, PdFe/C, PdMn/C, and PdCo/C (molar ratio: Pd_2M/C and PdM/C) in (0.5 M KOH solution + 0.5 M) EtOH, N_2 atmosphere using sweep rate of 50 mV / s. 78

Figure 5.7: Nyquist curves nano-eletrocatalysts at the potential of -0.2 V in electrooxidation of EtOH, a-b) the electrical equivalent fitted circuit (EEC). c-f) bode plots corresponding to Pd based electrocatalysts. 81

Figure 6.1: XRD diffractograms of electrocatalysts. 87

Figure 6.2: TEM micrographs of a) Pd_2M/C and b) PdM/C electrocatalysts. 89

Figure 6.3: CV profiles of catalysts (presented at varied atomic ratio of Pd_2M/C and PdM/C) in KOH solution (0.5 M), bubbles with N_2 atmosphere at a scan rate = 50 mV / s. 90

Figure 6.4: The CV curves of electrocatalyst at different atomic ratio of a) Pd_2M/C and b) PdM/C) immersed in 0.5 M KOH/EG solution under N_2 gas at a scan rate = 50 mV / s. 92

Figure 6.5: Comparison of mass and specific activities of Pd, PdFe/C, PdMn/C and PdCo/C atomic ratio of a) Pd2M/C and b) PdM/C) in 0.5 M KOH solution + 0.5 M EG N2 atmosphere at a sweep rate of 50 mV / s..... 93

Figure 6.6: The CA curves of electrocatalysts (at varied atomic ratios of a) Pd_2M/C and b) PdM/C) in 0.5 M KOH/ EG solution under the influence of N_2 gas at 0.2 V..... 94

Figure 7.3. Cyclic voltammetry of electrocatalyst in 0.5 M KOH solution under N_2 gas at a scan rate of 50 mV / s. 104

Figure 7.4: CV curves of Pd/C, PdFe/C, PdMn/C and PdCo/C (a) Pd_2M/C and b) PdM/C) in 0.5 M KOH/ 0.5 M Gly mixture under N_2 gas at a scan rate = 50 mV / s. 105

Figure 7.5: Comparison of mass and specific activities of (a) Pd_2M/C and b) PdM/C) in 0.5 M KOH solution / Gly, N_2 gas at a sweep rate of 50 mV / s. 106

Figure 7.6: The CA curves (a) Pd_2M/C and b) PdM/C) in KOH/ Gly (0.5 M) solution under N_2 atmosphere at 0.2 V. 106

Figure 8.1: XRD patterns of electrocatalysts. 115

Figure 8.2 XPS spectra of (a, e, i) with the wide survey spectra, deconvoluted elementals scans b, f, j) Pd 3d, c, g, k) O 1s, d, h, l) C 1s and m,n) of PdFeC, PdFeMn/C and PdFeCo/C electrocatalysts. 117

Figure 8.3: SEM images of PdFe/C, PdFeMn/C and PdFeCo/C electrocatalysts. 118

Figure 8.4: Comparative HRTEM images of (a) PdFeC, (b) PdFeMn/C; Particle size histogram distribution insert b, PdFeC and d, PdFeMn/C. Insert in (c) and (d) the SAED pattern of PdFeC and PdFeMn/C electrocatalysts. 119

Figure 8.5: Cyclic voltammograms of electrocatalysts containing a solution of (0.5 M) KOH at a sweep rate = 50 mV / s. 121

Figure 8.6: The CV of Pd/C, PdFeC, PdFeMn/C, and PdFeCo/C for EGOR was reached at 50 mV / s in a KOH/Gly solution containing 0.5 M. 123

Figure 8.7: Comparison between mass & specific activities of Pd, PdFeC, PdFeMn/C and PdFeCo/C in KOH/EG containing 0.5 M solution under N_2 gas, 50 mV / s..... 123

Figure 8.8 Current-times curve of Pd/C, PdFe/C, PdFeMn/C and PdFeCo/C electrocatalysts, potential of -0.2 V in (0.5 M) KOH/EG solution. 124

Figure 8.9: Cyclic voltammetry of electrocatalysts for EOR, reached = 50 mV / s, containing the solution of 0.5 M KOH / EtOH. 126

Figure 8.10: Comparison of various activities to study the electrocatalysts in 0.5M KOH/ EtOH solution, bubbled with N_2 gas at a sweep rate = 50 mV / s..... 127

Figure 8.11: Current-times curve of examined electrocatalysts with a -0.2 V, containing 0.5 M KOH / 0.5 M ethanol..... 128

Figure 8.12: Cyclic voltammetry of electrocatalysts for GOR with a scan rate of 50 mV / s, 0.5 M KOH / 0.5 M Gly..... 129

Figure 8.13: Comparison of mass and specific activities of Pd, PdFe/C, PdFeMn/C and PdFeCo/C, containing (0.5 M) KOH / Gly under N_2 gas at 50 mV/ s..... 130

Figure 8.14: Current-times curve of Pd/C, PdFe/C, PdFeCo/C with PdFeMn/C electrocatalysts at -0.2 V in 0.5 M KOH/ 0.5 M Gly solution..... 131

Figure 8.15: Comparative cyclic voltammetry of a) PdFeMn/C and b) PdFeCo/C nano-catalysts in the solution containing 0.5 M KOH / alcohols (EG, EtOH, GOR) @ 50 mV / s. 133

Figure 8.16: a) Nyquist plot of a) PdFeMn/C and b) PdFeCo/C electrocatalysts using the same parameters as CV and c) insert is the EEC (equivalent external circuit) used to fit the spectra. 134

Figure 8.18: (a) Voltage (I-V) and power density curves for PdFe/C and PdFeMn/C, (b) galvanostatic discharge curves, (c) Nyquist plots, and (d) Voigt EEC for PdFe/C and PdFeMn/C supplied with 4 M KOH/EG solution. 138

Figure 8.19: (a) Voltage (I-V) and power density curves, (b) galvanostatic discharge curve, (c) Nyquist curves and (d) Voigt EEC for PdFe/C and PdFeMn/C fed with 4 M KOH/ Gly solution. 139

Figure. 9.1: XRD diffractogram of (a) Pd/C, PdFeC, PdMn/C and PdFeMn/C electrocatalysts. 147

Figure 9.2: XPS spectra of a-c) with the wide survey spectra, deconvoluted elementals scans d-f) Pd 3d, g-i) O 1s, j-l) C 1s and m,n) Fe 2p of PdFeC, PdMn/C and PdFeMn/C electrocatalysts. 150

Figure 9.3: Comparative TEM images of (a) Pd/C, (b) PdFe/C, (c) PdMn/C, (d) PdFeMn/C; HRTEM images of (e) PdFe/C and (f) PdFeMn/C electrocatalysts. Particle size distribution histogram insert (b) PdFe/C and (d) PdFeMn/C. Insert in (e) and (f) show the SAED pattern of PdFe/C and PdFeMn/C. 151

Figure 9.4: CV curves of catalysts in KOH (0.5 M), with 50 mV/s scan rate. 153

Figure 9.5: CV for EGOR on the electrocatalysts in 0.5 M KOH / EG, scan rate: 50 mV / s. 154

Figure 9.6: EGOR mass and specific activities of Pd, PdFeC, PdMn/C, and PdFeMn/C catalysts. 155

Figure 9.7: a) The LSV and (b) Tafel plots towards EGOR on the Pd/C, PdFe/C, PdMn/C and PdFeMn/C, EG, Scan rate of 1.0 mV / s. 156

Figure 9.8: LSV of EGOR at the a) Pd/C and b) PdFeMn/C electrocatalysts at varied scan rates, c) Tafel plots of current density vs square root of the scan rate for both electrocatalysts, scan rate 1.0 mV / s. 157

Figure 9.9: (a) LSV, (b) Tafel plot and (c) The log-log plot of current density vs EG concentration obtained for PdFeMn/C in 0.5 M KOH solution containing different EG concentration at scan rate: 1.0 mV / s. 158

Figure 9.10: The LSV of the EGOR on the PdFeMn/C electrocatalysts in 0.5 M EG solution containing KOH solution of various concentrations. Scan rate: 1.0 mV / s. ... 159

Figure 9.11:Chronoamperometric curves of Pd/C, PdFe/C, PdMn/C and PdFeMn/C in 0.5 M KOH / EG solutions at -0.2 V. 162

Figure 9.12: (a) Nyquist curves of electrocatalysts at -0.2 V, b) the EEC used in fitting the spectra. 163

Figure 9.15: ORR polarisation curves of Pd/C, PdFe/C, PdMn/C and PdFeMn/C electrocatalysts in 0.1 M KOH electrolyte purged with O_2 at the scan rate 10 mV / s with rotating speeds from 400 to 4000 rpm. 164

Figure 9.16: The ORR polarisation curves compare the electrocatalysts measured at 1600 rpm. 165

Figure 9.17: Koutecky-Levich Plots of ORR polarisation curves of electrocatalysts taken at varied potentials (0.3, 0.35, 0.40, 0.45. 0.50, 0.55 V vs RHE). 166

LIST OF TABLES

Table ***Description*** ***Page***

Table 2.1: Description and performance of FCs type 11

Table 2.2: Summary of electrocatalysts for ORR applications 24

Table 3.1: Summarises the materials and reagents used in this research work. The chemicals used for this study were not purified. 42

Table 4.1: Computational studies of Pd and PdFe electrocatalysts in glycerol. 51

Table 4.2: Physisorption data obtained from Brunauer-Emmett-Teller (BET) for as-prepared nano-electrocatalysts..... 57

Table 4.3: Raman data of Pd-based electrocatalysts showing peak positions and intensity ratios..... 59

Table 4.4: Comparison of electrochemical parameters of Pd-based nano-electrocatalysts. ... 63

Table 4.5: EIS data for the Pd-based nano-electrocatalysts in a solution of 0.5 M KOH + 0.5 M Gly at -0.2 V (vs Ag|AgCl, sat'd KCl)..... 66

Table 5.1 Computational simulation of various bimetallics in ethanol..... 72

Table 5.3: Comparison study of electrochemical parameters of electrocatalysts towards EOR in an alkaline environment. 77

Table 5.4: Electrochemical Impedimetric data of catalyst containing a (0.5 M) KOH & 0.5 M ethanol at -0.2 V..... 81

Table 6.1 Computational studies of catalysts adsorbed on EG. 86

Table 6.2: XRD data of Pd-based electrocatalysts at different atomic ratios..... 87

Table 6.3: Comparison effect between bimetallic electrocatalysts at varied atomic ratios towards EGOR in alkaline electrolyte. 91

Table 7.1 Computational research in glycerol adsorption on bimetallic catalyst. 99

Table 7.2: XRD data of Pd-based electrocatalysts at different atomic ratios..... 101

Table 8.3: Summary of ECSA results for nano-catalysts..... 121

Table 8.5: Comparison of catalysts performance for EOR 125

Table 8.6: Comparison of electrocatalysts performance for GOR. 130

Table 8.7: The electrochemical performance comparing different alcohols with PdFeMn/C and PdFeCo/C electrocatalysts. 133

Table 8.8: Electrochemical impedance parameters at a specific voltage of -0.2 V. 135

Table 8.9: Electrochemical impedance measurements of EOR. 137

Table 8.10: Electrochemical impedance measurements of EGOR. 138

Table 8.11: Electrochemical impedance measurements of GOR. 140

Table 9.1: Computational studies of Pd, PdFe, PdMn and PdFeMn in ethylene glycol 146

Table 9.2: XRD structure analysis of Pd-based electrocatalysts. 148

Table 9.3: The electrochemical parameters of Pd-based electrocatalysts toward EGOR..... 153

Table 9.4: Electrochemical Impedimetric data for EGOR on Pd/C, PdMn/C, PdFe/C and PdFeMn/C catalysts. 163

LIST OF ABBREVIATIONS

AFCs:	Alkaline Fuel cells
Ag/AgCl:	Silver/Silver chloride
AEM:	Anionic Exchange Membrane
AOR:	Alcohol Oxidation Reaction
BET:	Brunauer-Emmett-Teller
C:	Carbon matrix
CA:	Chronoamperometry measurements
CO:	Carbon Monoxide
CO_2:	Carbon Dioxide
CV:	Cyclic voltammetry
DAFCs:	Direct Alcohol Fuel-Cells
µ-DEFCs:	Direct Ethanol micro-fuel cells
µ-DEGFCs:	Direct Ethylene glycol micro-Fuel-cells
µ-DGFCs:	Direct Glycerol micro-Fuel-cells
DEFCs:	Direct Ethanol Fuel-cells
DEGFCs:	Direct Ethylene glycol Fuel-cells
DFT:	Density Functional Theory
DGFCs:	Direct Glycerol fuel cells
DOS:	Density of states
ECSA:	Electrochemical active surface area
EG:	Ethylene glycol
EIS:	Electrochemical Impedance Measurements
EtOH:	Ethanol
FCs:	Fuel Cells

G:	Glycerol
Gly:	Glycerol
GCE:	Glassy carbon electrode
H_2:	Hydrogen gas
KCl:	Potassium chloride
LSV:	Linear sweep voltammetry
MCFCs:	Molten carbonate fuel cells
N_2:	Nitrogen gas
O_2:	Oxygen gas
ORR:	Oxygen reduction- reaction
PAFCs:	Phosphoric acid fuel cells
PEMFCs:	Polymer exchange membrane fuel cells
PDOS:	Partial density of state
Pd:	Palladium
PdFe/C:	Palladium-iron on carbon.
PdMn/C:	Palladium-manganese on carbon.
PdCo/C:	Palladium-cobalt on carbon.
PdFeMn/C:	Palladium-based ferroalloy on carbon.
PdFeCo/C:	Palladium-based ferroalloy on carbon.
Pt:	Platinum
RDE:	Rotating disc electrode
SEM:	Scanning Electron Microscopy
TEM:	Transmission Electron Microscopy
XPS:	X-ray photoelectron spectroscopy
XRD:	X-ray Diffraction

CHAPTER 1

INTRODUCTION

This chapter provides insight information about the motivation and rationale, objectives, and the outline of the thesis.

1.1 Motivation and Rationale

The issue of energy impacts our human life, economic development, surroundings, and health. Global energy consumption is expected to triple by 2100 due to moderate economic growth and population increase. Burning fossil fuels continue to play a dominant role in fulfilling our energy needs. However, it comes at a bigger price, which includes the rapid rise in emitting greenhouse gases, lasting pollution, and climate change disasters [1]. Therefore, governments worldwide regard renewable energies as prominent technologies for transitioning to cleaner and sustainable energy [2, 3]. The government's plans and objectives are to develop sustainable renewable energy technologies with significant cost savings and contribute to world energy needs [2].

Various renewable energy technologies currently being explored include solar, wind, biomass, and hydropower [4, 5]. These types of technology have proven highly reliable and affordable and produce energy repeatedly [4]. However, it is worth noting that the latter has intractable issues and barriers that must be overcome. Wind and solar are especially weather-dependent. Therefore, their intermittent nature can hinder the performance of these technologies for future commercialisation [[6]. However, introducing advanced energy storage and conversion, particularly fuel cell technology, offers a promising solution. Amongst several types of advanced energy storage and conversion, fuel cell technology stands out as a potential driver of the rise in energy needs and demand in society [7, 8], as demonstrated (Figure 1.1).

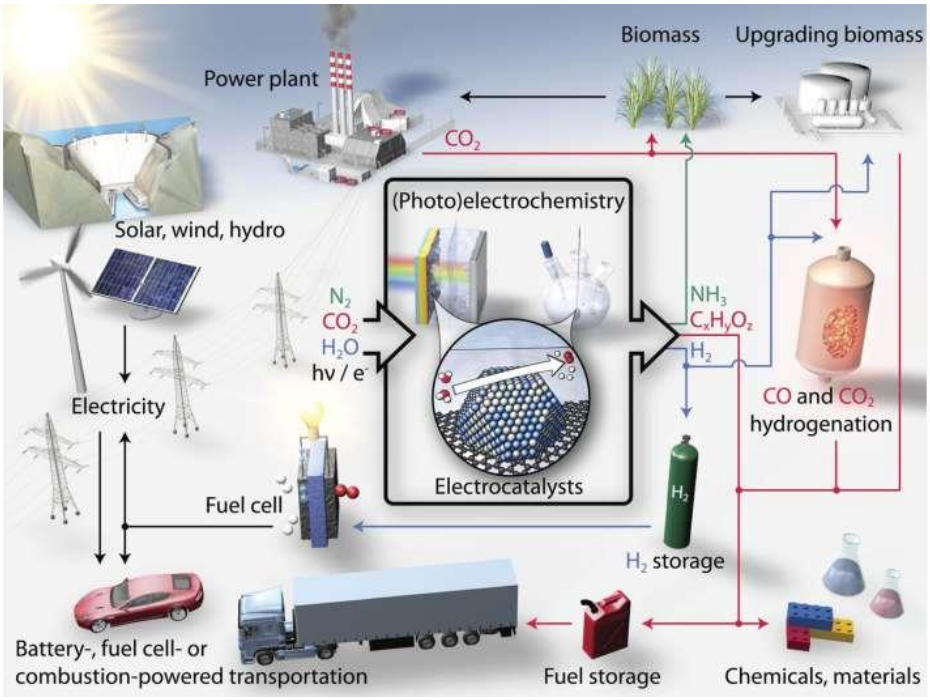


Figure 1.1 A schematic diagram describing the sustainable landscape [8]

Fuel cells are electrochemical devices that can convert the chemical energy of fuel into electrical energy, producing low emissions and high efficiency [9]. Compared to other fuel cells, DAFCs have drawn attention as sustainable/off-grid power supply for electronic (portable) devices [10]. Using liquid/renewable polyhydric alcohol fuels (Gly, EtOH, and EG) over hydrogen has become more advantageous. They became one of the hotspots in the research and development direction of DAFCs owing to their less toxicity, higher energy density, accessible storage, and handling [11].

Nevertheless, there are factors such as the use of electrocatalysts that are susceptible to poisoning during the oxidation of Gly, EtOH, and EG reaction in basic medium and end up hindering the progression of these devices. These limiting factors have a massive impact in such a way that they cause sluggish kinetics in anodic reactions, which leads to low efficiency, power loss, and the stability of the device [11, 12]. The great selection of electrocatalysts in DAFCs that run in an alkaline medium is more prominent than in other types of fuel cells [13]. In a basic environment, Pt-free electrocatalysts with a wide range of 3d transition metals are permitted to decrease the cost of noble metals and their loading. The electrocatalysts should be more stable and electrochemically active to realise the potential of DAFCs in the future.

The potential of Pd-based electrocatalysts is promising. Their ability to allow intermediate species to adhere to the surface catalysts, facilitating successful oxidation during the alcohol oxidation reaction, is a significant step forward. The alloying of Pd with one or two co-metals, such as Fe, Co, and Mn, has modulated the electronic structure of the Pd lattice through a bifunctional mechanism and synergistic effect between Pd and co-metals. These metals reduce the Pd content and contribute to the beneficiation of abundant minerals in South Africa, further enhancing the potential of Pd-based electrocatalysts in the future of DAFCs**.**

Building on the promising factors mentioned above, this research successfully synthesised Pd-based electrocatalysts supported on carbon (PdM/C where M = Fe, Co, Mn) using the $NaBH_4$ and MW methods. These methods were instrumental in enhancing the physicochemical properties of bimetallic catalysts at varied Pd: M ratios (1:1 and 2:1). The results unequivocally demonstrated that the MW method can effectively tune the physicochemical properties of these catalysts, leading to superior crystallinity and the generation of defects, particularly O_2 vacancies, which significantly improved the electrocatalytic activities towards the oxidation of Gly, EtOH, and EG.

Trimetallic Pd-based electrocatalysts (PdFeM/C where M = Fe, Co, Mn) were further synthesised via the MW method to investigate the effect of two co-metals. MW method was employed in this research study to provide an excellent acumen of physicochemical properties and electrochemical activity of Pd-based catalysts. It was observed that the use of MW had tuned the structural properties and reduced the nanoparticles of the electrocatalysts to sub 10 nm, which in turn led to the improvement of electrochemical behaviour towards AOR and ORR in an alkaline medium.

1.2 Study objectives.

The research objectives were stated as follows:

- To synthesise Pd based catalysts (Pd/C andPd_2Fe/C) using $NaBH_4$ method.
- To synthesis bimetallic Pd based electrocatalysts (PdFe/C, PdMn/C, and PdCo/C) supported on carbon using a microwave synthetic method (Pd_2M/C and PdM/C).
- To synthesise trimetallic Pd-based electrocatalysts (PdFeMn/C and PdFeCo/C supported on carbon using a microwave synthetic method.
- To investigate the physicochemical properties of the catalysts using MW methods through microscopic analysis such as TEM, SEM, BET, XRD, and XPS.
- To determine the electrocatalysts' performance and electrochemical evaluation (CV, CA, linear sweep, EIS, etc.) towards various alcohols (EG, Gly, and EtOH) in an alkaline medium.
- To determine electrochemical evaluation (linear sweep and ORR polarisation) of Pd/C, PdMn/C, PdFe/C and PdFeMn/C towards reducing oxygen.

1.3 Thesis outline

Chapter 1 (Introduction): This chapter introduces the thesis and elaborates more about the motivation, rationale, and objectives of the study. It also presents the outline of the thesis.

Chapter 2 (Literature Survey): This chapter provides an overview of DAFCs, the operations mechanism, and the intensive research on Pd-based electrocatalysts for AOR and ORR applications. The study also discusses the electrochemical characterisation employed in this work.

Chapter 3 (Experimental Method): This chapter describes the experimental procedure, materials and reagents, and characterisation conditions in depth.

Chapter 4 (Results and Discussion): This chapter elucidates the two different methods for preparing Pd/C and PdFe/C electrocatalysts. It thoroughly discusses their physicochemical properties and the electrochemical behaviour of both electrocatalysts toward glycerol electrooxidation in a basic environment.

Chapter 5 (Results and Discussion): This chapter probes the electrochemical behavior of bimetallic electrocatalysts at varied ratios toward ethanol oxidation reactions. Various electrochemical approaches were employed to obtain the electrocatalytic activity of the bimetallic electrocatalysts.

Chapter 6 (Results and Discussion): This chapter presents the electrochemical activity of bimetallic electrocatalysts in varied ratios toward the EG oxidation reaction in a basic environment.

Chapter 7 (Results and Discussion): This chapter discusses the electrochemical behavior of bimetallic electrocatalysts at various ratios toward the glycerol oxidation reaction in an alkaline environment.

Chapter 8 is the Results and Discussion: This chapter elucidates the comparison study of the trimetallic electrocatalysts for the oxidation of EtOH, Gly, and EG in an alkaline medium. Various electrochemical approaches were employed to obtain the electrocatalytic activity of the trimetallic electrocatalysts.

Chapter 9 (Results and Discussion): This chapter reports the electrochemical behaviour of palladium-based ferromanganese as an excellent anode electrocatalyst for ethylene glycol oxidation and oxygen reduction reactions.

Chapter 10 (Conclusions and Recommendations): This chapter reports the overall conclusions obtained from the study. Future work and recommendations are also included.

1.4 References

[1] A. Manthiram, A.V. Murugan, A. Sarkar, T. Muraliganth, Energy and Environmental Science. 1 (2008) 621-638.

[2] R. Gross, M. Leach, A. Bauen, Environment International. 29 (2003) 105-122.

[3] A.Z. Arsad, M.A. Hannan, A.Q. Al-Shetwi, M. Mansur, K.M. Muttaqi, Z.Y. Dong, F. Blaabjerg, International Journal of Hydrogen Energy (2022).

[4] N.L. Panwar, S.C. Kaushik, S. Kothari, Renewable and sustainable energy reviews. 15 (2011) 1513-1524.

[5] J.S. Zheng, X.S. Zhang, P. Li, J. Zhu, X.G. Zhou, W.K. Yuan, Electrochemistry Communication. 9 (2007) 895-900.

[6] M.Y. Worku, Sustainability. 14 (2022) 5985.

[7] L. Fan, Z. Tu, S.H. Chan, Energy Reports. 7 (2021) 8421-8446.

[8] Z.W. Seh, J. Kibsgaard, C.F. Dickens, I.B. Chorkendorff, J.K. Nørskov, T.F. Jaramillo, Science. 355 (2017) 4998.

[9] M.A. Abdelkareem, K. Elsaid, T. Wilberforce, M. Kamil, E.T. Sayed, A. Olabi, Science of the Total Environment. 752 (2021) 141803.

[10] M.H. de Sá, A.M. Pinto, V.B. Oliveira, Energies. 15 (2022) 3787.

[11] A. Kaur, G. Kaur, P.P. Singh, S. Kaushal, International Journal of Hydrogen Energy. 46 (2021) 15820-15849.

[12] A. Sandoval-González, J.A. Navarro, M.R. Martínez, F. Paraguay-Delgado, S.A. Gamboa, International Journal of Hydrogen Energy (2022).

[13] M.P.M. Kaninski, Z.V. Šaponjić, M.D. Mudrinić, D.S. Milovanović, B.M. Rajčić, A.M. Radulović, V.M. Nikolić, International Journal of Hydrogen Energy. 46 (2021) 38270-38280.

CHAPTER 2

LITERATURE REVIEW

The research and development of functional fuel cells (FCs) was first discovered in the early 1800s [1]. Sir W. R Grove coined the first FCs in 1839 - 1842. He accidentally found this device by reversing water electrolysis into H_2 and O_2 to generate electrical power, known as fuel cells, as demonstrated in Figure 2. 1a. Therefore, fuel cell technology was increasingly in demand. Furthermore, in the 1930s, a British scientist, Francis Thomas Bacon, invented alkaline electrolyte fuel cells, which differs from the acid electrolyte fuel cell discovered by Grove (Fuel Cells NIGEL BRANDON Imperial College London, United Kingdom). Bacon's discovery was further followed by the first achievable fuel cells (Alkaline fuel cells) coined in the 1950s in the search to produce the power for space flight by NASA Apollo space programme [2]. A diagram representing the achievable alkaline fuel cells used on a space flight is shown in Figure 2.1b. Since then, fuel cell development has become increasingly attractive when it gained recognition as an energy power source [1].

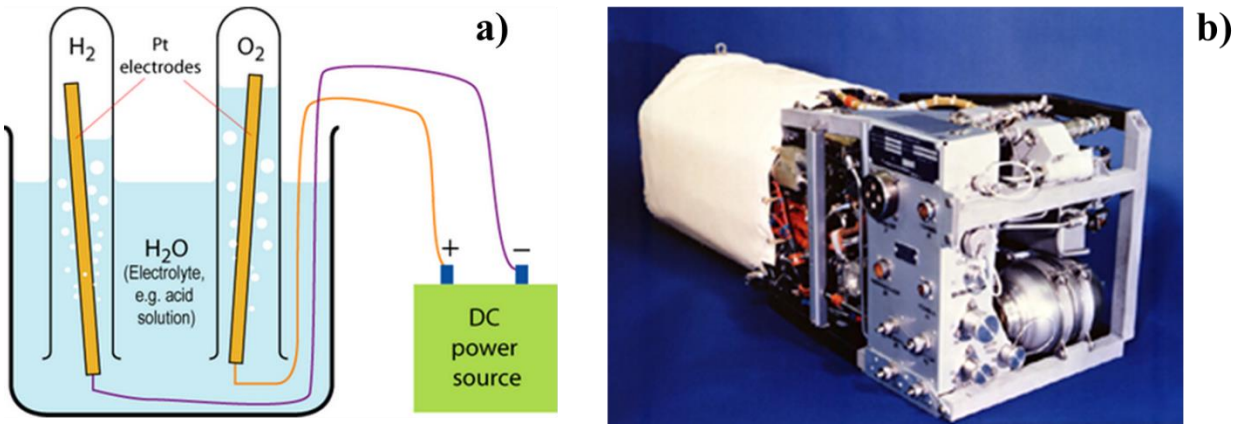


Figure 2.1: a) Electrolysis setup b) An Alkaline fuel cells used on space flight [103, 104]

2.1 Batteries, Heat engine, and Fuel cell comparison

As demonstrated by Grove, fuel cells possess electrochemical similarities with batteries, using internal redox reactions to convert electrical energy from chemical energy at the anode and

cathode reaction [3]. They are both squeezed with an electrolyte and an ionic conductor between the two electrodes (anode and cathode). However, their differences lie in that batteries are used for energy storage and conversion, allowing them to store energy for a while but ultimately depleting when consuming chemical reactants. On the other hand, fuel cells are energy conversion, which continue to operate as long as the reactants and oxidants are supplied to the electrode [3], as shown in Figure 2.3.

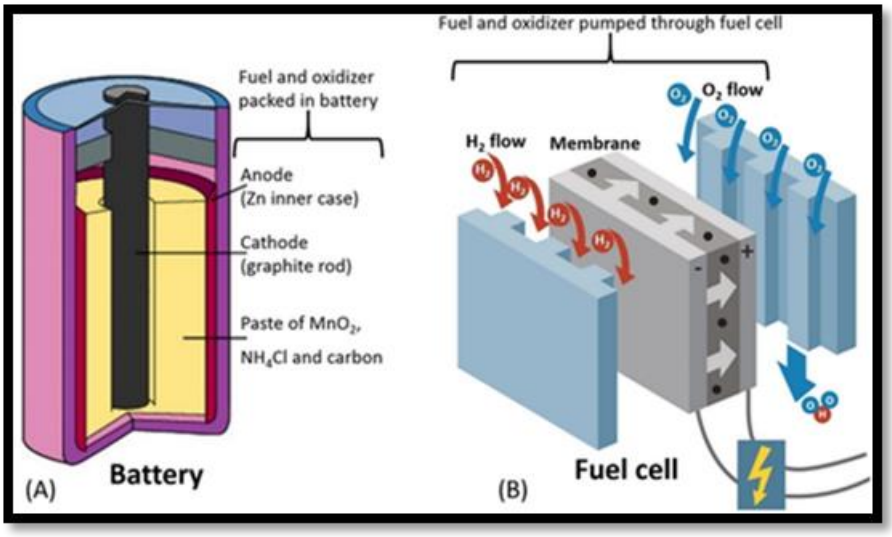


Figure 2.3: A schematic diagram displaying the A, Batteries and B Fuel cells. The picture shows how the fuel cells are supplied with fuel. [105]

In comparison to internal combustion engine energy conversion, fuel cell technology requires only one step to generate electrical power. In contrast, internal combustion engines apply numerous energy conversion steps to produce electrical power (From chemical to thermal to mechanical to electrical, as shown in Figure 2.4 [1, 3]. The drawback of this type of energy conversion is their unfriendliness to the environment, as they release harmful gasses (CO_2, SO_2) that can cause harm to the globe. In contrast, fuel cells have been a clean and more efficient technology that releases water as the only by-product to produce electricity, thus having no negative impact on the environment [4].

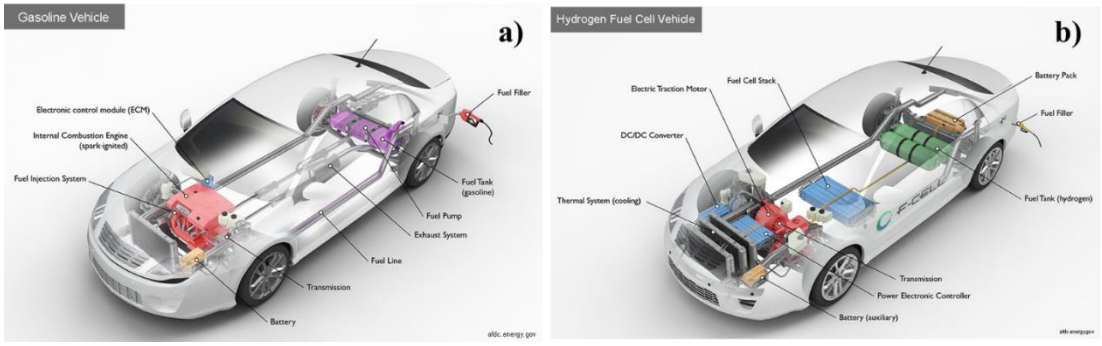


Figure 2.4: a) Typical gasoline car using a spark-ignited internal combustion engine, and b, Typical diagram showing a hydrogen-powered fuel cell [106, 107].

2.2 Operating Principles of FCs

A fuel cell is an electrochemical device comprising an anode - the oxidation of fuel, and a cathode - the reduction of oxidant [5]. Both electrodes are sandwiched with electrolytes in between to permit the flow of positively charged ions (protons) across the electrodes. For an active and functional performing fuel cell, electrocatalysts with extensive properties are required on both electrodes' surfaces to carry them out at a reasonable rate [5]. A fuel cell typically produces electrical energy from hydrogen (H_2), methanol, polyhydric alcohols (EtOH, Gly, EG), and hydrocarbons. They are named based on the type of fuel used, such as hydrogen fuel cells (H_2FCs), direct alcohol fuel cells (DAFCs) and direct formic fuel cells (DFAFCs).

At the crux of the hydrogen-fuelled cell, the hydrogen is supplied on the anode side, where electrocatalysts oxidise it into a proton (hydrogen ion) and electrons. The electrolyte only permits the movement of protons, and it is sandwiched between the positive (cathode) and the negative (anode) electrodes. Thus, the protons migrate through the electrolyte to the cathode side (+ve). Meanwhile, electrons circulate through the collector plates and pass the external circuit into the cathode side, forming an electrical current for any load connected to fuel cells [6]. The oxidant on the cathode side interacts with the hydrogen ions and electrons to produce water as its by-product. The structure of the simple Polymer exchange membrane Fuel Cells (PEMFCs) is demonstrated in (Figure 2.5):

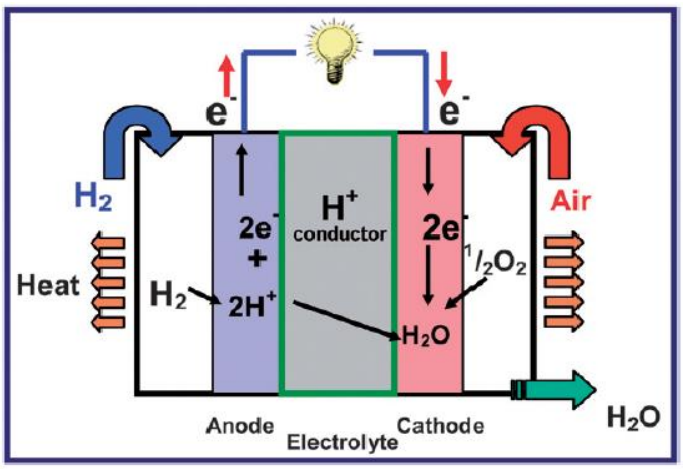


Figure 2.5: Operating principles of Polymer exchange membrane Fuel Cells (PEMFCs) [20]

2.3 Types and Classifications of Fuel Cells.

Fuel cells (FCs) are categorised into various kinds of technologies. They are classified according to the choice of electrolytes, the type of catalyst needed, the operating temperature, and other valuable factors. These varied factors make them unique to each other and easy to identify. Solid oxide fuel cells (SOFC), Phosphoric acid fuel cells (PAFC), and Molten carbonate fuel cells (MCFCs) use different electrolyte membranes to yield a superior amount of power. However, their high operating temperature delayed their use. Besides operating in low temperatures, PEMFCs and alkaline fuel cells still need compressed hydrogen as fuel and are limiting their production. DAFCs are not facing all these challenges due to unquestionable advantages. It does not require a fuel reformer because it can obtain hydrogen from liquid alcohol [4]. Table 2.1 briefly describes the fuel cell types and their specification [7, 8, 9].

Table 2.1: Description and performance of FCs type

Types of fuel cells	Operating temperature	Electrolytes	Type of Fuel	Advantages	Challenges	Application	Efficiency
Polymer electrolyte membrane fuel cell (PEMFC)	~ 80 °C	Solid polymer electrolyte (Teflon like membrane)	Hydrogen and direct alcohol	Quick start, low temperature	Expensive catalysts, Sensitive to impurities from fuel	Transportation, and mobile applications (i.e laptops and mobile phones)	Low efficiency (~30 – 35%)
Phosphoric acid fuel cell (PAFC)	175 – 200 °C	Liquid phosphoric acid	Hydrogen	Tolerant to impurities from fuel	Expensive catalysts, structural design problem	Transportation and stationary industries	~Efficiency (35 – 40%)
Molten carbonate fuel cell (MCFC)	600 – 700 °C	Liquid molten carbonate	Hydrogen	No catalysts and separate reformer not needed	Intolerant to sulfur and slow start up	Large stationary power generation	High efficiency (50 – 60%)
Solid oxide fuel cell (SOFC)	1000 °C	Dense yttrium stabilized zirconia	Hydrocarbons	No need for separate reformer to extract H_2	Slow start up, very expensive and intolerant to sulfur	Stationary power and distribution generation	High efficiency (50 – 60%)
Alkaline fuel cell (AFC)	100 °C	Potassium hydroxide (KOH)	Hydrogen	Rapid start, low cost	Sensitive to CO_2 , require separator system to eliminate CO_2 , utilizes corrosive electrolyte	Space exploration, fleet vehicles and boats	Efficiency (60 - 70%)

2.4 An overview of DAFCs in alkaline environments

DAFCs are electrochemical devices that transform electrical power from chemical energy stored in liquid [9, 10]. These FCs have attracted considerable attention over gaseous fuel as a power supply for electronics (portable) and stationary devices [11]. They perform at low temperatures quietly, with no noise or vibration. In 1954, Palve conducted the first FCs pumping alcohol as a fuel of choice. His first discovery was using methanol in aqueous electrolytes to develop DMFCs [12]. It has been reported that the delay in commercialising these types of fuel cells is due to their drawbacks, which still need more rapid development. These limitations have the propensity to produce the deficient performance of the device and below are the disadvantages [12]:

- Alcohol crossover occurred between anode and cathode electrodes via the Nafion (DuPont)electrolyte membrane.

- Reaction mechanism is complex.
- CO poisoning of the anode electrocatalysts hampering the development of DAFCs.
- To design and develop a stable, low-cost, highly active electrocatalyst [13].

Since then, primary alcohols such as EtOH, 2-propanol, gly, and EG emerged to be the most considered fuels thus far inspired by their high volumetric energy density, less toxicity, facile storage, handling, and transportation over methanol [12, 14]. Thus far, the use of ethanol in DEFCs has received considerable attention. This carbon-neutral fuel source is less toxic, possesses higher energy density (theoretical energy density 8.0 kW h/kg) and can be regenerated from biomass in enormous quantities through a fermentation process of sugar and cellulose-containing raw materials [15]. Since then, scientists have paid much attention to the incubation of DEFCs.

DEGFCs have garnered significant interest among the known fuel cells as the most prospective energy power source for mobile and stationary applications [16]. These phenomenal types of FCs employ EG as a potential fuel. EG stands out among other fuels owing to its renewability from biomass, low toxicity, low cost, and high theoretical energy density of approximately 5.2 kW h / kg [15, 17, 18].

In contrast, glycerol as polyhydric alcohol is produced massively as a co-product of the biodiesel industry. It is initially obtained through methanolysis from vegetable oils as a natural by-product. It has stimulated enormous attention in the past decades due to its low virulence; it theoretically possesses an energy of about 5 kW h / kg and a more significant number of exchanged electrons (14 electrons/glycerol molecules) for the successful oxidation completion from mesoxalate to carbonate (CO_3^{2-}) [19, 20].

All the potential DAFCs use an electrolyte membrane, which operates in two different environments: an alkaline and an acidic medium. It was discovered that this type of fuel cell exhibits exceptional performance when operating in an alkaline medium, unlike in an acidic medium. In an alkaline medium, Kamarudin and co-workers (2013) mentioned that DAFCs exhibit good polarisation characteristics in methanol oxidation on the surface of the platinum electrode [21]. It endows the possibility of utilising non-noble metals to decrease the challenges faced with the cost of noble metals catalysts, less susceptible of electrocatalysts towards corrosion and rapid kinetics of both AOR and ORR, which enhances the performance of the

cell, alleviate the conduction of hydroxyl ions from cathode to anode [22]. From then forth, alkaline-type DAFCs have attracted much interest over acidic, and enormous electrocatalysts were designed specifically for these devices with high cell performance.

2.5 Operating principles of DAFCs in alkaline medium

During operation, suitable alcohol is oxidized on the anode side by the designed electrocatalysts to yield carbon dioxide and electrons. The electrons are transported across the current collector/external circuit into the cathode side and interact with the oxygen/air. The reduction process (oxygen with electrons) occurs at the cathode, generating- OH ions. The produced ^{-}OH ions penetrate back to the anode via the electrolyte membrane (anionic exchange membrane) [12, 23]. Anionic exchange membrane (AEM) assists in preventing the cell from being vulnerable to alcohol crossover. The reaction mechanism is presented in Equation 2.1 for DAFCs taken as an example:

Anode oxidation:

$$CH_3OH + 6OH^- \longrightarrow 6e^- + CO_2 + 5H_2O \quad E° = -0.18\ V$$

Cathode reduction:

$$3/2O_2 + 3H_2O + 6e^- \longrightarrow 6OH^- \quad E° = 0.40\ V$$

Overall reaction

$$CH_3OH + 3/2O_2 \longrightarrow CO_2 + 2H_2O \quad E° = 1.21\ V \qquad (2.1)$$

2.6 Electrocatalysts in DAFCs

The development of heterogeneous electrocatalysts has rapidly become a versatile class of catalysts with a wide range of applications over the past decades. Electrocatalysts are materials that can accelerate chemical reactions without being used. The exciting view about electrocatalysts can be applied in various domains such as fuel cells, water purification, biodiesel production, medicine, and dye industries over a conventional catalyst [24]. Each electrocatalyst field benefits from converting crude oil, coal, and natural gas to fuels, producing petrochemical and chemical products, and emission control of Carbon monoxide, hydrocarbons, and nitrogen oxide [24]. Thus, the electrocatalysts in DAFCs play the role of

breaking down/reducing the oxygen at the cathode and oxidizing the alcohol at the anode side of the cell. Furthermore, a good electrocatalyst choice can enhance the cell's performance without compromising its durability [25]**.** During the past decade, efforts have been devoted to developing the electrocatalyst's performance to reach a successful corollary. The reason is that the electrocatalysts can be poisoned effortlessly, and kinetics tend to be sluggish during oxidation.

Ideally, nano-sized catalysts with large surface area are needed to optimise the surface of the electrode; when the surface is enhanced with the small number of atoms in nanoparticles, the intrinsic catalytic performance changes beyond and extends the surface area [24, 26]. The exciting prospect of nanosizing the material is the ability to enhance the electrocatalytic properties by eliminating the intermediate on the surface of the catalysts. For these reasons, several catalysts have been studied for the anode, such as single, double, and multiple components catalysts [25, 27].

2.7 Pd catalysts for the oxidation of alcohol in an alkaline environment.

2.7.1 Single components catalysts

Single-component catalysts, sometimes called monometallic catalysts, contribute significantly to fuel cell development. Catalysts such as platinum, gold, palladium, etc., have shown practical corollary in DAFCs systems even though commercialisation is confined. A tremendous study has been conducted on platinum as an essential catalyst, notably in an acidic medium for DMFCs. It also reveals an excellent performance in ethanol fuel cells when treated in an acidic platform. Much research has shown that platinum is mostly stable when operating in an acidic medium, unlike in an alkaline environment, because it is an excellent oxidizing promoter in low pH [25]. It can minimize the blockage on the electrode surface caused by salt formation during the reaction of the reactant [25].

Due to the low pH, the selection of catalysts is limited in an acidic medium. Some catalysts, such as palladium and gold, exhibit poor reactivity in a low pH medium, albeit, in high pH, their reactivity is the best. Due to that reason, extensive effort has been made to reduce the damage of the palladium and gold catalysts caused by the low pH while enhancing the cell

performance. Even the high cost and vulnerability to intermediates of platinum are forcing researchers to explore other metals and diversify their use of alcohols besides methanol.

Many researchers have paid attention to palladium, the analogy of platinum but more electroactive in a high pH medium/an alkaline medium. Palladium is 50 times more abundant in nature, has a lower price than platinum, and can oxidize extensive alcohols in an alkaline environment [28, 29]. Even though they show excellent activity and stability in alkaline medium, their surfaces aggregate with time if not supported with a conductive material, causing the surface area to decrease [28]. Conductive material possesses varied structure, sizes, and morphology.

Support materials such as a wide range of oxides (CeO_2 and NiO) [11], the use of carbon matrix like Vulcan XC-72, tungsten carbide nanocrystals, carbon microspheres, ultrahigh surface hollow carbon spheres, carbonized TiO_2 nano-sized tubes, multiwalled carbon nanotubes, and activated carbon nanofibers were studied thoroughly to enhance the conductivity and electroactivity of Pd/C. [30]. Xu and his co-workers 2008 examined the effect of introducing remarkable oxides such as (CeO_2 and NiO) to the Pt/C and Pd/C electrode for ethanol oxidation in an alkaline electrolyte. They revealed that the oxide-promoted electrocatalysts have the highest catalytic activity towards ethanol oxidation than those without the oxide [31]. The work performed by Su and colleagues 2012 used Pd/C to investigate alcohol electrooxidation in an alkaline medium, and it showed that Pd supported on carbon has higher oxidation activity in EtOH and isopropanol than in methanol [32]. Pd/C was extensively studied and realised that alloying with co-metals would enhance the activity and strengthen the binding energy between the co-metals and Pd.

2.7.2 Bimetallic and trimetallic electrocatalyst

Developing a highly recommended and active electrocatalyst is a significant challenge for application in DAFCs. Recently, it was proposed that using Pd-based bimetallic and trimetallic electrocatalysts has what it takes to enhance the performance of this notorious device over monometallic catalysts. However, the extensive performance was only shown in an alkaline environment rather than an acid electrolyte, especially when utilising the 3d transition elements as co-metals. The attractive benefit of an alkaline medium involves expediting the reaction kinetics of both anodic oxidation and cathodic reduction [25, 27].

The rationale for alloying is similar for platinum as they all contribute to strengthening the electron configuration, altering the Pd-Pd or Pt-Pt bonding length, improving their lattice compressive stress, modifying the electronic structure between the two metals, and changing the surface condition [13]. The slight structural modification of the alloy has a massive impact on the synergistic effect between the metals and Pd caused by the stress and ligand effect [33].

In addition, the bi-functional mechanism reported by Sheikh and colleagues 2014 assumed that the integration of co-metals to Pd/Pt can supply a surplus of hydroxide species at the anodic side of the electrode to facilitate the oxidative desorption of Co-intermediate product [34, 35]. Zhang and co-workers 2008 further reported the following three steps to describe the bi-functional mechanism of typical Pt-Au catalysts as indicated in Equation 2.2 [36]:

$$\begin{aligned} &Pt\text{-}CO_{ad} + Au\text{-}OH_{ad} \longrightarrow CO_2 + H^+ + Pt + Au + e^- \\ &Au\text{-}CO_{ad} + Au\text{-}OH_{ad} \longrightarrow CO_2 + H^+ + Au + e^- \\ &Pt\text{-}CO_{ad} + Pt\text{-}OH_{ad} \longrightarrow CO_2 + H^+ + Pt + e^- \end{aligned} \qquad (2.2)$$

Based on these steps, it is evident that Au played a significant role in Pt reactivity due to the upshift of the surface's d-band center, which aligns with the prediction made by the Hammer-Norskov model [36, 37]. According to the Hammer-Norskov model, the shift in the d-band center results from the surface alloying or pseudomorphic overlayer formation to several adsorbates [37]. Their study also demonstrated that when the metallic atoms are tiny and integrated with giant atoms, their neighbors shift away and cause a smaller d-band width than at the surface of the elemental metals. Thus, the d-band position is upshifted to control the similar d-band filling locally [37]. Adding Au to Pt/C has significantly enhanced the catalytic activity and has stronger poison resistance than commercial Pt [36].

2.7.3 The role of electrocatalysts in ethanol electrooxidation reactions.

Thorough research on electrocatalysts towards ethanol oxidation has been excessively explored for alkaline environments. Shen and co-workers (2010) reported that Ni into Pd/C consistently enhances ethanol electrooxidation's stability and activity over Pd/C [38]. Their studies revealed

the satisfactory performance of PdNi/C with a higher power density of 90 mW cm^{-2} operated at 60 °C for ADEFCs using AEM. Ni is an excellent oxygen-species attractor that contributes an abundance of the hydroxyl groups on the surface of Pd to further mitigate the poisoning during the adsorption/desorption phase [38]. Due to the excellent behaviour of Ni towards Pd/C, various researchers performed extensive studies, and the pair showed outstanding catalytic activity.

It is imperative to meticulously design experiments before use and determine the optimum ratio of the catalysts that endow the highest AOR results. Various ratios of the catalysts performed differently in the alcohol oxidation reaction. This study was confirmed by the research conducted in 2022 by Climaco and co-workers, who found that adding Fe and Ni to Pd at different ratios (80:10:10, 70:15:15, and 60:20:20) enhanced the electrocatalytic activity in ethanol electrooxidation [39]. Their research displayed higher activity and stability in ethanol oxidation at 70:15:15 ratios [39].

2.7.4 The role of electrocatalysts in ethylene glycol electrooxidation reactions.

Limited research addresses the use of both Pd-based bimetallic and trimetallic electrocatalysts toward the oxidation of EG in alkaline electrolytes. The work performed by Ramulifho and co-workers 2013 has reported that the bimetallic mixture between PdNi/MWCNT and PdSn/MWCNT delivered better electrocatalysis towards the oxidation EG over monometallic Sf-MWCNT-Pd [40]. Other metals and oxides were explored to improve the activity and durability of Pd based on the electrooxidation of ethylene glycol. The research conducted by Ren and colleagues in 2021 established the use of Pd/RGO decorated with MnO_2 rod-like for ethylene glycol electrooxidation [41]. Adding MnO_2 to Pd/RGO boosted the electroactivity and the long-term stability relative to pure Pd towards ethylene glycol [41].

The research carried out by Li and co-workers in 2016 was to design and synthesise trimetallic electrocatalysts (PdRuBi/N-Graphene) for improving ethylene glycol electrooxidation. The synergistic behaviour formed between Ru and Bi promoted the catalytic activity and durability of Pd towards the oxidation of EG [42]. Fashedemi and Ozoemena in 2014 reported the comparative electrocatalyst properties of core-shell Pd-based trimetallic towards the oxidation of three various alcohols (EtOH, EG, and Gly) oxidation in the basic medium [43]. By varying the alcohols, the results revealed that Pd-based ferroalloys exhibited a superior electrocatalytic

response to EG oxidation than EtOH and Gly [43]. Even though the research on electrocatalysts towards the oxidation of EG is a paucity, the work reported from the past literature has shown that adding co-metals into Pd enhances activity and durability.

2.7.5 The role of electrocatalysts in glycerol electrooxidation reactions.

A few researchers have reported using Pd-based bimetallic and trimetallic electrocatalysts toward Gly oxidation reactions in an alkaline medium. Serov and their colleagues in 2013 described the use of un-supported Pd-Ir at varied ratios towards the electrochemical oxidation of CH_3-OH, EtOH, EG, and Gly [44]. Their electrochemical evaluation has shown that the electrocatalyst possesses superior EG and Gly activity. The other study was conducted by Geraldes and fellow workers in 2014 on using Pd/C, Au/C and PdAu/C electrocatalysts towards Gly electrooxidation in alkaline medium. It was reported that PdAu/C, at 50:50, displayed a higher electrochemical activity towards Gly oxidation to Pd/C and Au/C electrocatalysts [45]. Another research study was conducted by Cassani and colleagues in 2021 using Fe-modified Pd supported with either Vulcan or RGO for ORR and Gly reaction in an alkaline medium [46]. They have observed the synergistic effect of the bimetallic PdFe/RGO or PdFe/C electrocatalysts, increasing electrocatalytic activity. These excellent findings from previous work make using Pd-based electrocatalysts for Gly oxidation more interesting to study and explore.

2.7.6 Pd-based ferroalloy nanostructures

A low toxicity, low cost, environmentally benign, and abundant anode and cathode electrocatalysts have been proposed in this thesis for the oxidation of alcohol and ORR in a basic medium. Research in alloying palladium with ferroalloys is one of the cost-saving mechanisms this fuel cell is longing for. The Pd-based electrode diluted with ferroalloys has multiple advantages, intending to decrease the costs of catalysts and augment the electrocatalytic behaviour. The usage of ferromagnetic electrocatalysts such as iron (Fe), cobalt (Co), and manganese (Mn) was explored towards ORR activity in the acidic medium [47-50]. However, these metals are eroded in the acidic medium, and there is severe aggregation and poor hydrothermal stability on the active surface area [51, 52]. Thus, motivated by the scarcity mentioned above in the report on ferroalloys towards alcohol oxidation in alkaline environments, it is desired to employ Fe, Co, and Mn as alternative ferroalloys to non-noble

metals to close the gap. Fe, Co and Mn metals have been investigated as the second and third metals for Pd ferroalloy electrocatalysts due to their permanent magnetic moment when leached out with Pd in the alkaline environment [53]. Their alloys were found to be face-centered cubic in crystalline structure and a single phase below the melting point [54].

Iron has been described as one of the fourth most excessive metals in nature, with a composition of 5%. It is in group eight on the periodic table and is classified as brittle and hard substances. This element is also abundant in South Africa and found in various mines, such as iron ore mines like the Sishen and Kolomela in the Northern Cape and the Thabazimbi mine in Limpopo [55]. It is the main ingredient in steel to manufacture cars, ships, and general machinery. In PEMFC, Fe has attracted increasing interest as a magnetic nano-sized transition metal for CH_3OH oxidation and ORR. Fe itself could vividly influence the catalytic activity of noble metals compared to other metals. Adding Fe^{3+} on Pt or Pd intensifies the catalytic activity in the alkaline medium toward methanol oxidation. Fe metal can change the structure of Pt and its surface state, promoting hydroxyl species' adsorption by inhibiting the active surface's intermediates [54, 56].

Cobalt is a rare ferromagnetic metal found in the earth's crust, about 0.001%. It belongs to the first row of transition elements; hence, their magnetic properties are similar to the one stipulated for Fe [57]. It has been integrated with iron to create different alloy magnetic materials in many applications. Co has been utilised in various industries and commercial and military applications. In fuel cells, the addition of the nanostructured Pd with Co has been explored for CH_3OH electrooxidation and ORR. The effect of alloying Pd with cobalt is similar to that of Au, Ru and Fe. Vecchio and co-workers 2018 investigated the electrochemical behaviour, such as the performance, the tolerance to permeated methanol, and the durability of PdCo/C in half-cell and direct methanol fuel cells compared to Pd/C and commercial Pt. They have reported that the small amount of cobalt in the crystalline structure of Pd resulted in better durability and higher performance than Pt/C and Pd/C [58]. Luo and co-workers carried out further studies of Co on Pd nanostructured in 2019, where they found that the trimetallic CoAuPd electrocatalysts have enhanced catalytic performance by surface reconstruction towards methanol oxidation and oxygen reduction reaction than AuPd [59].

Manganese is found in the earth's crust as the 12th most abundant element, with about 0.1% average concentration. In 1774, manganese was discerned and isolated as a separate chemical

element by Carl Wilhelm Scheele and Johan Gottlieb Gahn. Potassium permanganate ($KMnO_4$) was the first commercial use of manganese produced in 1659 by Johann Glauber [60]. Therefore, since then, Mn production has continued to thrive nationwide. Commercial ferromanganese production was first discovered in France in 1875, containing 65% of Mn using blast furnace technology. South Africa has about 75% of the world's manganese resources. Over 90% of manganese are found in the Kalahari manganese field situated in the Northern Cape. The important commercial use of Mn ferroalloys is in steelmaking [60]. In DAFCs application, the first report of alloying Pd nanostructured with Mn appeared in 2008 by Xu and co-workers [61]. These authors demonstrated the use of metal oxides such as (CeO_2, Co_3O_4, Mn_3O_4, and NiO) onto PdC electrocatalysts towards alcohol oxidation, resulting in much higher catalytic activity and better electrochemical stability than those of any Pd/C electrocatalysts.

Cerium is a rare metal that is most abundant, with about 0.0046% of its crust. It has been reported that cerium is attained through the ion exchange process from monazite sand (Ce, La, Th, Nd, Y) PO_4 [62]. Pure cerium has the propensity to ignite if scratched with a sharp object; however, alloying cerium with other metals was safely used. Its application is to make Carbon arc lights used in the motion picture industry for studio lighting and projector light. As a catalyst, refine petroleum and an alloying agent to fabricate a unique metal [63]. In direct alcohol fuel cell applications, Ce has often been reported as a metal oxide alloyed with Pd, sometimes as a support material for the alcohol oxidation reaction. Bambagioni and co-workers 2012 reported using Pd-CeO_2/C to oxidize ethanol in alkaline media in half-cells and passive and active direct ethanol fuel cells. Compared with Pd/C, the co-support ceria has significantly decreased the onset potential towards ethanol oxidation [30]. The study also demonstrated that ceria promotes species-absorbed formation on Pd and Pd-OH at low potential.

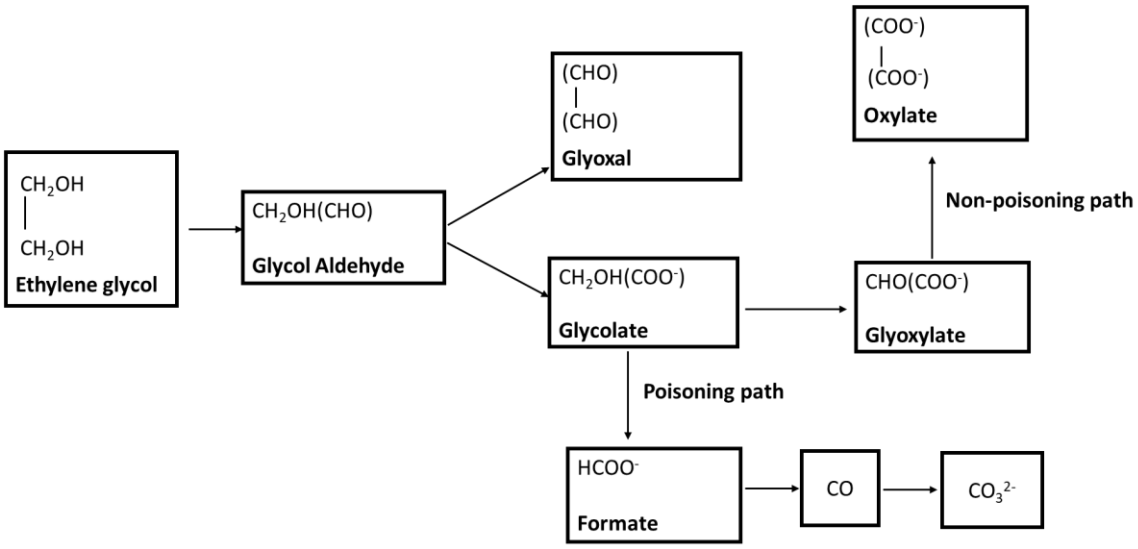
2.8 Reaction mechanism

Alcohol oxidation has demonstrated superior performances in alkaline species compared to acidic medium. While methanol requires six electrons for complete oxidation, EtOH, EG, and Gly are more difficult to completely oxidize to CO_2 due to their higher electrons exceeding ten. Therefore, identifying suitable and effective catalysts was considered to recover the maximum energy of an alcohol molecule to lead to CO_2 [64]. Even though the mechanism using the non-

noble metals remains unclear, the following steps may be proposed to fathom the mechanism as shown in Equation 2.3 of EtOH oxidation on Pd electrodes [65, 66]:

$$\begin{aligned}
&Pd\text{-}CH_3CH_2OH \longleftrightarrow Pd\text{-}(CH_3CH_2OH)_{ads} && 1\\
&Pd\text{-}(CH_3CH_2OH)_{ads} + 3OH^- \longrightarrow Pd\text{-}CH_3CO_{ads} + 3H_2O + 3e^- && 2\\
&OH^- \longleftrightarrow OH_{ads} + e^- && 3\\
&Pd\text{-}CH_3CO_{ads} + Pd\text{-}OH_{ads}^- \xrightarrow{r.d.s} Pd\text{-}CH_3COOH + Pd && 4\\
&Pd\text{-}CH_3COOH + OH^- \xrightarrow{fast} Pd + CH_3COO^- + H_2O && 5
\end{aligned} \tag{2.3}$$

Expressly, Equation 1 and Equation 2 represent the dissociative dehydrogenation/adsorption of acetyl group (CH_3COads) and CO- species on the catalyst surface. Equation 3 describes the adsorption of OH^- species on the surface of the catalyst. Equation 4 is postulated as the rate-determining step, which indicates that the adsorbed ethoxy intermediates ($Pd\text{-}CH_3COOH$) were stripped away by OH^- on the active site to yield an acetate ion (CH_3COO^-) and augmented the current density. The EOR cannot be further oxidized to CO_2. Instead, it produces an acetic acid involving only two or four electrons. The first reported mechanism behaviour towards the electrochemical oxidation of EG in a basic media was in 2005 [67, 68]. According to their perspective, the oxidation of EG undergoes oxalate, representing the non-poisoning path, and formate is the poisoning path. Their studies further discussed that the formation of oxalate is very stable in alkaline solutions. No CO poisoning species are expected at this path since it cannot be oxidized further while formate adsorbed CO poisoning species [67, 68]. The proposed reaction pathways of ethylene glycol are represented in Scheme 2.1:



Scheme 2.1: Schematic diagram representing the ethylene glycol pathways indicating the poisoning and non-poisoning paths [72]

The electro-oxidation of Gly has been investigated, and several products have been reported. Glycerate was the first obtained product, leading to tartronate, which can also be produced straight from Gly oxidation. Ozoemena has reported that by breaking down the C-C bond, tartronate species are replaced into glycolate and formate paths, forming carbonate. The complete oxidation of Gly to carbonate requires fourteen electrons [69]. The produced glycolate was further oxidized to oxalate. The work reported by Fashedemi and co-workers on Gly oxidation revealed that FeCo@Fe@Pd –MWCNT-COOH delivered a better amount of carbonate to around 73% than Pd/MWCNT-COOH (47%). This work has speculated that Pd-based core shells can oxidize Gly completely with improved efficiency [15].

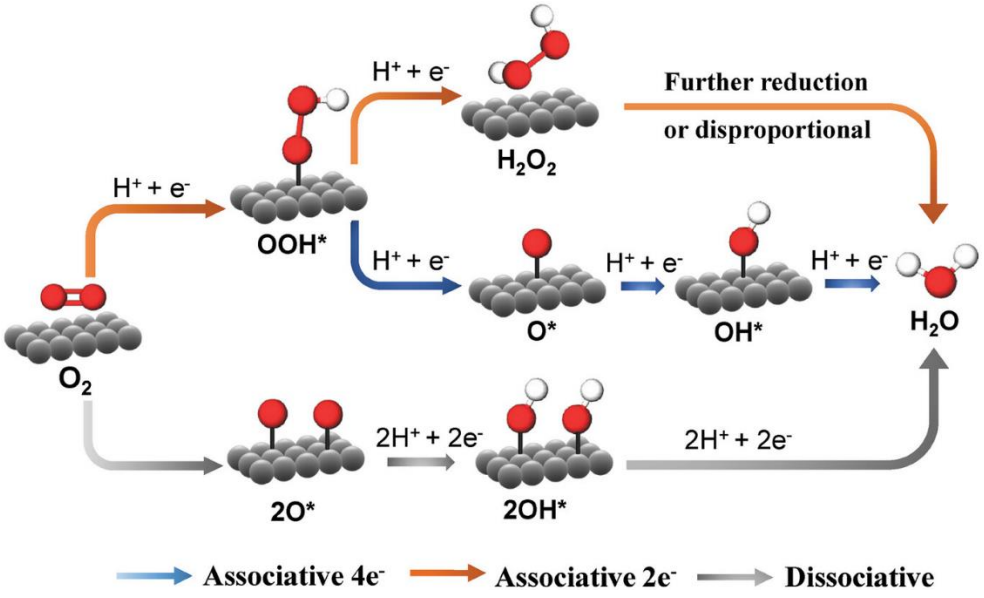
2.9 Cathode material

2.9.1 ORR in alkaline environment

Research on the ORR is significant for the progression of ADAFCs, whereby oxygen is employed as a gaseous fuel source. In DAFCs, the ORR plays a vital role as a cathodic process to permit oxygen flow. Despite the significant role of this device, the cathodic process has severe challenges in finding efficient and affordable electrocatalysts to enhance the ORR kinetics. The ORR's slow kinetics impede the commercialisation and development of the low-temperature device [70]. The desired ORR catalysts should be able to minimize the oxygen (O_2) species to produce water through a four-electron process.

2.9.2 Operating principles of ORR in alkaline medium

During the reduction of O_2 molecules, two parallel mechanism pathways are generated when operating in alkaline conditions. The first stage involved the "direct" four-electron path that occurred during the reduction of O_2 to water (H_2O) and is more favourable and stable. The subsequent stage involves the "partial'' two-electron transfer reaction where hydrogen peroxide (H_2O_2) is formed as an intermediate species and can be unstable and easily converted to H_2O [71, 72]. Scheme 2.2 illustrates all reaction pathways [103].



Scheme 2.2: Schematic diagram of the two and four ORR pathways in neutral environment [108].

2.9.3 Kinetics of ORR

The kinetics of the four-electron pathway can be described using the Tafel equation, in which the current density is related to the overpotential. In general, the rate of an electrochemical reaction as a function of the overpotential when applied to the ORR concept can be discussed using the Butler-Volmer equation, which illustrates the analog between the exchange current density, reaction rate constant, and overpotential occuring at the electrode. This concept helps us understand the kinetic reactions of the electron transfer involved in the system. It accounts for both the oxidation and reduction happening in the ORR. A kinetic model can be expressed using a corresponding Butler – Volmer Equation 2.4 [109].

$$j = j0\ \left[\exp(\frac{\alpha nF\eta}{RT}) - \exp(\frac{-(1-\alpha)nF\eta}{RT})\right] \quad (2.4)$$

Where j is the current density, $j0$ is the exchange in current density, α is the charge transfer coefficient, n is the no. of electrons involved in the rate-determining step (n = $4e^-$), F is the Faraday's constant, η is the overpotential, R is the universal gas constant and T is the Temperature

2.9.4 Electrocatalyst For ORR application

Platinum (Pt), platinum-based catalysts have been extensively studied as catalysts for ORR. They exhibit excellent catalytic responses, among other catalysts reported in the literature. However, Pt-based electrocatalysts suffer from expediting the kinetics of fuel cells; therefore, without any doubt, the need to find and develop a new catalyst is underway [73]. Palladium-based catalysts were selected as the viable alternative to Pt-based cathode since they enabled the ORR kinetics in alkaline media and offered a higher activity [74]. Table 2.2 summarises other work conducted on ORR using various Pd-based catalysts.

Table 2.2: Summary of electrocatalysts for ORR applications

Catalysts	**Synthetic method**	**Electrolytes**	**Tafel slopes mV dec^{-1}**	**References**
Pd/PANI/C	Carbon – nitrogen method	O_2 saturated 0.1 M KOH.	a = - 59.5 b = - 111.7	111
Porous PdFe nano hydrangeas	Cyanogel-derived method	O_2 saturated 0.1 M KOH.		112
Pd_3 Fe/C	a low-temperature single step co-reduction method	0.1 M $HClO_4$ saturated with oxygen	69	113
Nanoporous Pd-Cu	Electrochemical de-alloying of pre-deposited Pd-Cu films	0.1M KOH	-58	114
Pd/MnO_2	Hydrothermal method.	O_2 saturated KOH	84	115
PdZn	Co – reduction method	O_2-saturated 0.1 M KOH	b = 81.3	116

Pd@Au/RGO core-shell NPs	Reduced graphene oxide (RGO) support by a facile two-step protocol	O_2-saturated 0.1 M KOH		117
TiO_2Pd_3	Sonochemical reduction method	1 M KOH electrolyte solution	36.7	118
PdCo/rGO	Chemical reduction	0.1 M KOH	a = 62 b = 125	119
PdNi	Polyol technique	0.1 M NaOH solution saturated with oxygen	a = 60 b = 120	120

The Pd-based nano-catalyst discussed in this research study will be tested for ORR in alkaline behaviour. The reason is that the Pd-based ferroalloys are reported in the literature as the best catalysts for both anode and cathode. Mohanraju and co-workers have studied the trimetallic alloys (PtFeCo and PdCoFe) for ORR using the solvothermal method. The ORR studies revealed that both the trimetallic alloys belong to the four-electron transfer mechanism with faster kinetics and higher efficiency. The performance was higher than that of Pt alone and pure Pd catalysts [49].

2.10 Preparation and methodology of electrocatalysts

The synthetic method significantly influences the physicochemical properties of catalysts, including their structure, size, and morphology. Choosing a suitable method for developing electrocatalysts is crucial in determining the electrochemical activity of DAFCs. Extensive research has been conducted on various techniques, reflecting the breadth of the field. The reported methods for nano-catalysts in DAFCs include co-impregnation reduction [75], micro-emulsion synthesis [76], electrochemical deposition [77], vapour deposition [77], organic sol [78], thermal decomposition [79], microwave synthetic method [80], and chemical reduction in aqueous solution [11].

2.10.1 Microwave assisted technique.

The synthesis method of inorganic nanomaterials utilising microwave-assisted technique has recently attracted attention [81]. Generally, microwave irradiation has been utilised to heat the

materials rapidly at a short reaction time and low reaction temperature compared to conventional heating. This popular method provides a metastable phase and polymorphs at a low temperature. The metastable phase (convectional process) cannot form at high temperatures [82, 83]. A metastable phase has the propensity to show the physiochemical modification of the catalysts with a typical valence state [84]. Microwave irradiation is electromagnetic waves consisting of perpendicular electric and magnetic fields with frequencies ranging between 300 MHz – 300 GHz and corresponding wavelengths of 1 mm – 1 m [81, 85]. The electric field transfers energy to heat substances, while the magnetic field is inactive. On the electromagnetic spectrum, it falls between infrared and radio frequencies [86].

The microwave-assisted technique is a unique and facile technique that can be carried out using standard organic solvents such as dimethyl sulfoxide, 1-methyl-2-pyrrolidone, 1, 2-dichlorobenzene and ethylene glycol under open or sealed vessel conditions [87, 88]. The microwave provides fast, clean, and efficient processing of materials with a higher yield [89]. It is, thus far, considered as green chemistry [90]. It appeared as a crucial new tool for reducing particle size distribution, dissolution enhancement of the materials, and containing high purity compared to conventional method approaches. During the microwave process, the material's polar molecules interact with the microwaves, resulting in the formation of rotation and vibrational motion of polar molecules. Therefore, heat is generated within the material. The process is believed to develop a uniform material heating, resulting in suitable structural modification [86]. Figure 2.6 below represents the comparison of the heating process between microwave and conventional heating. MW heating is better than conventional heating because, during conventional heating, the material's surface is first exposed to the heat, followed by the heat circulating inside the material. In contrast with MW heating, the heating begins from the inside of the material and transfers to the surface of the material.

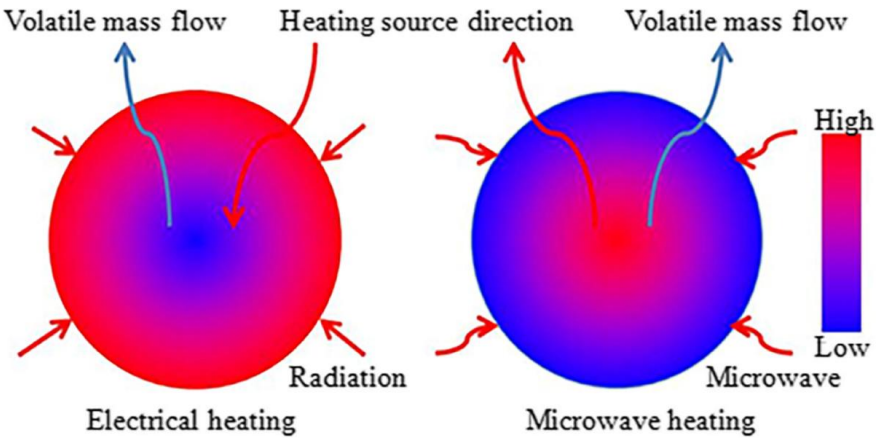


Figure 2.6: A schematic diagram representing microwave vs conventional heating [110]

This research work used the MW method to prepare the Pd-based ferro electrocatalysts. This method was used to further probe the physicochemical properties of the Pd-based electrocatalysts after the annealing process. Therefore, after the microwave subjection, the resultant product had a small particle size of about 10 nm, affirmed by TEM analysis. The smaller the particle sizes of the electrocatalysts, the more positive influence they possess on the electrocatalytic activity towards alcohol oxidation reaction.

2.11 Electrochemical characterisation of Anodic and cathodic Catalysts

The electrochemical characterisation of the anodic and cathodic catalysts is a highly prominent study investigating the electroactivity and performance of the catalysts. Once the electrochemical behaviour has been studied, we must determine if the prepared electrocatalysts suit DAFC applications. In this study, several electrochemical measurements such as cyclic voltammetry (CV), linear sweep (LSV), chronoamperometry (CA) and electrochemical impedance spectroscopy (EIS) were investigated for all the mentioned Pd-based ferro-electrocatalysts.

2.11.1 The study of Cyclic Voltammetry

Cyclic voltammetry (CV) is the most potent electrochemical tool for studying electroactive species and electrode surfaces. In most cases, CV is the initial electrochemical parameter to be conducted to provide qualitative information about the nano-catalysts [91]. This technique requires two or three-electrode cells immersed in the unstirred solution to produce a triangular

waveform, as shown in Figures 2.7a and b [92]. The electrodes include the working electrode, where the reduction and oxidation processes occur. The counter electrode is usually used to complete the circuit; it conducts electrons from the signal source through the solution to the working electrode. Lastly, the reference electrode, a saturated calomel electrode (SCE) or silver/silver chloride, is used to measure the constant potential exerted on the cell.

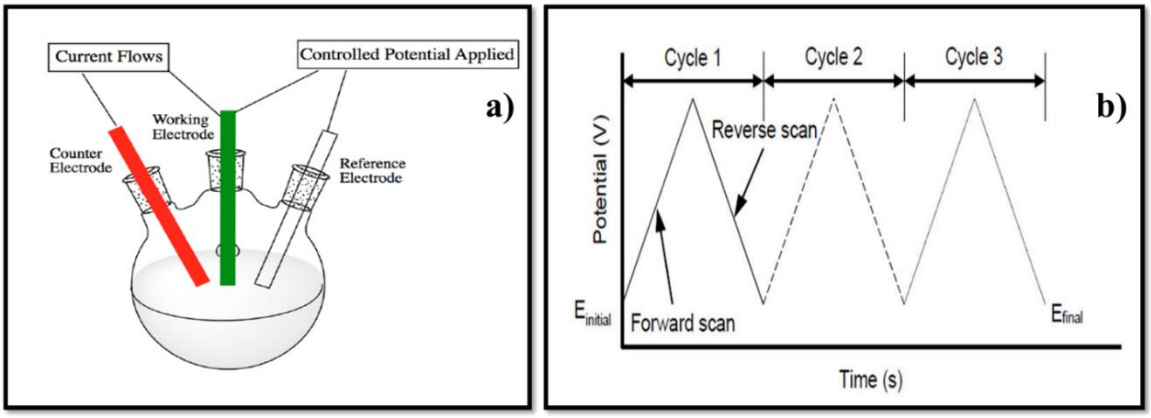


Figure 2.7: a) Typical three-electrode system [91] and b) The excitation signal of CV via a triangular potential waveform with switching potentials at (0.8, -0.2 V) vs SCE [92]

The reduction and oxidation (forward and reverse scan) processes occur in the working electrode. The counter electrode usually completes the circuit; it conducts electrons from the signal source through the solution to the working electrode. Lastly, the reference electrode, an SCE or silver/silver chloride, measures the constant potential exerted on the cell.

The potential of the electrode is linearly swept between the working and the reference electrode until the pre-set limit is reached, at which point the scan direction is swept back in a reverse direction. The results are presented as a duck-shaped plot, a cyclic voltammogram. An example is indicated in Figure 2.8 with the scan voltage of -0.4 V. A cyclic voltammogram is a plot acquired during a potential scan against the current at the working electrode site. The highly significant parameters on a cyclic voltammogram that reveal the reaction mechanism after scanning the potential and current of the working electrode are anodic potential peak (E_{pa}) and cathodic potential peak (E_{pc}). Their two peak currents are labeled anodic (current) peak (Ipa) and cathodic (current) peak (Ipc) [91, 92], as demonstrated in Figure 2.8.

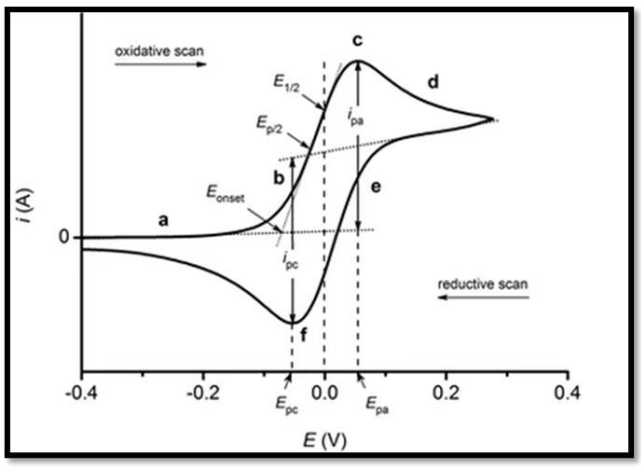


Figure 2.8: A typical CV curve representing an electrochemical of reversible one and electron redox process [93].

The electrochemical reaction occurring inside the electrochemical cell was further explored by three reaction types: reversible, irreversible, and quasi-reversible, as shown below in Figure 2.9.

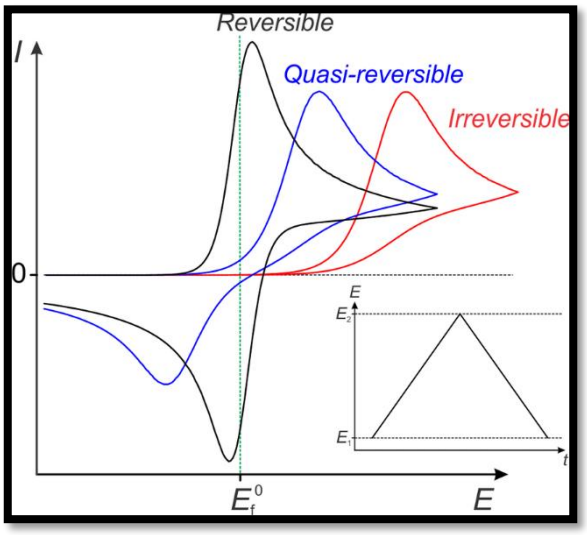


Figure 2.9 Compares CV wave-shapes of three types of reactions that occurred inside electrochemical cells [94].

2.11.2 Reversible reactions

A reversible process is a heterogeneous process whereby electrons transfer between the electrode and the analyte at the surface of the electrode, as shown in Equation 2.5. Once the electron is fast and the function of the concentration of the reacting species is in equilibrium, this indicates that the reversible process obeys the Nernst equation, as demonstrated in Equation 2.6.

$$O_x + ne^- \leftrightarrow R_{ed} \tag{2.5}$$

O_x is the oxidation reaction, e^- is the no.of electrons, and R_{ed} represents the reduction reaction.

$$E = E^o + \frac{RT}{nF}\ln\frac{[C_{ox}]}{[R_{ed}]} = E^0 + 2.3026\,\frac{RT}{nF}\log 10\,\frac{[C_{ox}]}{[Red]} \tag{2.6}$$

Where: $E^0$is the formal reduction potential, R is the gas constant, T is the temperature, n = is the number of electrons transferred, F is the Faraday's constant and C_{ox}, and R_{ed} are the oxidized and reduced species concentration at the surface electrode [95]. In CV, during the potential scan, we experience a change in the concentration of redox-active species at the electrode's interface time and again by undergoing the Nerst equation, leading to a change in the current response [95].

The peak current ratio for the reversible process is equal to one and independent of the scan rate. Equation 2.7 represents the number of electrons involved in the redox reaction for a reversible process for the difference of peak potentials of about 59 mV [95]:

$$\Delta E_p = \left[E_{pa} - E_{pc}\right] = \frac{RT}{nF} = \frac{59\,mv}{n} \tag{2.7}$$

Where ΔE_p is a change in peak potential, E_{pa} and E_{pc} represent the anodic & cathodic peak potentials, R is a gas constant, T is a temperature measured in K, n = number of electrons and F is Faraday's constant.

For an electrochemically reversible process, a redox couple is measured in half-reaction between anodic and cathodic peaks and is about $E_{1/2} = E^o$. The formal reduction potential E^o for a reversible process is given as a means of E_{pa} and E_{pc} and is shown in the Equation 2.8:

$$E^o = \frac{E_{pa} - E_{pc}}{2} \quad (2.8)$$

The Randles-Ševčík equation gives the peak current in the reversible process for the forward scan and it further determines the mass transport as expressed in Equation 2.9 [95]:

$$i_{pc} = (2.69\ x\ 10^5) n^{\frac{3}{2}} A\ D^{1/2}\ v^{1/2}\ C \quad (2.9)$$

Where, i_{pc} = peak current, n = number of electrons present, A = area of the electrode in m^2, D = diffusion coefficient in m^2 / s, C = concentration in mol / L and v = scan rate in V / s
A planar diffusion-controlled process is one in which the peak current increases with the square root and is directly proportional to the species concentration. It also indicates that the analyte is freely diffusing/adsorbed in solution.

2.11.3 Irreversible Process

The process is termed electrochemically irreversible because electron transfer, compared to mass transport, is slow at the electrode surface. In the process, the reverse peak is not aligned with the peak potential and the forward reaction's current due to the electron transfer's kinetic limitations. Similar to the reversible reaction, where the current peak is directly proportional to the square root of the scan rate, the difference is the relationship between the peak potential and scan rate.

The peak potential for an irreversible reaction is expressed as follows in Equation 2.10, where it displays the relationship between peak potential and scan rate:

$$\Delta E_p = E^0 - \frac{RT}{\propto n_{aF}} \left[0.78 - \ln \frac{\kappa^o}{D^{\frac{1}{2}}} + \frac{\left(\frac{\alpha n_a F v}{RT}\right) 1}{2} \right] \frac{59\ mV}{n} \quad (2.10)$$

Where E^0 is the standard peak potential, κ^0 represents the standard rate constant of the electron transfer (cm / s), v is the scan rate, R is the gas constant of 8.314 J / mol, and K and T are the gas constant and Temperature, respectively.

For irreversible reactions, the Randles-Ševčík equation can be used to describe the peak current as shown in Equation 2.11 [96]

$$i_p = (2.99x10^5)\, n\, (\alpha n_a)^{\frac{1}{2}}\, ACD^{1/2}\, v^{1/2}C \qquad (2.11)$$

Where i_p is the peak current, k^0 is the standard rate constant, α is the electron transfer coefficient, A is the area of the electrode, C_0 is the concentration of the electroactive species, D_0 is the diffusion coefficient of the electroactive species and v is the scan rate.

2.11.4 Quasi-reversible process

Both mass transfer and the kinetics of the electrode control a quasi-reversible process. This process has parameters that control the voltammetric characteristics and is given as Equation 2.12 [94]:

$$\kappa = k^o \frac{(\theta D)1}{2}\ where, \theta = \frac{nFv}{RT} \qquad (2.12)$$

The dimensionless kinetic parameter (k) that amalgamates the diffusion coefficient (D) signifies the mass transfer. The standard rate constant (k^0) controls the electrode reaction, whereas the scan rate simplifies the available time for the electrode reaction.

2.11.5 Study of Linear Sweep Voltammetry

Linear sweep voltammetry (LSV) is the most widely used technique, measuring the potential exerted at the working electrode, which differs linearly with time. In LSV, the voltammogram indicates that the first potential is scanned to the final potential. At the activation potential Ea, the current resumes to rise, indicating that the electrochemical reaction occurs at this onset potential, as shown in Figure 2.11. At this stage, the current response continues to increase until it reaches the peak potential E_p and drops again. At the peak potential, the electrochemically reactive species are formed. In the AOR work, the LSV, which is presented as a quasi-steady state LSV, was also utilised to attain the Tafel plot information to investigate the kinetics of the electrode [97].

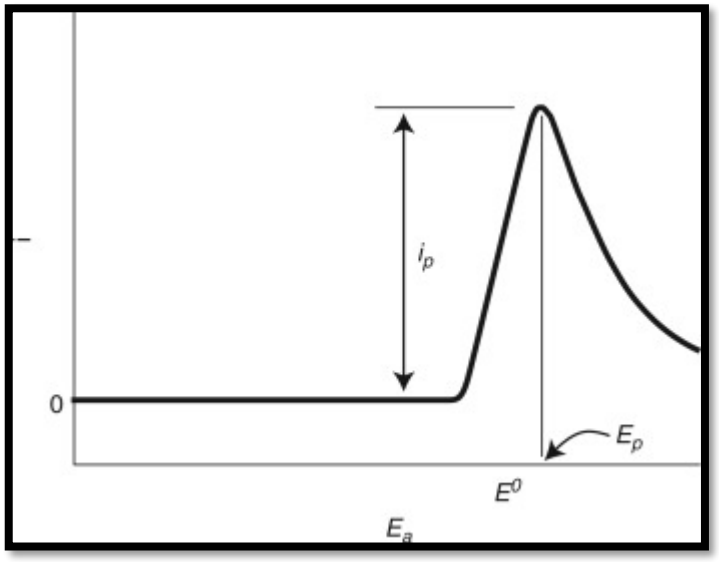


Figure 2.11: Linear sweep voltammogram [97].

2.11.6 The Study of Chronoamperometry

Chronoamperometry (CA) is a well-established technique used to measure the flow of current in the cell as a function of time. During the chronoamperometric experiment, the solution is unstirred to limit the mass transport by diffusion. The catalytic stability of the catalysts in the fuel cell shows that at the initial stage, the current of the catalysts decreases rapidly because of the formation of the intermediates during alcohol oxidation. At a later stage, the current response maintains its steady state and gradually increases in time. When the current response of the catalyst is higher, it is attributed to the material being stable and tolerant of poisoning species. The flow of current is at any time after applied potential and the Cottrell Equation is obeyed in Equation 2.13 [98]:

$$i\,(t) = \frac{nFACD^{1/2}}{\pi^{1/2}\,t^{1/2}} \qquad (2.13)$$

These quotients indicate the following: n = number of electrons, F = Faraday constant, A = surface area, C concentration, D diffusion coefficient, and I (t)= current at the time.

2.11.7 The study of Electrochemical Impedance spectroscopy.

Electrochemical impedance spectroscopy (EIS) is a technique widely used in electrochemistry to investigate the material's electrical properties and interfacial process [99]. EIS has been studied before to examine electron transport in many fields, such as dye-sensitized solar cells, biosensors, and fuel cells. The electrochemical impedance measurements are obtained by applying a small amplitude sinusoidal signal to the electrochemical cell and measuring the response. The resultant response signal can be either current or voltage. If the cell is pseudo-linear, a small excitation signal is typically used to measure the electrochemical impedance [100]. The potential and current responses are sent over a wide range of frequencies but shifted in phase with respect to perturbation [100]. The excitation signal measured as a function of time is given by the expression in Equation 2.14:

$$E_t = E_0 \sin(wt) \quad (2.14)$$

Where E_t is expressed as potential at times$t$ domain, E_o= the amplitude of the signal and ω is the radical frequency (rad s^{-1}). The radical frequencies are stated as (radians over a second) and are depicted in Equation 2.15 to express the relationship with frequencies (hertz):

$$\omega = 2\pi f \quad (2.15)$$

In a linear system, the excitation response has amplitude and is given in the Equation 2.16:

$$I_t = I_o \sin(\omega t + \phi) \quad (2.16)$$

Where I_t is the response signal, the response signal shifted up in phase and I_o = various amplitudes.

The impedance measurement is expressed as a complex number and the expression is given in Equation 2.17:

$$Z = \frac{E}{I} = Z' + jZ'' = Z_{real} + Z_{imaginary} \quad (2.17)$$

The data are presented as a Bode plot or Nyquist plot during an EIS experiment. The Bode plot exhibits the relationship between the log magnitudes of impedance versus the log of frequency. In contrast, the Nyquist plot shows the relationship between the imaginary and real impedance. In Nyquist plot, a semi-circle is attained. It indicates the charge or electron transfer limiting process at the surface of the electrode. The value is obtained via the measurement of the semi-circle's diameter. When the semi-circle diameter is amplified, the charge transfer resistance

increases or vice versa. The Nyquist plot can be fitted with several equivalent circuits, as shown in Figure 2.12. For fuel cells, the Randles equivalent circuits. The Randles equivalent circuits are composed of several factors such as electrolyte resistance (Rs), charge transfer resistance (R_{ct}), Warburg impedance (Zw) and constant phase element (CPE).

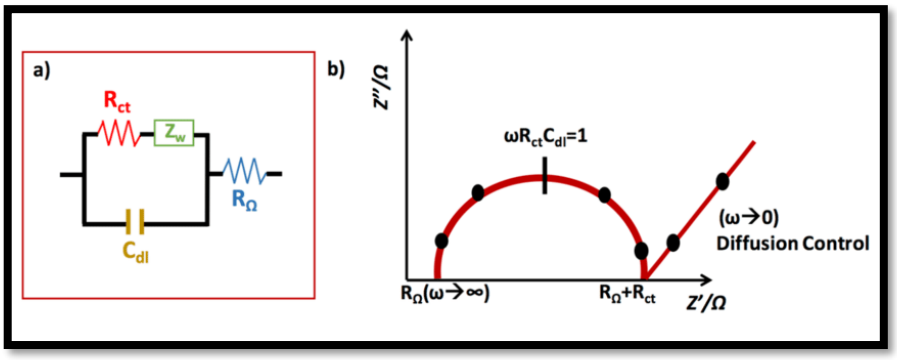


Figure 2.12: a). The Randles equivalent circuit and b). Nyquist plot obtained from the Randles circuit [101]

The charge transfer resistance is vital to redox reaction kinetics at the active surface area. When the charge transfer resistance is lower in direct alcohol fuel cells, alcohol electrooxidation's electron transfer kinetics are faster [102].

2.12 References

[1] O.Z. Sharaf, M.F. Orhan, Renewable and sustainable energy reviews. 32 (2014) 810-853.

[2] T. Wilberforce, A. Alaswad, A. Palumbo, M. Dassisti, A. Olabi, International Journal of Hydrogen Energy. 41 (2016) 16509-16522.

[3] M. Winter, R.J. Brodd, What are batteries, fuel cells, and supercapacitors? (2004).

[4] K. Xu, D.T. Pierce, A. Li, J. Xiaojun Zhao, Synthesis and Reactivity in Inorganic and Metal-Organic Chemistry. 38 (2008): 394-399.

[5] A.J. Bard, Journal of the American Chemical Society. 132 (2010) 7559-7567.

[6] R.S. Banfield, (2012).

[7] A. Kirubakaran, S. Jain, R.K. Nema, Renewable and Sustainable Energy Reviews. 13 (2009) 2430-2440.

[8] S. Hardman, A. Chandan, R. Steinberger-Wilckens, Journal of Power Sources. 287 (2015) 297-306.

[9] D. Hotza, J.D. Da Costa, International Journal of Hydrogen Energy. 33 (2008): 4915-4935.

[10] Z.X. Liang, T.S. Zhao, J.B. Xu, L.D. Zhu, Electrochimica Acta. 54 (2009) 2203-2208.

[11] R.M. Modibedi, T. Masombuka, M.K. Mathe, International Journal of Hydrogen Energy. 36 (2011) 4664-4672.

[12] E.H. Yu, U. Krewer, K. Scott, Energies. 3 (2010) 1499-1528.

[13] Y. Wei, C. Liu, W. Kang, C. Lai, L. Tsai, K. Wang, Journal of Electroanalytical Chemistry. 660 (2011) 64-70.

[14] C. Bianchini, P.K. Shen, Chem. Rev. 109 (2009) 4183.

[15] O.O. Fashedemi, K.I. Ozoemena, Electrochimica Acta. 128 (2014) 279-286.

[16] J.M. Sieben, M.M.E. Duarte, International Journal of Hydrogen Energy. 36 (2011) 3313-3321.

[17] A. Falase, M. Main, K. Garcia, A. Serov, C. Lau, P. Atanassov, Electrochimica Acta. 66 (2012) 295-301.

[18] C. Wen, Y. Wei, D. Tang, B. Sa, T. Zhang, C. Chen, Scientific reports. 7 (2017) 4907.

[19] E. Habibi, H. Razmi, International Journal of Hydrogen Energy. 37 (2012) 16800-16809.

[20] V.L. Oliveira, C. Morais, K. Servat, T.W. Napporn, G. Tremiliosi-Filho, K.B. Kokoh, Electrochimica Acta. 117 (2014) 255-262.

[21] M.Z.F. Kamarudin, S.K. Kamarudin, M.S. Masdar, W.R.W. Daud, International Journal of Hydrogen Energy. 38 (2013) 9438-9453.

[22] K. Kakaei, M. Dorraji, Electrochimica Acta. 143 (2014) 207-215.

[23] C. Zhong, J. Luo, B. Fang, B.N. Wanjala, P.N. Njoki, R. Loukrakpam, J. Yin, Nanotechnology. 21 (2010) 062001.

[24] S. Chaturvedi, P.N. Dave, N.K. Shah, Journal of Saudi Chemical Society. 16 (2012) 307-325.

[25] M. Akhairi, S.K. Kamarudin, International Journal of Hydrogen Energy. 41 (2016) 4214-4228.

[26] D. Nkosi, K.I. Ozoemena, Electrochimica Acta. 53 (2008) 2782-2793.

[27] J.N. Tiwari, R.N. Tiwari, G. Singh, K.S. Kim, Nano Energy. 2 (2013) 553-578.

[28] L. Li, M. Chen, G. Huang, N. Yang, L. Zhang, H. Wang, Y. Liu, W. Wang, J. Gao, Journal of Power Sources. 263 (2014) 13-21.

[29] H. Rostami, A. Omrani, A.A. Rostami, International Journal of Hydrogen Energy. 40 (2015) 9444-9451.

[30] V. Bambagioni, C. Bianchini, Y. Chen, J. Filippi, P. Fornasiero, M. Innocenti, A. Lavacchi, A. Marchionni, W. Oberhauser, F. Vizza, ChemSusChem. 5 (2012) 1266-1273.

[31] C. Xu, Z. Tian, Z. Chen, S.P. Jiang, Electrochemistry communications. 10 (2008) 246-249.

[32] Y. Su, M. Zhang, X. Liu, Z. Li, X. Zhu, C. Xu, S.P. Jiang, International Journal of Electrochemical Science 7 (2012) 4158-4170.

[33] W. Xiao, M.A. Cordeiro, G. Gao, A. Zheng, J. Wang, W. Lei, M. Gong, R. Lin, E. Stavitski, H.L. Xin, Nano Energy. 50 (2018) 70-78.

[34] A.M. Sheikh, P.S. Correa, E.L. da Silva, I.D. Savaris, S.C. Amico, C.F. Malfatti, Renewable Energies and Power Quality Journal. 11 (2013) 300.

[35] P. Su, H. Chen, T. Chen, C. Liu, C. Lee, J. Lee, T. Chan, K. Wang, International Journal of Hydrogen Energy. 38 (2013) 4474-4482.

[36] J. Zhang, H. Ma, D. Zhang, P. Liu, F. Tian, Y. Ding, Physical Chemistry Chemical Physics. 10 (2008) 3250-3255.

[37] A. Ruban, B. Hammer, P. Stoltze, H.L. Skriver, J.K. Norskov, Journal of Molecular Catalysis A: Chemical. 115 (1997) 421-429.

[38] S.Y. Shen, T.S. Zhao, J.B. Xu, Y.S. Li, Journal of Power Sources. 195 (2010) 1001-1006.

[39] F.R. Clímaco, C.V. Almeida, S.S. Aristides, K.I. Eguiluz, G.R. Salazar-Banda, Chemical Physics Letters. (2022) 139745.

[40] T. Ramulifho, K.I. Ozoemena, R.M. Modibedi, C.J. Jafta, M.K. Mathe, Journal of Electroanalytical Chemistry. 692 (2013) 26-30.

[41] F. Ren, X. Chen, R. Xing, Y. Du, Journal of Colloid and Interface Science. 582 (2021) 561-568.

[42] T. Li, Y. Huang, K. Ding, P. Wu, S.C. Abbas, M.A. Ghausi, T. Zhang, Y. Wang, Electrochimica Acta. 191 (2016) 940-945.

[43] O.O. Fashedemi, K.I. Ozoemena, Electrochimica Acta. 128 (2014) 279-286.

[44] A. Serov, U. Martinez, P. Atanassov, Electrochemistry Communications. 34 (2013) 185-188.

[45] A.N. Geraldes, D.F. Silva, J. Silva, R.F. Souza, E.V. Spinacé, A. O Neto, M. Linardi, M.C. Santos, Journal of the Brazilian Chemical Society. 25 (2014) 831-840.

[46] A. Cassani, N. Tuleushova, Q. Wang, H. Guesmi, V. Bonniol, J. Cambedouzou, S. Tingry, M. Bechelany, D. Cornu, Y. Holade, ACS Applied Energy Materials. 4 (2021) 9944-9960.

[47] C. Venkateswara Rao, B. Viswanathan, The Journal of Physical Chemistry C. 113 (2009) 18907-18913.

[48] M.A. Matin, J. Jang, Y. Kwon, Journal of Power Sources. 262 (2014) 356-363.

[49] K. Mohanraju, L. Cindrella, International Journal of Hydrogen Energy. 41 (2016) 9320-9331.

[50] M. Rethinasabapathy, S. Kang, Y. Haldorai, M. Jankiraman, N. Jonna, S.R. Choe, Y.S. Huh, B. Natesan, International Journal of Hydrogen Energy. 42 (2017) 30738-30749.

[51] T. Gunji, R.H. Wakabayashi, S.H. Noh, B. Han, F. Matsumoto, F.J. DiSalvo, H.D. Abruña, Electrochimica Acta. 283 (2018) 1045-1052.

[52] Q. Sun, N. Wang, Q. Bing, R. Si, J. Liu, R. Bai, P. Zhang, M. Jia, J. Yu, Chem. 3 (2017) 477-493.

[53] G.J. Nieuwenhuys, Advances in Physics. 24 (1975) 515-591.

[54] D. Bagguley, W.A. Crossley, J. Liesegang, Proceedings of the Physical Society. 90 (1967) 1047.

[55] Taylor, DJC, Page, DC & Geldenhuys, P, Journal of the Southern African Institute of Mining and Metallurgy. 88 (1988) 73-95.

[56] Y. Pan, F. Zhang, K. Wu, Z. Lu, Y. Chen, Y. Zhou, Y. Tang, T. Lu, International Journal of Hydrogen Energy. 37 (2012) 2993-3000.

[57] S. Hannis, T. Bide, (2009).

[58] C.L. Vecchio, D. Sebastián, C. Alegre, A.S. Aricò, V. Baglio, Journal of Electroanalytical Chemistry. 808 (2018) 464-473.

[59] L. Luo, W. Zhan, R. Zhang, D. Chen, Q. Hu, Y. Guo, X. Zhou, Journal of Power Sources. 412 (2019) 142-152.

[60] J.D. Steenkamp, J. Basson, Journal of the Southern African Institute of Mining and Metallurgy. 113 (2013) 667-676.

[61] C. Xu, Z. Tian, P. Shen, S.P. Jiang, Electrochimica Acta. 53 (2008) 2610-2618.

[62] M.E. Weeks, Journal of Chemical Education. 9 (1932) 1751.

[63] G. J. Bryant. Examining Perspectives on China\u27s Near-Monopoly of Rare Earths. (2015)

[64] C. Lamy, A. Lima, V. LeRhun, F. Delime, C. Coutanceau, J. Léger, Journal of Power Sources. 105 (2002) 283-296.

[65] Z.X. Liang, T.S. Zhao, J.B. Xu, L.D. Zhu, Electrochimica Acta. 54 (2009) 2203-2208.

[66] J. Liu, J. Ye, C. Xu, S.P. Jiang, Y. Tong, Electrochemistry Communications. 9 (2007) 2334-2339.

[67] K. Matsuoka, Y. Iriyama, T. Abe, M. Matsuoka, Z. Ogumi, Journal of Power Sources. 150 (2005) 27-31.

[68] E.H. Yu, U. Krewer, K. Scott, Energies. 3 (2010) 1499-1528.

[69] K.I. Ozoemena, RSC Advances. 6 (2016) 89523-89550.

[70] H. Erikson, A. Sarapuu, K. Tammeveski, ChemElectroChem. 6 (2019) 73-86.

[71] L. Khotseng, Electrocatalysts for Fuel Cells and Hydrogen Evolution-Theory to Design (2018).

[72] E.H. Yu, U. Krewer, K. Scott, Energies. 3 (2010) 1499-1528.

[73] N. Yuan, Q. Jiang, J. Li, J. Tang, Arabian Journal of Chemistry. 13 (2020) 4294-4309.

[74] T. Gunji, R.H. Wakabayashi, S.H. Noh, B. Han, F. Matsumoto, F.J. DiSalvo, H.D. Abruña, Electrochimica Acta. 283 (2018) 1045-1052.

[75] H. Mao, L. Wang, P. Zhu, Q. Xu, Q. Li, International Journal of Hydrogen Energy. 39 (2014) 17583-17588.

[76] Q. He, S. Mukerjee, Electrochimica Acta. 55 (2010) 1709-1719.

[77] A.C. Mkhohlakali, X. Fuku, R.M. Modibedi, L.E. Khotseng, S.C. Ray, M.K. Mathe, Applications of Surface Science. 502 (2020) 144158.

[78] Y. Tang, L. Zhang, Y. Wang, Y. Zhou, Y. Gao, C. Liu, W. Xing, T. Lu, Journal of Power Sources. 162 (2006) 124-131.

[79] F. Li, X. Gao, S. Li, Y. Chen, J. Lee, NPG Asia Materials. 7 (2015) 219.

[80] O.O. Fashedemi, K.I. Ozoemena, Physical Chemistry Chemical Physics. 15 (2013) 20982-20991.

[81] K.J. Rao, B. Vaidhyanathan, M. Ganguli, P.A. Ramakrishnan, Chemistry of Materials. 11 (1999) 882-895.

[82] G. Assat, A. Manthiram, Inorganic Chemistry.54 (2015) 10015-10022.

[83] M.H. Bhat, B.P. Chakravarthy, P.A. Ramakrishnan, A. Levasseur, K.J. Rao, Bulletin of Material Science. 23 (2000) 461-466.

[84] Z. Moorhead-Rosenberg, K.L. Harrison, T. Turner, A. Manthiram,)52 (2013) 13087-13093.

[85] L. Li, J. Ren, Mater. Res. Bull. 41 (2006) 2286-2290.

[86] T. Kim, J. Lee, K. Lee, Carbon letters. 15 (2014) 15-24.

[87] N.E. Leadbeater, H.M. Torenius, J. Org. Chem. 67 (2002) 3145-3148.

[88] D. Dallinger, C.O. Kappe, Chem. Rev. 107 (2007) 2563-2591.

[89] Z. Moorhead-Rosenberg, K.L. Harrison, T. Turner, A. Manthiram, Inorganic Chemistry.52 (2013) 13087-13093.

[90] A. de la Hoz, A. Díaz-Ortiz, P. Prieto, RSC Green Chemistry, Royal Society of Chemistry, (2016)1–33

[91] K.L. Walz Mitra. (2022) Doctor of Philosophy, University of Washington.

[92] P.T. Kissinger, W.R. Heineman, Journal of Chemical Education. 60 (1983) 702.

[93] Cyclic Voltammetry Basic Principles and Theory: https://www.ossila.com/pages/cyclic-voltammetry, retrieved 20 July 2022

[94] J. Lee. (2022). Doctor of Philosophy, Curtin University

[95] C. Sandford, M. A. Edwards, K. J. Klunder, D. P. Hickey, M. Li, K. Barman, M. S. Sigman, H. S. White and S. D. Minteer, Chemical Science., 10, (2019)26.

[96] M.G. Trachioti, A.C. Lazanas, M.I. Prodromidis, Microchimica Acta 190 (2023)

[97] A. Escarpa, M. C. González and M. Á López, Agricultural and food electroanalysis, John Wiley & Sons (2015).

[98] C. Orha, C. Bandas, C. Lazau, M.I. Popescu, A. Baciu, F. Manea, Advanced Electrodegradation of Doxorubicin in Water Using a 3-D Ti/SnO_2 Anode, Water (Switzerland) 14 (2022).

[99] W. S. Jung, J. Han and S. Ha, Journal of Power Sources., 173, (2007)1.

[100] G. Instruments, G. Instruments, Complex impedance in Corrosion., (2007).

[101] S. Carrara, Towards new efficient nanostructured hybrid materials for ECL applications., (2017).

[102] J. Brock, Electrochemical Impedance Spectroscopy, Nova Science Publishers, Incorporated (2017).

[103] University of Cambridge source: www. doitpoms.ac.uk/tlplib/fuel-cells/history.php, retrieved on 13 July 2022

[104] W.T.J. Al-Rubaye, A. Al-Araji, H.A. Dhahad, A.S. Al-Araj, H.A. Dhahad, International Journal of Science and Research (2020)

[105] E. Katz, P. Bollella, Fuel Cells and Biofuel Cells: From Past to Perspectives, Israel Journal Chemistry 61 (2021) 68–84. https://doi.org/10.1002/ijch.202000039.

[106] U.S Department of Energy, source: https://afdc.energy.gov/vehicles/how-do-gasoline-cars-work, retrieved on 13 July 2022

[107] U.S Department of Energy, source https://afdc.energy.gov/vehicles/how-do-fuel-cell-electric-cars-work, retrieved on 13 July 2022

[108] T.G. Vo, J. Gao, Y. Liu, Recent Development and Future Frontiers of Oxygen Reduction Reaction in Neutral Media and Seawater, Adv Funct Mater 34 (2024).

[109] E.J.F. Dickinson, G. Hinds, J Electrochem Soc 166 (2019) 221–231

[110] S. Li, C. Li, Z. Shao, Sustainable Environment Research 32 (2022)

[111] 1. M. S. Matseke, T. S. Munonde, K. Mallick, and H. Zheng, Electrocatalysis, 10, (2019) 436–444.

[112] J. Wan, Z. Liu, X. Yang, P. Cheng, and C. Yan, Nanomaterials, 11 (2021).

[113] M. Neergat, V. Gunasekar, and R. Rahul, Journal of Electroanalytical Chemistry, 658, 25–32 (2011).

[114] Y. Xie, C. Li, E. Castillo, J. Fang, and N. Dimitrov, Electrochimica Acta, 385 (2021).

[115] I. Cruz-Reyes, B. Trujillo-Navarrete, K. García-Tapia, M.I. Salazar-Gastélum, F. Paraguay-Delgado, R.M. Félix-Navarro, Fuel 279 (2020).

[116] H. Yang, K. Wang, Z. Tang, Z. Liu, and S. Chen, Journal of Catalysis, 382, (2020) 181–191.

[117] P. Raghavendra, G. Vishwakshan Reddy, R. Sivasubramanian, P. Sri Chandana, and L. Subramanyam Sarma, International Journal of Hydrogen Energy, 43, (2018) 4125–4135.

[118] L. Karuppasamy, C. Y. Chen, S. Anandan, and J. J. Wu, International Journal of Hydrogen Energy, 44, (2019) 30705–30718.

[119] M. G. Hosseini, F. Hosseinzadeh, P. Zardari, and M. Darbandi, International Journal of Hydrogen Energy, 46, (2021) 28513–28526.

[120] M.S. Khan, R. Khattak, A. Khan, Q. Chen, J. Nisar, Z. Iqbal, A. Rashid, A.W. Kamran, I. Zekker, M. Zahoor, K.J. Alzahrani, G.E.S. Batiha, Molecules 26 (2021).

CHAPTER 3

EXPERIMENTAL PROCEDURE

This chapter explains the experimental techniques and characterisation conditions used in this study. The initial part of the chapter describes the materials and reagents employed during the synthesis of the as-prepared materials. The methodology and characterisation techniques used were thoroughly discussed in this particular chapter. The final part of this chapter is to explain the electrochemical measurements using a three-electrode system.

3.1 Materials and Reagents

Table 3.1: Summarises the materials and reagents used in this research work. The chemicals used for this study were not purified.

Chemicals and materials	Specification	Supplier
Carbon black	Vulcan XC-72	Sample Chemiphos, chemical & specialties
Iron (II) Chloride tetrahydrate ($FeCl_2.H_2O$)	Puriss=> 99%	Sigma Aldrich
Cobalt (II) Chloride hexahydrate ($CoCl_2.6H_2O$)	ACS reagent 98%	Sigma Aldrich
Manganese (II) Chloride tetrahydrate ($MnCl_2.4H_2O$)	ACS reagent > 98%	Sigma Aldrich
Cerium (III) Chloride	99.999% (trace metal basis)	Sigma Aldrich
Palladium (II) Chloride ($PdCl_2$)	60% Pd basis	Sigma Aldrich
Ethylene glycol ($HOCH_2CH_2OH$)	Assay Min 99.5%	Associated Chemicals Enterprises (ACE)
Glycerol ($C_3H_5(OH)_3$)	Assay Min 99.5%	Associated Chemicals Enterprises (ACE)
Ethanol Absolute C_2H_6O	Assay Min 99.8%	Associated Chemicals Enterprises (ACE)
Nafion perfluorinated resin solution mixture $C_9HF_{17}O_5S$	(5 wt /%) A mixture of lower aliphatic alcohols and water contains 45% water.	Sigma Aldrich

Potassium hydroxide pellets (KOH)	Assay 85%	Associated Chemicals Enterprises (ACE)
Potassium Chloride (KCl)	Assay 99.5%	Merck

3.1.1 Preparation procedure of Pd-based electrocatalysts.

3.1.1.1 Synthesis of bimetallic electrocatalysts utilising the $NaBH_4$ method

The Pd-based electrocatalysts were prepared utilising an established method, as reported previously in the literature by Zhu and co-workers [110]. In brief, known amounts of $FeCl_2.4H_2O$ (0.1034 g) and $PdCl_2$ (0.0513 g) were dissolved in EG to give a Pd: Fe mole ratio of (2:1). The mixture was ultra-sonicated for 30 min and further stirred for 1 h. After that, a mixture of $NaBH_4$ and NaOH (1:10 M ratio) was added dropwise to adjust the pH to 12 under vigorous stirring. Carbon black (80 mg) was introduced and ultrasonically dispersed in the mixture for 2 h. The obtained catalyst was washed thoroughly several times through a filtration process with H_2O and acetone and subsequently dried in an oven at 120 °C. The produced final product is abbreviated as follows PdFe/C. The monometallic Pd/C was synthesised using a similar method for comparison evaluation.

3.1.1.2 Synthesis of bimetallic nano-electrocatalysts using MW technique

The synthetic method of all the Pd-based electrocatalysts was conducted using a simple two-step method, as reported previously [29], with modifications. In summary, $FeCl_2.4H_2O$ (0.0596 g) was dissolved in 50 mL de-ionised H_2O and vigorously stirred for 30 min. Carbon black (80 mg Vulcan XC-72) was added, and the mixture was ultra-sonicated for about 30 min, followed by stirring overnight at 25 °C until the formation of a slurry. The slurry was oven-dried at 60 °C for overnight. Then, the resultant powder was pre-annealed in a tube furnace at 300 °C under the H_2/Ar mixture flow for 2 h, then sintered at 500 °C for 2 h, and cooled to room temperature under an Ar environment.

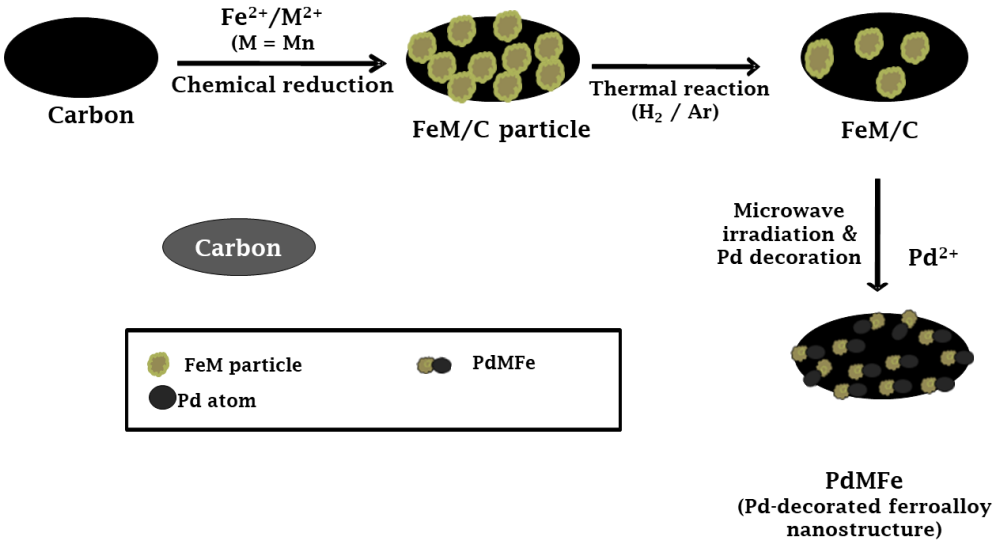
The fine powder of Fe/C alloy was utilised as a support composite to produce Pd-based catalysts. The as-prepared Fe/C was thoroughly mixed with 20% $PdCl_2$ (0.0205 g) in 30 mL EG (ensuring Pd:Fe mole ratio of 2:1) and subjected to rapid MW at 500 W, ~20 bars, and 198 °C for 20 min. The resultant product (labelled Pd_2Fe/C MW) was repeatedly washed with

deionized H_2O and acetone to remove EG traces and then dried at 60 °C. The Pd/C, Pd_2Mn/C and Pd_2Co/C were also synthesised following the abovementioned process. The metal loading was recorded to be 0.2105 µg.

3.1.1.3 Synthesis of trimetallic electrocatalysts utilising MW method

The preparation methods of all the Pd-based electrocatalysts were rendered by adopting a simple two-step technique, as reported previously [29], with facile modifications. Briefly explained: $FeCl_2.4H_2O$ and $MnCl_2.4H_2O$ (0.0726 g) were dissolved in 50 mL deionised H_2O and stirred for 30 min. Carbon black with a weight quantity of (80 mg Vulcan XC-72) was put on the mixture, ultra-sonicated for about 30 min, and subsequently stirred overnight at room temperature until the mixture became a slurry. For proper drying, the slurry was oven-dried at 60 °C for overnight. The resultant powder was pre-heated in a tube furnace at 300 °C under the flow of H_2/Ar mixture for 2 h and then annealed at 500 °C for 2 h and allowed to be cooled down to 25 °C under the Ar atmosphere.

The fine powder of FeMn/C alloy was employed as a support composite to produce Pd-based catalysts. The as-prepared FeMn/C was thoroughly mixed well with the addition of 20% $PdCl_2$ (0.0205 g) in 30 mL EG (ensuring Pd:Fe:Mn molar ratio of 1:1:1) and subjected to rapid MW at 500 W, ~20 bars, and 198 °C for about 20 min. The resultant product (PdFeMn/C MW mole ratio 1:1:1 wt%) was washed multiple times with deionized H_2O and acetone to eliminate the unreacted EG residues and then followed by drying at 60 °C in a conventional oven. The Pd/C, PdCo/C, PdMn/C, PdFe/C, and PdFeCo/C electrocatalysts were synthesised following a similar procedure.



Scheme 3.2: Schematic diagram representing the preparation of trimetallic electrocatalysts.

3.2 Physical characterisation conditions

Physico-chemical characterisation of the as-prepared materials was conducted in this research work to investigate their physicochemical properties. The techniques used in this study are X-ray diffractometer (XRD), Scanning Electron Microscopy (SEM), Transmission Electron Microscopy (TEM), Brunauer-Emmett-Teller (BET), Raman spectroscopy and X-ray photoelectron spectroscopy (XPS). The measurements were all captured at room temperature.

3.2.1 XRD

XRD was employed in this research to evaluate the phases and structural properties of the crystalline materials. The diffraction patterns obtained during the analysis with this technique can provide helpful information, including the lattice parameter, d-spacing & crystalline size. A Rigaku Ultima (IV) XRD model equipped with Cu Kα radiation source (λ= 0.15418 nm) was used - 40 kV and 20 mA. The XRD diffractograms were collected in a scan range between 0 and 90°. The method used for obtaining the data: approximately 0.5 g of the samples were transferred onto the glass plates and inserted into the stainless-steel sample holder. The holder was placed inside the XRD chamber to display the XRD diffractograms at varied diffraction peaks.

3.2.2 SEM

SEM uses high-energy electrons to produce a different signal on solid objects. In this study, this technique was utilised to probe the morphology and particle size of the catalysts. SEM images were obtained using the LEO 1525 model Field Emission SEM with 2.0V acceleration voltage. The samples were prepared by inserting about 0.1 mg of the sample on a carbon tape subsequently coated with conductive material (using carbon film) to prohibit charging.

3.2.3 TEM

TEM produced a highly magnified image of specimens utilising a beam and a particle beam of electrons. The technique can determine particle size distribution and morphology with nanosized samples smaller than 100 nm. The obtained TEM) micrographs were collected from the JEOL JEM 2100F TEM model operating at 200 kV. The samples were prepared by dispersing them in a methanol solution and later sonicating them for a few seconds. A few drops of the suspension were cast onto a carbon film covered with a Cu-grid for analysis.

3.2.4 BET

BET analysis gave insight into the specific surface area and porosity of the catalysts. The analysis was carried out using Tristar II, manufactured by Micromeritics (USA). The materials were degassed before the experiment at 100° C for 2 h. The BET surface area, pore size, and volume were measured using nitrogen at 77 K.

3.2.5 Raman Spectroscopy

Raman spectroscopy is a technique used to obtain the structural and quality of carbon materials, particularly their degree of defect formation and ordered and disordered structure. The spectra were obtained using the Bruker Senterra Raman spectrometer model with an excitation wavelength of 514.5 nm, beam power of the sample of 0.4 mW, spectra resolution of 3 cm^{-1}, and scanning in a range of 250–2500 cm^{-1}.

3.2.6 XPS

In this research work, XPS spectra were studied to prone the surface oxidation state and the binding energies of the elements present in the materials. The measurements were done using a Thermo Fisher Scientific ESCALAB 250Xi with the X-rays of monochromatic Al Kα at 1486.7 eV radiation. The X-ray power was recorded to be 300 W, along with an X-ray spot size of 900 µm, the pass energy (survey) of 100 eV, the pass energy obtained using Hi-res of 20 eV and the pressure of $< 10^{-8}$ mBar.

3.2.7 Density Functional Theory (DFT) Simulation

DFT simulations were performed with the supercomputational facilities at the Centre for High Performance Computing (CHPC, Cape Town, South Africa). The DFT calculations were performed using Adsorption locator tools and DMol^{3}modules of the BIOVIA® Materials Studio suite. The adsorption locator tool absorbed Glycerol onto Pd and Pd/Fe surfaces. Prior to the modeling, the primitive atomic positions for Pd and PdFe were obtained from the Materials Project database [15]**.** The surfaces were modelled into periodic supercells as follows: Pd a 3×3 in the (1 1 1) plane while the Pd/Fe, 3×3 in the (1 1 1) and (1 1 0) planes. The adsorbate (glycerol) molecule was placed on top of the modelled surfaces. The surface adsorption distance for the selected atoms was set as 5Å, which was the maximum acceptable (software-dependent) distance for the simulation to run. The accuracy was set at 10^{-6} kcal/mol. Before the adsorption of the glycerol, ethylene glycol and ethanol the systems were optimised using the DMol^3 module, with a convergence threshold energy set as 10^{-6} eV. The Perdew-Wang generalized-gradient approximation (PW91) functionals were used for DMol^3 calculations, which yielded band structures and density of states (DOS). These functionals are known to increase the accuracy of predicted energies of structures and minimize the computational time [16].

3.3 The electrochemical characterisation conditions.

3.3.1 Electrochemical characterisation of electrocatalysts

The electrochemical measurements were recorded at room temperature using a standard three-electrode cell system. A Pt rod was used as the counter electrode, Ag/AgCl saturated (3 M KCl) was employed as the reference electrode, and a modified 3 mm diameter glassy carbon electrode (from BASi) was used as the working electrode. An AutoLab PGSTAT302 potentiostat/galvanostat system was employed to conduct the following measurements: CV, LSV, CA, and EIS. All these measurements were carried out at 25 °C.

3.3.2 Modification of the AOR electrode

The preparation of catalyst ink was thoroughly conducted as follows for proper dispersion: 0.002 g of catalyst powder was sonicated in 0.1 mL Nafion solution with the addition of 0.2 mL deionised H_2O. The mixture was ultrasonicated for 30 min to make a uniform ink. Cleaning the glassy carbon electrode (GCE) includes the following steps: Firstly, the GCE was polished with alumina (area= 0.07068 cm^2) until the surface was mirror-like and subsequently sonicated in ethanol/deionized H_2O mixture for 5 min. Then, 2 µL of the prepared ink was quantitatively pipetted onto the surface of the polished GCE to avoid the formation of bubbles and allowed to dry for about 30 min in air. All experiments were conducted in 0.5 M KOH solution in 0.5 M alcohol (EG, EtOH, Gly) concentration at varied scan rate intervals. The solution was bubbled with nitrogen (N_2) before every electrochemical measurement.

3.3.3 Modification of the ORR electrode

The electrochemical measurements of ORR were collected using the same technique as AOR (AutoLab PGSTAT302 potentiostat/galvanostat), composed of three electrode systems. A Pt rod is the counter electrode, a working electrode is a glassy carbon connected to the RDE electrode, and a reference electrode (is Ag/AgCl saturated (3 M KCl). Nevertheless, all the electrodes employed were converted to reversible hydrogen electrodes (RHE). The RDE experiments were performed in 0.1 M KOH electrolyte at varied rotation speeds with a scan rate of 10 mV / s. The solutions were bubbled with oxygen (O_2) before the experiment.

CHAPTER 4

Microwave-induced defective PdFe/C nano-electrocatalyst for highly efficient alkaline glycerol oxidation reactions.

4.1 Introduction

Among various FC technologies, DAFCs are widely discerned as the most attractive device for portable electronic devices and electric vehicle applications [1, 2]. This device converts the chemical energy of various liquid fuels into electrical energy. Primary alcohols such as methanol and ethanol, and even polyhydric alcohols such as ethylene glycol and glycerol, are widely employed as alternative fuels due to their numerous advantages: high energy density, high boiling points, less volatile, accessible storage, and handling [3-5]. Gly as a fuel has emerged to be an attractive alternative to conventional fuels due to its theoretical density of 5 $kWhkg^{-1}$ and high theoretical number of exchanged electrons (14 electrons/glycerol molecules) [6, 7]. Today, the use of direct glycerol fuel cells towards the oxidation of alcohol in basic media is more recognized than ever before, as biodiesel-derived Gly is attained at a low market value compared to other alcohols [1, 7]. Although their properties seem appealing, one of the most critical challenges with this fuel cell is the intermediates species that arise during complex oxidation reactions. The intermediates strongly bind to and block the active sites of the catalysts and produce undesirable products, leading to the sluggish kinetics of the reactions and incomplete total oxidation of glycerol [8]. Thus, there has always been the need for a new synthesis method that can improve the ability of the nano-electrocatalyst to tolerate poisoning activities.

Among the Pt-free catalyst, palladium electrocatalysts have exhibited high activity, better resistance to poisoning arising from the alcohol oxidation such as the carbonaceous intermediates (e.g., CO) [9, 10], and better steady-state behaviour for the alcohol fuel cells in alkaline media. Alloying Pd lattice with 3d transition metals (Ni, Cu, Co, Fe, etc) has been explored without affecting the activity of the catalysts [11]. These studies show that exploring the alloying effect, particularly with 3d transition metals, leads to a noticeable rise in the electronic, synergistic effect, and bi-functional mechanism.

[1]

The synthesis methods of Pd-based electrocatalysts play a vital role in the structure, particle size, surface morphology, and particle distribution to aid in improving the electrochemical activity of the electrocatalysts [4]. This work employs two preparation techniques to synthesise the bimetallic electrocatalysts: microwave-assisted and sodium borohydride. Using two techniques provides better insight into the physicochemical properties and electrochemical behaviour of bimetallic electrocatalysts on both conventional and microwave methods. Manthiram and colleagues have reported the benefit of using microwave techniques on catalysts [12], as the method can enhance the activity toward reducing oxygen and alcohol oxidation. The technique is further reported to be faster, simple, and cleaner than the conventional method [12]. On the other hand, the traditional method is a well-known technique that many researchers have pursued to synthesise electrocatalysts.

Pd-based bimetallic electrocatalysts are known for their high performance toward alcohol oxidation. Unlike other alcohols, such as methanol and ethanol, glycerol has been explored the least. Also, the traditional method for synthesizing these bimetallic catalysts uses sodium borohydride ($NaBH_4$) as the reducing agent. Cassini and co-workers [13] recently reported that Fe-modified Pd had improved the electrocatalytic performance of glycerol electrooxidation in an alkaline environment. The use of the microwave-assisted method as an alternative is the least explored. Microwave-assisted synthesis has been observed to promote electrocatalysis, but little or nothing is reported as the possible reason(s) for such performance.

Motivated by the above reasons, this work studies simple Pd-based bimetallic catalysts (PdFe/C) obtained via the conventional $NaBH_4$ and microwave-assisted solvothermal methods. First, DFT simulation provides an insight into the influence of the second metal atom (Fe) on Pd when glycerol is adsorbed onto the surface of the Pd (111) and proves that incorporation of Fe leads to an increased electron density (in terms of partial density of states, PDOS). Also, DFT shows that it is easier for the glycerol to be released at the PdFe surface than at the Pd alone. Second, microwave irradiation tunes the physicochemical properties of the bimetallic

[1] Part of this chapter has been published:

Nonhlanhla Eugenia Mphahlele, Adewale Kabir Ipadeola, Aderemi Bashiru Haruna, Patrick Vaati Mwonga, Remegia Mmalewane Modibedi, Nithyadharseni Palaniyandy, Caren Billing, Kenneth Ikechukwu Ozoemena., Microwave-induced defective PdFe/C nano-electrocatalyst for highly efficient alkaline glycerol oxidation reactions, Electrochimica Acta 409 (2022) 139977

catalysts by increasing their crystallinity and creating defects (notably, oxygen vacancies) which, in turn, lead to improved electrocatalytic activities toward glycerol oxidation.

4.2 Results and Discussion

4.2.1 Computational Studies

First, DFT calculations were performed to observe the effect of glycerol adsorption on both the Pd and its bimetallic counterpart (PdFe). As indicated in the theoretical section and summarised in Figure 4.1, the Pd (111) was chosen as the model catalyst surface, considering that the (111) plane gives the highest alcohol oxidation activity amongst the low-index surfaces. At the same time, Fe (110) is usually the most prominent plane for Fe species. The adsorption energy of the PdFe-based electrode is slightly stronger (*A.E.* = -48.89 kcal/mol) than the Pd-based electrode (*A.E.* = -48.60 kcal/mol), which means that it is slightly difficult for the glycerol to be regenerated at the PdFe surface than at the Pd surface. In this work, binding energy (BE) can be defined as the strength of the bond between the alcohol and the catalyst. In contrast, the adsorption energy (AE) is the attraction between the alcohol and the catalyst surface. From Table 4.1 below, the BE is weaker (-45.094 eV) than that of the PdFe (85.081 eV), which means that it is easier for the bond between glycerol and Pd to be broken than that of the glycerol and PdFe. Interestingly, it is observed that the free energy is reduced from 2.707 kcal/mol (Pd) to 2.415 kcal/mol (Pd/Fe), indicating that the presence of Fe on Pd easily accelerates the potential limiting step, thereby lowering the free energy. The band gap energy was null for all the electrocatalysts.

Table 4.1: Computational studies of Pd and PdFe electrocatalysts in glycerol.

Electrocatalysts Glycerol	**Free energy (G) (kcal/mol)**	**Adsorption Energy, A.E (kcal/mol)**	**Binding energy, (eV)**	**Band gap energy, Eg (eV)**
Pd	2.707	-48.606	-45.094	None
PdFe	2.415	-48.898	-85.081	None

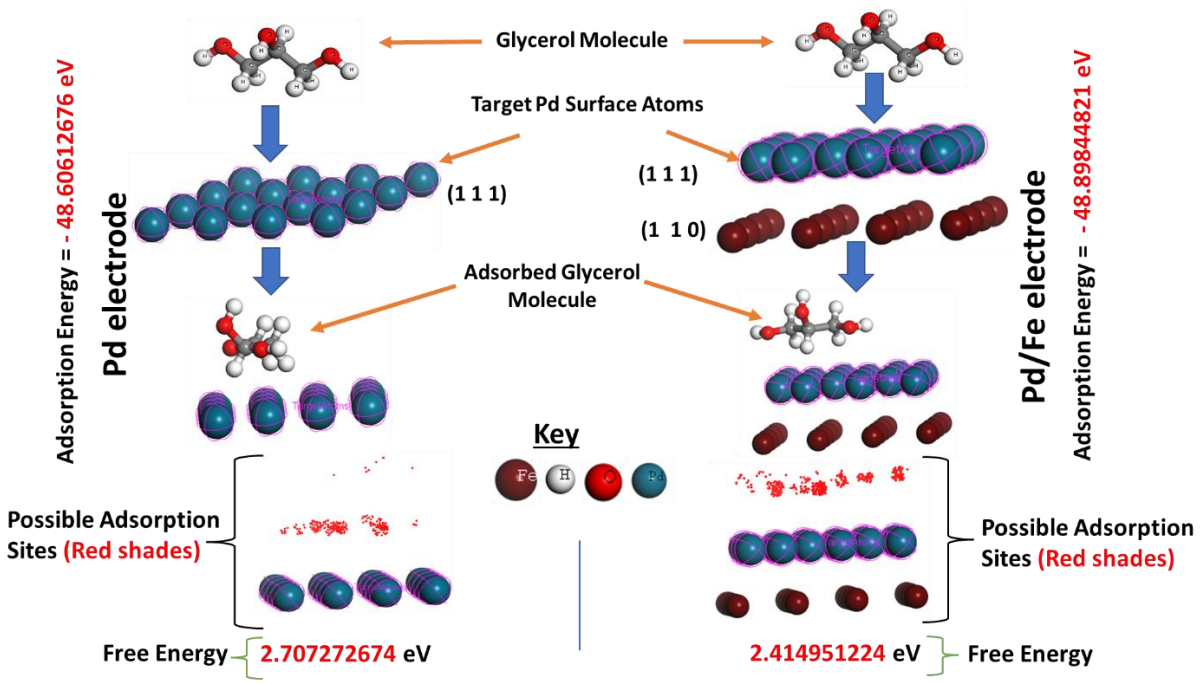


Figure 4.1: Glycerol molecule adsorption sites for Pd- and Pd/Fe-based electrodes. The dark blue dots (shades) show the possible site where glycerol is adsorbed.

To understand the electronic properties of glycerol on the active Pd and PdFe electrocatalysts before and after the adsorption process, calculations on the electronic band structures and the projected density of states (PDOS) were performed. As shown in Figure 4.2a-d, before the adsorption of glycerol on the active surfaces of the electrocatalysts, there are few available states in the Pd (shown by the band structure, Figure 4.2a) compared to the PdFe (Figure 4.2c), which means that more electrons are available on the PdFe than on the Pd alone. This is further supported by the PDOS where PdFe is about twice (95.4 electrons/eV, Figure 4.2d) that of the Pd alone (51.4 electrons/eV, Figure 4.2b).

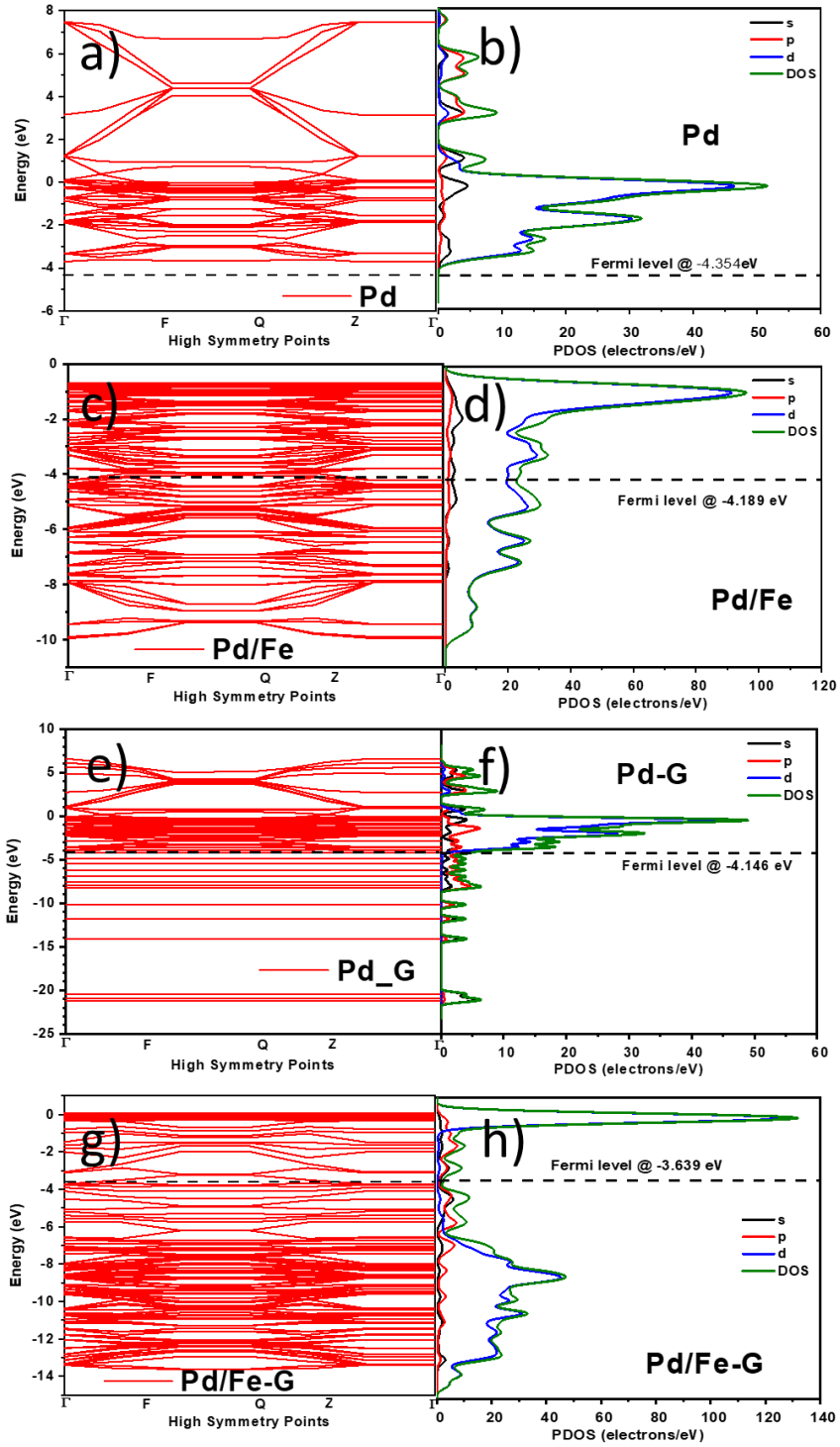


Figure 4.2: a,c,e,g) Band structure and b,d,f,h) partial density of states (PDOS) of the a,b,e,f) Pd and c,d,g,h) PdFe. The dotted lines represent the Fermi energy level, the PDOS shows that the electrons in the conduction band are mainly from the 3d orbital of the 3d orbital of the Pd and Fe.

However, after the adsorption of the glycerol (G) on the electrocatalysts shown in Figure 4.2e-h, the PDOS data clearly show that PdFe is more than twice (131 electrons/eV) that of the Pd alone (49 electrons/eV). This result suggests that the Lewis acid-base interaction of the glycerol with the Pd active surface site involves electron transfer from glycerol to the electrocatalyst (i.e., Pd cation, Pd^{2+}). Babaei and co-workers have observed the same phenomenon [14] for glycerol and TiO_2. Indeed, the intrinsic activity of the Pd-based electrocatalyst is intricately linked with its electronic structure. As already observed, upon the interaction of the glycerol molecule with the catalysts, there is a mismatch in Fermi levels (E_f) that leads to the charge-transfer process. Electrons flow from the glycerol to Pd active surface, thereby modifying the electronic states of the Pd or Pd/Fe atoms and increasing the Fermi energy levels. This charge-transfer process leads to a redistribution of partial charge, which is likely to enhance the reactivity of the PdFe over its Pd counterpart (as will be observed in the electrocatalytic section).

4.2.2 Physico-chemical Characterisation

4.2.2.1 TEM analysis

Figure 4.3 presents the TEM images of all the Pd-based electrocatalysts. The samples from the conventional method (Figure 4.3a, c) are smaller (2.48 – 3.02 nm) compared to the microwave-assisted samples (Figure 3b,d; 5.30 – 7.40 nm), indicating that microwave irradiation caused some agglomeration of the electrocatalysts, as observed previously [15, 16]. All the Pd-based catalysts generally show uniform dispersion on the carbon support.

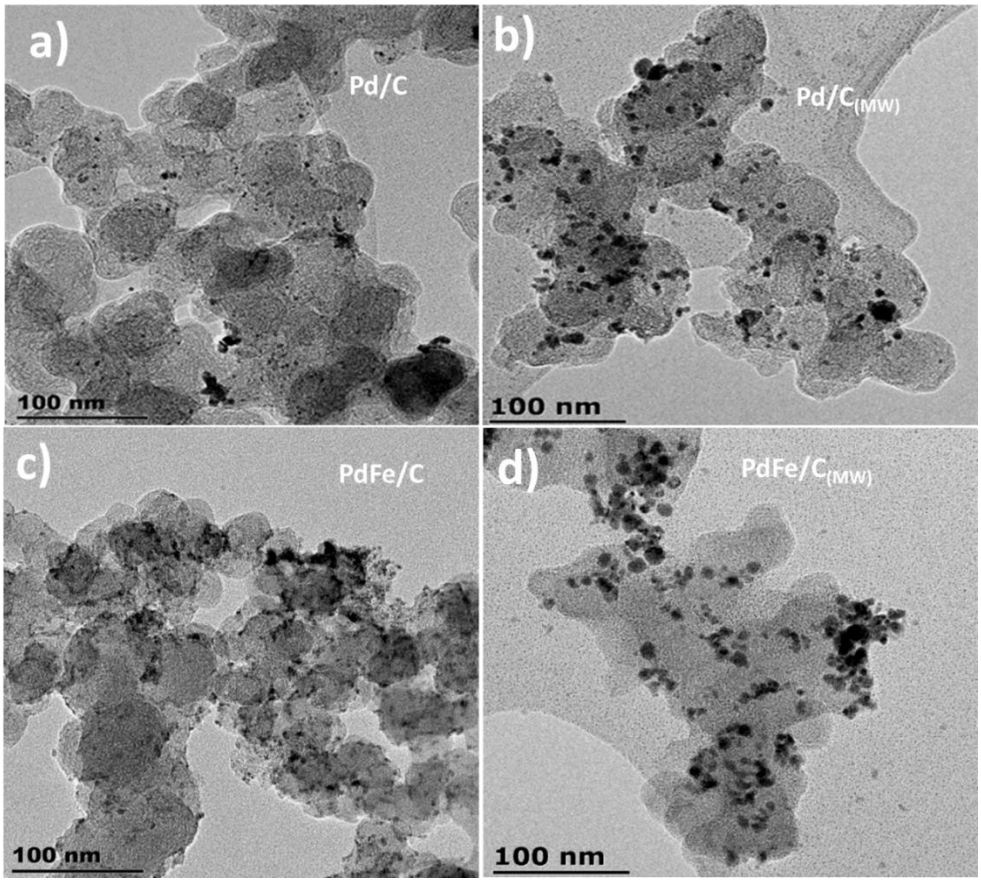


Figure 4.3: TEM images of Pd-based catalysts obtained from the conventional $NaBH_4$ method: a) Pd/C and c) PdFe/C; and microwave-assisted method: b) Pd/C and d) PdFe/C.

4.2.2.2 XRD Analysis

Figure 4.4 compares the XRD patterns of the Pd-based nano-electrocatalysts supported on carbon (Pd/C and PdFe/C) prepared by the conventional $NaBH_4$ method (Figure 4a) and microwave-assisted method (Figure 4b). All the nano-electrocatalysts displayed the diffraction peaks at 2θ (h k l) and values. The diffraction peak values are consistent with the (111), (200), (220), (311), and (222) planes consistent with the Pd face-centered cubic (fcc) crystalline structure. A common peak observed around 2θ to 25° in all the nano-electrocatalysts corresponds to the (002) carbon plane of the Vulcan XC-72 carbons as support. The XRD reveals an interaction between Pd and Fe to form an alloy, evidenced by similar diffraction indices of the same fcc of Pd in the PdFe/C, as the alloy contains mixed phases. The peaks of the samples from the microwave-assisted method (Figure 4.4b) are sharp, while those from the conventional method (Figure 4.4a) are broad. The result indicates that the catalysts obtained

from the microwave-assisted method exhibited higher crystallinity than those obtained from the conventional method.

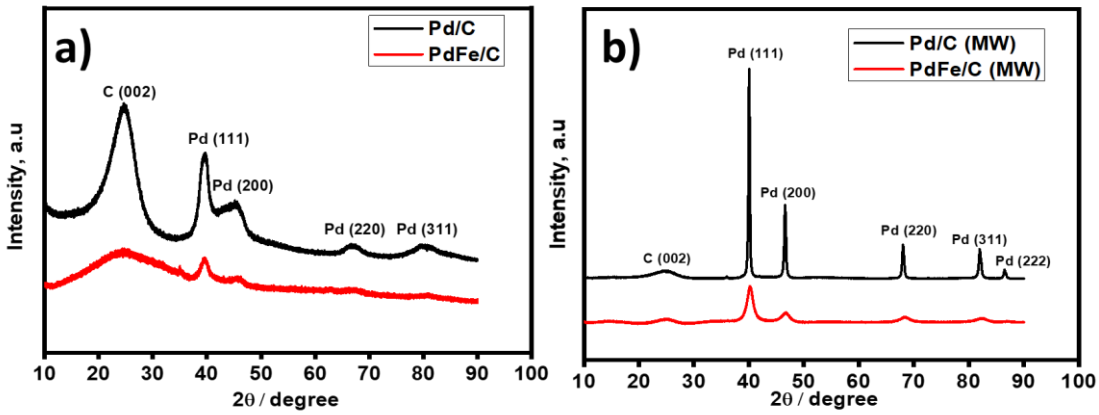


Figure 4.4: Comparison of the XRD patterns of the various Pd-based nano-electrocatalysts supported on carbon synthesised using a) the $NaBH_4$ and b) the microwave-assisted methods.

4.2.2.3 Nitrogen Desorption-Adsorption (Surface Area) Analysis

Brunauer-Emmett-Teller (BET) analysis was used to get information on the specific surface area and porosity of the samples. The summarised data are listed in Table 4.2. The results revealed that the specific surface area, pore sizes, and pore volumes of the PdFe/C nano-electrocatalysts are relatively smaller compared to the Pd/C obtained by both $NaBH_4$ and microwave irradiation methods. This might be because some available porous space inside carbon support is clotted and scattered with metal contents or chemical reactions [17]. These results corroborate with the TEM images whereby a little aggregation of the nano-electrocatalysts was observed, thus leading to a small specific surface area. Interestingly, the isotherms of all the nano-electrocatalysts displayed a type IV with an H1 hysteresis loop, which indicates a typical mesoporous material (according to pore classification ~ 2 – 10 nm) [18, 19] as shown in Figure 4.5. Furthermore, it was noticed that the isotherms of the bimetallic electrocatalysts absorbed less than 200 cm^3 / g of the gas compared to the monometallic Pd (absorbed more than 200 cm^3 / g).

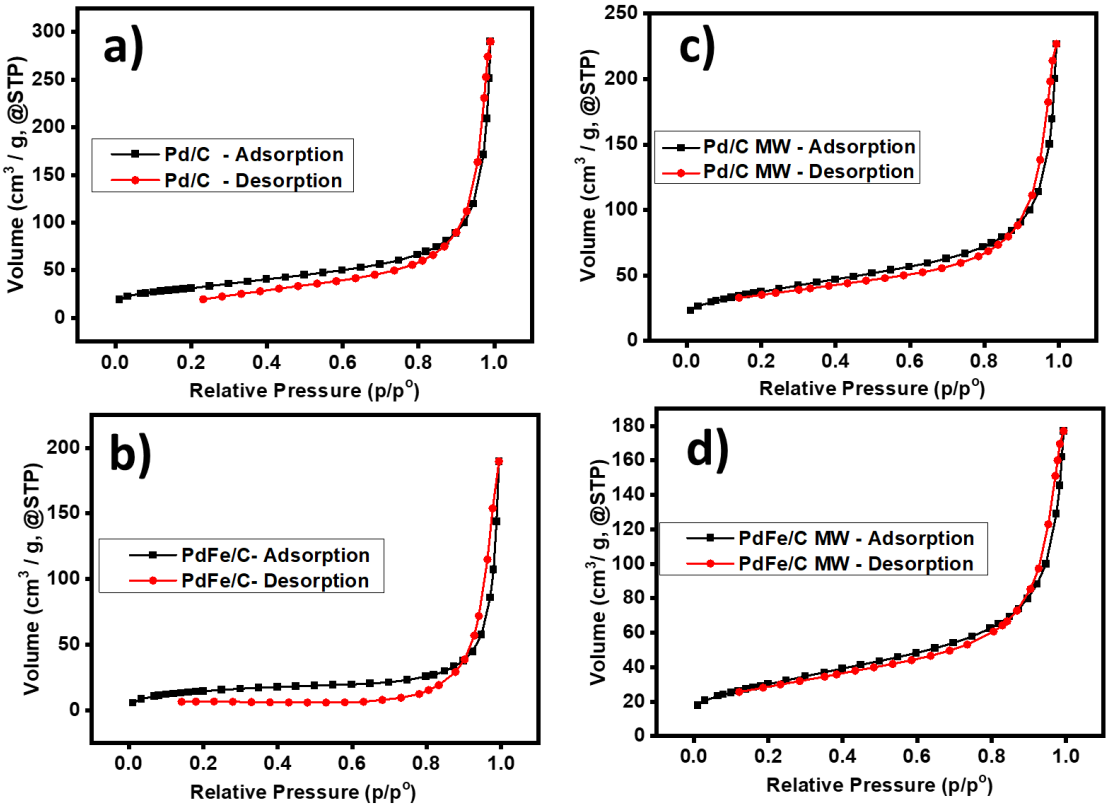


Figure 4.5: N_2 adsorption and desorption isotherms of Pd-based catalysts obtained from the conventional $NaBH_4$ method: a) Pd/C and b) PdFe/C; and microwave-assisted method: c) Pd/C and d) PdFe/C.

Table 4.2: Physisorption data obtained from Brunauer-Emmett-Teller (BET) for as-prepared nano-electrocatalysts.

Electrocatalysts	Pore size (nm)	Pore volume ($cm^3\ g^{-1}$)	SBET ($m^2\ g^{-1}$)
Pd/C ($NaBH_4$)	5.49	0. 194	123.95
Pd/C (MW)	5.88	0.182	132.00
PdFe/C ($NaBH_4$)	7. 19	0. 095	52.20
PdFe/C (MW)	6.92	0.136	65.32

4.2.2.4 Raman Spectroscopic Analysis

Raman spectroscopy was used to measure the structure and quality of carbon materials, particularly their degree of defect formation and ordered and disordered structure. Figure 4.6 shows the Raman spectra and deconvoluted peaks of all the Pd-based electrocatalysts.

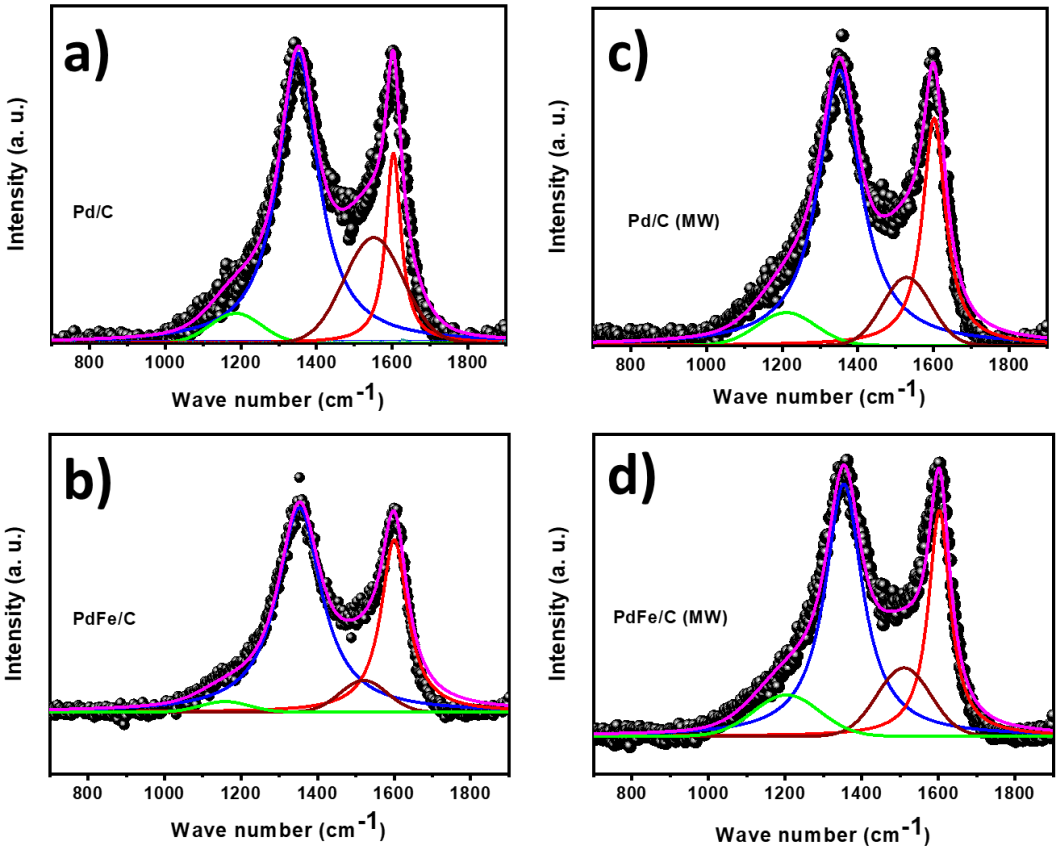


Figure 4.6: Raman spectra of $NaBH_4$ a) Pd/C, and b) PdFe/C and MW c) Pd/C, and d) PdFe/C.

The Raman spectra exhibit bands' positions around 1350 and 1600 cm ^{1}, which are related to the D and G bands, respectively. The D band is attributed to the structural defects and disorder-induced features of the sp^2 carbon domain. In contrast, the G band is associated with the E_{2g} vibration mode of a single crystal graphite structure [20-23]. Also, all the spectra have weak (amorphous carbon) and medium (disordered graphitic lattice) bands at around 1200 and 1500 cm^{-1}, respectively [21].

Table 4.3: Raman data of Pd-based electrocatalysts showing peak positions and intensity ratios.

Electrocatalysts	D band (cm^{-1})	G band (cm^{-1})	I_D/I_G
Pd/C ($NaBH_4$)	1350	1605	2.16
Pd/C (MW)	1358	1598	2.24
PdFe/C ($NaBH_4$)	1358	1605	2.11
PdFe/C (MW)	1350	1601	2.33

The D and G bands and the ratio of the peak intensities of the D and G bands (I_D/I_G) values are summarised in Table 4.3. The values of the I_D/I_G are more significant than unity, meaning that both synthesis methods introduced defects onto the carbon support. However, defects are more pronounced in the microwave samples than in the conventional synthesis method. Interestingly, microwave irradiation increased the I_D/I_G ratios by 3.7 and 10.4% for the Pd/C and PdFe/C, respectively. Defects are known to be widely present in nanostructured materials [24-31] and are well-recognized as the active sites that positively influence the electrochemical properties of electrode materials, both catalysts and energy storage materials alike. Thus, the samples from the microwave-assisted synthesis are expected to enhance the electrocatalytic properties of the Pd-based electrocatalysts.

4.2.2.5 XPS Analysis

XPS spectra are studied to investigate the surface oxidation state and binding energies of the elements in the Pd-based catalysts, shown in Figure 4.7. Figures 4.7a,b show the wide surveys of the PdFe/C ($NaBH_4$) and PdFe/C (MW) with both samples having the following elemental composition: Pd, Fe, C and O. The deconvoluted Pd 3d (Figures 4.7c,d) shows quartet spin-orbital splitting of Pd $3d_{5/2}$, Pd $3d_{3/2}$, PdO $3d_{5/2}$ and PdO $3d_{3/2}$ at the binding energies of 335.2 eV, 340.6 eV, 336.7 eV and 342.4 eV, respectively, for both electrocatalysts with no significant shifts. These spectra are ascribed to Pd and PdO_y ($0 < y < 2$), indicating that the electrocatalysts have a mixture of metallic palladium and its oxides.

This observation is similar to a previous report on Pd-based catalysts [138]. Figures 4.7 e,f show the deconvolution of Fe 2p to six distinct spectra at binding energies of 709.3, 711.5, 715.2, 718.6, 724.7 and 731.8 eV for PdFe/C ($NaBH_4$), attributed to Fe $2p_{3/2}$, FeO $2p_{3/2}$, FeOOH

$2p_{3/2}$, Fe $2p_{1/2}$, FeO $2p_{1/2}$, and FeOOH $2p_{3/2}$, respectively. The PdFe/C (MW) has corresponding Fe 2p deconvolution at binding energies of 706.7 eV, 710.2 eV, 713.3 eV, 718.3 eV, 722.8 eV, and 729.5 eV. However, Fe oxides formed less but more metallic Fe because the composite support (Fe/C) was heated in a reducing (H_2/Ar) environment. The slight shifts of the Fe 2p deconvoluted spectra to lower binding energies in the PdFe/C (MW) compared to the PdFe/C ($NaBH_4$) are traced to increased electron density (which corroborate the DFT data), increased oxygen vacancies and defect in the Fe lattice caused by microwave-irradiation. These intriguing properties in the Fe lattice of the PdFe/C (MW) are beneficial for strong synergistic properties with the Pd catalyst for enhanced electrocatalysis [32, 33].

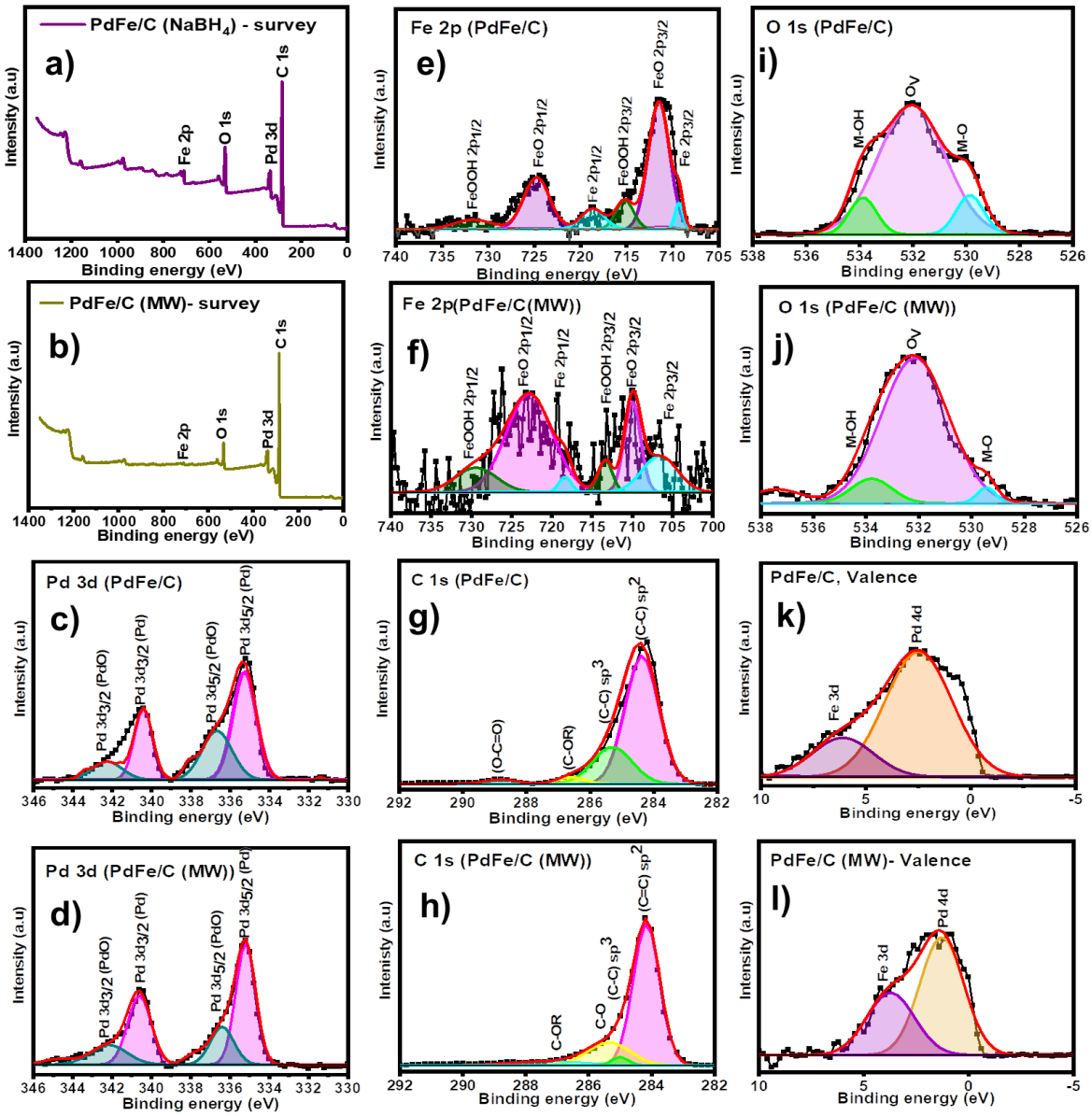


Figure 4.7: a,b) Wide survey, deconvoluted elementals scans c,d) Pd 3d, e,f) Fe 2p, g,h) C 1s, i,j) O 1s and k,l) Pd 4d and Fe 3d valences of PdFe/C ($NaBH_4$) and PdFe/C (MW) electrocatalysts.

The C 1s deconvoluted spectra of PdFe/C and PdFe/C (MW) catalysts (Figures 4.7g,h) show the C=C (sp^2), C-C (sp^3), C-OR and O-C=O in PdFe/C at the binding energies of 284.4, 285.3, 286.7, and 288.8 eV, respectively. In contrast, the microwaved Pd-based materials show the same at 284.1 eV (C=C, sp^2), 284.9 eV (C-C, sp^3), 285.5 eV (C-OR) and 287.1 eV (C–O). The absence of the O-C=O but the presence of C-O and the occurrence of the remaining C 1s deconvoluted spectra at slightly lower binding energies of the PdFe/C (MW) are equally due to defect and deficiency of oxygen, induced by microwave-irradiation in the carbon lattice [34]. Figures 7 i,j show O 1s deconvolution into three distinct spectra of metal oxides (M-O, 529.8 eV), oxygen vacancies (O_v, 532.1 eV) and hydroxide coverage on metal (M-OH, 533.9 eV) for the PdFe/C, but PdFe/C (MW) has the following O 1s deconvoluted spectra of M-O (529.4 eV), O_v (532.1 eV) and M-OH (533.8 eV) [35]. Both electrocatalysts have oxygen vacancies in their O 1s spectra. Still, the absorbed oxygen and hydroxides on the metals in the PdFe/C (MW) were suppressed by microwave irradiation, which suggests that a large amount of oxygen species have been removed (i.e., increased oxygen vacancies).

Finally, the Pd 4d and Fe 3d valences of the catalysts are shown in Figures 4.7 k,l. For the PdFe/C, these appear at the binding energies of 2.6 and 6.1 eV, respectively, whereas for the PdFe/C (MW), these appear at 1.3 and 3.8 eV, respectively. The shifts of the valences of the metals in the PdFe/C (MW) are confirmation of increased electron densities of the metals, oxygen vacancies, and defects created due to the microwave-assisted synthetic approach relative to the use of the conventional $NaBH_4$ reductive approach.

4.2.3 Electrochemical and Electrocatalytic Properties

4.2.3.1 Cyclic voltammetry in 0.5 M KOH in the absence and presence of glycerol

Figure 4.8 compares the cyclic voltammograms (CV) of the four Pd-based catalysts in 0.5 M KOH solution purged with nitrogen (Figures 4. 8a, b) at 50 mV / s. All the electrocatalysts display the signature responses of typical Pd electrocatalysts: (i) hydrogen adsorption/desorption redox processes around -0.8 V to -0.9 V, and (ii) reduction of palladium (II) oxide (PdO) to Pd^{o} around -0.35 V to -0.3 V window. The processes exhibit well-defined voltammetric curves for the Pd/C (MW) and PdFe/C (MW) catalysts compared to their counterparts obtained from the conventional $NaBH_4$ method. Unlike the Pd/C and Pd/C (MW), the peaks of the PdFe/C and PdFe/C (MW) shifted slightly to the negative voltage, indicating some alteration of the electronic structure of the Pd/C upon the incorporation of the Fe atoms. This result agrees with the DFT calculation that showed increased electron density for the PdFe compared to the Pd alone.

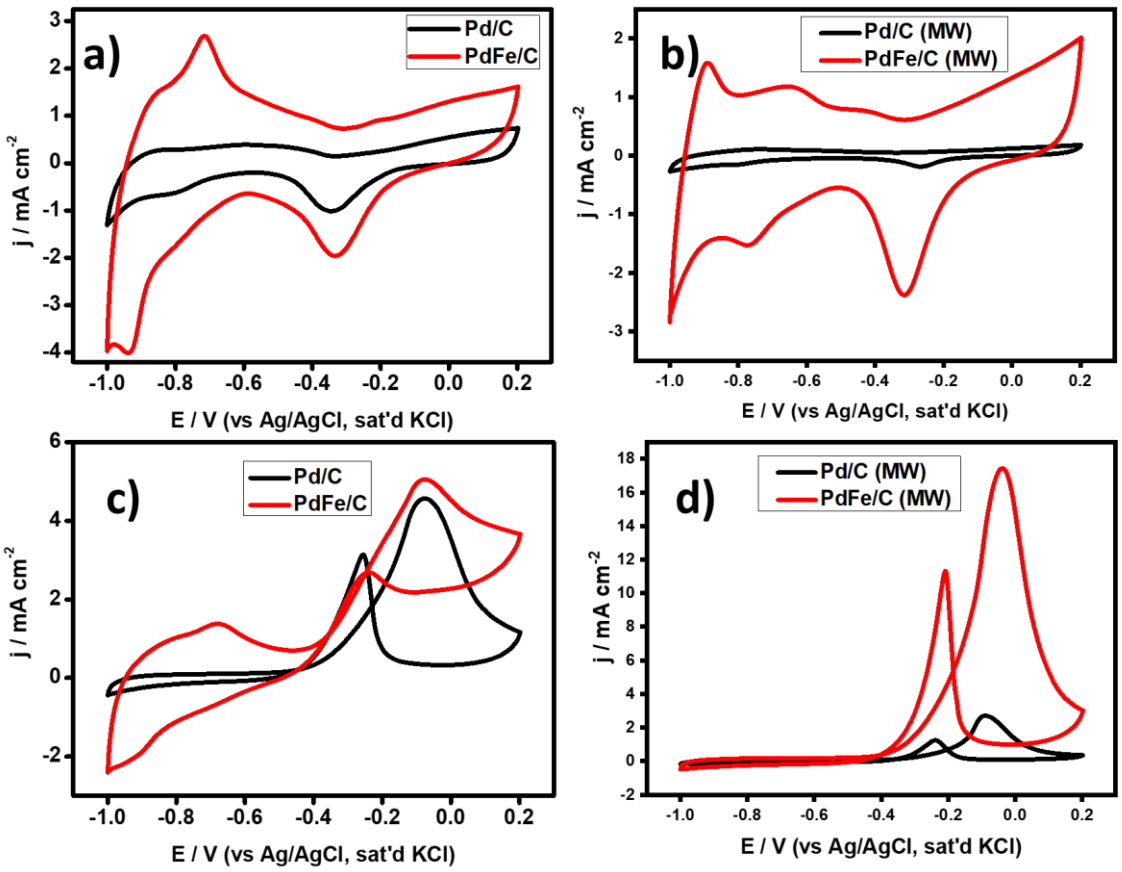


Figure 4.8: Cyclic voltammograms of Pd-based nano-electrocatalysts from conventional $NaBH_4$ method: a) Pd/C and PdFe/C, and microwave-assisted synthesis b)

Pd/C(MW) and PdFe/C(MW) in 0.5 M KOH solution under N_2 atmosphere at a sweep rate of 50 mV / s.

Cyclic voltammograms of Pd-based nano-electrocatalysts from conventional $NaBH_4$ method: c) Pd/C and PdFe/C, and microwave-assisted synthesis d) Pd/C (MW) and PdFe/C (MW) in 0.5 M KOH + 0.5 M glycerol solution under N_2 atmosphere at a sweep rate of 50 mV / s.

The electrochemical active surface area (ECSA) for each electrocatalyst was estimated from the PdO peak using equation 1 in accordance with the literature [34, 35].

$$ECSA = \frac{Q}{S.I} \qquad (4.1)$$

where Q denotes the integrated Coulombic charge for the reduction of PdO (in mC), S is a proportionality constant (0.424 mC cm^{-2}) assuming the formation of the monolayer on the surface of Pd during the cathodic scan, and Pd II is the amount of Pd loading measured in µg (13 µg).

As summarised in Table 4.4, the ECSA follows the trend: PdFe/C (MW) (38.99 $m^2 g^{-1}$) > PdFe/C (30.15 $m^2 g^{-1}$) > Pd/C (19.18 $m^2 g^{-1}$) > Pd/C (MW) (2.7 $m^2 g^{-1}$). The high ESCA of the bimetallic catalysts confirms the need to introduce the second metal (low-cost transition metal) to the expensive Pd (also corroborated by the DFT simulation). In addition, the highest ESCA value recorded for the PdFe/C (MW) confirms the positive effect of microwave irradiation on the bimetallic catalyst.

Table 4.4: Comparison of electrochemical parameters of Pd-based nano-electrocatalysts.

Electrocatalysts	EASA / m^2g^{-1}	E_{onset} (V)	J_f/J_b
Pd/C ($NaBH_4$)	19.18	-0.40	1.30
Pd/C (MW)	2.7	-0.33	2.17
PdFe/C ($NaBH_4$)	30.15	-0.42	1.70
PdFe/C (MW)	38.99	-0.39	1.56

Figure 4.8c, d compares the cyclic voltammetric performances of the four Pd-based electrocatalysts toward the oxidation of glycerol in KOH solution (i.e., 0.5 M KOH with 0.5 M Gly, in N_2 gas blanket) at 50 mV / s. All the CV curves displayed the two characterized peaks

of the glycerol oxidation (GOR) in alkaline media [2]. The forward peak current ((J_f) is associated with the oxidation of the Pd surface, while the return or backward peak current (J_b) represents the reduction of PdO. In every case, the Pd/C (MW) and PdFe/C (MW) gave the best-defined CV curves compared to their counterparts from the borohydride method. In addition, both Pd/C (MW) and PdFe/C (MW) showed the highest ratio of the forward and backward peak current densities (J_f/J_b), which signifies higher resistance to poisoning by carbonaceous species during glycerol oxidation compared to the Pd/C and PdFe/C from the conventional $NaBH_4$ method. Our previous work [1] shows that the ultimate glycerol oxidation product is the carbonate (which requires OH* species to occur in alkaline media: $CO_2 + 2OH^- = CO_3^{2-} + H_2O$). Thus, it is highly possible that one of the contributory factors for the high electrocatalytic performance of the PdFe/C(MW) toward glycerol electro-oxidation could be the ability of this electrocatalyst to adsorb and retain hydroxyl species (OH*) on the Pd surface.

4.2.3.2 Chronoamperometry and Electrochemical Impedance Spectroscopy

Figure 4.9 compares the results of the chronoamperometric (CA) tests (Figures 4.9a, b) conducted to gain some insights into the long-term stability and tolerance ability of the carbonaceous species. The CA experiments were performed in 0.5 M KOH / 0.5 M Gly solutions at a constant potential of -0.2 V (vs Ag/AgCl, saturated KCl). Each catalyst experienced noticeable decay in the current response in the first few minutes, indicating the accumulation of the poisonous carbonaceous intermediates from the glycerol oxidation. At the end of the 1800 seconds, the current responses follow the same trend as observed for the ECSA: PdFe/C (MW) (1.10 mA cm^{-2}) > PdFe/C (0.93 mA cm^{-2}) > Pd/C (0.35 mA cm^{-2}) > Pd/C (MW) (0.20 mA cm^{-2}). The higher current response by the PdFe/C (MW) indicates its higher ability to mitigate the poisoning from the carbonaceous intermediaries arising from the incomplete oxidation of the glycerol.

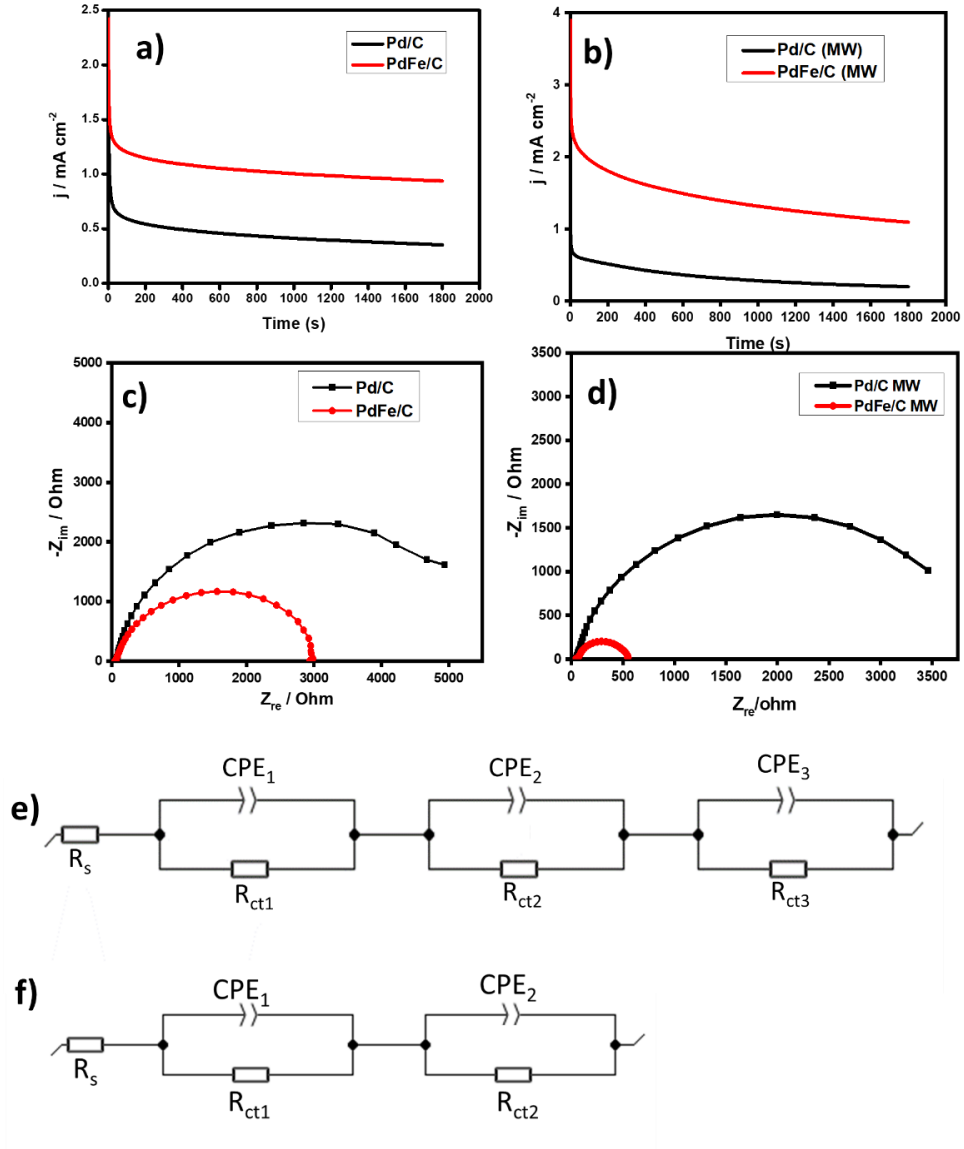


Figure 4.9: Chronoamperometric measurements of the Pd-based nano-electrocatalysts from conventional $NaBH_4$ method: a) Pd/C and PdFe/C, and microwave-assisted synthesis b) Pd/C (MW) and PdFe/C (MW) in 0.5 M KOH/0.5 M glycerol solution under N_2 atmosphere at -0.2 V and their corresponding Nyquist plots curves of the Pd-based nano-electrocatalysts obtained from the c) $NaBH_4$ method and d) microwave-assisted method, respectively. All data were obtained at a fixed potential of -0.2 V in glycerol electrooxidation. The electrical equivalent circuit (EEC) was used to fit e) monometallic while f) bimetallic.

Electrochemical impedance spectroscopy (EIS) probed the catalyst-electrolyte interfacial properties. As shown in the Nyquist plots (Figures 4.9c, d), the EIS data (Table 4.5) were

satisfactorily fitted using a simple RC electrical equivalent circuit (EEC) where R_s is the electrolyte resistance, R_{ct} is the charge transfer resistance and *CPE* is the constant phase element. The most critical parameter, *R*ct values decrease as follows: PdFe/C (MW) (0.55 kΩ) << PdFe/C (3.02 kΩ [2]) < Pd/C (MW) (3.68 kΩ) < Pd/C (5.25 kΩ), with the PdFe/C (MW) giving the best heterogeneous electron charge transfer kinetics. The presence of the CPE is indicative of the pseudocapacitive nature (Faradaic process) of the catalysts as well the roughness of the electrode surfaces, also confirmed by the corresponding exponent (n) values of 0.8 which are less than the ideal value of unity for pure double-layer capacitance (C_{dl}).

Table 4.5: EIS data for the Pd-based nano-electrocatalysts in a solution of 0.5 M KOH + 0.5 M Gly at -0.2 V (vs Ag|AgCl, sat'd KCl)

EIS Parameter	Pd/C	PdFe/C	Pd/C (MW)	PdFe/C (MW)
Rs / Ω	34.90±3.20	38.03±19.32	49.03± 0.44	38.34±2.453
CPE_1 / $mF.s^{(n-1)}$	1.183±0.308	3.54±0.21	0.310±0.15	267.14±0.31
n_1	0.36	0.25	0.97	0.48
R_{CT1} / Ω	66.30±15.60	76.731±202.106	803.26±31.10	31.58±7.07
CPE_2 / $F.s^{(n-1)}$	438.59±11.51	29.53±2.68	345.33±0.76	127.70±1.87
n_2	0.98	0.88	0.78	0.90
R_{CT2} / kΩ	1.65±0.96	2.91±2.77	1.13±0.22	0.48±0.06
CPE_3 / $F.s^{(n-1)}$	107.75±0.03		378.91±0.28	
R_{CT3} / kΩ	3.50±0.044		1.70±0.25	
n_3	0.93		0.98	

4.3 Conclusions

This work synthesised Pd-based mono and bimetallic nano-electrocatalysts (Pd/C and PdFe/C) with the conventional $NaBH_4$ route and that of the microwave-assisted reduction process. To understand the importance of bimetallic nano-electrocatalysts for glycerol oxidation reaction (GOR), DFT was used to study the adsorption of glycerol on Pd and PdFe. The bimetallic catalysts showed an increased electron density compared to the Pd alone, proving the need for a bimetallic nano-electrocatalyst in GOR. The adsorption energy of glycerol adsorbed on the surface of PdFe is weaker than on the Pd alone, which confirms the ease with which glycerol can be regenerated at the PdFe surface than at the Pd alone. Physico-chemical characterisation (XRD, TEM, XPS, BET, Raman) shows that microwave irradiation confers on the nano-electrocatalysts unique properties that enhance electrocatalysis: high crystallinity, nano-sized

particulate (< 8 nm), crystal defects, and high surface area. Subsequently, the microwave samples showed the best electrocatalytic performance for GOR (i.e., high electrochemical active surface area, high current density response, high resistance to poisoning by the carbonaceous intermediates arising from the GOR, and high conductivity or low interfacial resistance) compared to the samples obtained from the traditional $NaBH_4$ method. This work proves that microwave irradiation can be an essential tool for manipulating bimetallic nano-electrocatalysts to develop high-performance direct alkaline glycerol fuel cells.

4.4 References

[1] O.O. Fashedemi, H.A. Miller, A. Marchionni, F. Vizza, K.I. Ozoemena, Journal of Materials Chemistry A. 3 (2015) 7145-7156.

[2] L. Su, W. Jia, A. Schempf, Y. Lei, Electrochemistry communications. 11 (2009) 2199-2202.

[3] O.O. Fashedemi, K.I. Ozoemena, Electrochimica Acta. 128 (2014) 279-286.

[4] P.S. Fernández, M.E. Martins, G.A. Camara, Electrochimica Acta. 66 (2012) 180-187.

[5] J. Zhang, Y. Liang, N. Li, Z. Li, C. Xu, Electrochimica Acta. 59 (2012) 156-159.

[6] E. Habibi, H. Razmi, International Journal of Hydrogen Energy. 37 (2012) 16800-16809.

[7] V.L. Oliveira, C. Morais, K. Servat, T.W. Napporn, G. Tremiliosi-Filho, K.B. Kokoh, Electrochimica Acta. 117 (2014) 255-262.

[8] A. Falase, M. Main, K. Garcia, A. Serov, C. Lau, P. Atanassov, Electrochimica Acta. 66 (2012) 295-301.

[9] K.I. Ozoemena, RSC Advances. 6 (2016) 89523-89550.

[10] O.O. Fashedemi, K.I. Ozoemena, RSC Advances. 5 (2015) 22869-22878.

[11] S. Imhanria, X. Deng, T. Tan, J. Deng, L. Xu, W. Wang, Journal Alloys Compounds. 868 (2021) 159058.

[12] A. Sarkar, A. Vadivel Murugan, A. Manthiram, Fuel Cells. 10 (2010) 375-383.

[13] A. Cassani, N. Tuleushova, Q. Wang, H. Guesmi, V. Bonniol, J. Cambedouzou, S. Tingry, M. Bechelany, D. Cornu, Y. Holade, ACS Applied Energy Materials (2021).

[14] Z. Babaei, A.N. Chermahini, M. Dinari, Journal of Colloid and Interface Science563 (2020) 1-7.

[15] T. Ramulifho, K.I. Ozoemena, R.M. Modibedi, C.J. Jafta, M.K. Mathe, Electrochimica Acta. 59 (2012) 310-320.

[16] T. Ramulifho, K.I. Ozoemena, R.M. Modibedi, C.J. Jafta, M.K. Mathe, Journal of Electroanalytical Chemistry. 692 (2013) 26-30.

[17] N. Yahya, S.K. Kamarudin, N.A. Karim, S. Basri, A.M. Zanoodin, Nanoscale research letters. 14 (2019) 1-17.

[18] P. Nithyadharseni, M.V. Reddy, H. Fanny, S. Adams, B. Chowdari, RSC Advances. 5 (2015) 60552-60561.

[19] S.A. Ananthan, R. Suresh, K. Giribabu, V. Narayanan, Journal of Chemical Sciences. 125 (2013) 1365-1374.

[20] H. Yang, H. Wang, S. Ji, Y. Ma, V. Linkov, R. Wang, Journal of Solid-State Electrochemistry. 18 (2014) 1503-1512.

[21] A. Sadezky, H. Muckenhuber, H. Grothe, R. Niessner, U. Pöschl, Carbon. 43 (2005) 1731-1742.

[22] Z. Ni, Y. Wang, T. Yu, Z. Shen, Nano Research. 1 (2008) 273-291.

[23] S.N.M. Nawi, M.U. Khandaker, S.A. Sani, S.S. Ismail, K.S. Al-Mugren, M.A. Islam, K. Naher, D.A. Bradley, Radiation Physics and Chemistry. 189 (2021) 109709.

[24] J.P. Perdew, K. Burke, M. Ernzerhof, Physical Review Letter. 77 (1996) 3865.

[25] T.P. Mofokeng, Z.N. Tetana, K.I. Ozoemena, Carbon. 169 (2020) 312-326.

[26] T.P. Mofokeng, A.K. Ipadeola, Z.N. Tetana, K.I. Ozoemena, ACS omega. 5 (2020) 20461-20472.

[27] X. Yan, Y. Jia, X. Yao, Chem. Soc. Rev. 47 (2018) 7628-7658.

[28] Y. Jia, K. Jiang, H. Wang, X. Yao, Chemistry. 5 (2019) 1371-1397.

[29] P.V. Mwonga, R. Barik, S.R. Naidoo, A. Quandt, K.I. Ozoemena, Physical Chemistry Chemical Physics. 20 (2018) 28232-28240.

[30] C.J. Jafta, M.K. Mathe, N. Manyala, W.D. Roos, K.I. Ozoemena, ACS applied materials & interfaces. 5 (2013) 7592-7598.

[31] A.B. Haruna, P. Mwonga, D. Barrett, C.B. Rodella, R.P. Forbes, A. Venter, Z. Sentsho, P.J. Fletcher, F. Marken, K.I. Ozoemena, ACS omega (2021).

[32] A.K. Ipadeola, P.V. Mwonga, S.C. Ray, R.R. Maphanga, K.I. Ozoemena, Electroanalysis. 32 (2020) 3060-3074.

[33] H. Lv, H. Zhao, T. Cao, L. Qian, Y. Wang, G. Zhao, Journal of Molecular Catalysis A: Chemical. 400 (2015) 81-89.

[34] S.S. Hossain, Arabian Journal for Science and Engineering. 46 (2021) 6543-6556.

[35] A.K. Ipadeola, N.Z. Lisa Mathebula, M.V. Pagliaro, H.A. Miller, F. Vizza, V. Davies, Q. Jia, F. Marken, K.I. Ozoemena, ACS Applied Energy Materials. 3 (2020) 8786-8802.

[36] D. Rand, R. Woods, Journal of Electroanalytical Chemistry and Interfacial Electrochemistry. 31 (1971) 29-38.

CHAPTER 5

Interrogating the effect of microwave irradiation on bimetallic electrocatalysts toward ethanol oxidation reaction

5.1 Introduction

In previous years, DEFCS has garnered much attention due to their nontoxicity, higher energy density, greater availability, and higher theoretical mass energy (8 kW h g^{-1}) [1] compared to DMFCs. In addition, ethanol can be generated in enormous quantities as biofuel from biomass fermentation [2]; hence, it is chosen as one of the best fuels. However, the commercialisaton of DEFCs has also been constrained because, during the EtOH oxidation, H_2O and CO_2 are expected to be produced as a by-product; for instance, there are some difficulties in cleaving the C-C bond. Secondly, there is an issue with the formation of CO intermediates, which subsequently poisons the anode catalysts [3]. These drawbacks yield a low efficiency of ethanol oxidation with sluggish kinetics, which in many cases are caused by the type of catalysts that have been chosen.

Therefore, it is imperative to fathom the detailed reaction pathway and search for novel anode catalysts [4] to oxidize ethanol completely. Platinum (Pt) based nano-catalysts have been widely used as an alternative anode catalyst for DEFCs and have shown satisfactory results in acidic medium. Unfortunately, Pt-based catalysts have the propensity to be easily poisoned by intermediates on the surface, which decreases their efficiency. Moreover, their problems have not been resolved, primarily when operating in an alkaline medium [5].

Another alternative catalyst that is more viable than Pt was suggested to overcome this challenge: a Pd-based electrocatalyst. The use of Pd-based electrocatalysts as a suitable candidate has been intensively studied due to their excellent properties, such as being abundant in nature. It can eliminate poisoning species on the surface, mainly when operating in an alkaline medium. Various observations have been made in an alkaline medium, including rapid kinetic and improved fuel efficiency towards ethanol electrooxidation [6]. Extensive studies have been conducted to further enhance the electrocatalytic behaviour of Pd-based catalysts. These were carried out by alloying Pd with non-noble metals such as Fe, Ni, Au, Co, etc. since

bimetallic Pd-based catalysts have more significant catalytical activity than pure Pd [7]. Recently, Mkhohlakali and his co-workers reported the preparation of Pd monometallic and PdIr bimetallic using the E-ALD method. In his work, they demonstrated that the presence of iridium unto Pd has shown a remarkable influence on improving the activity and durability of Pd in the oxidation of EtOH [8]. Ipadeola and his colleagues alloyed Pd with SnO_2/MOFs using MW methods, resulting in Pd/SnO_2/MOFs becoming the promising catalyst for EOR with improved electro-catalytical activity [9].

Specifically, non-noble metals such as iron (Fe), manganese (Mn), and cobalt (Co) alloyed with Pd have been investigated to provide OH- groups needed to enhance ethanol oxidation [10, 11]. Nevertheless, limited research has been conducted on utilising Fe, Mn, and Co as co-metals towards alcohol oxidation. In addition, the work performed by Xu and co-workers has shown how these metals in the form of oxides enhanced Pd/C catalysts towards the electrooxidation of alcohols in alkaline space [12]. Motivated by this article, herein we report the synthesis of PdFe/C, PdMn/C, and PdCo/C using microwave synthetic methods at various ratios (Pd_2M/C & PdM/C) towards ethanol electrooxidation in an alkaline medium.

The electrochemical behaviour of these electrocatalysts has shown significant improvement in activity and stability. The various ratios were explored to examine the effect of molar ratios on the structure of electrocatalysts. As reported before, the physiochemical properties of electrocatalysts depend on the ratios of metal precursors. Motivated by the work conducted in Chapter 4, this research focuses on examining other non-noble metals in Pd/C to compare their performance with PdFe/C electrocatalyst. The performance of the latter was conducted in glycerol; therefore, in this chapter, the electrocatalysts are explored towards ethanol in an alkaline medium. It was depicted that PdFe/C from both ratios delivered more activity towards the EOR than other bimetallic.

5.2 Results and Discussion

5.2.1 Computational work on the development of bimetallics.

DFT calculations were first performed on PdFe, PdCo, and PdMn to identify the role of EtOH adsorption. As indicated in Chapter 3, summarised in Table 5.1, and further elaborated upon in Chapter 4.

Table 5.1 Computational simulation of various bimetallics in ethanol.

Electrocatalysts Ethanol	ΔG (kcal/mol)	A.E (kcal/mol)	Binding energy (eV)	Band gap energy, Eg (eV)
PdFe	-1.427	-9.931	-79.728	0.406
PdCo	-1.449	-9.953	-78.967	0.425
PdMn	-1.445	-9.949	-79.765	0.375

In this work, it was noticeable that the PdFe-based electrode exhibits a slightly weaker (Adsorption energy, *A.E.* = -9.931 kcal/mol) in comparison to other bimetallic catalysts (A.E. = -9.953, -9.949 kcal/mol, PdCo and PdMn, respectively), indicating that EtOH can easily be reproduced at the PdFe surface than its counterparts. Intriguingly, the Gibbs free energy (ΔG**)** was observed to be decreasing as follows from -1.449 and -1.445 kcal/mol (PdCo and PdMn, respectively) to -1.427 kcal/mol (PdFe), indicating that the presence of Fe on Pd can expedite the limiting potential step, thereby minimizing the free energy. PdMn exhibits a smaller band gap of 0.375 eV across PdFe (0.406 eV) and PdCo (0.425 eV), indicating excellent electron transfer and can promote the adsorption/desorption towards ethanol oxidation. The prediction from this study is more aligned with the electrochemistry of these catalysts, even though there is a discrepancy with the smaller band attained for PdMn.

5.2.1 Physico-chemical Characterisation

5.2.1.1 X-Ray Diffraction Measurements

The XRD measurements were conducted to investigate the crystallinity and structural characteristics of the as-prepared Pd-based electrocatalysts at different atomic ratios (a)Pd_2M/C and b) PdM/C atomic ratios), as shown in Figure 5.1.

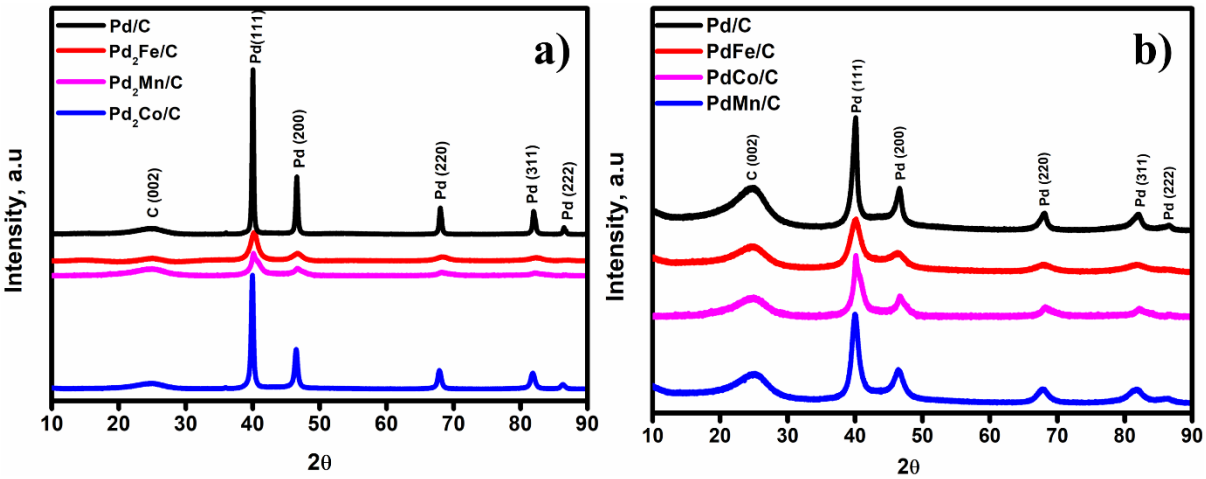


Figure 5.1: XRDs patterns of bimetallic electrocatalysts (at varied Pd_2M/C and PdM/C).

Table 5.2: XRD data of Pd-based electrocatalysts at different atomic ratios.

Electrocatalysts	Pd (111) (2 θ)	d (111) (nm)	Lattice Parameter (nm)	Crystalline size (nm)
Pd/C	40.05	0.2249	0.3896	36.54
PdFe/C	40.08	0.2247	0.3891	5.81
Pd_2Fe/C	40.00	0.2251	0.3900	3.69
PdCo/C	40.03	0.2242	0.3895	8.59
Pd_2Co/C	40.12	0.2250	0.3889	7.53
PdMn/C	40.13	0.2247	0.3892	6.56
Pd_2Mn/C	40.02	0.2252	0.3905	9.82

The broad C (002) peaks appear in both patterns at about 25° for all the electrocatalysts, signifying amorphous Vulcan XC 72 carbon material [13]. The diffraction peaks located at 40°, 48°, 69°, 82° and 88° for all the Pd-based electrocatalysts are attributed following this sequence (111), (200), (220), (311) and (222) as the fcc crystalline Pd, respectively [14, 15]. We observed no shift of the Pd (111) diffraction peaks for all the Pd-based electrocatalysts, signifying that the insertion of co-metals does not affect the Pd crystalline lattice [16]. There was no evidence of oxides or co-metals diffraction peaks, probably because their phases are amorphous and cannot be detected by XRD [17]. The Scherrer equation was used to calculate the interplanar distance, lattice parameter, and crystallite sizes, and the data are presented in

Table 5.2. It is imperative to point out that the estimated crystallite size of all the bimetallic electrocatalysts is smaller than that of the Pd alone. The sizes agree with the TEM images histogram.

5.2.1.2 TEM analysis

TEM micrographs were employed to discern the morphology and particle sizes of Pd-based catalysts, as noted in Figure 5.2. The micrographs of the catalysts exhibited several agglomerations on the carbon support with a relatively dispersed particle size distribution between 2 nm and 10 nm. However, it was also reported that when the electrocatalysts have smaller particle sizes, fuel adsorption can occur by increasing EtOH activities [18].

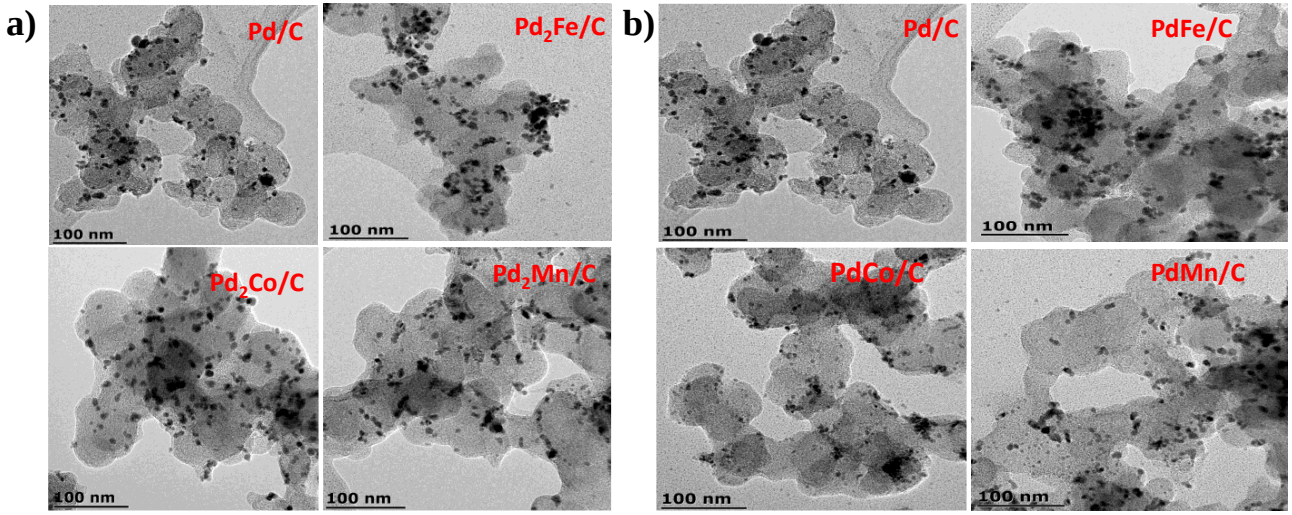


Figure 5.2: TEM micrographs representing a) Pd_2M/C) and b) PdM/C electrocatalysts.

5.2.2 Electrochemical characterisation

CV was used to study the electrochemical behaviour of Pd, PdFe/C, PdMn/C, and PdCo/C nano-catalysts at varied atomic molar ratios (Pd_2M/C and PdM/C) in KOH (0.5 M) bubbled with N_2 gas at 50 mV / s sweep rate, shown in Figure 5.3. Figure 5.3a represents the CV profile of Pd-based electrocatalysts at Pd_2M/C, while Figure 5.3b exhibits the CV profile at PdM/C. Significant potentials emerged between (-0.8 V to -0.9 V) vs. Ag/AgCl on both the anodic and cathodic sweep, attributed to the hydrogen desorption/desorption peak currents on the Pd surface [7, 19]. Anodic sweeps display a weak peak potential shoulder at around -0.2 V vs Ag/AgCl) corresponding to the formation of the PdO layer at different oxidation states Pd (0), Pd (I), Pd (II), and Pd (IV) [18, 20].

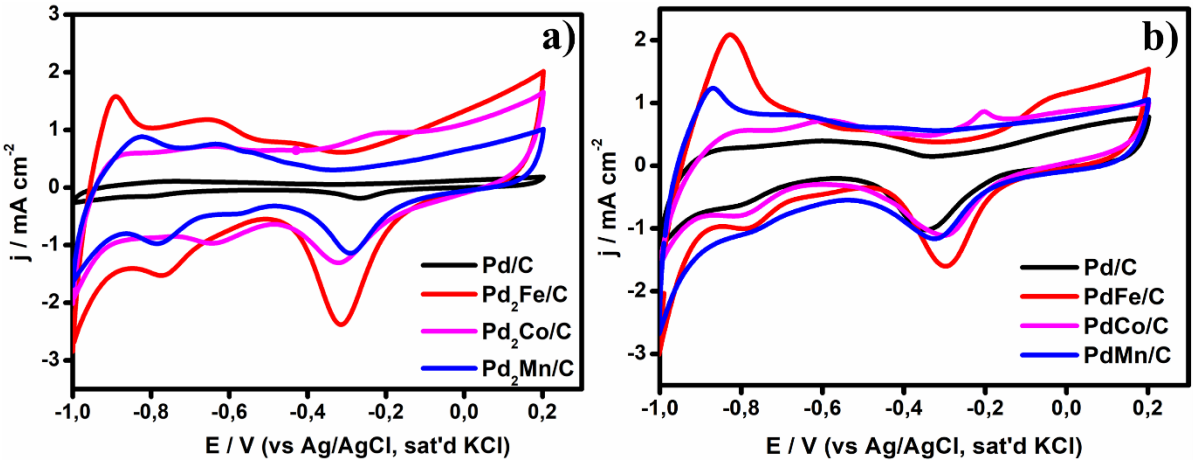


Figure 5.3: Cyclic voltammetry of Pd, PdFe/C, PdMn/C, and PdCo/C (atomic ratio of Pd_2M/C and PdM/C in (0.5 M) KOH solution, N_2 gas - sweep rate = 50 mV / s.

During the cathodic sweep, a strong potential peak displayed at (-0.1 V) indicates the reduction of PdO. The peaks were instrumental in predicting the ECSA across the electrocatalysts. The estimated ECSA values are reported in Table 5.3. The Pd_2Fe/C and PdFe/C electrocatalysts display higher values of ECSA than their counterparts, indicating that the surface area is more significant for the electrooxidation of ethanol. Douk and co-workers have previously reported that the more excellent ECSA value could correspond to the synergistic effect referring to the bifunctional mechanism and electronic effect occurring [7] between Fe and Pd in PdFe/C.

Table 5.3: Comparison study of electrochemical parameters of electrocatalysts towards EOR in an alkaline environment.

Electrocatalysts	ECSA/ $m^2 g^{-1}$	E_{onset} (V)	J_f/J_b	Specific Activity (mA cm^{-2})	Mass Activity (mA mg^{-1})
Pd/C	2.7	-0.50	1.07	1.65	550
PdFe/C	30.17	-0.53	0.91	4.15	1380
Pd_2Fe/C	38.99	-0.55	0.80	11.59	3690
PdCo/C	16.89	-0.51	0.67	3.36	1010
Pd_2Co/C	16.07	-0.53	0.82	9.11	3060
PdMn/C	16.89	-0.52	0.86	3.82	1250
Pd_2Mn/C	16.72	-0.53	0.79	7.40	2320

Figure 5.4: exhibit the CV of Pd, PdFe/C, PdMn/C, and PdCo/C (atomic ratio of Pd_2M/C and PdM/C) in 0.5 M KOH solution + EtOH (0.5 M) in the presence of N_2 gas using the sweep rate of 50 mV / s. Two distinct current density peaks were noted at the anodic sweep (forward scan) and the cathodic sweep (reverse scan). The anodic sweep can be ascribed as the oxidation of freshly chemisorbed species obtained during ethanol adsorption. On the other hand, the cathodic sweep observed on all the Pd-based electrocatalysts corresponds to the removal of carbonaceous species that are not completely oxidized during ethanol adsorption [19, 21]. Table 5.3 shows the electrochemical conditions of all the electrocatalysts. It is noticeable that PdFe/C exhibits a highly negative value of onset potential of about -0.55 V (Pd_2Fe/C) and -0.53 V (PdFe/C) compared to all the electrocatalysts. Indicating that the insertion of Fe into Pd improved the kinetics of EOR in a basic environment.

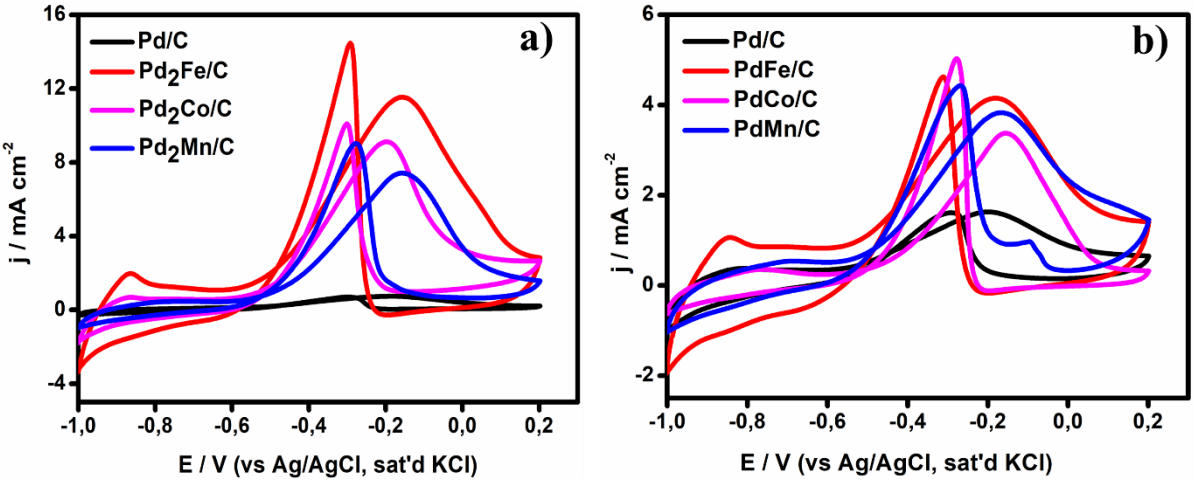


Figure 5.4: CV of Pd, PdFe/C, PdMn/C, and PdCo/C (molar ratio: Pd_2M/C and PdM/C) in (0.5 M KOH solution + 0.5 M) EtOH, N_2 atmosphere using sweep rate of 50 mV / s.

Significantly, the Pd_2Fe/C and PdFe/C electrocatalysts evinced a higher current density of about 11.59 (Pd_2Fe/C) and 4.15 (PdFe/C) mA cm^{-2}, which is about 2 times higher than respective counterparts indicating an enhancement in ethanol electrooxidation, as displayed in Figure 5.5. In addition, the mass activities obtained for Pd_2Fe/C and PdFe/C exhibit a superior value of 3690 and 1380 mA mg^{-1} than that of the counterparts and the data is summarised in Table 5.3.

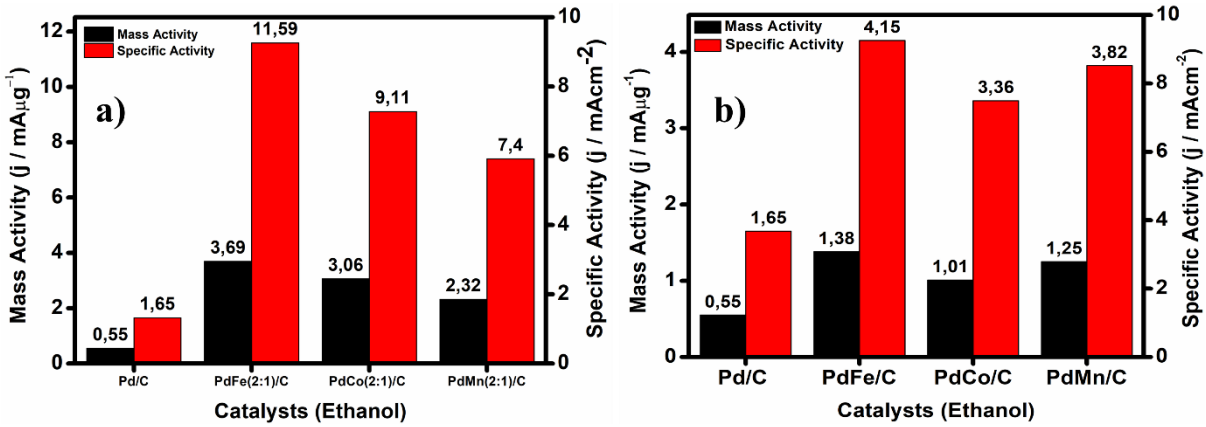


Figure 5.5: Comparison of mass and specific activities of Pd, PdFe/C, PdMn/C, and PdCo/C (Pd_2M/C and PdM/C) in KOH + EtOH both in (0.5 M), N_2 gas at a scan rate = 50 mV / s.

5.2.2.1 Chronoamperometric analysis

The electrochemical stability was carried out using chronoamperometric analysis. Figure 5.6 displays the chronoamperometric analysis of all the Pd-based electrocatalysts prepared in (0.5 M) KOH + ethanol solution under an N_2 atmosphere at the potential of -0.2 V. At the initial stage, the current density dropped off continuously with time, and thereafter the current densities became a pseudo steady state. The current density decay corresponds to surface poisoning and unstable catalysts. The higher current densities were mainly observed on Pd_2Fe/C and PdFe/C electrocatalysts, denoting better electrocatalytic durability towards EOR in alkaline electrolytes [19, 20].

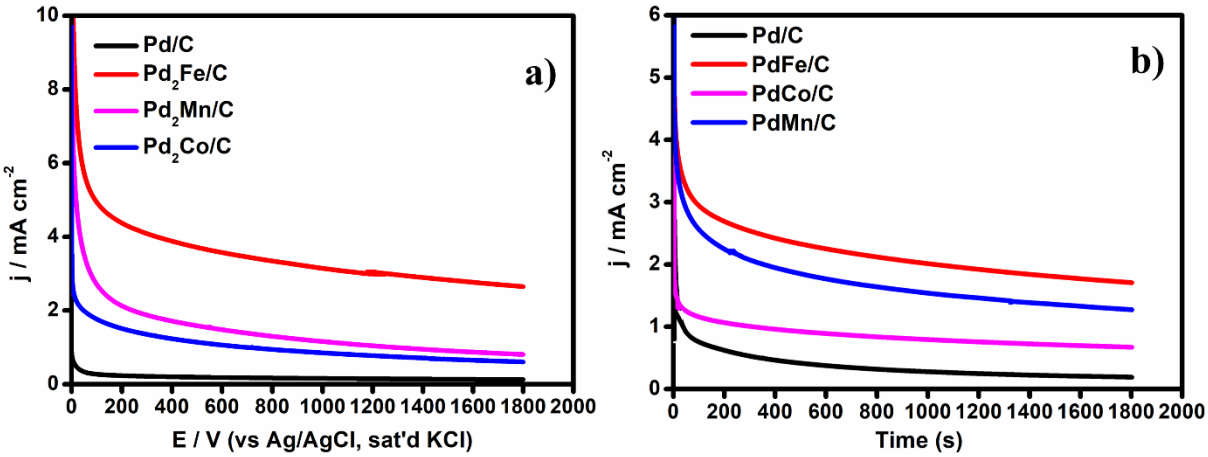
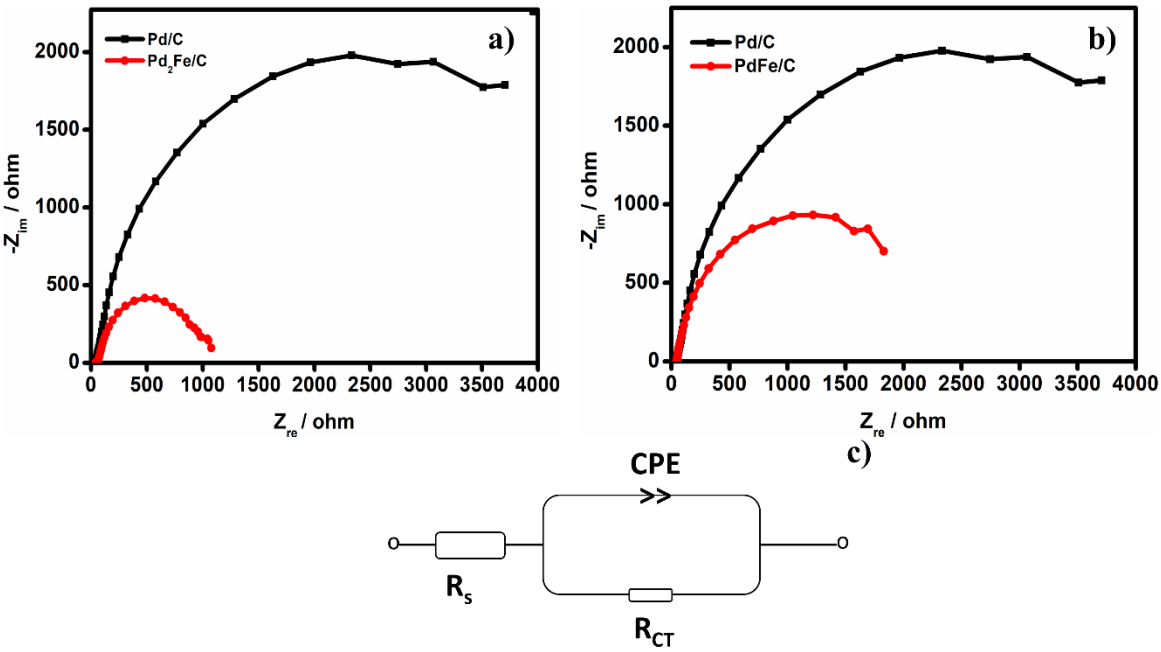


Figure 5.6: Chronoamperometry curves for of Pd, PdFe/C, PdMn/C, and PdCo/C (a) Pd_2M/C and b) PdM/C) in (0.5 M - KOH solution, ethanol) bubbled with N_2 atmosphere at -0.2 V.

5.2.2.2 The of EIS on various bimetallics.

The EIS technique is well-known for probing the electrochemical process at the solution or electrode interface. The Nyquist plots at different atomic ratios (Pd_2M/C and PdM/C) were measured in the mixture of 0.5 M KOH - EtOH at the fixed potential of -0.2V vs. Ag/AgCl, KCl saturated as shown in Figure 5.7 a & b. Figure 5.7 c exhibits the equivalent circuit components, such as Rs is the electrolyte resistance, Rct is the charge transfer resistance, and CPE is the constant phase element. Table 5.4 illustrates the electrochemical impedance parameters and shows that the diameter of the semicircles resonates with the charge transfer resistance (R_{ct}). The Pd_2Fe/C and PdFe/C electrocatalysts offered a feeble charge transfer

resistance than monometallic, possibly because ethanol has fast electro-oxidation kinetics in an alkaline medium. The faster electro-oxidation kinetics could be attributed to the excellent electron transfer ability of Fe on the surface of the electrode to remove carbonaceous species.



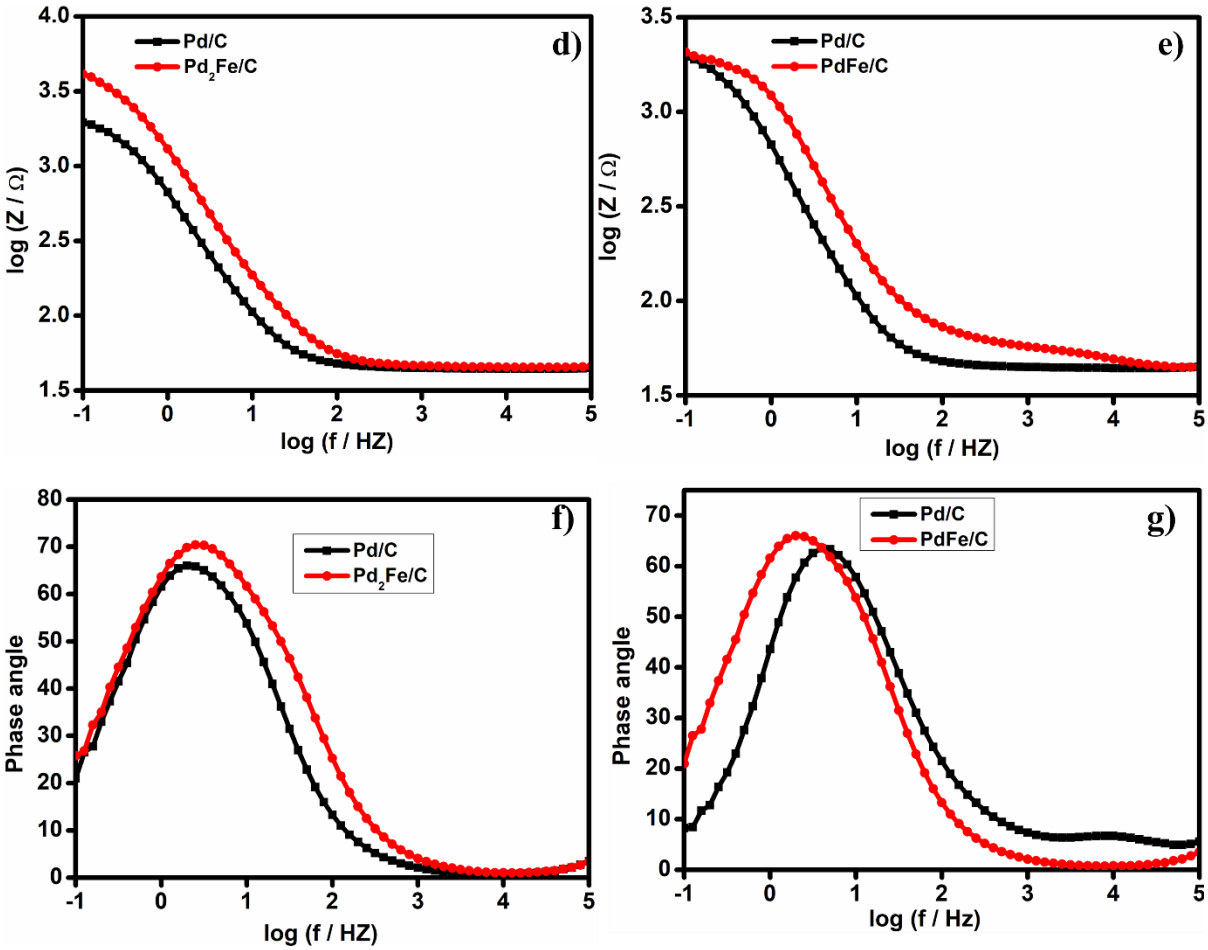


Figure 5.7: Nyquist curves electrocatalysts at the potential of -0.2 V in electrooxidation of EtOH, a-b) the electrical equivalent fitted circuit (EEC). c-f) bode plots corresponding to Pd-based electrocatalysts.

Table 5.4: Electrochemical Impedimetric data of catalyst containing a (0.5 M) KOH & 0.5 M ethanol at -0.2 V.

	EIS conditions			
	R_s (Ω)	R_{ct} (kΩ))	n	*CPE* ($F.s^{(1-n)}$) x 10^2
Pd/C (MW)	41.89±0.43	1.74±0.001	0.80	0.27±1.28
Pd_2Fe/C	34.85±0.55	0.17±0.001	0.87	0.78±0.57
PdFe/C	44.25±0.37	0.79±0.001	0.85	0.28±0.33

Thus, the Pd_2Fe/C exhibits a higher CPE value than PdFe/C and its monometallic counterparts, revealing its ability to store more charges during the ethanol oxidation, and the ideality values ($n < 1.0$) for all the electrocatalysts correlate directly to the pseudo-capacitive behaviour. Figure 5.7 d-g exhibits the bode plots corresponding to Pd2Fe/C, PdFe/C, and Pd/C electrocatalysts, respectively. The total impedance log Z of Pd_2Fe/C displays a superior value of about 3.5 Ω than its counterparts at low-frequency regions. The exceptional value of total impedance log Z aligns with the highest current density observed from the CV and the minimal value of Rct. The Pd_2Fe/C and PdFe/C electrocatalysts exhibit the highest phase angle, predominately owing to the most excellent conductivity compared to the Pd/C electrocatalysts [8].

5.3 Conclusions

Electro-oxidation of ethanol on Pd/C, PdFe/C, PdCo/C, and PdMn/C electrocatalysts was successfully conducted at different atomic ratios (Pd_2M/C and PdM/C) in alkaline electrolytes. PdFe (ethanol) adsorption energy was slightly more feeble than their counterparts, confirming the ease at which EtOH can be produced at the PdFe active site rather than at the Pd alone and its counterparts. The Pd_2Fe/C electrocatalysts electrode has been identified to possess high electrocatalytic activity regarding CV, stability, and electrochemical impedance measurements (EIS). According to the CV, CA, and EIS, it was observed that Fe on Pd/C has the highest current density, mass activity, and an increase in stability, as well as a low value of R_{ct} (0.17 and 0.79 kΩ). Amongst all studied bi-metallics, Pd_2Fe/C and PdFe/C electrocatalysts have shown better electrocatalytic activity towards ethanol electro-oxidation in an alkaline medium.

In summary, both theory and experiments have demonstrated that Fe-based Pd bimetallic (Pd_2Fe or PdFe) gives the best electrocatalytic properties towards ethanol oxidation.

5.4 References

[1] Y. Huang, J. Cai, M. Liu, Y. Guo, Electrochimica Acta. 83 (2012) 1-6.

[2] S.C. Lai, S.E. Kleyn, V. Rosca, M.T. Koper, The Journal of Physical Chemistry C. 112 (2008) 19080-19087.

[3] J. Goel, S. Basu, Energy Procedia. 28 (2012) 66-77.

[4] J. Friedl, U. Stimming, Electrochimica Acta. 101 (2013) 41-58.

[5] Y. Fornazier Filho, da Cruz, Ana Caroliny Carvalho, R. Pedicini, J.R.C. Salgado, P.P. Luz, J. Ribeiro, Materials for Renewable and Sustainable Energy. 10 (2021) 1-12.

[6] M.Z.F. Kamarudin, S.K. Kamarudin, M.S. Masdar, W.R.W. Daud, International Journal of Hydrogen Energy. 38 (2013) 9438-9453.

[7] A.S. Douk, H. Saravani, M. Noroozifar, International Journal of Hydrogen Energy. 42 (2017) 15149-15159.

[8] A.C. Mkhohlakali, X. Fuku, R.M. Modibedi, L.E. Khotseng, S.C. Ray, M.K. Mathe, Applications of Surface Science 502 (2020) 144158.

[9] A.K. Ipadeola, R. Barik, S.C. Ray, K.I. Ozoemena, Electrocatalysis (2019) 1-15.

[10] J.L. Tan, A.M. De Jesus, S.L. Chua, J. Sanetuntikul, S. Shanmugam, B.J.V. Tongol, H. Kim, Applied Catalysis A: General. 531 (2017) 29-35.

[11] D. Wang, Y. Li, Advanced Materials. 23 (2011) 1044-1060.

[12] C. Xu, Z. Tian, P. Shen, S.P. Jiang, Electrochimica Acta. 53 (2008) 2610-2618.

[13] R. Kottayintavida, N.K. Gopalan, International Journal of Hydrogen Energy. 45 (2020) 11116-11126.

[14] S. Jadali, M.A. Kamyabi, J. Solla-Gullón, E. Herrero, Applied Sciences. 11 (2021) 1315.

[15] J. Guo, R. Chen, F. Zhu, S. Sun, H.M. Villullas, Applied Catalysis B: Environmental. 224 (2018) 602-611.

[16] C. Xu, Z. Tian, P. Shen, S.P. Jiang, Electrochimica Acta. 53 (2008) 2610-2618.

[17] A.N. Geraldes, D.F. Da Silva, E.S. Pino, Da Silva, Júlio César Martins, De Souza, Rodrigo Fernando Brambilla, P. Hammer, E.V. Spinacé, A.O. Neto, M. Linardi, M.C. Dos Santos, Electrochimica Acta. 111 (2013) 455-465.

[18] A.N. Geraldes, D.F. da Silva, da Silva, Júlio César Martins, O.A. de Sá, E.V. Spinacé, A.O. Neto, M.C. dos Santos, Journal of Power Sources. 275 (2015) 189-199.

[19] H. Mao, L. Wang, P. Zhu, Q. Xu, Q. Li, International Journal of Hydrogen Energy. 39 (2014) 17583-17588.

[20] M. Yang, M. Pang, J. Chen, F. Gao, H. Li, P. Guo, ACS Applied Materials & Interfaces. 13 (2021) 9830-9837.
[21] M. Farsadrooh, M.Z. Yazdan-Abad, M. Noroozifar, N. Alfi, A.R. Modarresi-Alam, International Journal of Hydrogen Energy. 45 (2020) 27312-27319.

CHAPTER 6

Electrochemical activities of Palladium-based bi-metallic nano-electrocatalysts towards ethylene glycol oxidation in alkaline medium

6.1 Introduction

Ethylene glycol has emerged as an up-and-coming fuel candidate for electronics (portable) and stationary applications [1-3]. Compared to methanol, this device has remarkable advantages such as low toxicity, inexpensive and larger volumetric energy density of about 5.9 kWh L^{-1} [1, 4]. Despite all the remarkable superiorities, it is well-reported that their performance predominantly depends mainly on choosing the appropriate electrocatalyst [5]. Thus far, Pt-based electrocatalysts have been extensively used as effective catalysts. However, Pt has difficulties splitting the C-C bond, leading to poor activity and stability during electrooxidation [6].

Efforts have been made to address this issue by utilising Pd electrocatalysts owing to their tremendous catalytical activity towards ethylene glycol electrooxidation operating in an alkaline medium [7, 8]. Besides, the electrocatalytic activities of monometallic Pd still need to be addressed based on all types of promotion mechanisms [9]. However, several factors have been introduced to enhance the catalytical activity and durability of Pd by alloying with second metals [10]. Alloying Pd with second metals such as Sn, Ru, Co, Fe, Ni, and Mn modulates the structural and electronic properties and strain effect due to different lattice coordination. It enhances the electrochemical activity of Pd towards EGOR in the basic environment [11, 12]. The insertion of co-metals also reduces the metal utilization efficiency of Pd, which boosts its commercialisaton in the future. Nonetheless, when integrated with carbon support as electron carriers, bimetallic electrocatalysts are expected to limit the aggregation, provide high conductivity, and create a high superficial area for dispersion of the electrocatalysts for EGOR [13].

This work prepared bimetallics such as PdFe/C, PdMn/C, and PdCo/C electrocatalysts using a microwaved synthetic method at varied atomic ratios. The physicochemical properties of these electrocatalysts were explored utilising XRD, SEM and TEM analysis. This work is the continuation of Chapter 4, where we want to find out how these catalysts behave toward the

oxidation of EG in alkaline electrolytes. To observe the performance, we studied the electrochemical behaviour and electrocatalytic activity of the electrocatalysts using various techniques such as CV to observe the ECSA, SA and MA, together with CA. As anticipated, the bimetallic electrocatalysts displayed a superior electrocatalytic activity than monometallic Pd. Despite this, Pd_2Fe/C and PdFe/C electrocatalysts delivered the most remarkable performance compared to Pd/C, PdCo/C, and PdMn/C.

6.2 Results and Discussion

6.2.1 Computational work

The initial part of the research project was to conduct DFT calculations for PdFe, PdCo and PdMn to observe the effect of EG adsorption. As indicated in Chapter 3, summarised in Table 6.1 and further elaborated upon in Chapter 4.

Table 6.1 Computational studies of catalysts adsorbed on EG.

Electrocatalysts EG	ΔG (kcal/mol)	A.E (kcal/mol)	B.E (eV)	Band gap energy, Eg (eV)
PdFe	17.628	-133.108	-146.731	0.334
PdCo	17.587	-133.148	-123.953	0.401
PdMn	17.702	-133.033	-131.235	None

Note that the more positive the Gibbs free energy and AE values are, the more unstable or weaker the adsorbate and the catalyst interact. In terms of AE (Table 6.1), the ease at which EGOR will occur at these bimetallic catalysts follows this sequence: PdMn > PdFe > PdCo, meaning that the most favorable bimetallic electrocatalyst is the PdMn. This theoretical prediction will be true if every other factor (i.e., same synthesis method, same electrochemical surface area, mass and specific activities, etc.) remains constant for all the electrocatalysts. It is intriguing to observe that the free energy of PdCo is the lowest, possibly suggesting that this bimetallic electrocatalyst is the best for expediting the potential limiting step. It was noticeable that PdFe revealed a smaller band gap energy of about 0.334 eV compared to PdCo (0.401 eV), indicating excellent electron transfer, which can expedite the adsorption/desorption towards ethylene glycol, as proven by experimental data.

6.2.2 Physico-chemical Characterisation

6.2.3 X-Ray Diffraction Measurements

XRD examined the crystallinity and structural behaviour of the catalysts (varied atomic ratio Pd_2M/C and PdM/C), and the peaks are shown in Figure 6.1.

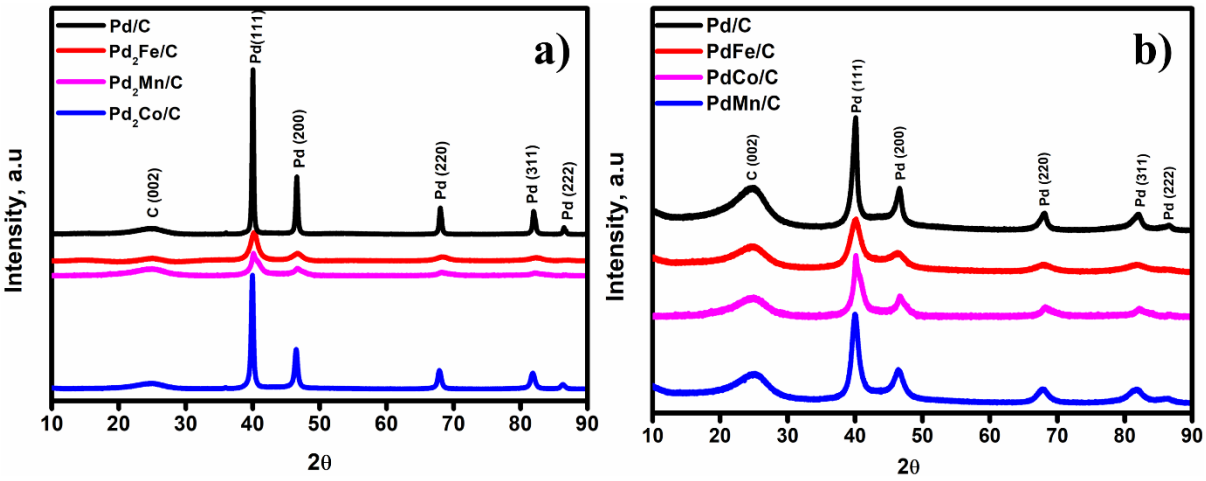


Figure 6.1: XRD diffractograms of electrocatalysts.

Table 6.2: XRD data of Pd-based electrocatalysts at different atomic ratios.

Electrocatalysts	Pd (111) 2 θ	d (111) (nm)	Lattice constant. (nm)	Crystalline/particle size (nm)
Pd/C	40.05	0.2249	0.3896	36.54
PdFe/C	40.08	0.2247	0.3891	5.81
Pd_2Fe/C	40.00	0.2251	0.3900	3.69
PdCo/C	40.03	0.2242	0.3895	8.59
Pd_2Co/C	40.12	0.2250	0.3889	7.53
PdMn/C	40.13	0.2247	0.3892	6.56
Pd_2Mn/C	40.02	0.2252	0.3905	9.82

The broad C (002) peaks appear in both patterns at about 25° for all the electrocatalysts, signifying the presence of amorphous Vulcan XC 72 carbon material [14]. The diffraction peaks located at 40°, 48°, 69°, 82°, and 88° signify the fcc crystalline Pd at (111), (200), (220), (311), and (222), respectively [15, 16]. No shift was observed for all the Pd-based

electrocatalysts at Pd (111) diffraction peaks, expressing that incorporating co-metals exhibits an effect free on the lattice crystallinity of palladium [17].

There was no evidence of oxides or co-metals diffraction peaks, probably because their phases are amorphous or cannot be detected by XRD [18]. The Scherrer equation was used to calculate the interplanar distance, lattice parameter, and crystallite sizes, and the results are presented in Table 6.2. It is essential to point out that the estimated crystallite size of all the bimetallic electrocatalysts is smaller than that of the Pd alone. The Fe on Pd/C shifts the lattice constraint to promote the synergistic effect. For instance, these 3d transition metals lower the binding energy to prevent the impact of reaction with intermediates on the Pd/C surface; this is in good accord with the DFT results. Under the compressive strain (lattice contraction), when the Pd/C is incorporated with smaller atoms, the d-band energies weaken the connection occurring in the middle of the substrate and the adsorbates, as reported by Bose and co-workers 2014. Therefore, introducing Fe to Pd/C positively impacts the catalytic performance due to the plethora of hydroxide species on the surface of the catalysts.

6.2.3.1 TEM analysis

TEM micrographs were employed particularly to examine the morphological structure and particle sizes of the Pd-based electrocatalysts, and the images are represented in Figure 6.2. The electrocatalyst micrographs exhibit the number of agglomerations on the carbon matrix with a uniform particle size distribution between 2 and 10 nm. The agglomeration on the carbon matrix has been reported to decrease the specific surface area required for EG adsorption. However, it was also reported that when the electrocatalysts have smaller particle sizes, it permits the fuel adsorption to take place by increasing the electrocatalytical activity of EG [19].

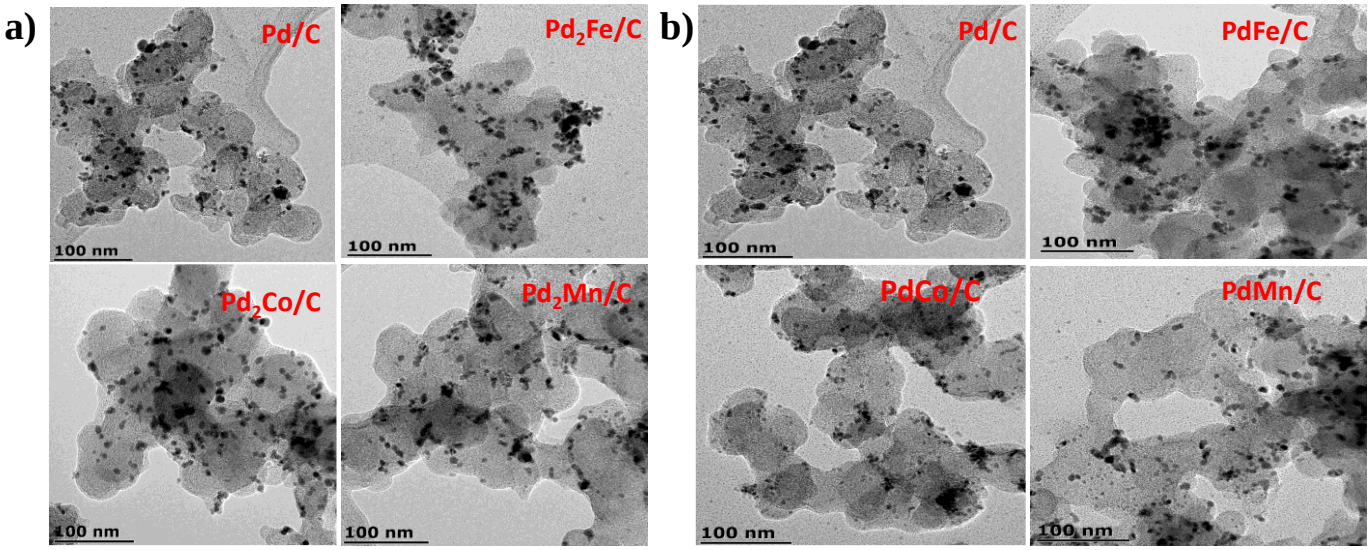


Figure 6.2: TEM micrographs of a) Pd_2M/C and b) PdM/C electrocatalysts.

6.2.4 Electrochemical characterisation

6.2.4.1 Cyclic Voltammetry of bimetallics.

CV was used to study the electrochemical behaviour of Pd, PdFe/C, PdMn/C, and PdCo/C nano-catalysts at varied atomic molar ratios (a) Pd_2M/C and b) PdM/C) in KOH (0.5 M) bubbled with N_2 gas at 50 mV / s scan rate, shown in Figure 6.3. Figure 6.3a represents the CV profile of Pd-based electrocatalysts at Pd_2M/C, while Figure 6.3b exhibits the CV profile at PdM/C. The significant potentials emerged in the middle of (-0.8 V to -0.9 V) on both the anodic and cathodic sweep, attributed to the hydrogen desorption/desorption peak currents on the Pd surface [20, 21]. Anodic sweeps display a weak peak potential shoulder at around -0.2 V vs. Ag/AgCl corresponding to the formation of the PdO layer at different oxidation states Pd (0), Pd (I), Pd (II), and Pd (IV) [19, 22]. Meanwhile, a strong -0.1 V potential peak was observed during the cathodic sweep, indicating a PdO reduction peak. The peaks were instrumental in estimating the ECSA across the electrocatalysts. The estimated ECSA values are recorded in Table 6.2. The PdFe/C from both atomic ratios display higher values of ECSA than its counterparts, indicating that the surface area is more significant for ethanol electrooxidation. Douk and co-workers have previously reported that the more excellent ECSA value plays a massive role in enhancing the synergistic effect between Fe and Pd in PdFe/C in relation to the electronic effect, geometry effect, and bifunctional mechanism [20].

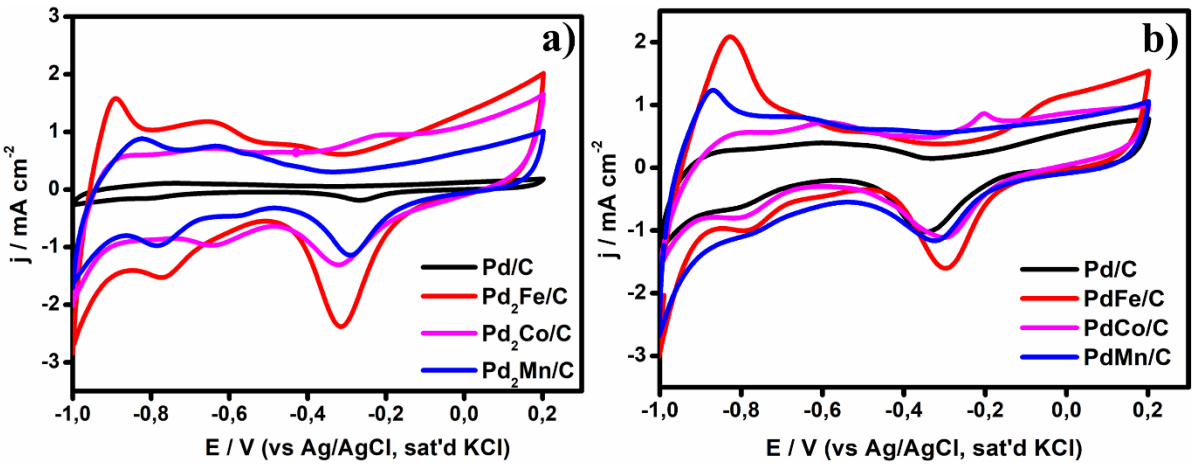


Figure 6.3: CV profiles of catalysts (presented at varied atomic ratio of Pd_2M/C and PdM/C) in KOH solution (0.5 M), bubbles with N_2 atmosphere at a scan rate = 50 mV / s.

The investigation of electrochemical activities towards EG oxidation at different atomic ratios a) Pd_2M/C and b) PdM/C) was conducted using CV analysis, prepared in a combination of 0.5 M KOH/EG at 50 mV / s scan rate, as shown in Figure 6.4 a,b. The CV profiles representing the electrocatalysts are characterized by two well-defined current peaks at the forward and reverse scans. The forward scan obtained at about -0.2 V corresponds to the oxidation of the chemisorbed ethylene glycol species, and the reverse scan attained at approximately -0.38 V signifies the oxidation of CO intermediates that were not fully oxidized during the forward scan.

Table 6.3: Comparison effect between bimetallic electrocatalysts at varied atomic ratios towards EGOR in alkaline electrolyte.

Electrocatalysts	**ECSA/ m^2 g^{-1}**	**E_{onset} (V)**	**J_f/J_b**	**Specific Activity (mA cm^{-2})**	**Mass Activity (mA mg^{-1})**
Pd/C	2.7	-0.36	1.53	1.35	250
PdFe/C	30.17	-0.46	1.3	5.51	1300
Pd_2Fe/C	38.99	-0.46	1.32	9.82	4220
PdCo/C	16.89	-0.46	1.23	5.01	740
Pd_2Co/C	16.07	-0.38	1.30	6.84	2710
PdMn/C	16.89	-0.38	1.31	4.18	1180
Pd_2Mn/C	16.72	-0.37	1.27	5.43	1290

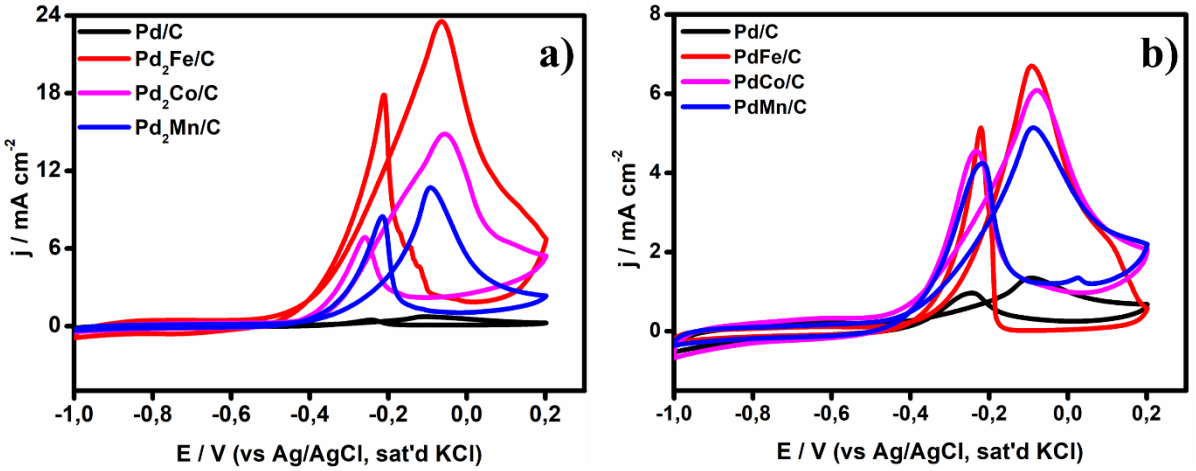


Figure 6.4: The CV curves of electrocatalyst at different atomic ratio of a) Pd_2M/C and b) PdM/C) immersed in 0.5 M KOH/EG solution under N_2 gas at a scan rate = 50 mV / s.

It was noticeable that PdFe/C electrocatalysts from both atomic ratios evinced a higher current density of about 9.82 (Pd_2Fe/C) and 5.51 (PdFe/C) $mAcm^{-2}$ which is about 1.5 times higher than their counterparts indicating an enhancement in ethylene glycol electrooxidation, as displayed in Figure 6.5 a,b. In addition, the mass activities obtained for a) Pd_2Fe/C and b) PdFe/C exhibit a higher value of 4220 and 1300 mA $mg^{-1,}$ respectively, than their counterparts, as described in Figure 6.5 a,b. Its enormous improvement could be due to the insertion of Fe to enhance Pd utilisation and accelerate EGOR in a basic environment. The electrocatalytic performances, such as the onset potential and the ratio of the current peak density, are summarised in Table 6.3, corresponding to the EGOR in alkaline space. The E_{onset} of Pd_2Fe/C and PdFe/C electrocatalysts are (-0.46 V, -0. 46 V), respectively, and are more negative than their counterparts, indicating there is a remarkable enhancement in the EGOR kinetics. The ratio peak current-density as denoted as (I_f / I_b) of electrocatalysts was relatively small in comparison to that of monometallic Pd electrocatalysts, signifying that the monometallic Pd has high tolerance towards carbonaceous species, as shown in Table 6.3.

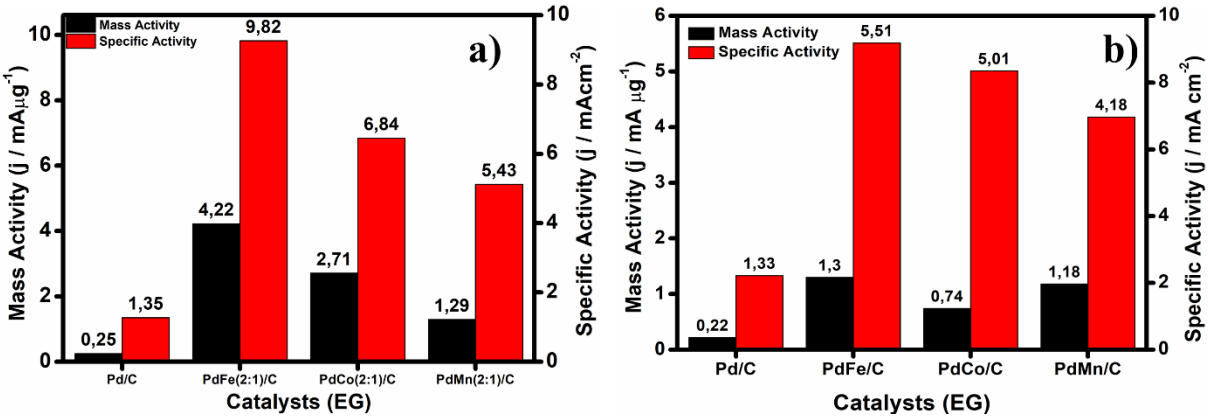


Figure 6.5: Comparison of mass and specific activities of Pd, PdFe/C, PdMn/C and PdCo/C (atomic ratio of a) Pd_2M/C and b) PdM/C) in 0.5 M KOH solution + 0.5 M EG N_2 atmosphere at a sweep rate of 50 mV / s.

6.2.4.2 Chronoamperometry study

The stability test of all the electrocatalysts in the mixture of 0.5 M KOH/EG at the potential of 0.2 V was further evaluated by chronoamperometric analysis, as stated in Figure 6.6 a,b. The first stage observed a gradual decline in the current densities of the catalysts, indicating that the poisoned species were strongly adsorbed on the electrode surface during the EGOR [24]. Lastly, in the final stage, we noticed that PdFe/C from both atomic ratios have the largest current density compared to its counterparts, which undoubtedly became the best-performing electrocatalyst.

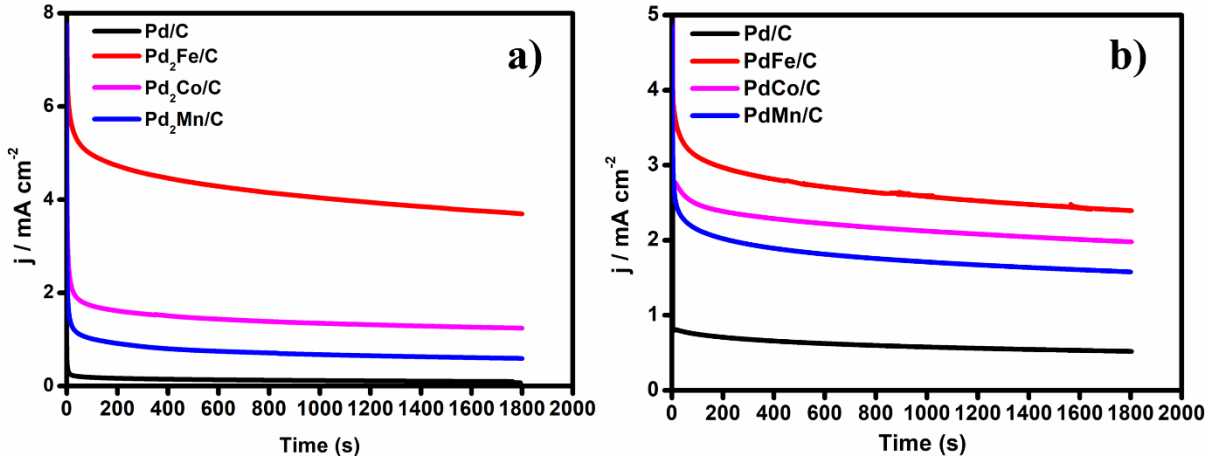


Figure 6.6: The CA curves of electrocatalysts (at varied atomic ratios of a) Pd_2M/C and b) PdM/C) in 0.5 M KOH/ EG solution under the influence of N_2 gas at 0.2 V.

6.3 Conclusions

Bimetallic electrocatalysts were successfully synthesised using the MW method at different ratios (Pd_2M/C and PdM/C). Adding 3d transition metals into Pd has shown a significant electrocatalytic behaviour towards EGOR in an alkaline environment, indicating the synergistic effect played by co-metal alongside Pd. The Pd_2Fe/C electrocatalyst provided a remarkable current density and improved EG oxidation reaction stability. Therefore, in general, Pd_2Fe/C exhibits the best electrocatalytic activity, making it a promising alternative electrocatalyst in DEGFC applications. This contrasts with the DFT simulation, which predicted that PdMn would be the best electrocatalyst for EG. It should be noted that the performance of the electrocatalysts depends on several factors (such as particle size, ECSA, mA, SA morphology, porosity, etc.), and DFT calculations in this work did not consider any of these factors. Thus, this discrepancy may be related to the poor ECSA of the PdMn (~ 17 $m^2\ g^{-1}$) compared to the PdFe (> 30 $m^2\ g^{-1}$).

6.4 References

[1] A. Falase, M. Main, K. Garcia, A. Serov, C. Lau, P. Atanassov, Electrochimica Acta. 66 (2012) 295-301.

[2] J.M. Sieben, M.M.E. Duarte, International Journal of Hydrogen Energy. 36 (2011) 3313-3321.

[3] H.J. Kim, S.M. Choi, S. Green, G.A. Tompsett, S.H. Lee, G.W. Huber, W.B. Kim, Applied Catalysis B: Environmental. 101 (2011) 366-375.

[4] L. Xin, Z. Zhang, J. Qi, D. Chadderdon, W. Li, Applied Catalysis B: Environmental. 125 (2012) 85-94.

[5] Q. Liu, Y. Xu, A. Wang, J. Feng, International Journal of Hydrogen Energy. 41 (2016) 2547-2553.

[6] Y. Huang, Y. Guo, Y. Wang, Journal of Power Sources. 249 (2014) 9-12.

[7] J. Duan, X. Zheng, H. Niu, J. Feng, Q. Zhang, H. Huang, A. Wang, Journal of Colloid and Interface Science560 (2020) 467-474.

[8] H. Xu, B. Yan, K. Zhang, J. Wang, S. Li, C. Wang, Y. Du, P. Yang, Electrochimica Acta. 261 (2018) 521-529.

[9] T. Li, Y. Huang, K. Ding, P. Wu, S.C. Abbas, M.A. Ghausi, T. Zhang, Y. Wang, Electrochimica Acta. 191 (2016) 940-945.

[10] E. Mari, P. Tsai, M. Eswaran, V.K. Ponnusamy, Fuel. 280 (2020) 118646.

[11] Y. Dong, J. Zhao, J. Han, Y. Kang, Y. Mi, W. Wang, Materials Science and Engineering: B. 252 (2020) 114467.

[12] J. Gao, M. Mao, P. Li, R. Liu, H. Song, K. Sun, S. Zhang, ACS applied materials & interfaces. 12 (2020) 6298-6308.

[13] R. Zhang, J. Duan, Z. Han, J. Feng, H. Huang, Q. Zhang, A. Wang, Applications of Surface Science 506 (2020) 144791.

[14] O.O. Fashedemi, K.I. Ozoemena, Electrochimica Acta. 128 (2014) 279-286.

[14] R. Kottayintavida, N.K. Gopalan, International Journal of Hydrogen Energy. 45 (2020) 11116-11126.

[15] S. Jadali, M.A. Kamyabi, J. Solla-Gullón, E. Herrero, Applied Sciences. 11 (2021) 1315.

[16] J. Guo, R. Chen, F. Zhu, S. Sun, H.M. Villullas, Applied Catalysis B: Environmental. 224 (2018) 602-611.

[17] C. Xu, Z. Tian, P. Shen, S.P. Jiang, Electrochimica Acta. 53 (2008) 2610-2618.

[18] A.N. Geraldes, D.F. Da Silva, E.S. Pino, Da Silva, Júlio César Martins, De Souza, Rodrigo Fernando Brambilla, P. Hammer, E.V. Spinacé, A.O. Neto, M. Linardi, M.C. Dos Santos, Electrochimica Acta. 111 (2013) 455-465.

[19] A.N. Geraldes, D.F. da Silva, da Silva, Júlio César Martins, O.A. de Sá, E.V. Spinacé, A.O. Neto, M.C. dos Santos, Journal of Power Sources. 275 (2015) 189-199.

[20] A.S. Douk, H. Saravani, M. Noroozifar, International Journal of Hydrogen Energy. 42 (2017) 15149-15159.

[21] H. Mao, L. Wang, P. Zhu, Q. Xu, Q. Li, International Journal of Hydrogen Energy. 39 (2014) 17583-17588.

[22] M. Yang, M. Pang, J. Chen, F. Gao, H. Li, P. Guo, ACS Applied Materials & Interfaces. 13 (2021) 9830-9837.

[23] Z. Gu, Z. Xiong, F. Ren, S. Li, H. Xu, B. Yan, Y. Du, Journal of the Taiwan Institute of Chemical Engineers. 83 (2018) 32-39.

CHAPTER 7

Electrochemical activities of Palladium-based bi-metallic nano-electrocatalysts towards the oxidation of Gly in an alkaline environment

7.1 Introduction

DAFCs are one of the highly promising alternative renewable and clean energy supplies for electronic devices [1]. These fuel cells can adapt to different fuels in an anode to yield several electrons and energize fuel cells. Glycerol has become one of the hotspots in the R&D direction of DAFCS due to its excellent properties compared to methanol [2]. In contrast, glycerol as polyhydric alcohol is produced massively as a co-product of the biodiesel industry. It is predominantly attained as an environmentally friendly product obtained as vegetable oils from methanolysis [3, 4]. It has stimulated enormous attention in the past decades due to its lower virulence, with a theoretical energy density of 5 kW h kg^{-1} and a high number of exchanged electrons (fourteen electrons/glycerol molecules) for the successful completion of mesoxalate to CO_3^{-2} oxidation [5,6,7].

Nevertheless, the crucial issue faced by these types of FCs is the incomplete electrooxidation kinetics of glycerol in generating CO_2, which hinders future commercialisation. Instead, it causes the formation of poisoning intermediates on an anode active site at low overpotential. During the electrooxidation of glycerol, there is an occurrence of parallel reactions to produce CO_2 such as glycerate, tartronate, hydroxy pyruvate and mesoxalate ions) that plays a huge role in decreasing the energy efficiency [8,9]. Their electrooxidation steps are very complicated; moreover, it is difficult for the anodic catalysts to promote the cleavage of the C-C and C-H bonds [10]. To resolve the latter, research efforts have been devoted to finding and developing desirable anode catalysts with optimised kinetics for anodic electrooxidation and excellent resistance to CO poisoning. Searching for electroactive catalysts with proper stability towards GOR in alkaline electrolytes is of considerable significance. Thus far, the set of bimetallic electrocatalysts has extensively investigated for electrooxidation of glycerol in an alkaline medium. Several non-noble metals, such as Ru, Sn, Au, Ni, and Pb, have been thoroughly explored as catalysts for the GOR in an alkaline environment. In comparison, monometallic Pd nano-catalysts inevitably decay catalytic activity more than bimetallic electrocatalysts, which

are believed to enhance the strongly bound adsorbed intermediates and produce a high yield of CO_2. This is because the bi-functional impact thoroughly conferred the promoting effect of non-noble metals into Pd due to the weakened d-band center by electronic force [10, 11]. Fathirid and co-workers studied different compositions of Pd-Mo /Vulcan-XC-72R towards the reaction of CH_3OH, EtOH, EG and Gly electrooxidation in alkaline electrolyte. Thus, Pd_3Mo/VC showed excellent catalytical activity, high stability, and durability towards all the alcohols [12]. Gerald and colleagues prepared the trimetallic PdAuSn/C electrocatalysts for GOR in the basic medium using an electron-beam irradiation method, and better catalytical activity was observed than Pd/C alone [10].

Surprisingly, the 3d transition metals, such as Fe, Co, and Mn, remain hugely unexplored/ not studied on Pd/C for glycerol oxidation in basic medium. Based on the scarcity report of 3d transition metals on Pd/C towards the oxidation of glycerol, this study aims to evaluate the electrocatalysts (denoted as PdFe/C, PdCo/C, PdMn/C, and Pd/C) in different ratios (Pd_2M/C and PdM/C) for electrooxidation of glycerol in basic medium. This study was published in Chapter 4 with only two catalysts (Pd/C and PdFe/C). However, we saw the potential need to introduce more co-metals to Pd/C and observe the performance. The results show that the bimetallic PdFe/C delivered excellent performance in GOR via MW. The results have also demonstrated that PdFe/C electrocatalysts for both ratios have highly enhanced catalytic activity and stability towards all the glycerol electrooxidation in an alkaline medium.

7.2 Results and Discussion

7.2.1 Computational evaluation

DFT calculations confirmed the first part of the research work, which was to observe the effect of glycerol adsorption on bimetallic electrocatalysts (such as PdFe, PdCo, and PdMn). As indicated in Chapter 3, summarised in Table 7.1, and further elaborated upon in Chapter 4.

Table 7.1 Computational research in glycerol adsorption on bimetallic catalyst.

Electrocatalysts Glycerol	ΔG (kcal/mol)	A.E (kcal/mol)	B.E (eV)	Band gap energy Eg (eV)
PdFe	2.415	-48.898	-85.081	None
PdCo	2.280	-49.033	-354.815	None
PdMn	2.332	-48.981	-376.535	0.209

From Table 7.1, the adsorption energy of the bimetallic catalysts toward GlyOR is as follows: PdCo > PdMn > PdFe, indicating that there is a rapid generation of glycerol at the PdFe surface than its counterparts. This is in support of the smaller binding energy of PdFe (-85.081 eV) as compared to PdCo (-354.815 eV) and PdMn (-376.535 eV), signifying that it is facile for the bond between Gly and PdFe to be cleaved to accelerate the kinetics of GOR. The band gap energies for PdFe and PdCo were not observed/recorded from the system. It is intriguing to realise that the Gibbs free energy is decreasing from PdFe (2.415 kcal/mol) to PdMn (2.332 EV) and PdCo (2.280 kcal/mol), indicating the presence of Co on Pd easily accelerates the potential limiting step, thereby lowering the free energy. These predictions should be true if every factor (including synthesis method, physico-chemical parameter such as the BET surface area, ECSA, etc) remains the same.

7.2.2 Physico-chemical Characterisation

7.2.2.1 XRD analysis

XRD measurements were collected to prone the crystallinity and structural behaviour of the electrocatalysts at different atomic ratios (a) Pd_2M/C and b) PdM/C), as shown in Figure 7.1

a,b. The broad C (002) peaks appear in both patterns at about 25° for all the electrocatalysts, signifying the presence of amorphous Vulcan XC 72 carbon material [13]. The diffraction peaks located at 40°, 48°, 69°, 82°, and 88° for all the Pd-based electrocatalysts are attributed to fcc crystalline Pd (111), (200), (220), (311), and (222), respectively [14, 15]. We observed no shift of the Pd (111) diffraction peaks for all the Pd-based electrocatalysts expressing the fact that the insertion of co-metals does not contribute to the crystalline lattice of palladium [16]. There was no evidence of oxides or co-metals diffraction peaks, probably because their phases are amorphous and cannot be detected by XRD [17].

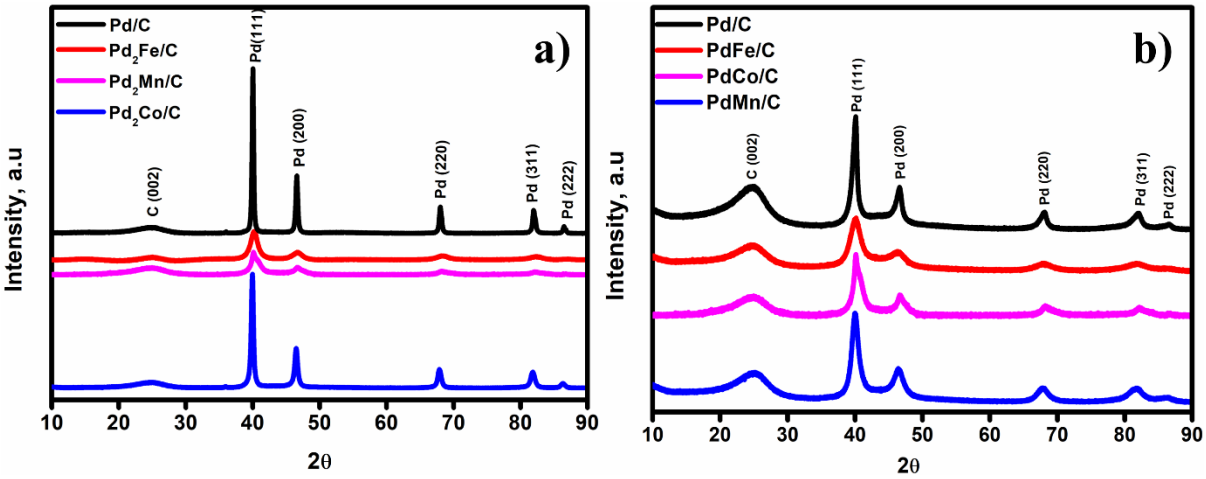


Figure 7.1. XRD diffractograms of (a) Pd_2M/C and (b) PdM/C) electrocatalysts.

The Scherrer equation was used to calculate the interplanar distance, lattice parameter and crystallite sizes and the results are presented in Table 7.2. It is essential to point out that the estimated crystallite size of all the bimetallic electrocatalysts is smaller than that of the Pd alone.

Table 7.2: XRD data of Pd-based electrocatalysts at different atomic ratios

Nano-catalysts	Pd (111) 2 θ	d-spacing (111), (nm)	Lattice constant, (nm)	Crystalline /particle size, (nm)
Pd/C	40.05	0.2249	0.3896	36.54
PdFe/C	40.08	0.2247	0.3891	5.81
Pd_2Fe/C	40.00	0.2251	0.3900	3.69
PdCo/C	40.03	0.2242	0.3895	8.59
Pd_2Co/C	40.12	0.2250	0.3889	7.53
PdMn/C	40.13	0.2247	0.3892	6.56
Pd_2Mn/C	40.02	0.2252	0.3905	9.82

TEM micrographs were employed particularly to examine the morphological structure and particle sizes of the Pd-based electrocatalysts, and the images are represented in Figure 6.2. The electrocatalyst micrographs exhibit the number of agglomerations on the carbon matrix with a uniform particle size distribution between 2 and 10 nm. The agglomeration on the carbon matrix has been reported to decrease the specific surface area required for Gly adsorption. However, it was also reported that when the electrocatalysts have smaller particle sizes, fuel adsorption is permitted to take place by increasing the electrocatalytic activity of Gly [9].

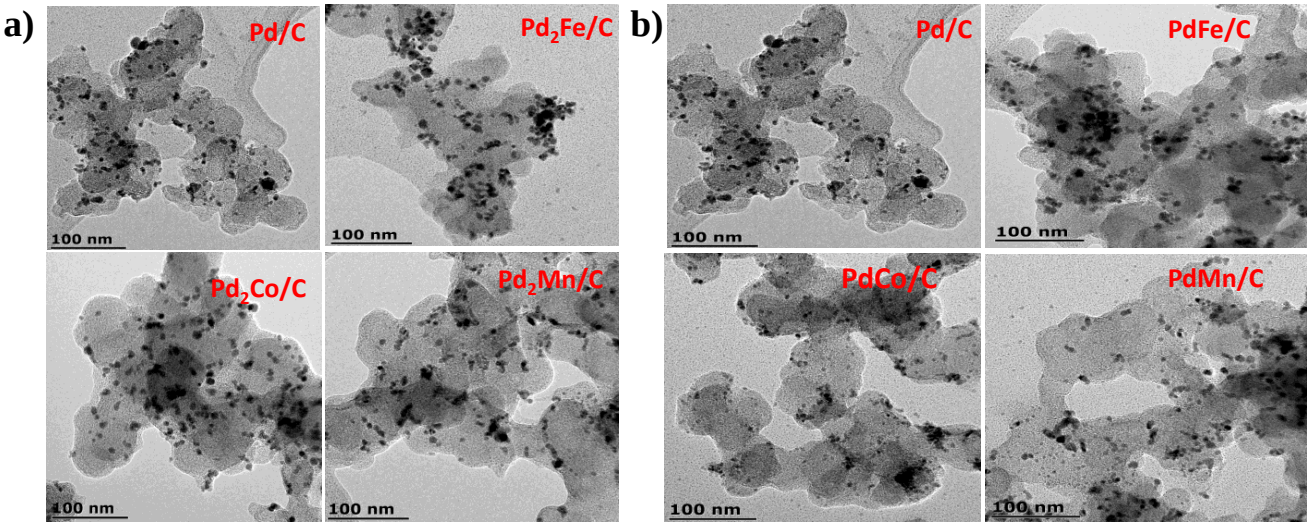


Figure 7.2: TEM micrographs of a) Pd_2M/C and b) PdM/C ratios of electrocatalyst.

7.2.3 Electrochemical characterisation

7.2.3.1 Cyclic Voltammetry of bimetallic.

CV was employed to study the electrochemical performance of Pd, PdFe/C, PdMn/C, and PdCo/C electrocatalysts at varied atomic ratios (Pd_2M/C and PdM/C) in the solution of (0.5 M) KOH under N_2 gas condition at a sweep rate of 50 mV / s as shown in Figure 7.3. Figure 7.3a represents the CV profile of Pd-based electrocatalysts at Pd_2M/C, while Figure 7.3b exhibits the CV profile at PdM/C. The potentials emerged in the middle of -0.8 V to -0.9 V (vs. Ag/AgCl) on both the anodic and cathodic sweep, attributed to the hydrogen desorption/desorption peak currents on the Pd surface [17, 18]. Anodic sweeps display a weak peak potential shoulder at around -0.2 V vs Ag/AgCl) corresponding to the formation of the PdO layer at different oxidation states Pd (0), Pd (I), Pd (II), and Pd (IV) [18,19]. A strong -0.1 V potential peak was observed during the cathodic sweep, indicating the PdO. The peaks were instrumental in predicting the ECSA across the Pd-based electrocatalysts. The estimated ECSA values are reported in Table 7.3 alongside other parameters. The Pd_2Fe/C and PdFe/C display higher values of ECSA than their counterparts, indicating that the surface area is greater for GOR to occur. Douk and co-workers have previously reported that the greater ECSA value corresponds to the synergistic effect between Fe and Pd in PdFe/C to enhance electronic, geometry effect and bifunctional mechanism properties [20]

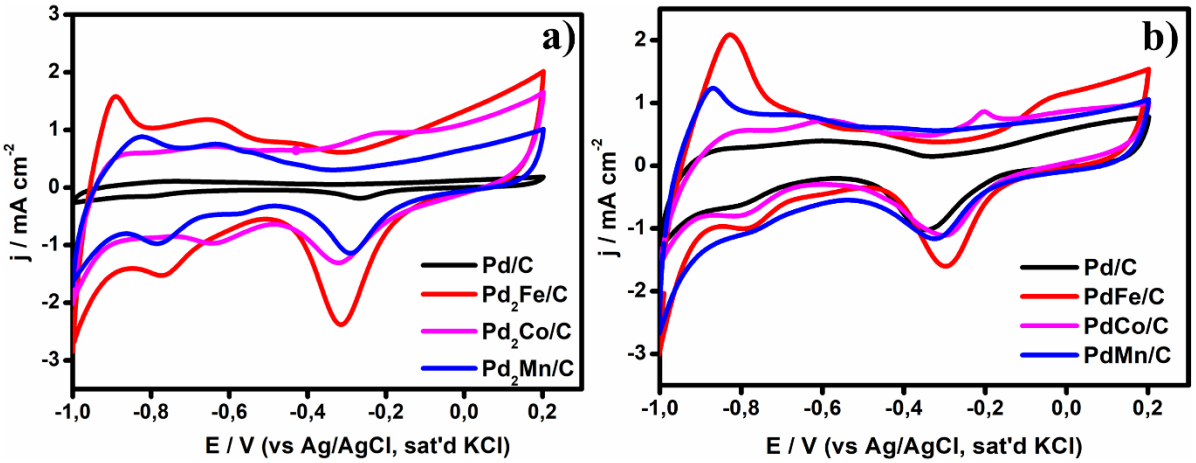


Figure 7.3. Cyclic voltammetry of electrocatalysts in 0.5 M KOH solution under N_2 gas at a scan rate of 50 mV / s.

To investigate the activities of the electrocatalyst towards the oxidation of Gly, cyclic voltammetry was performed in a mixture of 0.5 M KOH/Gly at 50 mV / s scan rate, as shown in Figure 7.4 a,b. The cyclic voltammograms of all the electrocatalysts are characterized by two well-defined current peaks at the forward and reverse scans. The forward scan obtained at about -0.2 V corresponds to the oxidation of the chemisorbed glycerol species, and the reverse scan obtained at approximately -0.35 V signifies the oxidation of carbonaceous intermediates that were not fully oxidized during the forward scan.

Table 7.3: Comparison of electrochemical conditions of Pd-based electrocatalysts towards GOR in a basic environment.

Electrocatalysts	ECSA $m^2 g^{-1}$	E_{onset} (V)	J_f/J_b	SA (mA/cm^2)	MA (mA/mg)
Pd/C	2.7	-0.33	2.17	2.8	240
PdFe/C	30.17	-0.45	2.23	4.73	990
Pd_2Fe/C	38.99	-0.39	1.56	8.94	2510
PdCo/C	16.89	-0.43	2.01	4.46	730
Pd_2Co/C	16.07	-0.38	1.45	7.94	2050
PdMn/C	16.89	-0.43	1.23	3.38	570
Pd_2Mn/C	16.72	-0.34	1.54	7.74	1570

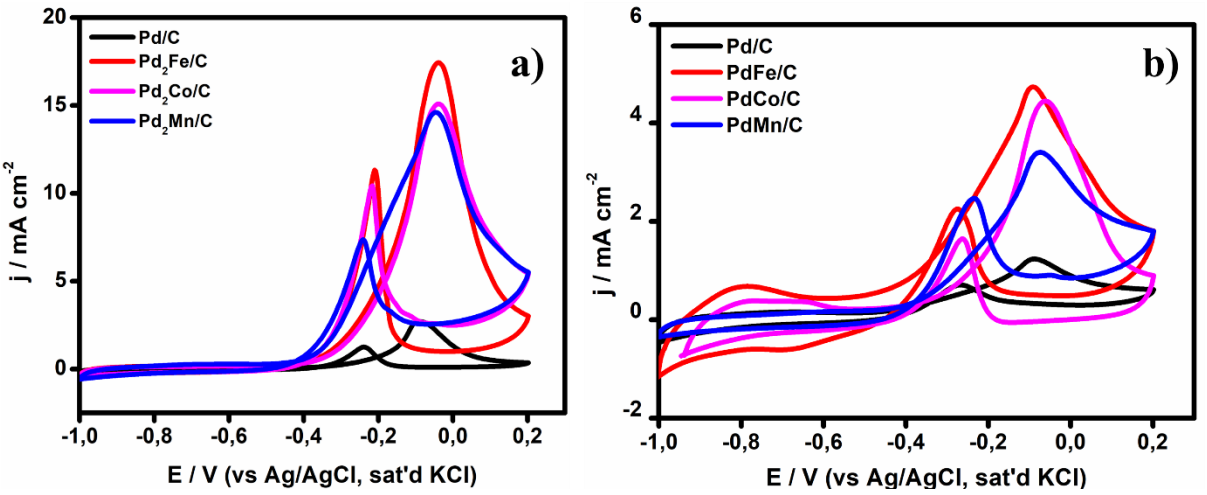


Figure 7.4: CV curves of Pd/C, PdFe/C, PdMn/C and PdCo/C (a) Pd_2M/C and b) PdM/C) in 0.5 M KOH/ 0.5 M Gly mixture under N_2 gas at a scan rate = 50 mV / s.

Figure 7.5 shows the peak current densities (SA) and mass activities (MA) of all the electrocatalysts at different weight ratios (Pd_2M/C and PdM/C). Pd_2Fe/C and PdFe/C electrocatalysts exhibit the highest peak current densities of 8.94 and 4.94 mA cm^{-2}, respectively, compared to their counterparts, as shown in Table 7.3. Its enormous improvement can be attributed to the successful insertion of co-metal boosting Pd utilisation and accelerating glycerol oxidation reaction in an alkaline environment.

The electrocatalytic performances corresponding to the electro-oxidation of glycerol in an alkaline medium, such as the onset potential and the ratio of the current peak density, are summarised in Table 7.3. The E_{onset} of Pd_2Fe/C and PdFe/C electrocatalysts are (-0.39 V, -0. 45 V), respectively, showing more negative values than their counterparts, indicating the remarkable enhancement in the glycerol oxidation reaction kinetics. The peak current density ratio (I_f / I_b) of the PdFe/C electrocatalyst contained a higher value of 2.23, which signifies the high tolerance towards carbonaceous species. The most contributing factor to the outstanding performance of PdFe/C electrocatalysts towards the oxidation of Gly is the ability to adhere and retain OH^- species on the Pd active site.

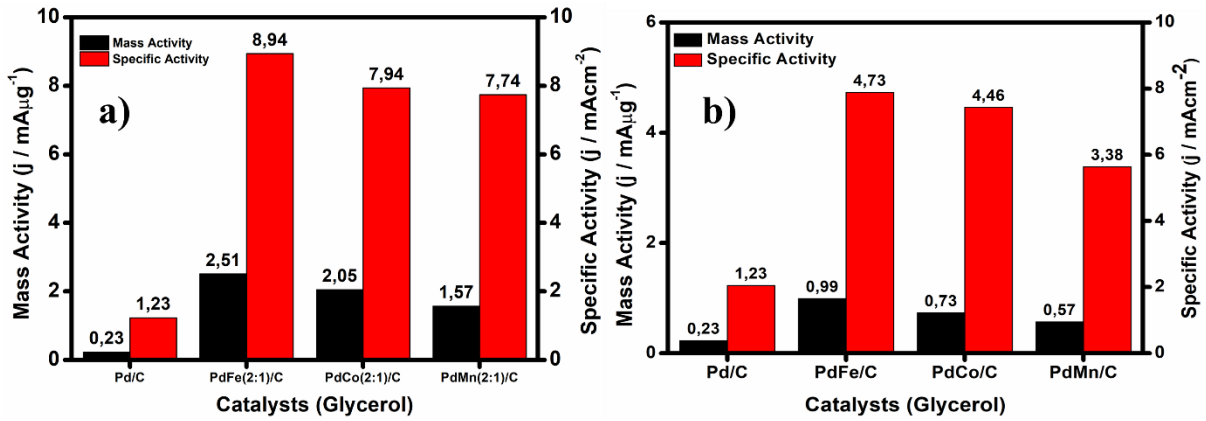


Figure 7.5: Comparison of mass and specific activities of (a) Pd_2M/C and b) PdM/C) in 0.5 M KOH solution / Gly, N_2 gas at a sweep rate of 50 mV / s.

7.2.3.2 Chronoamperometry study

The catalyst stability towards glycerol (KOH/Gly, 0.5 M) electrooxidation was investigated by conducting chronoamperometric measurements operated for the 1800s at -0.2 V. Figure 7.6 a,b shows that bimetallic electrocatalysts have excellent stability and activity towards GOR. It was noted that the current densities of Pd_2Fe/C and PdFe/C electrocatalysts surpassed those of their counterparts. This can be attributed to the synergistic behaviour enforced by Fe on Pd. These findings are aligned with the observation obtained from the CV [9].

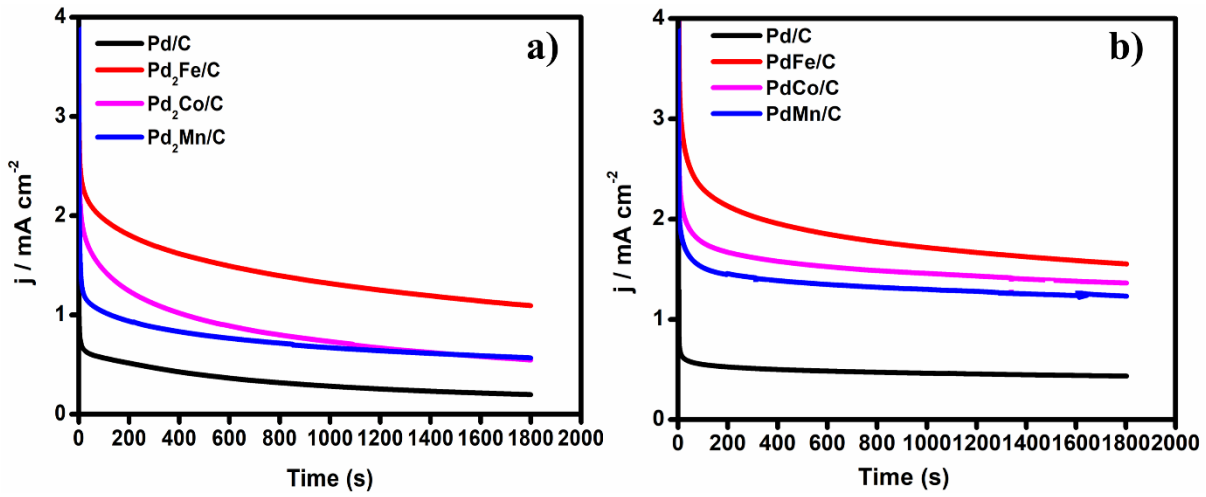


Figure 7.6: The CA curves (a) Pd_2M/C and (b) PdM/C) in KOH/ Gly (0.5 M) solution under N_2 atmosphere at 0.2 V.

7.3 Conclusions

Bimetallic electrocatalysts were successfully synthesised using the microwaved synthetic method at different ratios (Pd_2M/C and PdM/C). The addition of co-metals into Pd has shown a significant improvement in the electrocatalytic effect towards GOR in an alkaline environment because of the synergy between the metal and Pd. Overall, the Pd_2Fe/C electrocatalyst showed the most remarkable current density and higher stability towards glycerol oxidation reaction. Therefore, PdFe/C on both ratios exhibits the best electrocatalytic activity, leading to the promising alternative electrocatalyst in DGFC applications. This finding is consistent with the theoretical prediction from the DFT simulations; only the discrepancy was observed in the binding energy.

7.4 References

[1] Yu and J. Xi,International Journal of Hydrogen Energy., 37 (2012) 21.

[2] K. Ishiyama, F. Kosaka, I. Shimada, Y. Oshima and J. Otomo, Journal of Power Sources. 225 (2013).

[3] N. Rahmat, A. Z. Abdullah and A. R. Mohamed, Renewable and Sustainable Energy Reviews., 14, (2010) 3.

[4] C. H. Zhou, H. Zhao, D. S. Tong, L. M. Wu and W. H. Yu, Catalysis Reviews., 55, (2013).

[5] E. Habibi and H. Razmi, International Journal of Hydrogen Energy., 37, (2012) 22.

[6] M. Simões, S. Baranton and C. Coutanceau, Applied Catalysis B: Environmental., 93, (2010) 3 - 4.

[7] M. Mougenot, A. Caillard, M. Simoes, S. Baranton, C. Coutanceau and P. Brault, Applied Catalysis B: Environmental., 107, (2011) 3 - 4.

[8] P. S. Fernández, M. E. Martins and G. A. Camara, Electrochim.Acta., 66 (2012).

[9] V. L. Oliveira, C. Morais, K. Servat, T. W. Napporn, G. Tremiliosi-Filho and K. B. Kokoh, Electrochimica Acta, 117 (2014).

[10] N. Geraldes, D. F. da Silva, e Silva, Leonardo Gondim de Andrade, E. V. Spinacé, A. O. Neto and M. C. dos Santos, J.Power Sources., 293 (2015).

[11] M. Rethinasabapathy, S. Kang, Y. Haldorai, M. Jankiraman, N. Jonna, S. R. Choe, Y. S. Huh and B. Natesan, International Journal of Hydrogen Energy., 42, (2017)52.

[12] J. F. Gomes, A. C. Garcia, L. Gasparotto, N. E. De Souza, E. B. Ferreira, C. Pires and G. Tremiliosi-Filho, Electrochimica Acta., 144 (2014).

[13] F. Fathirad, A. Mostafavi and D. Afzali, International Journal of Hydrogen Energy., 42, (2017) 5.

14] R. Kottayintavida, N.K. Gopalan, International Journal of Hydrogen Energy. 45 (2020) 11116-11126.

[15] S. Jadali, M.A. Kamyabi, J. Solla-Gullón, E. Herrero, Applied Sciences. 11 (2021) 1315.

16] J. Guo, R. Chen, F. Zhu, S. Sun, H.M. Villullas, Applied Catalysis B: Environmental. 224 (2018) 602-611.

[18] C. Xu, Z. Tian, P. Shen, S.P. Jiang, Electrochimica Acta. 53 (2008) 2610-2618.

[19] A.N. Geraldes, D.F. Da Silva, E.S. Pino, Da Silva, Júlio César Martins, De Souza, Rodrigo Fernando Brambilla, P. Hammer, E.V. Spinacé, A.O. Neto, M. Linardi, M.C. Dos Santos, Electrochimica Acta. 111 (2013) 455 - 465.

[20] M. Yang, M. Pang, J. Chen, F. Gao, H. Li, P. Guo, ACS Applied Materials and Interfaces. 13 (2021) 9830-9837.

[21] H. Mao, L. Wang, P. Zhu, Q. Xu, Q. Li, International Journal of Hydrogen Energy. 39 (2014) 17583-17588.

[22] A.S. Douk, H. Saravani, M. Noroozifar, International Journal of Hydrogen Energy. 42 (2017) 15149-15159.

CHAPTER 8

Electrochemical activities of Palladium-based tri-metallic nano-electrocatalysts towards the oxidation of alcohols in basic medium.

8.1 Introduction

Fuel cells are well-known as electrochemical devices that convert electrical energy from chemical energy with the advantages of environmentally benign and supreme efficiency [1]. DAFCs have been investigated using methanol as a fuel for electronic (portable) devices and electric car applications [2, 3]. The restricted usage of this device comes from the toxicity of methanol [3, 4]. Hence, an alternative is required for future use. In recent years, high molecular weight alcohols such as EG, EtOH and Gly are explored as the most viable fuel candidates over methanol [5]. These significant potential fuel sources offer exceptional advantages, including low toxicity, flammability, renewable production from biomass, low cost, and high energy density [5-7]. Moreover, the relatively sluggish kinetics, alcohol crossover, and reaction intermediates cause the reduction in efficiency losses during alcohol electrooxidation [8]. These reasons render the researchers urgently searching for efficient catalysts that appear to be potentially attractive for a complete alcohol electro-oxidation reaction.

Long-term catalytical durability is also significant in actively reducing and strongly oxidizing environments during alcohol electro-oxidation. There is no need for high-performing catalysts that last for a few hours and depreciate; the nominated catalysts should withstand thousands of cycles before replacement, which will make them more realistic for commercialisaton purposes. As such, effort has been made to find and develop highly active and durable electrocatalysts to overcome the above difficulties in the electro-oxidation of EG, ethanol, and Gly in the basic environment [7].

The non-platinum (Pt) electrocatalysts such as palladium (Pd)-based have attracted considerable attention in an alkaline medium than Pt-based electrocatalysts due to high activity and more abundant [9]. Thus, the use of Pd-based electrocatalysts is of more interest to date. Moreover, alloying them with non-noble metals has been widely reported in the literature to enhance the alcohol electro-oxidation in basic electrolytes [10]. The alloying with non-noble

increases the electrochemical activity and can break down the bond C-C during alcohol electro-oxidation due to the synergy effect between adding co-metals to expedite the reaction kinetics [7]. Among Pd-based bimetallic electrocatalysts, ferro palladium (PdFe)-based catalysts have been reported predominantly for enhancing the electro-activity of ORR and MOR [11, 12]. However, there is little or no research on using trimetallic involving PdFe-based catalysts with other non-noble (M) metal co-catalysts for EGOR, EOR, and GOR. This research attempts to close this knowledge gap.

In this work, PdFe/C is alloyed with small-sized co-catalyst metals such as Co and Mn to amplify the structural, electronic, and catalytical activity for the electro-oxidation of EtOH, EG, and Gly. For example, Jacobs and co-workers reported the dependence on the potential of the effects of Ce in Pt-Sn-Ce catalysts on the EOR activity and reaction mechanism [13]. On the other hand, the Co and Mn metals are also expected to modify the Pd-Pd bond length through lattice contraction, ultimately decreasing the carbonaceous species adsorbed on the active site and accelerating the AOR. The MW technique synthesised carbon-supported PdFeCo/C, PdFeMn/C, and electrocatalysts. The physicochemical properties of the trimetallic electrocatalysts were thoroughly probed, and their electrochemical behaviour was tested for the AOR in an alkaline medium and compared with bimetallic and monometallic analogs. The investigation reveals that trimetallic electrocatalysts over PdFe/C and Pd/C are more stable and electroactive towards all the alcohols.

8.2 Results and Discussion

8.2.1 Computational Description Work

The initial part of the research was to conduct the DFT simulation/modelling to examine the role of alcohols during the adsorption period of the PdFeMn and PdFeCo catalysts. As indicated in Chapter 3, summarised in Table 8.1 and further elaborated upon in Chapter 4. This study revealed weaker adsorption energy of the PdFeCo-based electrode (A.E = -9.975 kcal/mol) as compared to that of (A.E. =-10.031 kcal/mol, PdFeMn), indicating the facile movement of ethanol at the PdFeCo surface than its counterpart. We further observed a decline in the energy band gap from 0.169 eV PdFeMn to 0.075 eV PdFeCo, signifying that the surface of PdFeCo is more conductive than that of PdFeMn. The binding energy of PdFeCo was reduced from -106.130 eV to -105.546 eV, amplifying that there is a strong interaction between PdFeCo and

the intermediates. However, the experimental results show that PdFeMn delivered a satisfactory electrochemical performance when it comes to (ECSA, Eonset, MA, SA Jb/Jf, and stability), signifying a strong adsorption interlinkage between the PdFeMn and existing intermediates. This can be elaborated further by the high value of Jb/Jf, indicating that this electrocatalyst can tolerate poisonous species. There is a lot of discrepancy between computational data and experimental data, which requires further investigation in the future.

We examined these catalysts (PdFeMn and PdFeCo) for ethylene glycol. We observed that the A.E of the PdFeMn-based electrode is slightly lower (A.E. = -133.082 kcal/mol) than the PdFeCo with an A.E value of 133.146 kcal/mol, indicating a rapid movement of EG at the PdFeMn surface than at the PdFeCo. This is in accord with the experimental analysis, whereby the E_{onset} of PdFeMn delivered a more negative value, meaning that there is a rapid kinetics for the electrochemical oxidation of ethylene glycol. Surprisingly, the other essential factors, such as Gibbs free energy and binding energy, indicate that PdFeCo is more conductive and strongly interacts with the catalyst and the intermediates. These findings disagree with the experimental data; however, the condition of preparing these materials should be considered.

The effect of Gly adsorption on the PdFeCo and PdFeMn electrodes was observed and delivered the adsorption energy of PdFeMn- is feeble (A.E. = -49.039 kcal/mol) than its counterparts (A.E. = -49.052 kcal/mol, PdFeCo), indicating the ease at which Gly can regenerate at the PdFeMn surface than at the PdFeCo. It is quite intriguing that PdFeMn exhibited a slightly stronger Gibbs free energy, binding energy, and band gap of about G =2.274 kcal/mol, B.E = -111.479 eV, and Eg = 0.171 eV as compared to PdFeCo with a G = 2.262 kcal/mol, B.E = -110.972 eV and = 0.010 eV. The anticipation was to obtain the weaker Gibbs free energy, binding energy, and band gap energy for PdFeMn, which will lead to more vital interaction between the adsorbate and the catalysts and accelerate the potential limiting step, to further agree with the experimental results. However, PdFeCo, for instance, gave weaker Gibbs free energy, binding energy, and band gap energy.

Table 8.1: Comparison of computational studies for trimetallic electrocatalysts at different alcohols.

Electrocatalysts Ethanol	**ΔG (kcal/mol)**	**A.E (kcal/mol)**	**Band gap energy Eg (eV)**	**Binding energy (eV)**
PdFeMn	-1.527	-10.031	0.169	-106.130
PdFeCo	-1.470	-9.975	0.075	-105.546
Electrocatalysts Ethylene glycol	**ΔG (kcal/mol)**	**A.E (kcal/mol)**	**Energy band gap Eg (eV)**	**Binding energy (eV)**
PdFeMn	17.653	-133.082	0.171	-108.317
PdFeCo	17.590	-133.146	None	-107.728
Electrocatalysts Glycerol	**ΔG (kcal/mol)**	**A.E (kcal/mol)**	**Energy band gap Eg (eV)**	**Binding energy (eV)**
PdFeMn	2.274	-49.039	0.171	-111.479
PdFeCo	2.262	-49.052	0.010	-110.912
Electrocatalysts OH species	**ΔG (kcal/mol)**	**A.E (kcal/mol)**	**Energy band gap Eg (eV)**	**Binding energy (eV)**
PdFeMn	-0.606	-8.635	0.171	-102.681
PdFeCo	-0.789	-8.818	0.165	-494.527

8.2.2 Physico-chemical characterisation

8.2.2.1 XRD of trimetallic electrocatalysts

Figure. 8.1 illustrate the XRD diffractogram of Pd/C, PdFe/C, PdFeMn/C, and PdFeCo/C electrocatalysts. The diffraction peaks of all the electrocatalysts at the 2 θ value of approx. 24.7° are noticeable and attributed to the (002) plane of the hexagonal structure of carbon black. The typical diffraction peaks that emerged near 2 θ = 40°, 46°, 68°, 81°, and 86° are reflections of Pd fcc crystalline structures with miller indices of (111), (200), (220), (311) and (222) respectively in References to JCPDS card no: 88-23335 [15, 16]. It is noted that all the diffraction patterns possess no critical oxides. However, their presence cannot be discarded mainly because their amorphous phases or particle sizes are too small to be detected in the XRD, as previously reported [14, 15].

The trimetallic Pd-based electrocatalysts (PdFeMn/C) on the (111) planes displayed a slight shift to the higher 2 θ domain obviously than those of Pd/C, indicating the lattice contraction owing to the insertion of small-sized metals (mixture FeMn) in the Pd lattice [16]. For example, the lattice parameters (a) of PdFeM/C (where M = Co, Mn, 0.3891 and 0.3872, respectively) are smaller than those of Pd/C (0.39005 nm), indicating a high degree of alloying. These observations agree with a previously reported study that alloying Pt-Co (0.3825 nm compared to 0.3915 nm for Pt/CNT and 0.3543 nm for Co/CNT) nanoparticle decreases the lattice parameters caused by the insertion of Co metal in the fcc structure of Pt [17]. Hu and his co-workers reported the same on PdNiCu/C trimetallic catalysts where CuNi is encapsulated into the Pd lattice to form Pd-M alloys in accordance with the latter [18], observed a similar phenomenon in the study. More interestingly, the attained crystalline sizes (4.19 and 8.52 nm) of PdFeMn/C and PdFeCo/C electrocatalysts, respectively, are smaller than that of Pd/C implying that the 3d transition metals can slightly reduce the particle sizes of Pd/C.

The interplanar distance (d) of all the electrocatalysts and lattice parameter (*a*) are estimated according to the enlargement of the diffraction peaks of Pd (111) by following the equations of Scherrer formula (equation 1) and Vergard's law (equation 2) respectively:

$$D = \frac{K\lambda}{\beta Cos\theta} \qquad (7.1)$$

Where D is the average diameter in nm, λ signifies the wavelength of X-ray (0.1542 nm), β is the corresponding full width at half maximum (FWHM) of the diffraction peak, θ is the angle of the (111) peak position.

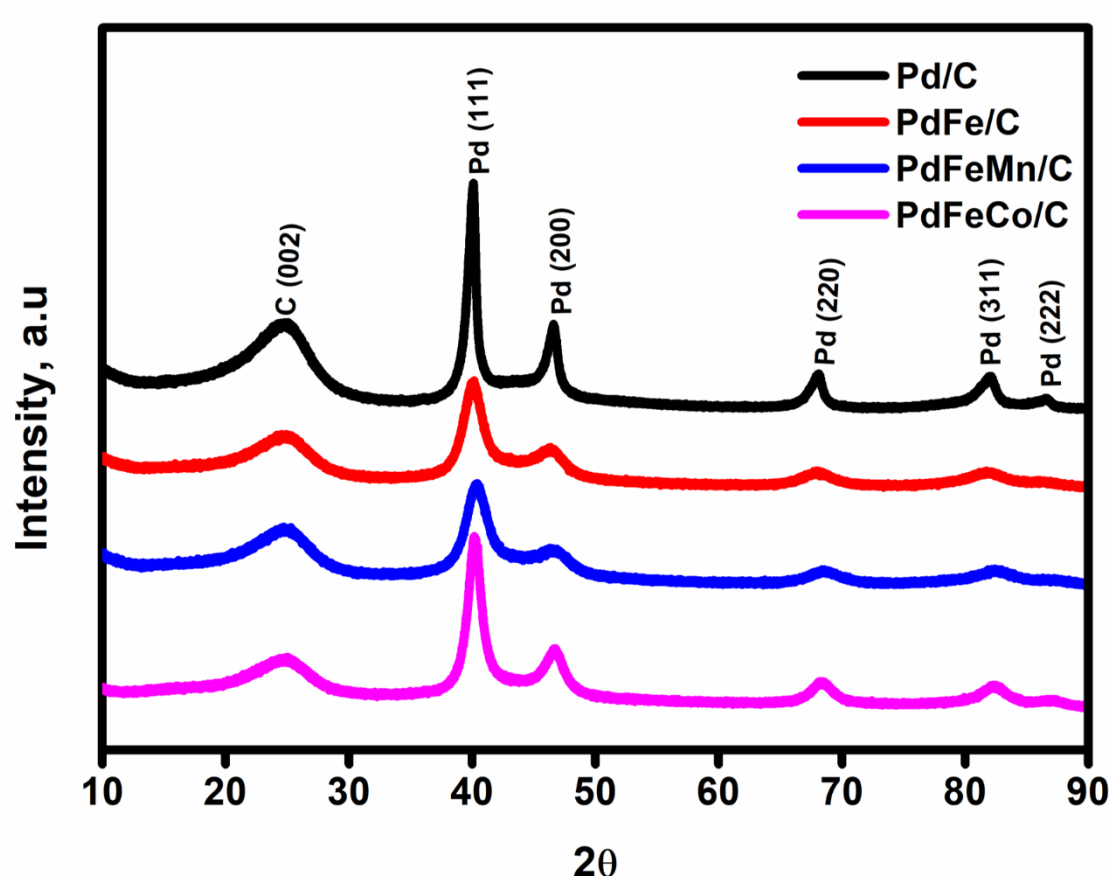


Figure 8.1: XRD patterns of electrocatalysts.

8.2.2.2 X-ray Photoelectron Spectroscopy Characterisation (XPS)

XPS spectra were conducted in this work to demonstrate the oxidation state and binding energies of Pd, Fe, Mn, Co, C and O surfaces from PdFeC, PdFeMn/C and PdFeCo/C electrocatalysts and as illustrated in Figure. 8.2 (a, e, i wide survey scan). Two oxidation states were observed in the Pd 3d regions for all the electrocatalysts, as shown in Figure. 8.2b, 2f and 2j. The Pd 3d signs (deconvoluted (Pd exist both as) into Pd and PdO_y ($0 < y < 2$) of PdFe/C, PdFeMn/C and PdFeCo/C are situated at around 335.2 eV (Pd $3d_{5/2}$), 340.6 eV (Pd $3d_{3/2}$), 335.2 eV (Pd $3d_{5/2}$), 340.8 eV (Pd $3d_{3/2}$) and 335.2 eV (Pd $3d_{5/2}$), 340.8 eV (Pd $3d_{3/2}$) respectively, no significant shift was observed for all the electrocatalysts. The binding energy values of Pd $3d_{5/2}$ and Pd $3d_{3/2}$ are similar for all the electrocatalysts presented in this chapter and are assigned to

metallic Pd (O) [34, 35]. These spectra are ascribed to Pd and PdO_y ($0 < y < 2$), indicating that the electrocatalysts have a mixture of metallic palladium and its oxides.

Figure. 8.2d, 8.2h and 8.2l show the C1s deconvoluted in three varied spectra of PdFeC, PdFeMn/C and PdFeCo/C with binding energy values of 284.2 eV (C - C sp^2), 285.0 eV (C – C sp^3) and 285.8 eV (C – O), 284.1 eV (C – C sp^2), 285.0 eV (C – C sp^3) and 285.8 eV (C – O) and 284.2 eV (C - C sp^2), 284.6 eV (C – C sp^3) and 285.8 eV (C – O), respectively. C 1S indicates graphitic carbon binding on the surface of the electrocatalysts to enhance the electron conductivity of the electrocatalyst [22]. Furthermore, C-O peaks will enhance the interaction with the metal active sites or improve electrocatalyst stability by removing intermediates during electrooxidation.

Figure. 8.2c, 8.2g and 2k show the O1s deconvoluted with two different peaks of PdFe/C, PdFeMn/C and PdFeCo/C electrocatalysts with binding energy values of 529.6 eV (metal oxide) and 531.7 eV (C – O), 529.5 eV (metal oxide) and 531.7 eV (C – O) and 529.4 eV (metal oxide) and 532.0 eV (C – O), respectively. The presence of O1s in all the stated electrocatalysts could be beneficial in producing the best electrolytic activities of EG, EOH, and Gly oxidation reaction as it can enhance the synergistic effect on the Pd active site. The presence of these species can contribute to the removal of carbonaceous species which tend to poison the active site.

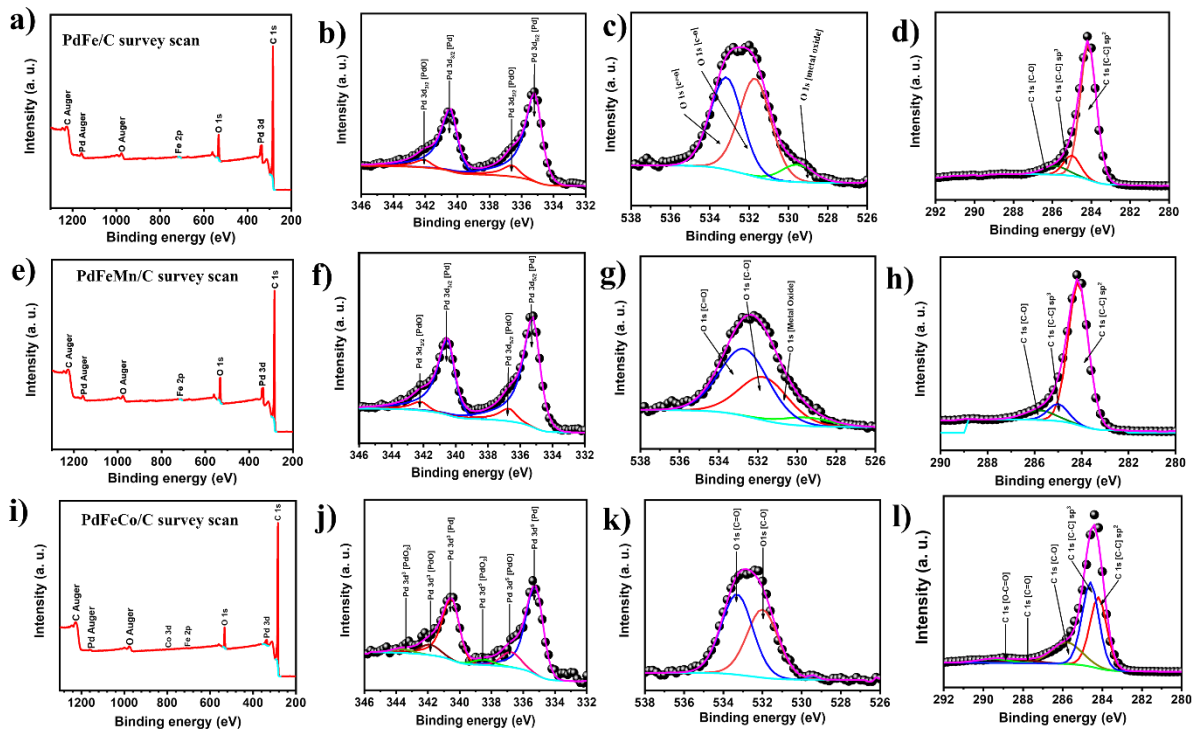


Figure 8.2 XPS spectra of (a, e, i) with the wide survey spectra, deconvoluted elementals scans b, f, j) Pd 3d, c, g, k) O 1s and d, h, l) C 1s) of PdFeC, PdFeMn/C and PdFeCo/C electrocatalysts.

8.2.2.3 SEM images

SEM analysis was employed to investigate the morphology and structure of PdFe/C, PdFeMn/C, and PdFeCo/C electrocatalysts and the images are shown in Figure. 8.3. SEM images display a small particle size to sub-10 nm for all the electrocatalysts. This is conciseness with the crystalline sizes from XRDs and the crystalline structure. There is no significant difference in surface morphology among all the electrocatalysts and the distribution is uniform on their surface.

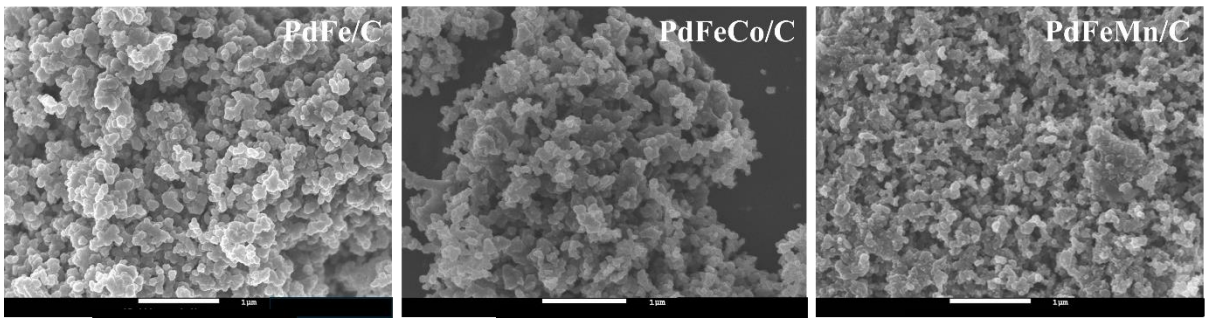


Figure 8.3: SEM images of PdFe/C, PdFeMn/C and PdFeCo/C electrocatalysts.

8.2.2.4 TEM images

Figure. 8.4 illustrates the HRTEM of PdFe/C and PdFeMn/C electrocatalysts. All electrocatalysts exhibit remarkable homogeneous distribution and high dispersion of metals on the carbon matrix with particle sizes of sub-10 nm. The decrease in particle sizes after microwave treatment affirmed the work reported by Fashedemi and co-workers [19], stating that using microwave on small-sized metals can tune the physicochemical properties of the electrocatalysts from micron to sub-10 nm.

Thus, the particle sizes obtained for the PdFeMn/C electrocatalyst almost follow the crystalline size obtained from the XRD. Figure. 8.4c and 8.4d exhibit a distinct lattice fringe alongside the interplanar distances (d) decreasing as follows: 0.228 nm for PdFe/C to 0.226 nm belongs to PdFeMn/C catalysts, indicating the (111) diffraction planes of the fcc Pd structure. The lattice fringes of PdFe/C were compressed from 0.228 nm to 0.226 nm upon the insertion of Mn metal, which confirmed the lattice stress that occurred during the alloying process [20]. The SAED exhibits about 4 rings, which are analogs to those of XRD miller indices, emphasizing the development of polycrystalline features of the electrocatalysts [21].

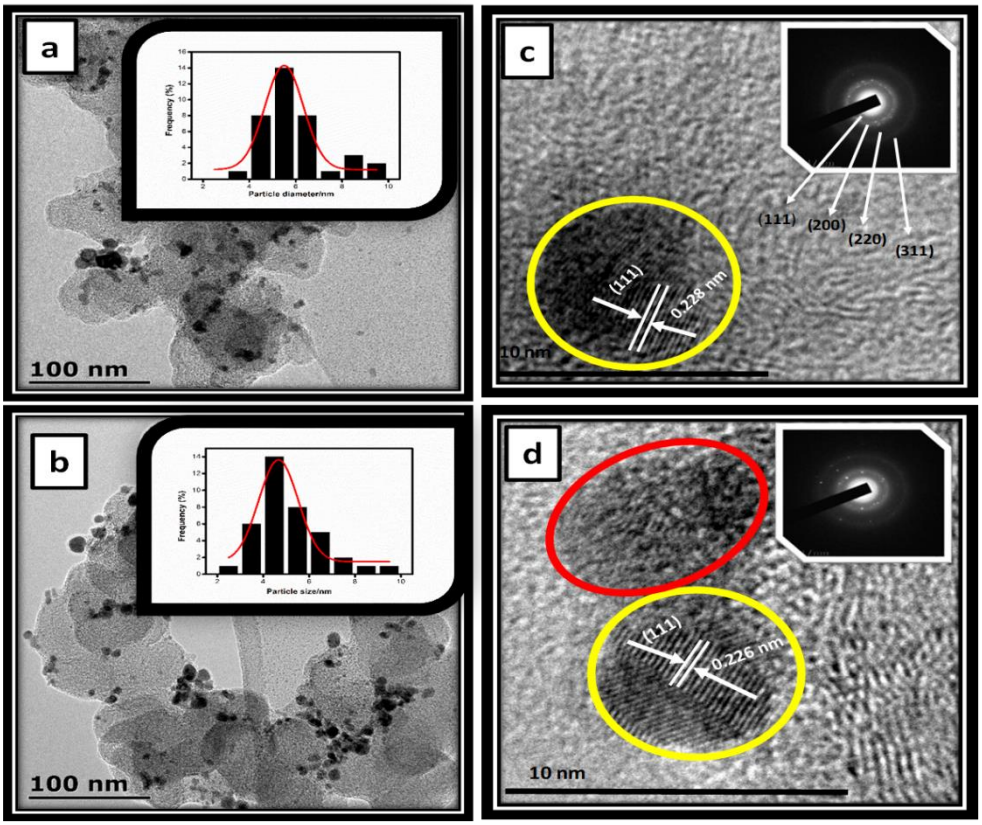


Figure 8.4: Comparative HRTEM images of (a) PdFeC, (b) PdFeMn/C; Particle size histogram distribution insert b, PdFeC and d, PdFeMn/C. Insert in (c) and (d) the SAED pattern of PdFeC and PdFeMn/C electrocatalysts.

Specific surface (SBET) of electrocatalysts were investigated using BET analysis, and the data are summarised in Table 8.2. The trimetallic electrocatalysts display increased pore size, perhaps due to more prolonged exposure to microwave irradiation [22]. However, the pore volume remains the same while the surface area reduces compared to the bimetallic and monometallic electrocatalysts.

Table 8.2: Physico-chemical characterisation data obtained from BET analysis.

Electrocatalysts	Pore-size @ (nm)	Pore-volume @ ($cm^3\ g^{-1}$)	$S_{BET@}$ ($m^2\ g^{-1}$)
PdC	6.32	0.153	96.69
Fe/C	5.78	0.153	105.59
FeMn/C	5.54	0.210	156.83
PdFe/C	7.52	0.147	78.10
PdFeMn/C	6.90	0.153	69.44
PdFeCo/C	6.88	0.155	87.60

8.2.3 Electrochemical characterisation

8.2.3.1 CV Test

Figure 8.5 illustrates the CV of all the different catalysts in the solution of (0.5 M) KOH at the scan rate of 50 mV / s. The cathodic peaks observed around -0.3 V for all the electrocatalysts are attributed to the PdO reduction peak. The results show that after Pd/C has been modulated with non-noble metals, the position and size of the PdO reduction peak are altered and become well-defined.

The reduction PdO peak was employed to estimate the ECSA with the Coulombic charge value of 0.424 mC cm^2. The values belonging to ECSA for all the electrocatalysts are estimated and summarised in Table 8.3. The trend in the ECSA values is as follows: Pd/C < PdFe/C < PdFeCo/C < PdFeMn/C. Obviously, from the displayed results, the modified electrocatalysts (PdFe/C, PdFeMn/C, and PdFeCo/C) have larger ECSA values in comparison to the monometallic Pd/C electrocatalyst. However, the PdFeMn/C electrocatalyst displays a highly prominent value than its counterparts; an indication of more available sites of the electro-reduction of PdO can be attributed to the strong synergy among the constituent metals.

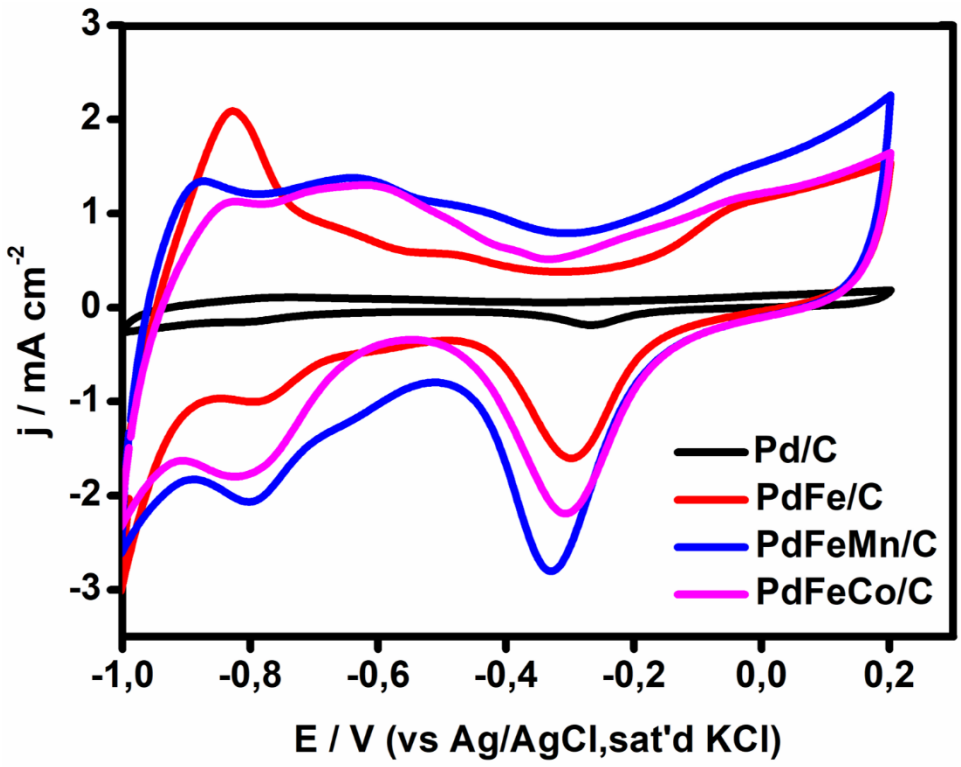


Figure 8.5: Cyclic voltammograms of electrocatalysts containing a solution of (0.5 M) KOH at a sweep rate = 50 mV / s.

Table 8.3: Summary of ECSA results for nano-catalysts.

Nano-catalysts	**ECSA @ m^2/ g**
Pd/C	2.7
PdFe/C	30.17
PdFeMn/C	62.60
PdFeCo/C	56.27

8.2.3.2 CV of monometallic, bimetallic and tri-metallic electrocatalysts for EGOR

The electro-catalytical performance of PdC, PdFeC, PdFeMn/C, and PdFeCo/C towards EGOR in an alkaline solution containing 0.5 M amount of KOH / EG were illustrated with CV profiles, shown in Figure. 8.6. Two well-distinct peaks were depicted, i.e., the forward and the backward scans. In a comparison study amongst monometallic (Pd/C) and bimetallic (PdFeC), the trimetallic electrocatalysts evinced prominent catalytic activities towards the EGOR in basic media. In detail, as summarised in Table 8.4, the PdFeMn/C and PdFeCo/C display superior

specific activity of 7.26 and 6.75 mA cm^{-2}, respectively, which are 5.6 times more than the Pd/C and 1.24 times PdFeC electrocatalyst. The current densities decrease following this trend: PdFeMn/C > PdFeCo/C > PdFe/C > Pd/C electrocatalysts. The PdFeMn/C (1430 mA/mg) and PdFeCo/C (1420 mA/mg) demonstrated the highest MA values, which are 5.8 times and 1.24 times that of Pd/C and PdFe/C, respectively, as shown in Figure 8.7 and summarised in Table 8.4. This advocated that trimetallic electrocatalysts are promising catalysts for EGOR due to the electronic structure modification after the insertion of Fe, Mn, and Co to Pd/C, resulting in the alteration of the surface adsorption of oxygenated species [23].

Table 8.4: Comparison of electrocatalysts performance for the EGOR.

Electrocatalysts	E_{onset} **(V)**	E_p	J_f / J_b	**SA (mA/cm^2)**	**MA (mA/mg)**
Pd/C	-0.36	-0.1	1.26	1.35	250
PdFe/C	-0.46	-0.1	1.30	5.51	1300
PdFeMn/C	-0.47	-0.1	1.35	7.26	1430
PdFeCo/C	-0.47	-0.1	1.30	6.75	1420

The onset potential (E_{onset}) of the PdFeMn/C electrocatalyst is 110 mV lower than that of Pd/C and 10 mV lower than that of the PdFe/C electrocatalysts, which is the most negative among the tested electrocatalysts. This indicates the importance of co-metals in lowering the required energy and thereby beneficially affecting the performance of Pd/C towards EGOR.

The peak current density ratio (Jf / Jb) was also examined to investigate the catalysts that are less susceptible to poisoning on the active sites by intermediates generated during EGOR. The higher J_f / J_b value represents that the catalysts are more tolerant to poisoning and that intermediates are successfully removed on the active site. Notably, PdFeMn/C and PdFeCo/C electrocatalysts display superior Jf / Jb values of 1.35 and 1.30, respectively, approximately 1.1 times greater than Pd/C (1.26). The prominent catalytic performance can be attributed to the bi-functional mechanism where Fe, Co, and Mn, to Pd/C, produce additional hydroxide species for fast intermediates' oxidation. However, the explanation of the electronic and bi-functional mechanism of Fe, Co, and Mn, as well as Pd/C, towards the electrochemical oxidation scheme remains the subject of debate.

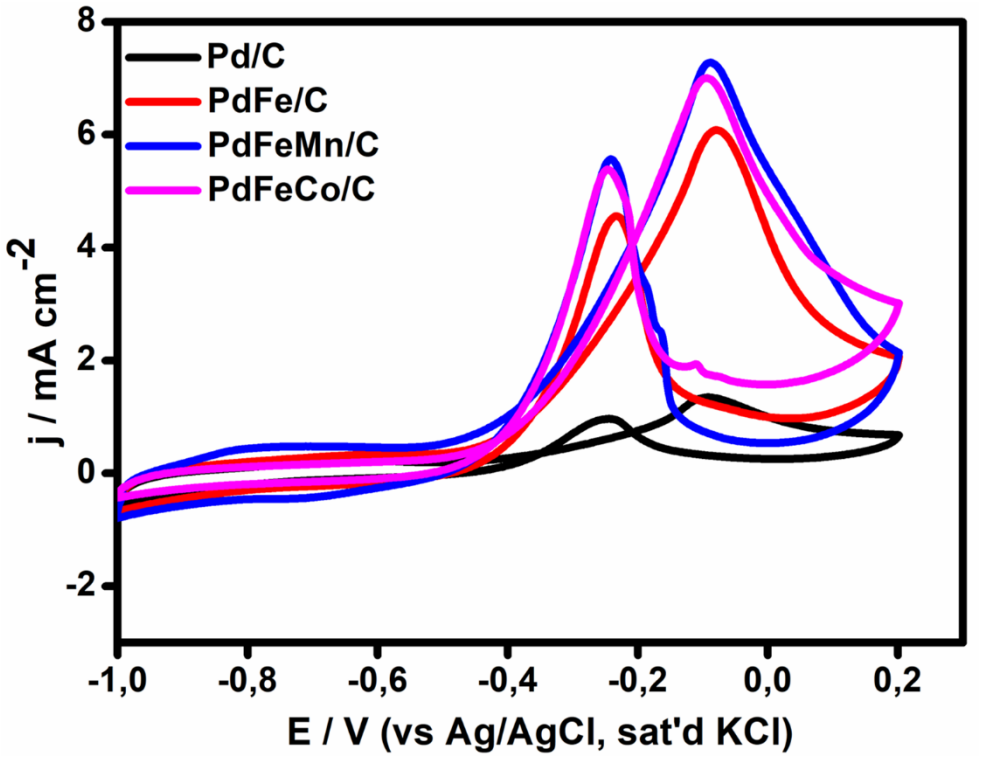


Figure 8.6: The CV of Pd/C, PdFeC, PdFeMn/C, and PdFeCo/C for EGOR was reached at 50 mV / s in a KOH/Gly solution containing 0.5 M.

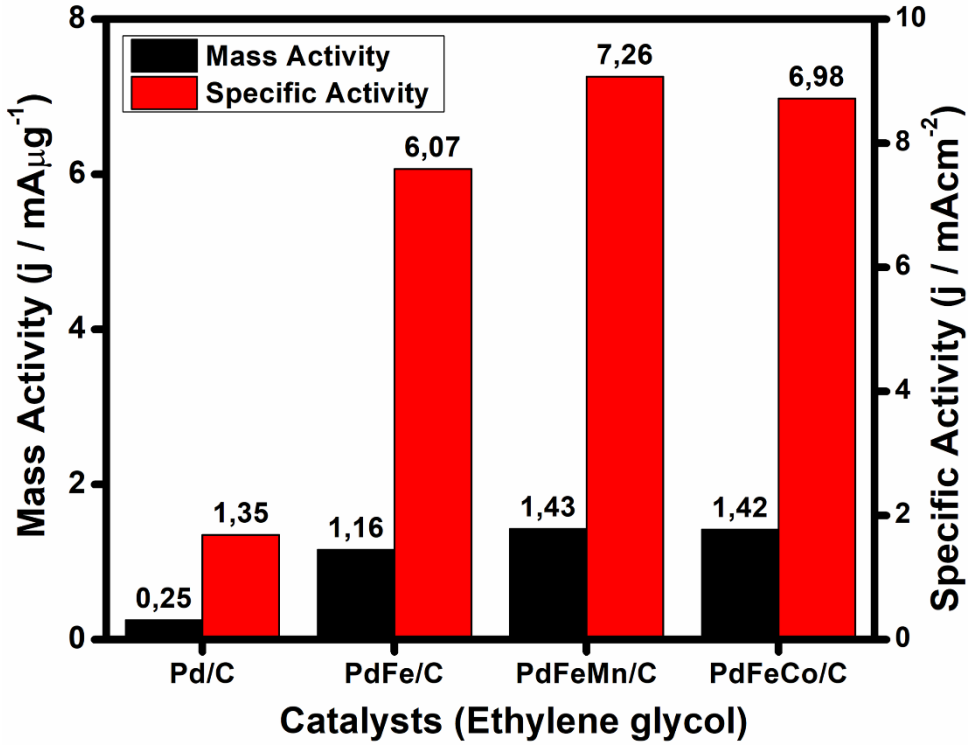


Figure 8.7: Comparison between mass & specific activities of Pd, PdFeC, PdFeMn/C and PdFeCo/C in KOH/EG containing 0.5 M solution under N_2 gas, 50 mV / s.

8.2.3.3 Chronoamperometric evaluation

Chronoamperometry is a prominent technique employed to investigate the long-term durability of the catalysts toward EGOR. Figure. 8.8 shows the current-time curve of PdC, PdFeC, PdFeCo/C and PdFeMn/C catalysts in the 0.5 M KOH/ EG solution at the fixed voltage of -0.2 V. In general, all the electrocatalysts exhibit a drop in current density at the initial stage and suddenly return to the quasi-steady state. The drop in current densities is attributed to the fact that the catalysts are strongly poisoned by adsorbed carbonaceous species, impeding the adsorption and oxidation of ethylene glycol [24]. The quasi-steady state of all the electrocatalysts exemplifies that the adsorption of oxygenated species from non-noble metals and strongly adsorbed species sustains the relative balance [187]. The overall stabilities of current densities performance are in the following order: PdFeMn/C > PdFeCo/C > PdFe/C > Pd/C. This order indicates that the trimetallic electrocatalysts present the best stability among all the electrocatalysts, owing to their sufficient oxygenated species generated on the Pd/C active site that managed to eliminate the CO poisoning species.

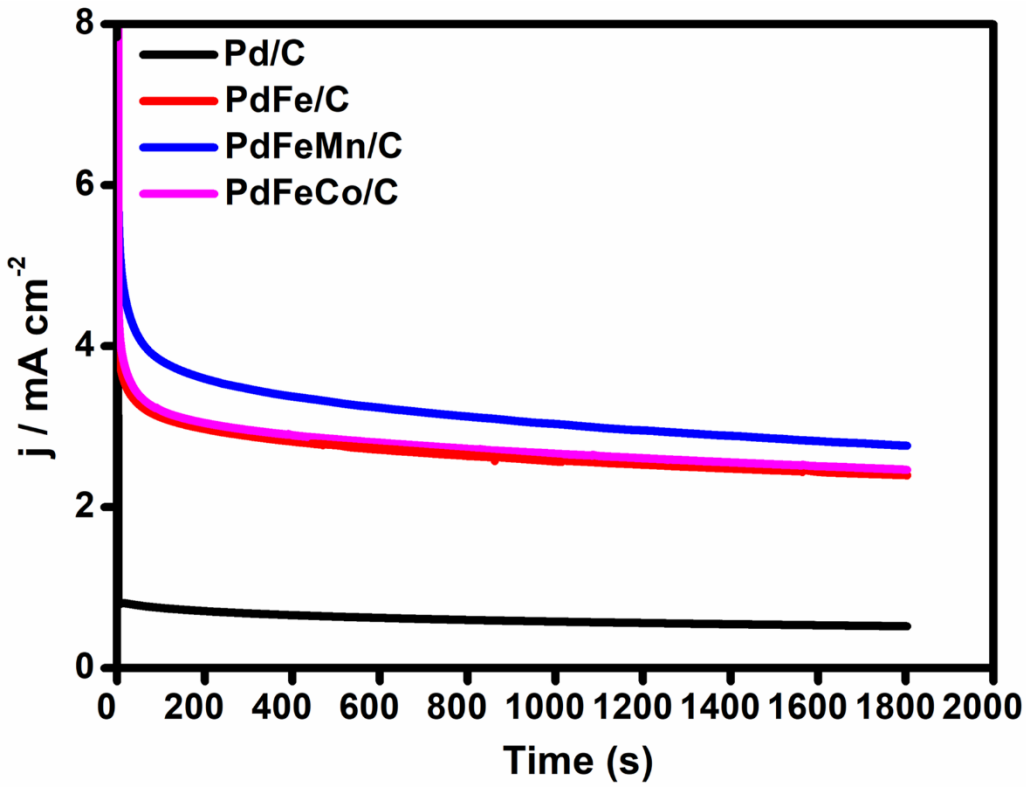


Figure 8.8 Current-times curve of Pd/C, PdFe/C, PdFeMn/C and PdFeCo/C electrocatalysts, potential of -0.2 V in (0.5 M) KOH/EG solution.

8.2.3.4 CV of monometallic, bimetallic, and tri-metallic electrocatalysts for EOR

Cyclic voltammetry was employed to investigate the activity of the catalysts in the solution of (0.5 M) KOH containing (0.5 M) ethanol, as signified in Figure. 8.9. It is interesting to note that the trimetallic electrocatalysts exhibit higher electrocatalytic activity for oxidation of ethanol than the PdFeC and PdC electrocatalysts, as parameters are indicated in Table 8.5. The PdFeMn/C (6.33 mA cm^{-2}) and PdFeCo/C (5.16 mA cm^{-2}) show high SA, 1.8 times the Pd/C and 1.42 times PdFe/C. It can be observed that the trimetallic electrocatalysts also exhibit the best mass activities, which are 2120 and 2010 mA mg^{-1} for PdFeMn/C and PdFeCo/C, respectively, as shown in Figure 8.10. These mass activities are approximately 3.87 times superior to Pd/C and 1.56 times higher than PdFe/C, indicating a significant improvement in the catalytic performance due to co-metals' dispersion on the Pd surface.

Table 8.5: Comparison of catalysts performance for EOR

Electrocatalysts	$E_{onset,}$ @V	E_p **@ V**	J_f/J_b	**SA (mA/ cm^2)**	**MA (mA/ mg)**
PdC	-0.52	- 0.18	1.07	1.65	550
PdFe/C	-0.53	-0.18	0.91	4.15	1380
PdFeMn/C	-0.58	-0.22	1.24	6.33	2120
PdFeCo/C	-0.58	-0.18	1.03	5.16	2010

Besides, the results indicate that the trimetallic electrocatalysts have greatly improved the rate of EOR at the same potential as attested by Yuanyuan Zhang and colleagues in 2018 [23]. The onset potential for trimetallic electrocatalysts is more negative than PdC and PdFeC, signifying the lower energy for EOR in basic environment. Moreover, the J_f / J_b values of the trimetallic electrocatalysts gave higher values, indicating that the Pd electrode is less likely to poison species than its counterparts, as shown in Table 8.5. This suggests that adding Fe, Mn, and Co to PdC greatly influences the Pd active site by weakening the accumulation of CO intermediates.

To attain a better understanding of the mechanism for the EOR on Pd-based electrode steps may be represented as follows even though the mechanism (Equation 1 – 5) using the non-noble metals remains unclear [25, 26]:

$$Pd\text{-}CH_3CH_2OH \longleftrightarrow Pd\text{-}(CH_3CH_2OH)_{ads} \quad (1)$$

$$Pd\text{-}(CH_3CH_2OH)_{ads} + 3OH^- \longrightarrow Pd\text{-}CH_3CO_{ads} + 3H_2O + 3e^- \quad (2)$$

$$OH^- \longrightarrow OH_{ads} + e^- \quad (3)$$

$$Pd\text{-}CH_3CO_{ads} + Pd\text{-}OH_{ads}^- \xrightarrow{r.d.s} Pd\text{-}CH_3COOH + Pd \quad (4)$$

$$Pd\text{-}CH_3COOH + OH^- \xrightarrow{fast} Pd + CH_3COO^- + H_2O \quad (5)$$

Expressly, Equations 1 and 2 represent the dissociative dehydrogenation/adsorption of the acetyl group (CH_3COads) and poisoning species on the surface of the catalyst. Equation 4 is postulated as the rate-determining step, which indicates that the adsorbed ethoxy intermediates ($Pd\text{-}CH_3COOH$) were stripped away by -OH on the active site to yield an acetate ion (CH_3COO) and augment the current density. The EOR cannot be oxidized to CO_2, producing an acetate, as demonstrated in Equation 5.

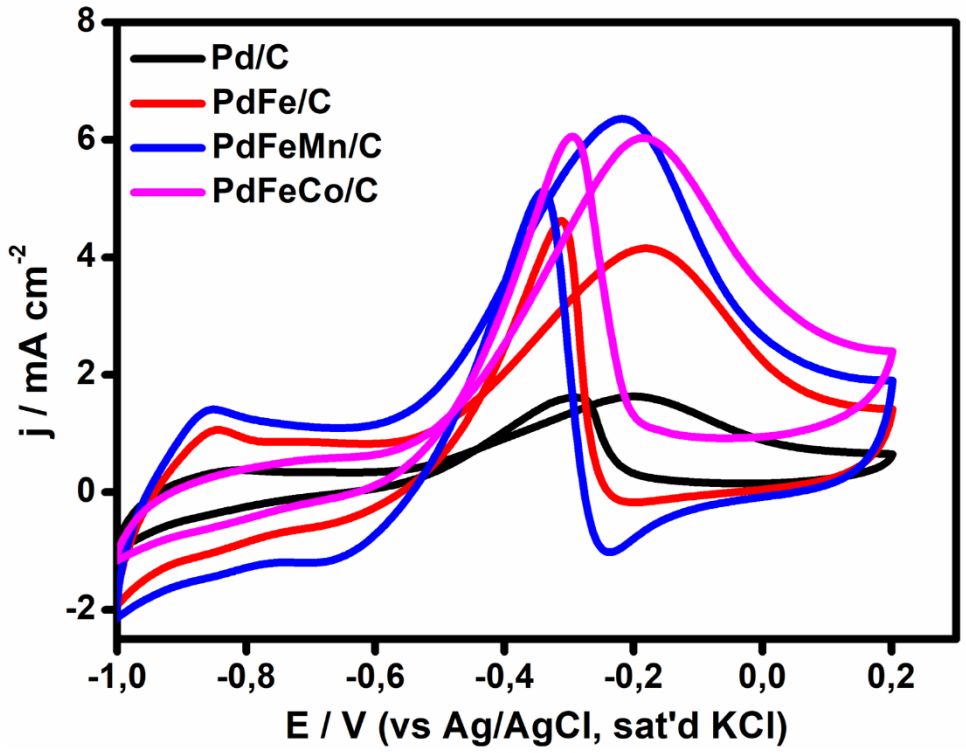


Figure 8.9: Cyclic voltammetry of electrocatalysts for EOR, reached = 50 mV / s, containing the solution of 0.5 M KOH / EtOH.

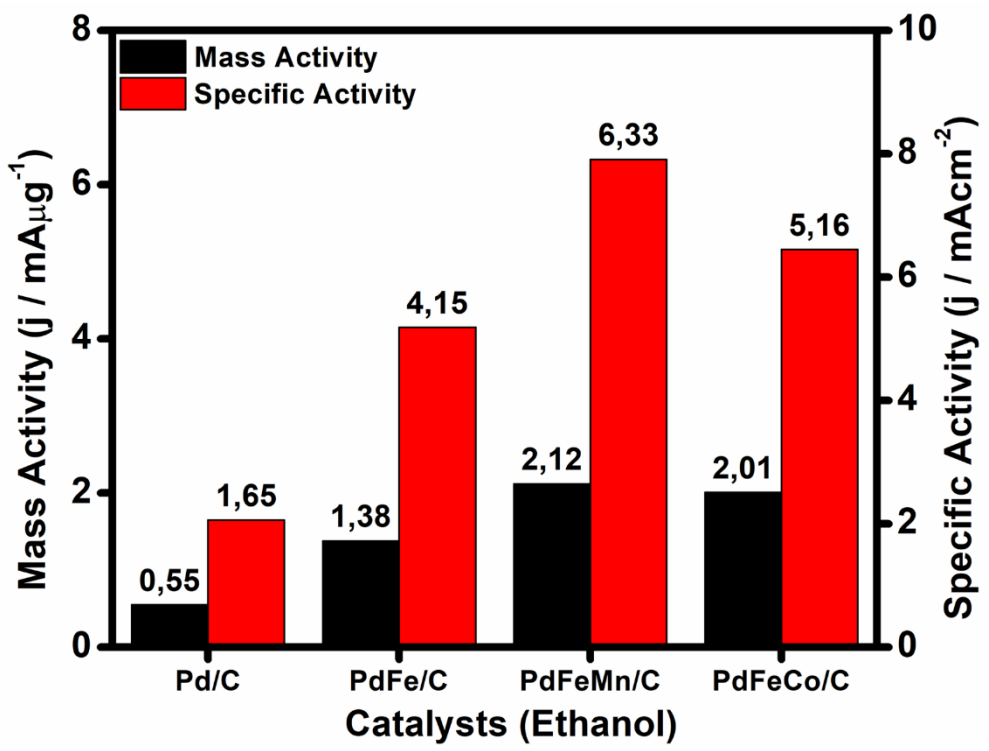


Figure 8.10: Comparison of various activities to study the electrocatalysts in 0.5M KOH/ EtOH solution, bubbled with N_2 gas at a sweep rate = 50 mV / s.

8.2.3.5 Chronoamperometry Test

The chronoamperometric technique is a powerful tool to thoroughly investigate the long-term activity of Pd/C, PdFe/C, PdFeMn/C, and PdFeCo/C electrocatalysts potential value of -0.2 V in the solution of (0.5 M) KOH/EtOH, as shown in Figure. 8.11. At the beginning state, we observe the decrease in current density for all the electrocatalysts caused by the accumulation of intermediates species such as ethoxy and CO on the active site of the electrode. The trimetallic electrocatalysts displayed the highest steady current densities for the EOR owing to their excellent tolerance to intermediates and gave high catalytical activity. This can be further explained by the bi-functional mechanism where non-noble metals contribute more of the oxygenated species into Pd/C to remove intermediate species (CH_3CO_{ads}) by enhancing the adsorption of OH_{ads}. In general, trimetallic electrocatalysts gave the best stability and higher activity towards EOR in an alkaline medium, and besides them all, PdFeMn/C electrocatalysts still gave an exceptional performance [27].

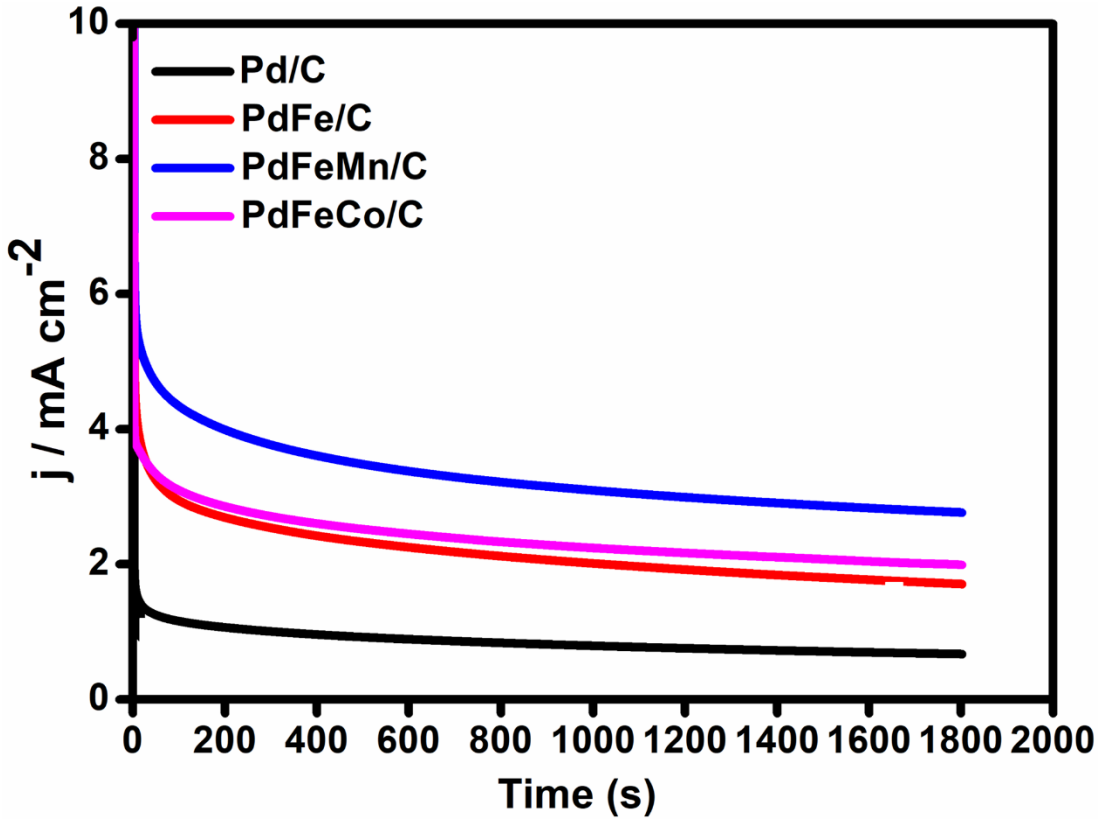


Figure 8.11: Current-times curve of examined electrocatalysts with a -0.2 V, containing 0.5 M KOH / 0.5 M ethanol.

8.2.3.6 CV of monometallic, bimetallic, and trimetallic electrocatalysts for GOR

Cyclic voltammetry was employed to examine the catalytic response of PdC, PdFeC, PdFeMn/C and PdFeCo/C electrocatalysts towards the GOR at the sweep rate equivalent to 50 mV / s, demonstrated in Figure. 8.12. Two well-defined anodic and cathodic peaks were observed related to the Gly oxidation and the removal of poisoning species, respectively [28]. The values of the onset potential (E_{onset}), (J_f /J_b), peak potential (E_p), MA, and SA were noted to determine the electro-catalytical activity of the electrocatalysts towards the GOR, and the values are summarised in Table 8.6. The onset potential of all the trimetallic electrocatalysts reveals more negative values of -0.45 V compared to Pd/C with -0.43. This indicates the rapid kinetics of the electrochemical oxidation of glycerol. In addition, Pd/C electrocatalysts have lower J_f / J_b values compared to the trimetallic and the bimetallic electrocatalysts, indicating that the electrocatalysts can tolerate poisoning species on the surface. It was observed that the SA and MA of the trimetallic electrocatalysts are more significant than those of PdC and PdFeC, following a trend of PdFeMn/C > PdFeCo/C > PdFeC > Pd/C, as expressed in Figure

8.13 and summarised in Table 8.6. In this regard, the results indicate that the trimetallic electrocatalysts have greatly enhanced the rate of GOR at the same potential.

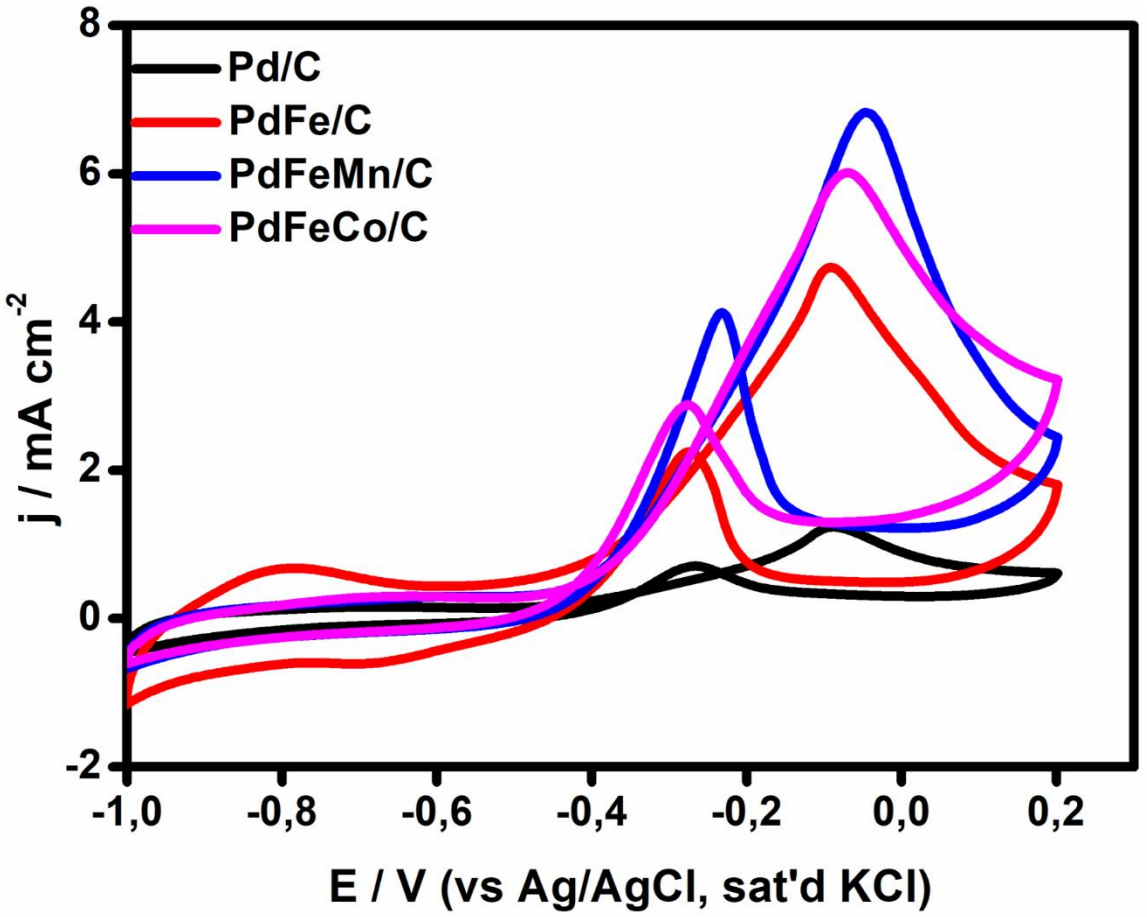


Figure 8.12: Cyclic voltammetry of electrocatalysts for GOR with a scan rate of 50 mV / s, 0.5 M KOH / 0.5 M Gly.

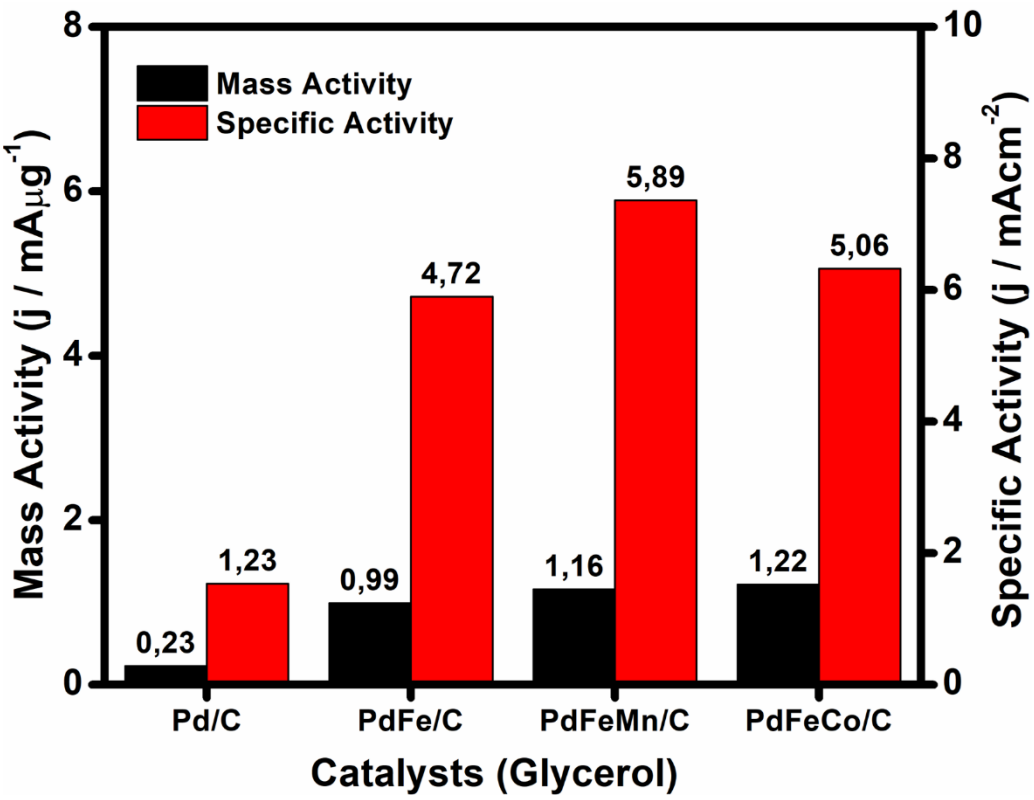


Figure 8.13: Comparison of mass and specific activities of Pd, PdFe/C, PdFeMn/C and PdFeCo/C, containing (0.5 M) KOH / Gly under N_2 gas at 50 mV/ s.

Table 8.6: Comparison of electrocatalysts performance for GOR.

Electrocatalysts	E_{onset} **(V)**	E_p **(V)**	J_f/J_b	**SA (mA/cm^2)**	**MA (mA/mg)**
Pd/C	- 0.43	-0.09	1.76	1.21	240
PdFe/C	-0.45	-0.09	2.01	4.72	990
PdFeMn/C	-0.45	-0.06	1.68	5.89	1160
PdFeCo/C	-0.45	-0.07	2.08	5.06	1220

8.2.3.7 Chronoamperometric analysis

The stability of Pd/C, PdFe/C, PdFeCe/C, PdFeMn/C and PdFeCo/C electrocatalysts towards the GOR in alkaline solutions have evinced in Figure. 8.14. The results display the sequential stability after the 1800 s towards glycerol electro-oxidation in alkaline medium: PdFeMn/C > PdFeCo/C > PdFe/C > Pd/C electrocatalysts. Based on the above analysis of these materials, we can conclude that PdFeMn/C electrocatalysts exhibited superior activity and better tolerance to poisoning towards GOR [3].

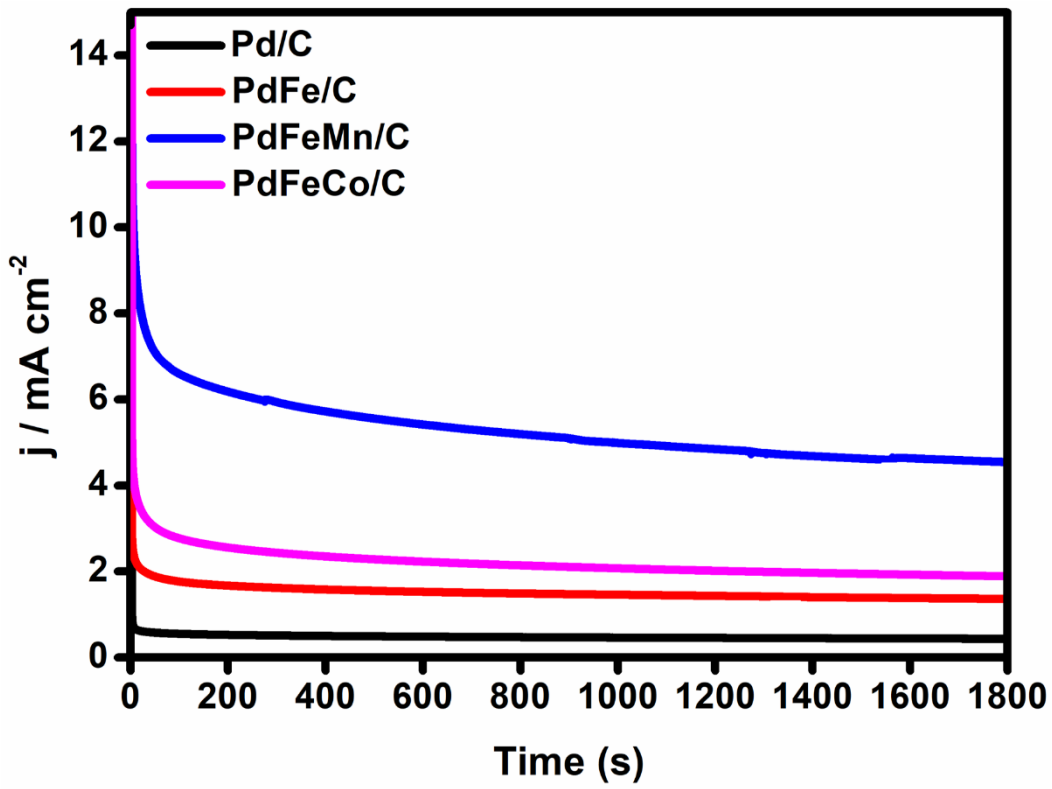


Figure 8.14: Current-times curve of Pd/C, PdFe/C, PdFeCo/C with PdFeMn/C electrocatalysts at -0.2 V in 0.5 M KOH/ 0.5 M Gly solution.

8.2.3.8 Comparison of alcohol electro-oxidation for the various electrocatalysts

The electrochemical performances of the electrocatalysts for the electro-oxidation of different alcohols are demonstrated with the CV. The varied trimetallic electrocatalysts (a) PdFeMn/C and b) PdFeCo/C) synthesised via microwave-assisted method are evaluated and compared for the oxidation of EG, EtOH, and Gly in a basic environment, as displayed in Figure. 8.15. The performance parameters for comparing the three alcohols on the best-studied trimetallic electrocatalysts such as E_{onset}, Js and J_f/ J_b are summarised in Table 8.7. The results revealed that all the electrocatalysts are highly active in oxidizing all the stated alcohols in the basic electrolytes. Therefore, the development of these reduced-cost electrocatalysts had a significant influence in enhancing the kinetics for anodic electro-oxidation and making it less prone to CO poisoning. The research study published by Fathrid and co-workers 2017 has shown that Pd-Mo nano-alloys improved the kinetics of CH_3OH, ethanol, Gly, and EG in alkaline electrolytes. The electronic structure was significantly affected after inserting elements with smaller atomic sizes into the substrate, which changed their catalytical properties [29].

Nevertheless, ethylene glycol confirmed the highest current densities towards the electro-oxidation in all the electrocatalysts over ethanol and glycerol. On the other hand, ethanol gave the best onset potential of PdFeMn/C (-0.58 V) and PdFeCo/C (-0.58 V) in all the electrocatalysts over ethylene glycol and glycerol. Even though the activity is very high in ethylene glycol, the ethanol fuel requires the lowest energies during the electro-oxidation of all the electrocatalysts. The ratio of J_f / J_b was solely probed to determine the tolerance ability of the electrocatalysts towards CO species accumulation (the higher the value, the less prone the catalyst is to poison). The J_f / J_b value of all the electrocatalysts towards glycerol oxidation displays a higher value over ethanol and ethylene glycol. These observations signify that the trimetallic catalysts are more tolerant to poisoning and produce better oxidation towards glycerol in basic media.

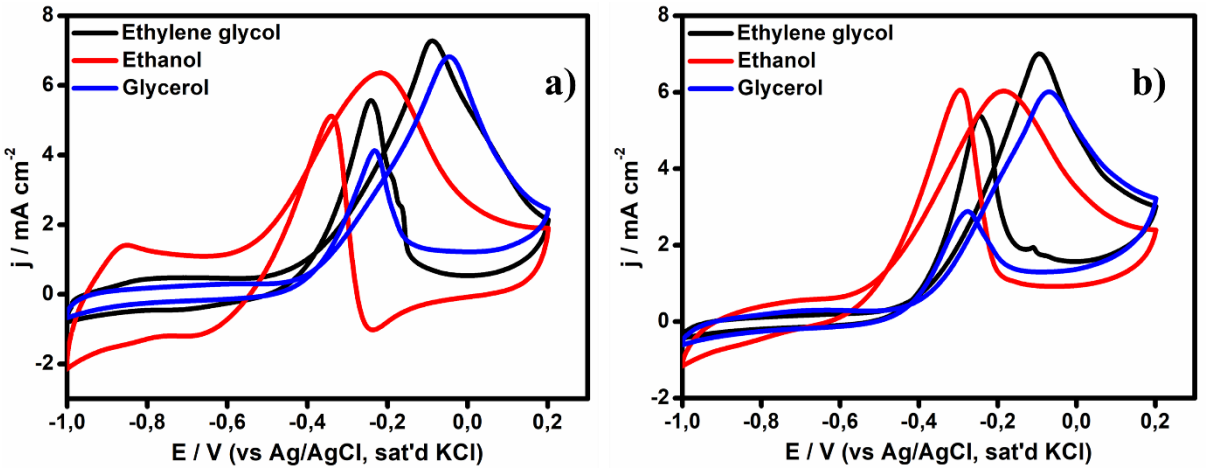


Figure 8.15: Comparative cyclic voltammetry of a) PdFeMn/C and b) PdFeCo/C nano-catalysts in the solution containing 0.5 M KOH / alcohols (EG, EtOH, GOR) @ 50 mV / s.

Table 8.7: The electrochemical performance comparing different alcohols with PdFeMn/C and PdFeCo/C electrocatalysts.

Alcohols	**E_{onset} (V)**	**J_f/J_b**	**SA**
		PdFeMn/C	
Ethylene glycol	-0.47	1.35	7.26
Ethanol	-0.58	1.24	6.33
Glycerol	-0.45	1.68	5.89
		PdFeCo/C	
Ethylene glycol	-0.47	1.30	6.98
Ethanol	-0.58	1.03	5.16
Glycerol	-0.45	2.08	5.06

8.2.3.9 Electrochemical impedimetric analysis of alcohol electro-oxidations on electrocatalysts.

EIS is a well-known tool for exploring the electrochemical process between the solution and electrode interface [30]. Figure. 8.16 shows the typical Nyquist plots of a) PdFeMn/C and b) PdFeCo/C electrocatalysts measured (0.5 M KOH/ 0.5 M (EG, EtOH, Gly) at the fixed voltage

of -0.2 V. The Nyquist plots for all the alcohols were perfectly fitted using the EEC as attached. The EEC comprises R_s, R_{ct}, and CPE, and they are described as follows: Rs refers to resistance electrolytes, Rct is known as charge transfer resistance, and *CPE* is the constant phase element. Table 8.8 shows the EIS measurements. All the electrocatalysts depict the smallest R_{ct} value for EGOR amongst ethanol and Gly, indicating the faster electrode kinetics for ethylene glycol electro-oxidation, followed by glycerol and ethanol being the most diminutive performer with the highest value of Rct. These results follow the high current densities from CV.

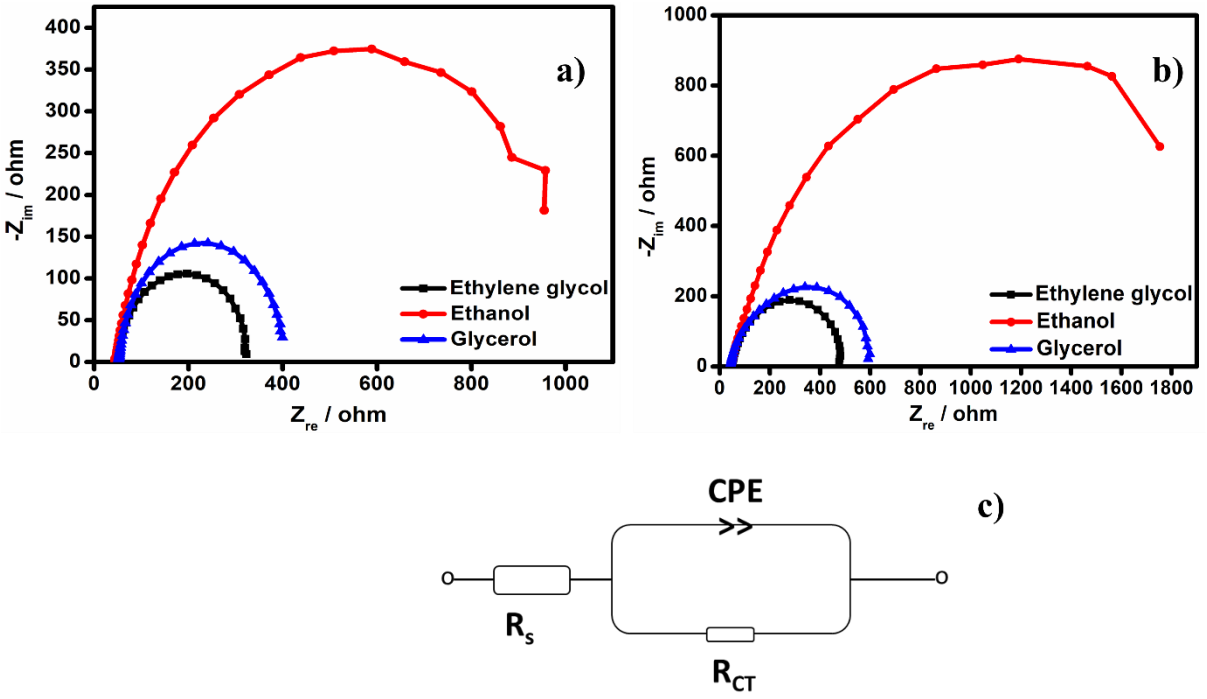


Figure 8.16: a) Nyquist plot of a) PdFeMn/C and b) PdFeCo/C electrocatalysts using the same parameters as CV and c) insert is the EEC (equivalent external circuit) used to fit the spectra.

Table 8.8: Electrochemical impedance parameters at a specific voltage of -0.2 V.

Alcohols	R_s (Ω)	R_{ct} (kΩ)	*n*	*CPE* x 10^2
		PdFeMn/C		
Ethylene glycol	45.33 ± 0.43	0.27 ± 0.001	0.87	0.13 ± 0.003
Ethanol	48.22 ± 0.52	1.34 ± 0.001	0.91	0.40 ± 0.001
Glycerol	51.22 ± 0.28	0.35 ± 0.001	0.88	0.43 ± 0.001
		PdFeCo/C		
Ethylene glycol	52.15 ± 0.66	0.56 ± 0.001	0.87	0.16 ± 0.003
Ethanol	48.27 ± 0.47	1.99 ± 0.001	0.87	0.21 ± 0.001
Glycerol	50.85 ± 0.47	0.75 ± 0.001	0.89	0.17 ± 0.002

8.2.3.10 Proof-of-concept of the DEFCs

To further investigate the as-prepared anode electrocatalysts' cell performance, the best-performing electrocatalysts PdFeMn/C amongst other nano-catalysts was employed for a direct alcohol micro-fuel cell (μ-DEFC) application (i.e., two electrode configuration). Because the PdFeMn/C exhibits the highest electrochemical activity and long-term durability towards all the electrooxidation of alcohol (EtOH) in basic media, in the half-cell (i.e., three-electrode configuration), amongst the electrocatalysts. The results show that adding an Mn atom into the lattice of the PdFe/C boosted the activity of the trimetallic electrocatalysts. Hence, the PdFe/C and PdFeMn/C electrocatalysts are tested in the proof-of-concept, and their performances and stability are compared.

The voltage and power density curves of PdFeMn/C and PdFe/C electrocatalysts in μ-DEFCs were displayed in the Figure. 8.17a. The curves were measured in a solution of 4.0 M KOH + 4.0 M EOH mixture at 100 mV / s. The PdFeMn/C electrocatalyst (33.27 mW cm^{-2}) gave 2 times the power density concerning PdFe/C (16.21 mW cm^{-2}). The higher maximum power density verifies that the PdFeMn/C electrocatalyst has superior activity towards ethanol electro-oxidation in an alkaline medium. From the voltage curve (I-V curve), the PdFeMn/C electrocatalyst displays a significant increase in OCV of about 1.09 V compared to that of PdFe/C with an OCV of 0.98 V. Hence, the EIS was carried out at their respective OCV.

Figure. 8.17 b shows the galvanostatic discharge experiment of the electrocatalysts was carried out at 40 mA cm^{-2} for 48 h. At 20 h, the PdFeMn/C electrocatalyst displays an energy loss of about 27%, and that of the PdFe/C electrocatalyst is -24 %. However, after 48 h, the PdFeMn/C electrocatalyst became more stable with an energy loss of about 30%, and the PdFe/C lost -36% simultaneously. No complete energy discharging was observed for both electrocatalysts even after 48 h, although adding Mn to the PdFe/C stabilizes the trimetallic electrocatalyst. This behaviour indicates that both the electrocatalysts are stable towards ethanol electro-oxidation in an alkaline medium [31]. The data was fitted using the electrical equivalent circuit (EEC) depicted in Figure. 8.15d and the results are summarised in Table 8.9. The PdFe/C has shown the Rct value of 3.85 Ω, Rs value of 4.42 Ω, and CPE value of 3.86.

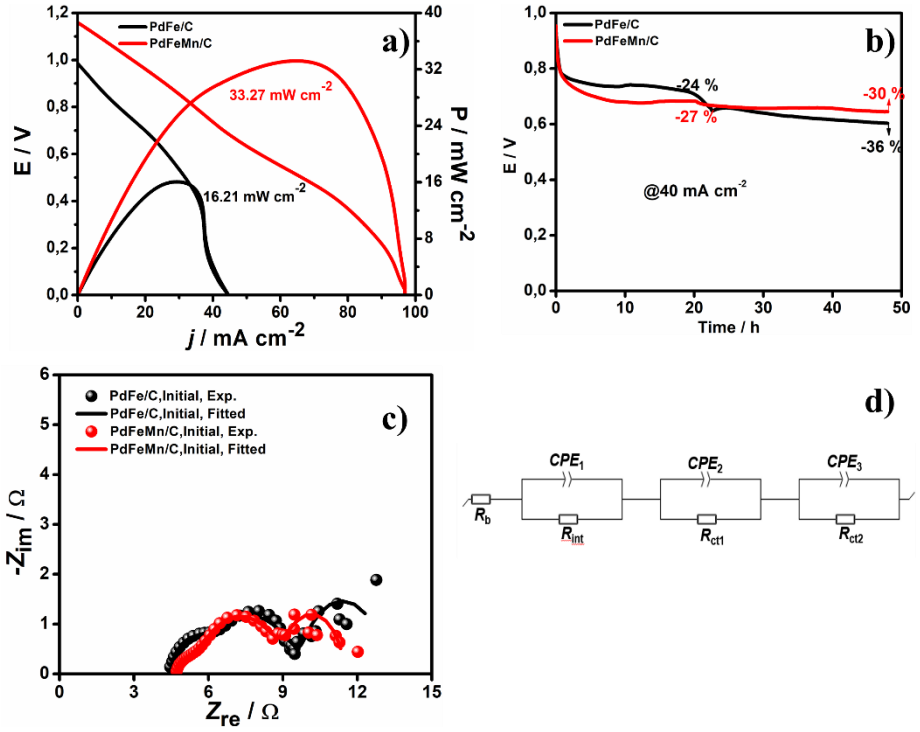


Figure 8.17: (a) Voltage (i-v) and power density curves, (b) galvanostatic discharge curve, (c) Nyquist plots and (d) Voigt EEC model for PdFe/C and PdFeMn/C fed with 4.0 M KOH/4.0 M Ethanol solution.

Table 8.9: Electrochemical impedance measurements of EOR.

EIS Parameters	PdFe/C	PdFeMn/C
R_b / Ω	4.42 ± 0.31	4.25 ± 0.10
R_{int} / Ω	1.03 ± 0.31	2.08 ± 0.10
CPE_1 / mF.s^(1-a_1)	6.30 ± 0.07	3.54 ± 1.00
a_1	0.86	0.80
R_{ct1} / Ω	4.35 ± 0.38	3.59 ± 0.10
CPE_2 / mF.s^(1-a2)	2.95 ± 0.02	42.84 ± 1
a_2	0.62	0.88
R_{ct2} / Ω	3.34 ± 1.22	1.88 ± 0.02
CPE_3 / mF.s^(1-a3)	233.30 ± 1.34	160.40 ± 1.00
a_3	0.89	1.00

8.2.3.11 Proof-of-concept of the DEGFCs

The Figure. 8.18a presents the voltage and power density curves of PdFeMn/C and PdFe/C electrocatalysts with a 4.0 M KOH/4.0 M EG solution operated at 100 mV / s. It shows that the peak power density of the PdFeMn/C electrocatalyst (45.80 mW cm^{-2}) is 1.5 times greater than that of the PdFe/C electrocatalyst (29.96 mW cm^{-2}) and OCV of 1.02 V for both were achieved. The performance of this electrocatalyst towards direct ethylene glycol micro-fuel cells (µ-DEGFCs) shows significant enhancement when compared to the µ-DEFC's performance. This result indicates that the ethylene glycol fuel has more energy and power than the ethanol and glycerol fuels in both the half-cell and full-cell configurations.

The constant current discharge behaviour of µ-DEGFC is shown in Figure. 8.18b, carried out at 20 mA/cm^2. It is observed that the µ-DEGFCs with PdFeMn/C electrocatalyst maintain a stable performance up to 35 h with an energy loss of 33.5%. After that, the voltage drops gradually with the discharge and returns to a quasi-steady state. At that point, the energy loss observed for the PdFeMn/C electrocatalyst is 42.7 % at 48 h. Compared to the PdFe/C electrocatalyst, fluctuation in the cell voltage was observed during the entire 48 hours. Thus, the energy losses are 22.9%, 41.2%, and 83.3% at about 12, 38, and 48 h, respectively. The PdFe/C electrocatalyst in the µ-DEGFC exhibits more significant energy losses than the µ-DEFC. The result indicates that PdFeMn/C electrocatalysts in ADEGFCs have great application potential, as it is more stable with respect to PdFe/C electrocatalysts [32, 33].

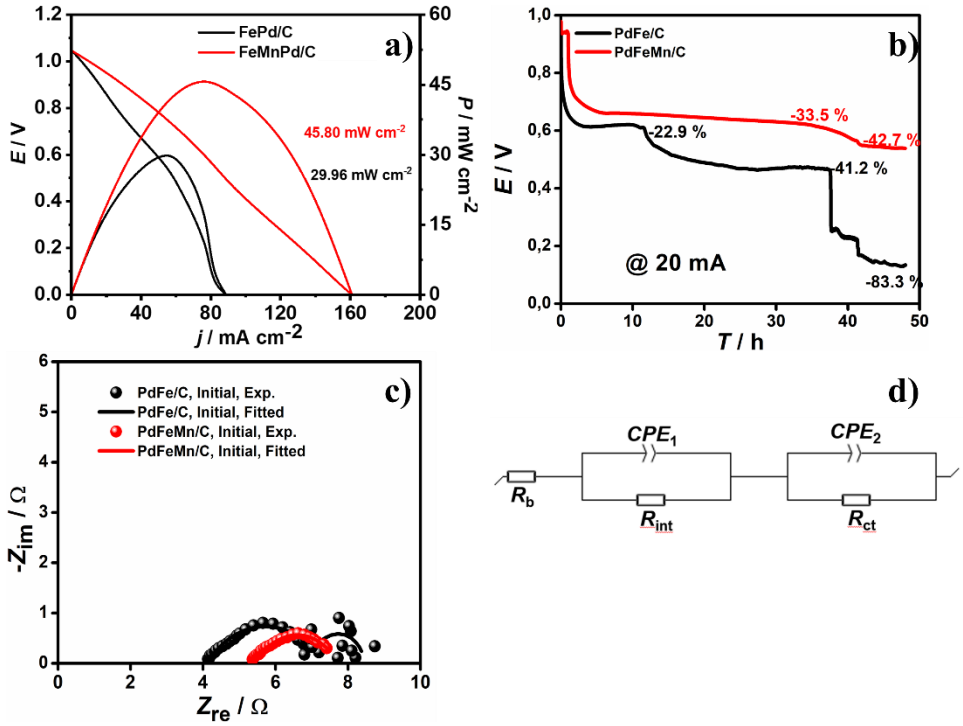


Figure 8.18: (a) Voltage (I-V) and power density curves for PdFe/C and PdFeMn/C, (b) galvanostatic discharge curves, (c) Nyquist plots, and (d) Voigt EEC for PdFe/C and PdFeMn/C supplied with 4 M KOH/EG solution.

Table 8.10: Electrochemical impedance measurements of EGOR.

EIS Parameters	PdFe/C	PdFeMn/C
R_b / Ω	4.11 ± 0.74	5.31 ± 0.98
R_{int} / Ω	1.2 ± 0.33	0.25 ± 0.52
CPE_1 / mF.s^(1-a_1)	250.20 ± 0.39	0.76 ± 0.31
a_1	0.89	0.74
R_{ct} / Ω	3.17 ± 0.57	2.15 ± 0.56
CPE_2 / mF.s^(1-a2)	5.31 ± 0.04	5.20 ± 0.24
a_2	0.55	0.61

8.2.3.12 Proof-of-concept of the DGFCs

The voltage (I-V) and power density curves are recorded in Figure. 8.19a for alkaline direct glycerol micro-fuel cells (µ-DGFCs) in a mixture of 4 M of KOH/Gly operated at 100 mV / s. The direct fuel cells powered with glycerol have demonstrated the maximum power density of 11.00 mW cm^{-2} and 16.18 mW cm^{-2} of PdFeMn/C and PdFe/C electrocatalysts, respectively.

Although the maximum power density is lower for the PdFe/C, the OCV measured for the bimetallic and trimetallic electrocatalysts is the same. The galvanostatic stability of the electrocatalysts is shown in Figure 8.19 b. The PdFeMn/C electrocatalyst shows a 5.2% energy loss at about 35 h and a 39.91% decay of the cell voltage at about 48 h. In contrast, the PdFe/C electrocatalyst displays 40.25% and 53.59% energy losses at about 20 h and 48 h, respectively.

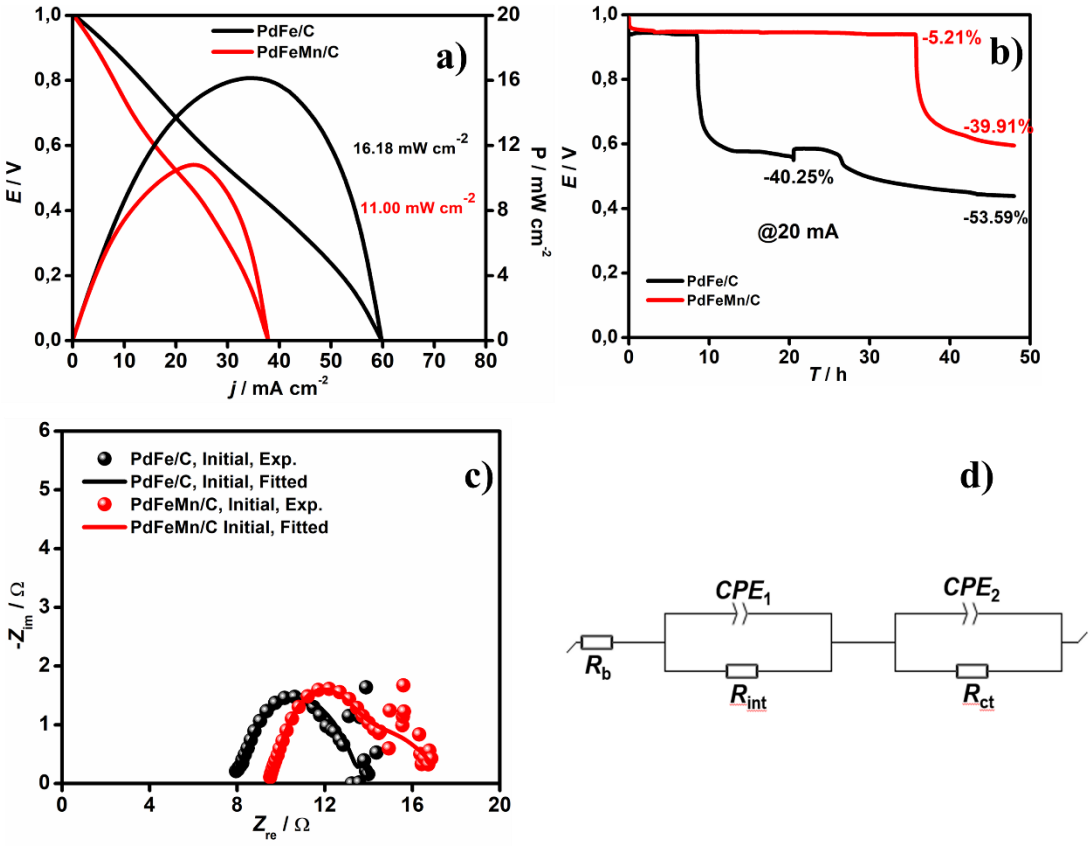


Figure 8.19: (a) Voltage (I-V) and power density curves, (b) galvanostatic discharge curve, (c) Nyquist curves and (d) Voigt EEC for PdFe/C and PdFeMn/C fed with 4 M KOH/ Gly solution.

Table 8.11: Electrochemical impedance measurements of GOR.

EIS Parameters	PdFe/C	PdFeMn/C
R_b / Ω	7.86 ± 1.00	9.31 ± 2.94
R_{int} / Ω	0.43 ± 0.05	2.60 ± 0.83
CPE_1 / mF.s^(1-a_1)	933.80 ± 1.00	0.22 ± 0.04
a_1	0.50	0.87
R_{ct} / Ω	5.76 ± 0.30	5.58 ± 0.51
CPE_2 / mF.s^(1-a2)	1.86 ± 0.45	28.50 ± 0.13
a_2	0.59	0.61

8.3 Conclusions

Trimetallic ferro-palladium-based electrocatalysts were successfully investigated in the electrooxidation of EOH, EG, and Gly in alkaline media as alternative anode electrocatalysts. The investigation revealed that trimetallic ferro-palladium-based electrocatalysts possess a more significant activity in all the alcohols than PdFe/C and Pd/C electrocatalysts. The excellent activities can be attributed to the bifunctional mechanism and electronic structure after co-metals (Mn, Co) were inserted into the PdFe/C, which modified their catalytical properties. Nevertheless, EGOR displayed the highest current densities over EOH and Gly electrooxidation in an alkaline media. PdFeMn/C and PdFeCo/C electrocatalysts showed more than 1.24 times current densities over PdFe/C electrocatalysts, indicating that the co-metals activated the interfacial water. The onset potential for EOH confirms the more negative values in all the trimetallic ferro-Pd-based than seen for EG and Gly. The J_f/J_b values are higher in GOR than in EG and EOH, suggesting that the electrocatalysts have higher CO tolerance and better electrooxidation towards Gly in alkaline media.

Overall, the PdFeMn/C electrocatalyst exhibits better stability and faster electrode kinetics towards all the alcohols than its counterparts. After that, the best two electrocatalysts (PdFe/C and PdFeMn/C) were explored as anode materials and tested for the proof-of-concept in the two-electrode configuration with the micro-3D printed cell, where the PdFeMn/C delivered improved micro-ethylene glycol fuel cell activity with respective to high power density and galvanostatic stability. The results signify that the trimetallic ferro-palladium-based electrocatalysts are more effective towards ethanol, ethylene glycol, and glycerol applications in alkaline media. In conclusion, the PdFeMn/C electrocatalyst showed the best performance

for EGOR compared to EOR and GOR, especially by giving the highest specific current density and lowest binding energy (observed from DFT calculation). On that note, we further investigated the use of PdFeMn/C as an electrocatalyst towards EGOR in full and towards ORR in an alkaline medium (see Chapter 9).

8.4 References

[1] S. Lee, H.J. Kim, S.M. Choi, M.H. Seo, W.B. Kim, Applied Catalysis A: General. 429 (2012) 39-47.

[2] K. Ye, S. Zhou, X. Zhu, C. Xu, P.K. Shen, Electrochimica Acta. 90 (2013) 108-111.

[3] L. Su, W. Jia, A. Schempf, Y. Ding, Y. Lei, The Journal of Physical Chemistry C. 113 (2009) 16174-16180.

[4] S.T. Nguyen, H.M. Law, H.T. Nguyen, N. Kristian, S. Wang, S.H. Chan, X. Wang, Applied Catalysis B: Environmental. 91 (2009) 507-515.

[5] A. Falase, M. Main, K. Garcia, A. Serov, C. Lau, P. Atanassov, Electrochimica Acta. 66 (2012) 295-301.

[6] J.M. Sieben, M.M.E. Duarte, International Journal of Hydrogen Energy. 36 (2011) 3313-3321.

[7] H.J. Kim, S.M. Choi, S. Green, G.A. Tompsett, S.H. Lee, G.W. Huber, W.B. Kim, Applied Catalysis B: Environmental. 101 (2011) 366-375.

[8] C. Bianchini, P.K. Shen, Chem. Rev. 109 (2009) 4183.

[9] T. Ramulifho, K.I. Ozoemena, R.M. Modibedi, C.J. Jafta, M.K. Mathe, Journal of Electroanalytical Chemistry. 692 (2013) 26-30.

[10] R.S. Amin, R.A. Hameed, K.M. El–Khatib, Applied Catalysis B: Environmental. 148 (2014) 557-567.

[11] M. Neergat, V. Gunasekar, R. Rahul, Journal of Electroanalytical Chemistry. 658 (2011) 25-32.

[12] H. Wang, S. Ji, W. Wang, V. Linkov, S. Pasupathi, R. Wang, Int J Electrochem Sci. 7 (2012) 3390-3398.

[13] J.M. Jacob, P.G. Corradini, E. Antolini, N.A. Santos, J. Perez, Applied Catalysis B: Environmental. 165 (2015) 176-184.

[14] R. Wang, S. Liao, H. Liu, H. Meng, Journal of Power Sources. 171 (2007) 471-476.

[15] J. Goel, S. Basu, International Journal of Hydrogen Energy. 39 (2014) 15956-15966.

[16] C. Venkateswara Rao, B. Viswanathan, The Journal of Physical Chemistry C. 113 (2009) 18907-18913.

[17] R. Ahmadi, M.K. Amini, J.C. Bennett, Journal of Catalysis. 292 (2012) 81-89.

[18] S. Hu, F. Munoz, J. Noborikawa, J. Haan, L. Scudiero, S. Ha, Applied Catalysis B: Environmental. 180 (2016) 758-765.

[19] O.O. Fashedemi, K.I. Ozoemena, Electrochimica Acta. 128 (2014) 279-286.

[20] Z. Guo, X. Kang, X. Zheng, J. Huang, S. Chen, Journal of Catalysis. 374 (2019) 101-109.

[21] Y. Chen, X. Zheng, X. Huang, A. Wang, Q. Zhang, H. Huang, J. Feng, Journal of Colloid and Interface Science. 559 (2020) 206 - 214.

[22] A.K. Ipadeola, N.Z. Lisa Mathebula, M.V. Pagliaro, H.A. Miller, F. Vizza, V. Davies, Q. Jia, F. Marken, K.I. Ozoemena, ACS Applied Energy Materials. 3 (2020) 8786 - 8802.

[23] Y. Zhang, Q. Yi, Z. Deng, X. Zhou, H. Nie, Catalysis Letters. 148 (2018) 1190 - 1201.

[24] T. Li, Y. Huang, K. Ding, P. Wu, S.C. Abbas, M.A. Ghausi, T. Zhang, Y. Wang, Electrochimica Acta. 191 (2016) 940 - 945.

[25] Z.X. Liang, T.S. Zhao, J.B. Xu, L.D. Zhu, Electrochimica Acta. 54 (2009) 2203-2208.

[26] J. Liu, J. Ye, C. Xu, Y. Tong, Electrochemistry Communications. 9 (2007) 2334-2339.

[27] S.T. Nguyen, D.S. Ling Tan, J.M. Lee, S.H. Chan, J.Y. Wang, X. Wang, International Journal of Hydrogen Energy (2011).

[28] A.K. Ipadeola, R. Barik, S.C. Ray, K.I. Ozoemena, Electrocatalysis (2019) 1-15.

[29] F. Fathirad, A. Mostafavi, D. Afzali, International Journal of Hydrogen Energy. 42 (2017) 3215-3221.

[30] H. Zhang, G. Yao, L. Wang, Y. Su, W. Yang, Y. Lin, Applications of Surface Science 356 (2015) 294 - 300.

[31] Z. Pan, B. Huang, L. An, International Journal of Energy Research. 43 (2019) 2583 - 2591.

[32] K.T. Cho, P. Ridgway, A.Z. Weber, S. Haussener, V. Battaglia, V. Srinivasan, Journal of the Electrochemical Society. 159 (2012) A1806.

[33] K. Tran, T.Q. Nguyen, A.M. Bartrom, A. Sadiki, J.L. Haan, Fuel Cells. 14 (2014) 834-841.

[34] H. Lv, H. Zhao, T. Cao, L. Qian, Y. Wang, G. Zhao, Journal of Molecular Catalysis A: Chemical. 400 (2015) 81-89.

[35] S. Yang, J. Dong, Z. Yao, C. Shen, X. Shi, Y. Tian, S. Lin, X. Zhang, Scientific reports. 4 (2014) 4501.

CHAPTER 9

Facile synthesis of Palladium Ferromanganese alloy supported on carbon as an excellent anode for Direct Ethylene Glycol Fuel Cell

9.1 Introduction

Recently, the world's energy demand has drastically increased. It will continue accumulating, along with the depletion of the direct combustion of fossil fuel currently serving as the energy source. Scientists are underway in developing clean, environmentally benign, and sustainable energy sources worldwide. Of the most electrochemical conversion systems, fuel cell technology has proven to provide better solutions to these issues. DEGFCs have garnered tremendous attention among the known fuel cells as the most prospective energy power supply for mobile and stationary applications [1]. These FCs employ ethylene glycol (EG) as a potential fuel as it stands out among other fuels owing to their renewability from biomass, low toxicity, low cost, and high theoretical energy density of 5.2 kW h kg^{-1} [2 - 4]. Although their properties seem appealing, DEGFCs encounter numerous challenges, including high cost due to excessive loading of platinum (Pt) catalyst, alcohol crossing over between the electrodes, slow kinetics, and easy poisoning of the Pt catalysts restraining the rapid commercialisaton of the device [5].

To overcome the drawbacks, developing efficient and inexpensive platinum (Pt)-free electrocatalysts has been an essential topic in recent years for the feasible growth of the DEGFCs to realise their potential. Among multitudinous platinum-free nano-catalysts, palladium (Pd) nano-catalysts are preferred as alternative catalysts to the Pt, owing to their unique electrochemical properties, abundant in nature, and better steady-state activity, particularly in alkaline media [5]. Moreover, the intense attraction with the Pd-based nano-catalysts is the ability to show outstanding performances towards alcohol oxidation reaction (AOR) in alkaline media, as articulated by Bianchi and co-workers in 2009 that pure Pd-based catalysts provide benefits such as [6, 7]: (i) the use of a variety of noble and non-noble co-metals catalysts on the electrode to boost the electrochemical properties and stability, and (ii) the ease at which EG can fully oxidize to carboxylic acid in alkaline media as it requires lower energy than the cleavage of the C-C bond in acidic media that requires high energy. Hence, the enhancement of their electro-catalytic performance with reduced Pd content is possible and

was previously reported as follows PdAu/C [8], PdNi/C [9], Pd/Ni/MOFDC [10], PdCo [11], PdMo/C [12], PdSn/C [13], PdRuSn/C [13], PdCuSn/CNTs [14], PdCuPb/C [15].

This research study gives an in-depth insight into the alloying effect, particularly between the non-noble metals and Pd, with the hope of modulating the electronic, synergistic behaviour and bi-functional mechanism towards the electrochemical properties of AOR in alkaline media [16, 17]. Concisely, according to the bifunctional mechanism, the non-noble metals alloyed on Pd eliminate the strongly adsorbed poisoning species at lower potential by offering the oxygen-containing species to the Pd adjacent site for further oxidation of intermediates and liberates the Pd active site for easy fuel electro-oxidation [4, 18]. Several research groups have successfully investigated using 3d transition metals with noble-metal catalysts. Among them, Demarconnay and colleagues 2007 reported that the multi-metallic Pt-based catalysts (PtBi and PtPdBi/C) show a maximum current density of about 28 mW cm^{-2} to pure Pt for EG electro-oxidation in an alkaline medium [19]. Li and co-workers in 2016 reported that the electro-catalytic performance of PdRuNi/C tri-metallic catalysts with space synergistic effect promotes EG electro-oxidation [20]. In contrast, Marchionni and co-workers demonstrated that adding Ni-Zn to Pd exhibits excellent electro-catalytic activity towards EG and Gly oxidation [21].

To the best of our understanding, no work has been published on utilising ferromanganese alloys onto Pd/C for the oxidation of EG in a basic medium. Using ferromanganese alloys nano-catalysts is explored in other avenues, such as ORR activities in an acidic environment [22-25]. The ferromanganese alloy has low-cost, readily available, and highly exophilic characteristics, predominantly hindering CO- species adsorption on the catalysts' active sites, leading to high electrochemical properties of the Pd toward alcohol electro-oxidation [26]. Thus far, the scarcity of the report for the ferromanganese alloys co-metal catalyst supported on Pd towards EG electro-oxidation in alkaline media is desirable to be employed to close the knowledge gap.

In this research work, a facile MW technique has been utilised to synthesise the carbon-supported Pd-based nano-catalysts with or without ferromanganese alloys (denoted as PdFeMn/C, PdFe/C, PdMn/C, and Pd/C) notably to tune the physicochemical properties of the former. Compared to conventional heating methods, the MW technique can address the challenges of long reaction rates or time and control the structure and size to improve the electrochemical properties of Pd-based ferromanganese alloy nano-catalysts.

The MW technique rapidly reaches a steady-state temperature more efficiently and uniformly [27, 28]. The PdFeMn/C electrocatalyst displayed a uniform distribution of particles on the carbon support, with the particle sizes reduced to sub-10 nm with improved synergistic interaction. Their electrocatalytic performance of the Pd-based supported ferro-manganese alloys towards EGOR was addressed whereby PdFeMn/C continues to outperform other electrocatalysts (Pd/C, PdFe/C and PdMn/C), showing high EGOR activity and stability.

9.2 Results and discussion: Ethylene glycol oxidation reaction

9.2.1 Computational studies

Table 9.1: Computational studies of Pd, PdFe, PdMn and PdFeMn in ethylene glycol

Electrocatalyst Ethylene glycol	ΔG @ (kcal/mol)	A.E @ (kcal/mol)	Binding energy (eV)
PdFe	17.628	-133.108	-146.731
PdMn	17.702	-133.033	-131.235
PdFeMn	17.653	-133.082	-108.317

Table 9.1 emphasizes the absorption/desorption behaviour towards ethylene glycol on the surface of PdFe, PdMn, and PdFeMn. From the theoretical findings, it is noticeable that there is a significant disparity between the stated catalysts. Incorporating two metals on the Pd surface (PdFeMn) only strengthened the interaction bond between PdFeMn and intermediates. This was expressed by the reduced value of binding energy for PdFeMn (B.E = -108.317 eV to -131.235 eV (PdMn) and -146.731 eV (PdFe)). Herein, we have noticed a slight decrease in Gibbs energy, which follows this sequence PdFe > PdFeMn > PdMn, indicating that PdFe is the most favorable one. Surprisingly, PdMn gave the best EG adsorption energy compared to PdFe and PdFeMn, meaning it is more stable and accessible for ethylene glycol to regenerate at the PdMn surface. However, this investigation would be believable if the critical factors from experimental findings such as ECSA, MA, SA, Jb/Jf, and BET remained the same.

9.2.2 Physicochemical Characterisations

9.2.2.1 XRD analysis

Figure. 9.1 exhibits the XRD pattern of PdC, PdFeC, PdMn/C and PdFeMn/C catalysts. It is observed that the diffraction peaks of all the electrocatalysts at the 2Θ value of approx. 24.7° is attributed to the (002) plane of the hexagonal structure of carbon black (Vulcan XC-72). The other typical diffraction peaks appearing near 2Θ = 40°, 46°, 68°, 81°, and 86° are reflections of Pd face-centered cubic crystalline (fcc) structures with miller indices of (111), (200), (220), (311) and (222), respectively in References to JCPDS card no: 88-23335. It is noted that all the diffraction patterns possess no critical oxides. However, their presence cannot be discarded mainly because their phases are in amorphous form or particle sizes are too small to be detected in the XRD, as previously reported [29, 30].

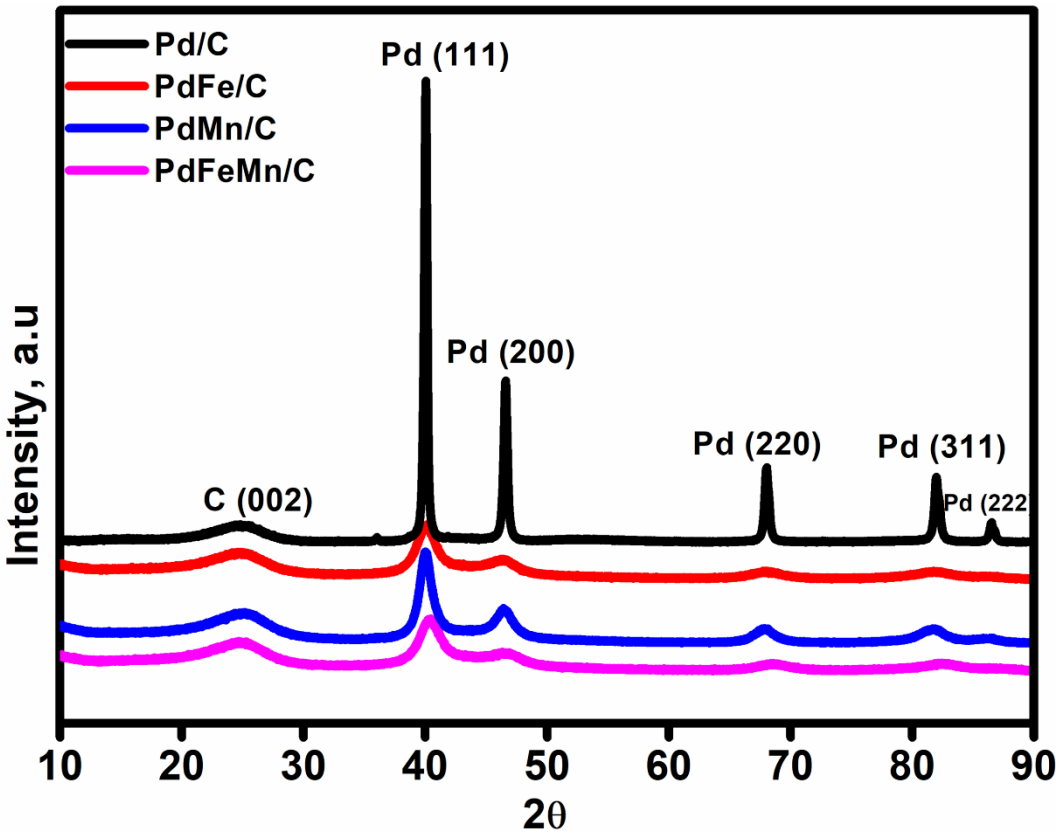


Figure. 9.1: XRD diffractogram of (a) Pd/C, PdFeC, PdMn/C and PdFeMn/C electrocatalysts.

The interplanar distance (d) of all the catalysts alongside lattice parameter (a) can be estimated according to the enlargement of the diffraction peaks of Pd (111) by following the Equation 9.1 of Scherrer formula and Vergard's law, respectively [13]:

$$D = \frac{K\lambda}{\beta Cos\theta} \quad (9.1)$$

Where D is the average diameter in nm, λ signifies the wavelength of X-ray (0.1542 nm), β is the corresponding full width at half maximum (FWHM) of the diffraction peak, and is the angle at the (111) peak position.

The trimetallic Pd-based electrocatalyst (PdFeMn/C) at the Pd (111) planes displayed slight shift to the higher 2Θ domain obviously over to those of bimetallic (PdFe/C and PdMn/C) and monometallic (Pd/C) electrocatalysts, which indicates the lattice contraction owing to the insertion of small-sized metals (mixture FeMn) in the Pd lattice [23]. For example, the lattice parameters (a) of PdFeMn/C (0.3872 nm) are smaller than those of PdFe/C (0.3891 nm), PdMn/C (0.3895 nm) and Pd/C (0.39005 nm), which indicates a high degree of alloying among the three metals [31, 32]. More interestingly, the attained crystalline size of PdFeMn/C (4.19 nm) is also smaller than those found for Pd/C (11.33 nm), PdFe/C (5.81 nm) and PdMn/C (8.59 nm) implying that 3d transition metals can slightly reduce the particle sizes of Pd/C. The d-spacing observed from the XRD data was confirmed to decrease from 0.2236 nm (PdFeMn/C) to 0.2247 nm (PdFe/C) after the insertion of Mn to PdFe/C substrate. The calculated crystallographic data of all the electrocatalysts are summarised in Table 9.2.

Table 9.2: XRD structure analysis of Pd-based electrocatalysts.

Electrocatalysts	2Θ	d-spacing Pd (111) (nm)	Lattice parameter. (nm)	Crystallite size (nm)
Pd/C	40.05	0.2249	0.3896	36.54
PdFe/C	40.05	0.2247	0.3891	5.81
PdMn/C	40.03	0.2242	0.3895	8.59
PdFeMn/C	40.31	0.2236	0.3872	4.19

9.2.2.2 X-Ray Photoelectron Spectroscopy

XPS spectra were conducted in this research to evaluate the oxidation state and binding energies of Pd, Fe, Mn, C and O surface from PdMn/C, PdFeC and PdFeMn/C electrocatalysts and as illustrated in Figure. 9.2 (a-c wide spectra). Two oxidation states were observed in the Pd 3d regions for all the electrocatalysts, as shown in Figure. 9.2d, 2e and 2f. The Pd 3d signs (deconvoluted into Pd and PdO_y ($0 < y < 2$) of PdMn/C, PdFe/C and PdFeMn/C are situated at around 335.0 eV (Pd $3d_{5/2}$) and 340.4 eV (Pd $3d_{3/2}$), 335.1 eV (Pd $3d_{5/2}$) and 340.5 eV (Pd $3d_{3/2}$), 335.2 eV (Pd $3d_{5/2}$) and 340.6 eV (Pd $3d_{3/2}$), respectively. The binding energy values of Pd $3d_{5/2}$ and Pd $3d_{3/2}$ are similar for all the electrocatalysts presented in this chapter and are assigned to metallic Pd (O) [33, 34].

Figure. 9.2j, 9.2k and 9.2l show the C1s deconvoluted in three varied spectra of PdMn/C, PdFeC and PdFeMn/C with binding energy values of 284.1 eV (C - C sp2), 285.0 eV (C – C sp3) and 285.9 eV (C – O), 284.2 eV (C – C sp2), 285.0 eV (C – C sp3) and 285.8 eV (C – O), sp2 C –C sp2 284.1 eV, 285.0 eV representing the sp3 belongs to C – C. Finally, the C-O has a value of 285.8 eV, respectively. C 1S indicates carbon binding on the surface of the electrocatalysts [10].

Figure. 9.2g, 9.2h and 9.2i shows the O1s deconvoluted with two different peaks of PdMn/C, PdFe/C and PdFeMn/C electrocatalysts with binding energy values of 529.5 eV (metal oxide) and 531.7 eV (C – O), 529.6 eV (metal oxide) and 531.7 eV (C – O), 529.5 eV (metal oxide) and 531.7 eV (C – O), respectively. The presence of O1s in all the stated electrocatalysts could be beneficial in producing the best electrolytic activities of EG, EOH, and Gly oxidation reaction as it can enhance the synergistic effect on the Pd active site.

Figure. 9.2m and 9.2n shows the peaks of PdFe/C and PdFeMn/C electrocatalysts with binding energy values of 711.4 eV (2p3/2 FeO) and 709.7 eV (2p3/2 FeO), respectively. Fe 2p3/2 indicates that the Fe element exists in the surface layer and is responsible for enhancing the synergistic effect of the electrocatalysts [34]. As for the third element (Mn) on PdFeMn/C electrocatalysts, no signature of the Mn^{2+} species was observed on the spectra, indicating that Mn loading was too small to be detected by XPS.

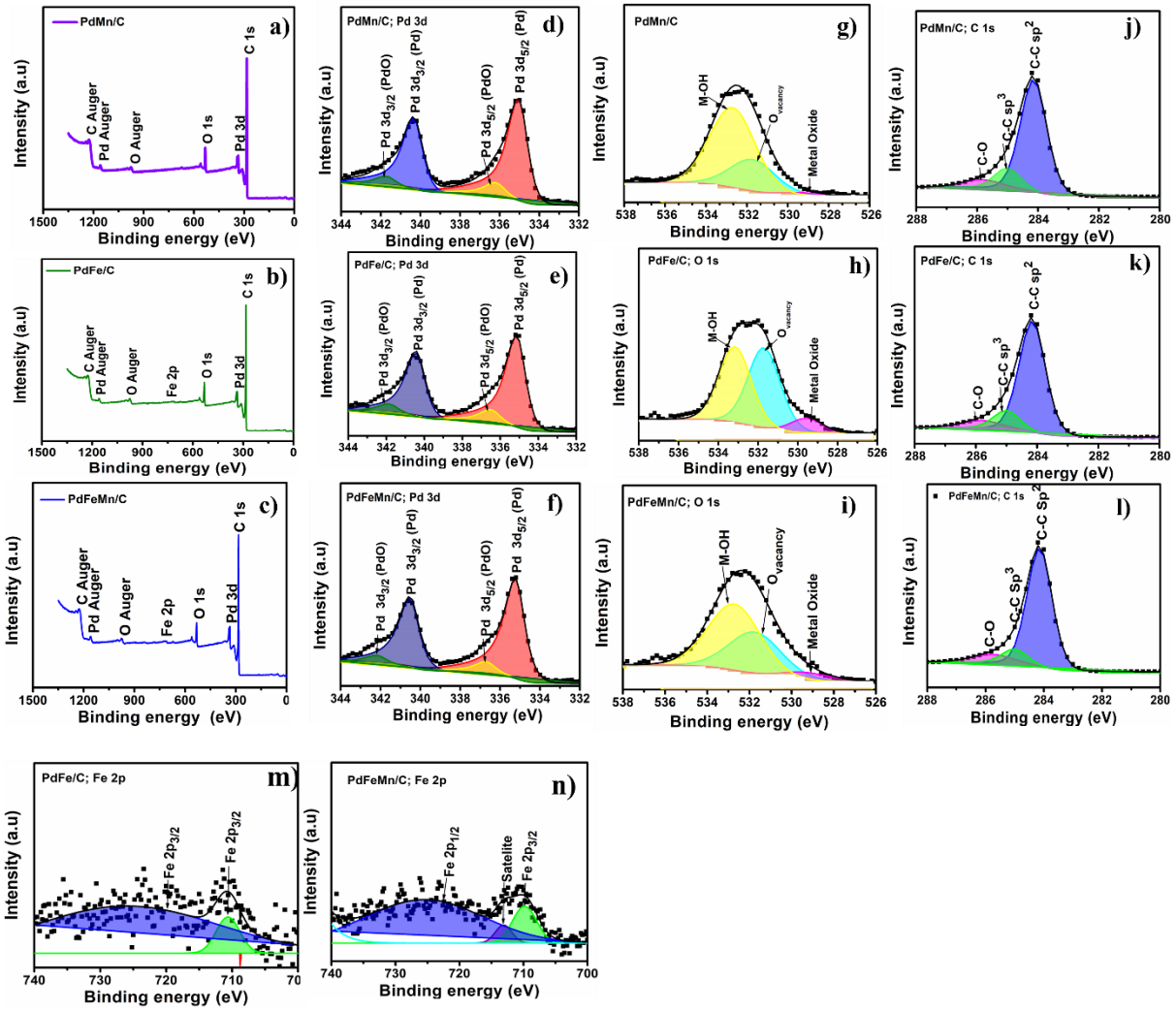


Figure 9.2: XPS spectra of a-c) with the wide survey spectra, deconvoluted elementals scans d-f) Pd 3d, g-i) O 1s, j-l) C 1s and m,n) Fe 2p of PdFeC, PdMn/C and PdFeMn/C electrocatalysts.

Figure. 9.3 illustrates the HRTEM images with particle size distribution histogram insert of a) Pd/C, b) PdFe/C, c) PdMn/C, and d) PdFeMn/C electrocatalysts. All electrocatalysts exhibit a remarkable homogeneous distribution and high dispersion of metals on a supported carbon matrix with particle sizes of sub-10 nm. The decrease of particle sizes after microwave treatment affirmed the tuning of the physicochemical properties of the electrocatalysts from micron to sub-10 nm [2]. Thus, the particle sizes obtained for all the electrocatalysts are almost in accordance with the crystalline size obtained from the XRD.

Figure. 9.3e and 9.3f exhibit a distinct lattice fringe alongside the interplanar distances (d) decreasing as follows: 0.2284 nm for PdFe/C, 0.2286 nm PdMn to 0.226 nm belongs to PdFeMn/C catalysts, indicating the (111) diffraction planes of the fcc Pd structure. The lattice fringes of PdFe/C were s compressed from 0.228 nm to 0.226 nm upon the insertion of Mn metal, which confirmed the lattice stress that occurred during the alloying process [35]. The SAED shows about 4 rings, which are analogs to those of XRD miller indices, emphasizing the development of polycrystalline features of the electrocatalysts [36]. The shorter the lattice fringes, the better the oxidation of alcohol.

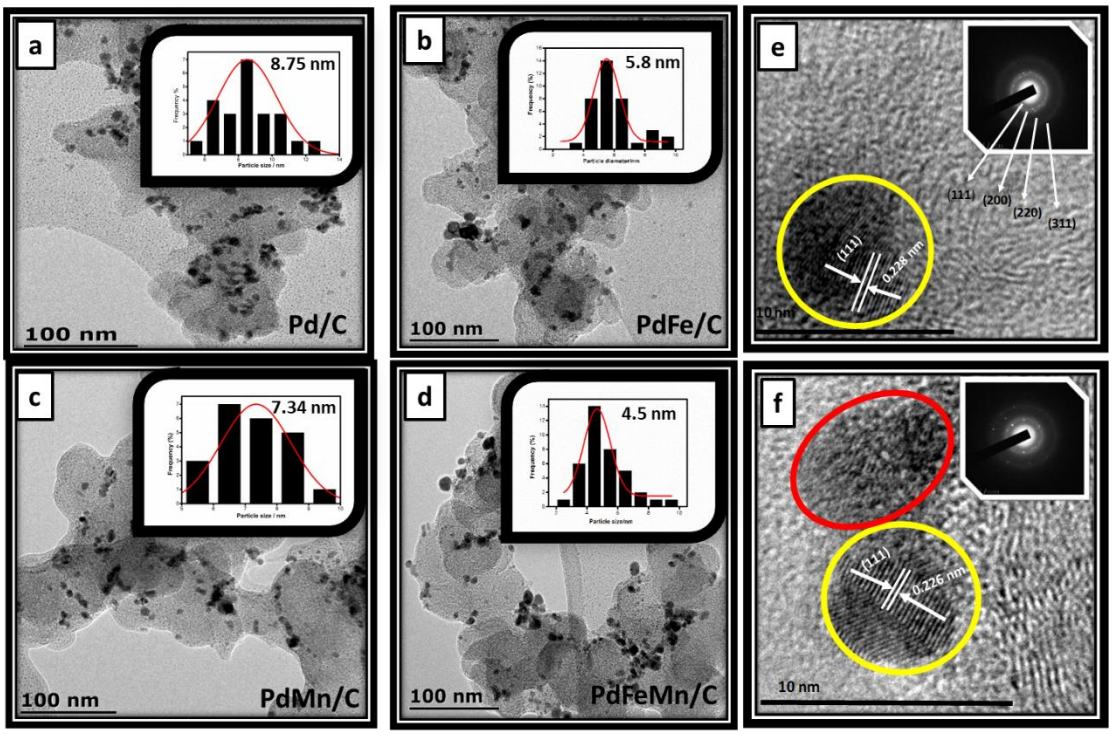


Figure 9.3: Comparative TEM images with particle size distribution histogram insert of (a) Pd/C, (b) PdFe/C, (c) PdMn/C, (d) PdFeMn/C; HRTEM with Insert in (e) and (f) show the SAED pattern of PdFe/C and PdFeMn/C.

9.2.3 Electrochemical measurements

9.2.3.1 CV studies in KOH electrolyte

Figure. 9.4 displays a cyclic voltammogram (CV) recorded on Pd/C, PdFe/C PdMn/C and PdFeMn/C electrocatalysts in purged N_2 saturated 0.5 M KOH solution at the scan rate of 50 mV/s. All the Pd-based electrocatalysts gave the expected signatures around (-0.8 V to -0.9 V vs. Ag/AgCl), 3 M KCl that may result from H_2 adsorption/desorption peaks occurred on the metal active site [200]. We further observed the prominent peaks at the cathodic peak potential from -0.35 V to -0.3 V, attributed to the palladium oxide (PdO) peak reduction in all the electrocatalysts. It can also be seen that the peak on the cathode side of the potentials displayed a positive shift upon the insertion of non-noble metals in comparison to Pd/C, which is indicative of the alteration in the electronic structure of PdFe/C, PdMn/C and PdFeMn/C. The PdO peaks were employed to estimate the ECSA of all the Pd-based catalysts towards the oxidation of EG in a basic medium, and the values are summarised in Table 9.3. The ECSA values were measured by integrating the Coulombic charge (Q) for the reduction of PdO using the following Equation 9.2 proposed by Rand and Wood and Ipadeola and co-workers [12, 37]:

$$ECSA = \frac{Q}{S.I} \qquad (9.2)$$

Where Q denotes the Coulombic charge in mC, S is a proportionality constant. (0.424 mC cm^{-2}) is assumed for the Pd monolayer, and I is the electrocatalyst loading measured in µg (0.2 µg).

The ECSA values were 15.90, 30.17, 25.10, 56.2 m^2/g of Pd/C, PdFe/C, PdMn/C and PdFeMn/C, respectively. The results mentioned above revealed that trimetallic PdFeMn/C electrocatalyst has a superior ECSA value compared to its counterparts, indicating the effect of adding one or two non-noble metals into Pd/C, which significantly lessens the rate of hydroxyl species adsorption on the Pd surface. Thus, the smaller particle sizes and higher ECSA value indicate the superior performance of the PdFeMn/C catalyst for the EGOR as compared to its bimetallic and monometallic counterparts.

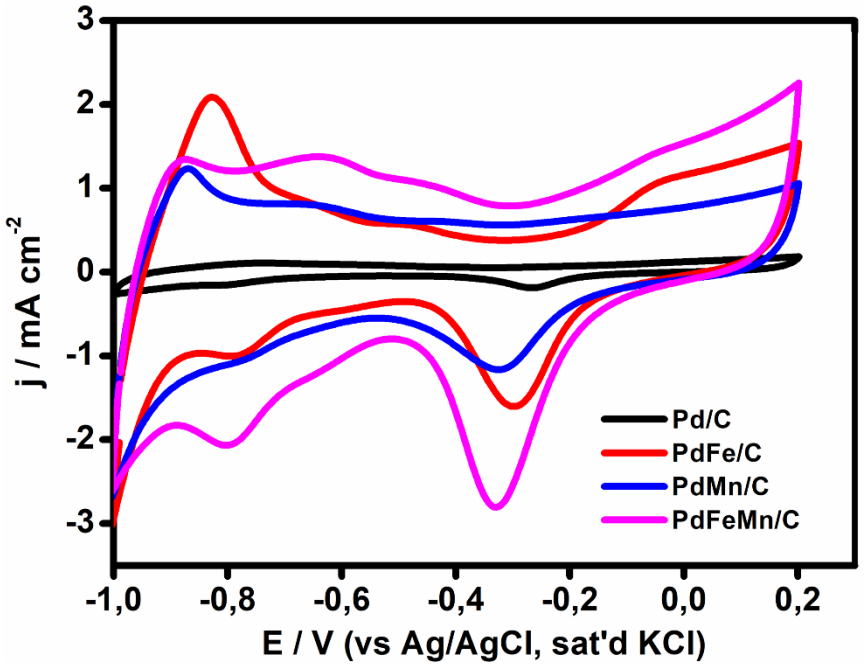


Figure 9.4: CV curves of catalysts in KOH (0.5 M), with 50 mV / s scan rate.

9.2.3.2 Cyclic Voltammetry in ethylene glycol

Table 9.3: The electrochemical parameters of Pd-based electrocatalysts toward EGOR.

Electrocatalysts	ECSA/ m^2/g	Onset potential (V)	E_p (V)	Ratio of J_f/J_b	SA (mA/cm^2)	MA (mA/mg)
Pd/C	15.90	-0.36	-0.1	1.26	1.35	250
PdFe/C	30.17	-0.46	-0.1	1.31	6.07	1160
PdMn/C	25.10	-0.46	-0.1	0.95	5.13	930
PdFeMn/C	56.27	-0.47	-0.1	1.35	7.26	1430

The CV technique was employed to affirm the electrocatalytic activities of the Pd/C, PdFe/C, PdMn/C, and PdFeMn/C electrocatalysts in 0.5 M KOH + 0.5 M EG bubbled in N_2 gas at the scan rate recorded to be 50 mV / s, as shown in Figure 9.5. All the CV curves display two characterized peaks ascribed to the forward and backward scans of the EGOR in alkaline media, as shown in Figure. 9.5. The forward scan represents the adsorption of the CO species formed on the Pd active site. In contrast, the reverse scan exemplifies the intermediate species not thoroughly oxidized during the forward scan [12, 37, 38]. The current density of the PdFeMn/C electrocatalyst is 5 times higher compared to a similarly treated pure Pd/C, which

emphasizes that the insertion of Mn and Fe can indeed enhance the activity of Pd/C towards EGOR.

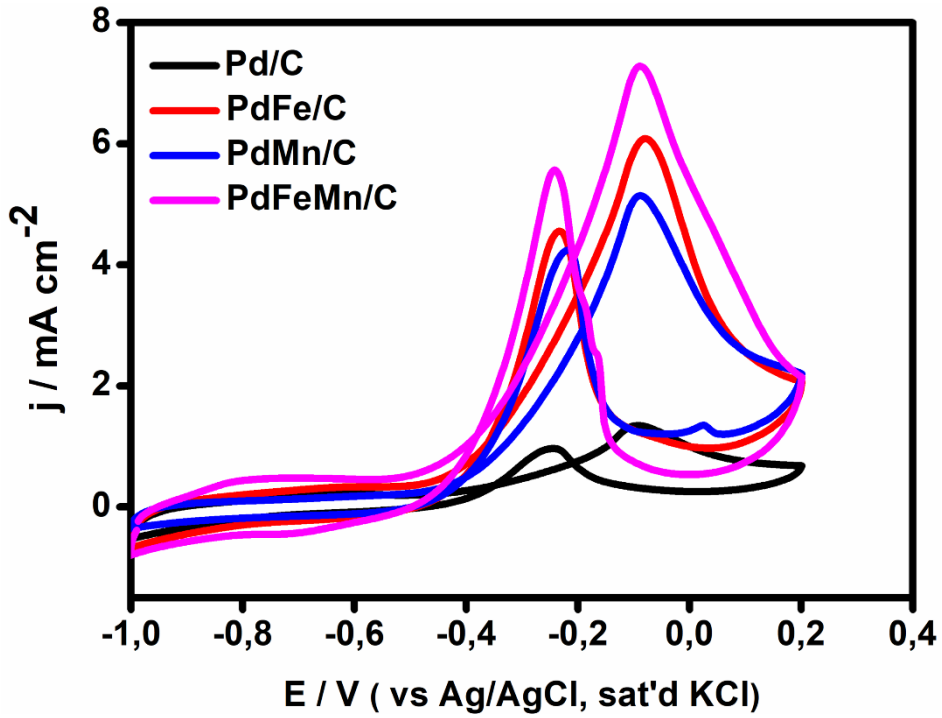


Figure 9.5: CV for EGOR on the electrocatalysts in 0.5 M KOH / EG, scan rate: 50 mV / s.

The PdFeMn/C (1430 mA mg^{-1}), PdFe/C (1160 mA mg^{-1}), and PdMn/C (930 mA mg^{-1}) also demonstrated the highest mass activity values, which are 5.7 times Pd/C, as shown in Figure 9.6 and summarised in Table 9.3. Further results reveal more negative onset potential of PdFeMn/C electrocatalyst, indicating rapid kinetics of PdFeMn/C electrocatalyst during EGOR; the data are summarised in Table 9.3. The PdFeMn/C electrocatalyst also displayed a higher value of J_f/J_b amongst all the electrocatalysts, which signifies a good tolerance towards carbonaceous species poisoning. The best performance of PdFeMn/C is due to incorporating Fe and Mn into pure Pd/C to help modulate the electronic and geometric structures, which predominantly enhances its EGOR activity and stability.

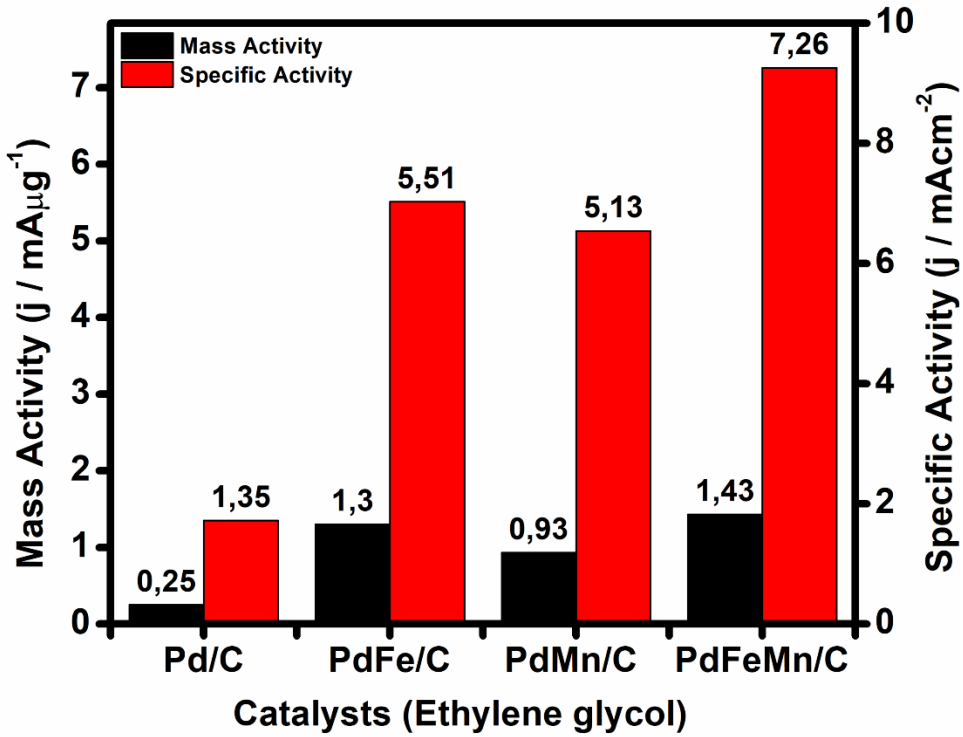


Figure 9.6: EGOR mass and specific activities of Pd, PdFeC, PdMn/C, and PdFeMn/C catalysts.

Figure. 9.7a, represent the linear sweep voltammograms (LSV) for EGOR on the Pd/C, PdFe/C, PdMn/C and PdFeMn/C electrocatalysts in 0.5 M KOH / EG at the scan rate of 1.0 mV / s. Figure. 9.7b shows the Tafel plots (η vs. $logj/mA\ cm^{-2}$) describes the reaction mechanism and kinetics captured from the quasi-steady state curve, fitted using Equation 9.3.

$$\eta = a + b\,log\,j \tag{9.3}$$

Where η is overpotential (the difference between the electrode and the standard electrode potentials ($\eta = E - E^{o}$)), a is a Tafel constant, b is the Tafel slope and j signifies the current density.

$$b = \frac{2.303RT}{(1-\alpha)nF} \tag{9.4}$$

Where α is the transfer coefficient, F is the Faraday constant, R is the universal gas constant, and T is the absolute temperature.

The Tafel slope values at lower potentials range from -0.65 V to -0.4 V are 167, 121, 124, 108 mV dec^{-1} for Pd/C, PdFe/C, PdMn/C, and PdFeMn/C, respectively. The PdFeMn/C electrocatalyst reveals the slightest Tafel slope compared to Pd/C, PdMn/C, and PdFe/C, suggesting the fast charge transfer kinetics of the EGOR in a basic environment. The slopes are almost identical (i.e., closed values range), indicating the exact EGOR reaction mechanism or rate-determining step at various potential regions. Liang and co-workers 2009 reported the same observation, highlighting that at a lower potential, between -0.6 V to -0.4 V, the kinetics of the alcohol oxidation reaction are dominated by the hydroxyl from co-metals to Pd electrode [39].

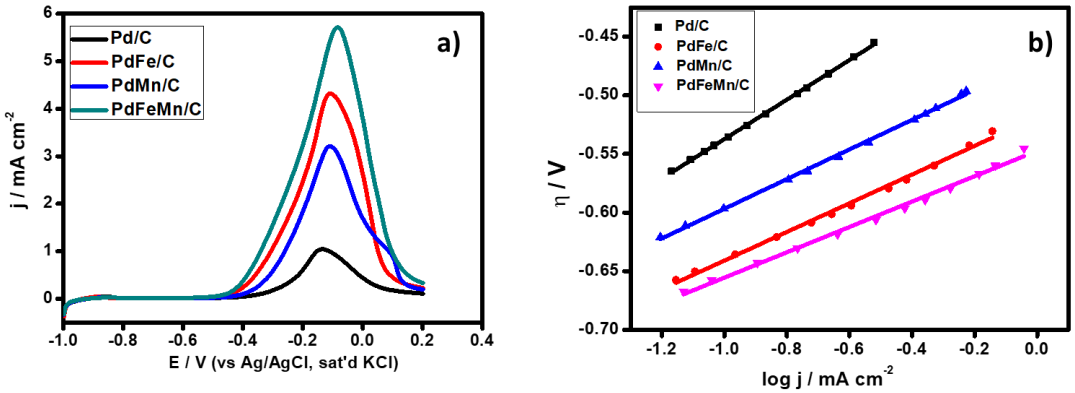


Figure 9.7: a) The LSV and (b) Tafel plots towards EGOR on the Pd/C, PdFe/C, PdMn/C and PdFeMn/C, EG, Scan rate of 1.0 mV / s.

Figure. 9.8 (a - b) displays the LSV of the Pd/C and PdFeMn/C electrocatalysts investigated in the mixture of 0.5 M KOH/ 0.5 M EG at varied scan rates. The LSV shows that all the electrocatalysts' peak-specific current densities increase with the scan rate. In the electrochemical reaction, two mechanisms are presented: diffusion-controlled and capacitive behaviour and it is worth noting to observe the best dominating one. Hence, as shown in Figure 9.8c, we overlook the linear relationship between peak current density for the Pd/C and PdFeMn/C electrocatalysts' scan rate. 9.8c. The straight line (linear relationship) observed indicates that both Pd/C and PdFeMn/C electrocatalysts in EGOR are diffusion-controlled, and their mass transport is enhanced, as stipulated by Zhang and colleagues 2012 [40] and Wang and co-worker 2012 [41].

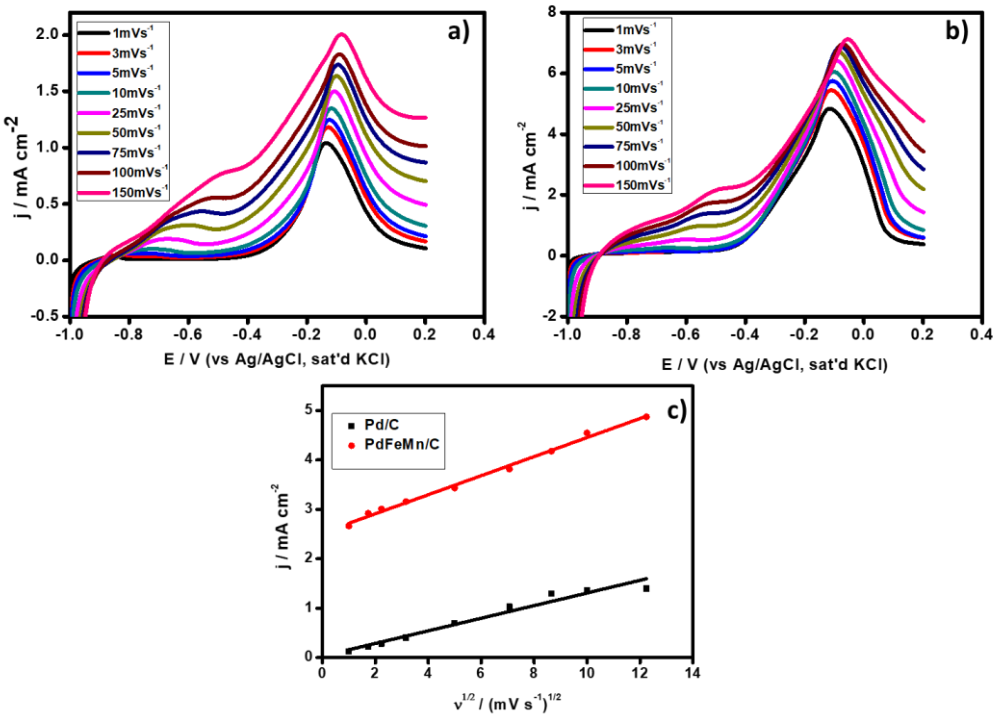


Figure 9.8: LSV of EGOR at the a) Pd/C and b) PdFeMn/C electrocatalysts at varied scan rates, c) Tafel plots of current density vs square root of the scan rate for both electrocatalysts, scan rate 1.0 mV / s.

9.2.3.3 The EG concentration on ethylene glycol oxidation

The effect of KOH and EG can have a dramatic influence on the reaction rate of EGOR. Figure. 9.9a displays the LSV of the PdFeMn/C electrocatalyst at a constant KOH concentration of 0.5 M and different EG concentrations at the scan rate of 1.0 mV / s. The increase in EG concentration influences the increase in the current density, ranging from 0.5 M to 2.0 M, indicating that EG's concentration is controlled by EG intermediates and OH^- species on the surface of the electrode. A sudden drop in peak current density was noticed when the EG concentration reached 3.0 M, attributed to the plethora of EG species and insufficient availability of OH^- ions on the electrode surface. It can be further elucidated that at high potentials, the adsorption of the EG intermediates dominates at the Pd active site, preventing hydroxyl ions from moving around the active area.

Thus, from this finding, it can be concluded that the activity and chemical kinetics of the PdFeMn/C electrocatalyst are lowered as they depend entirely on EG and OH^- species. The increase in current density also affected the potential of the electrocatalyst to shift positively

due to the mass transport and adsorbates built upon the surface of the active material. Likewise, the work performed by Wang and co-workers 2015 [16] observed the exact behaviour of increasing the EG concentration led to a decrease in peak current density.

Figure. 9.9b depicts the Tafel plot of PdFeMn/C electrocatalyst obtained from 0.5 M KOH with varied EG concentrations ranging from 0.25 M – 3.0 M. Thus when the concentration of EG is higher than 0.5 M, the slope is 130 mV dec^{-1}. When the EG concentration is below 0.5 M, the slopes increase to 150 mV dec^{-1}. This signifies those two reaction mechanisms of EGOR are observed and seem to favor the concentration of EG strongly. These observations agree with the work reported by Du and co-workers in 2012 [41].

Figure 9.9c shows the dependence of the logarithm of current densities against the logarithm of EG concentration for the PdFeMn/C electrocatalyst. Interestingly, the linear plot shows the sign of degradation of the Tafel slopes ranging from 237 -146 mV dec^{-1} when the potential rises.

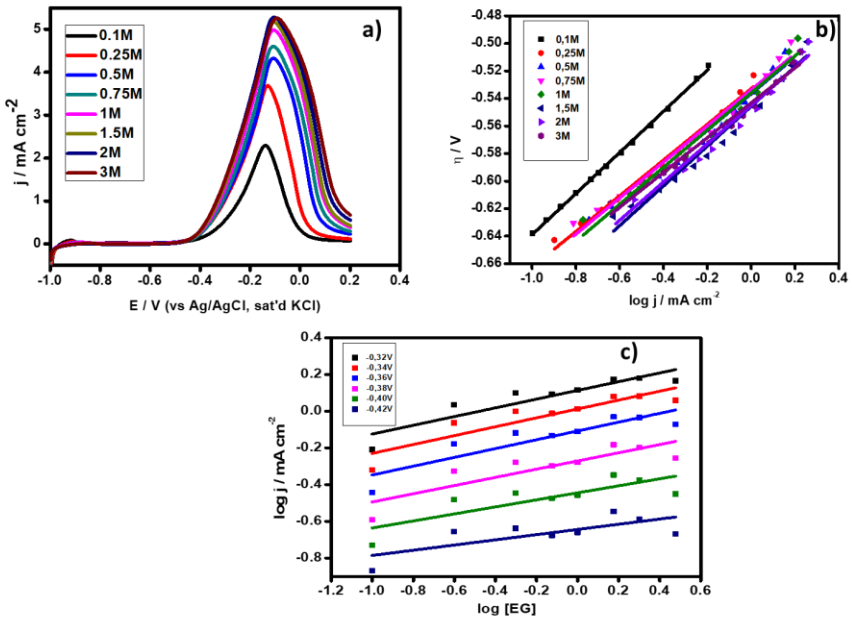


Figure 9.9: (a) LSV, (b) Tafel plot and (c) The log-log plot of current density vs EG concentration obtained for PdFeMn/C in 0.5 M KOH solution containing different EG concentration at scan rate: 1.0 mV / s.

9.2.3.4 The effect of KOH concentration on ethylene glycol oxidation

Figure. 9.10 illustrates the LSV of the EGOR on the PdFeMn/C electrocatalyst in 0.5 M EG solution containing KOH solution with varying concentrations ranging from 0.1 M to 3.0 M. A rapid increase in current density was depicted as the concentration of the KOH rises, indicating that there is a surplus of OH^- coverage (hydroxyl group) on the surface of Pd to aid in removing the EG intermediates during dissociative adsorption of EG. The remarkable increase of KOH at 3.0 M can enhance the kinetics of EGOR. However, a further increase in KOH concentration might reduce the number of sites of EG intermediate adsorption and result in poor performance, as imparted by An and colleagues 2010 [42]. A negative shift in peak potential was observed, which agrees with the notion that the greater availability of OH on the Pd surface has a favorable effect on EGOR.

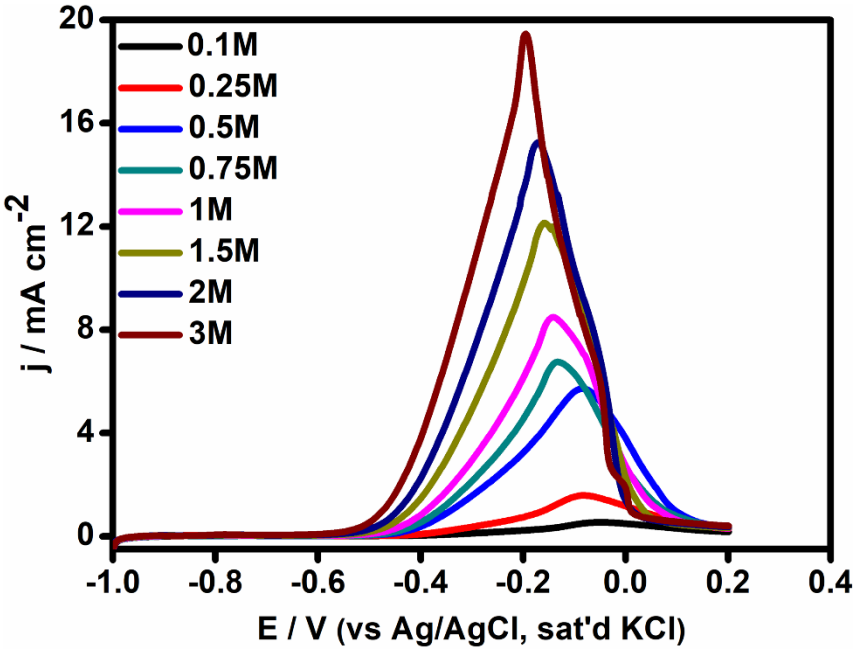


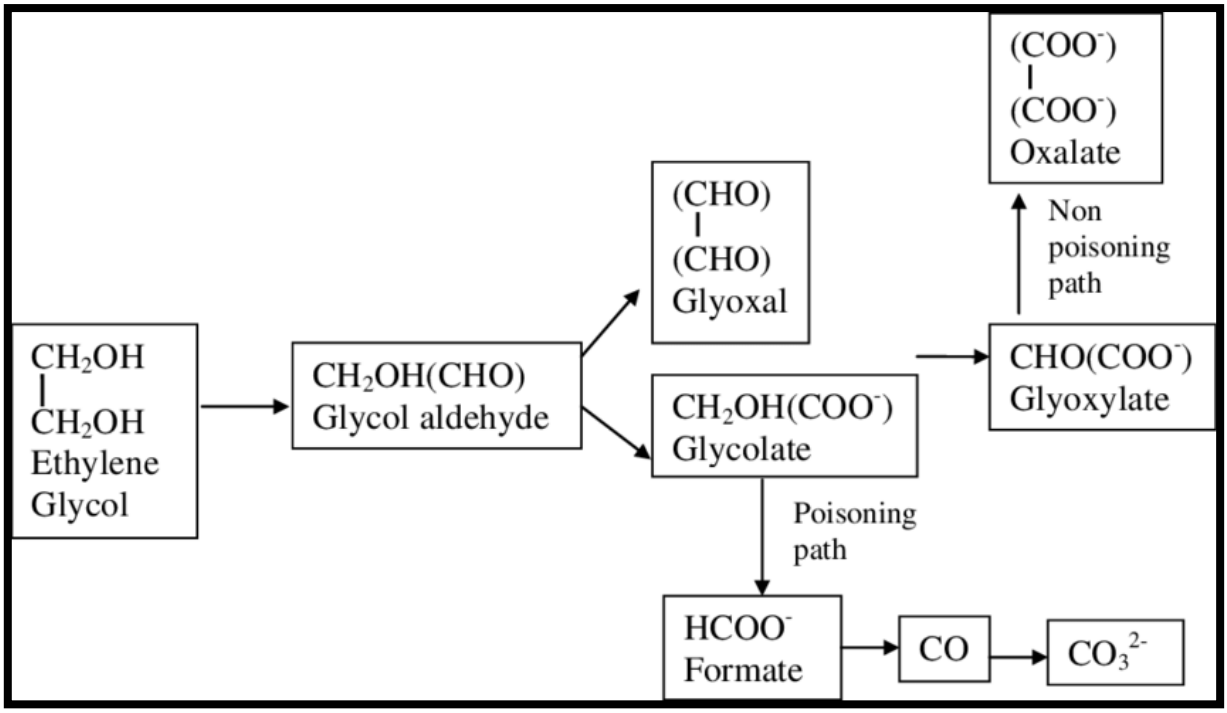
Figure 9.10: The LSV of the EGOR on the PdFeMn/C electrocatalysts in 0.5 M EG solution containing KOH solution of various concentrations. Scan rate: 1.0 mV / s.

9.2.3.5 Reaction pathways for EGOR over the PdFeMn/C

A catalytical surface reaction was evaluated to understand the effect of Mn and Fe in the PdFeMn/C electrocatalyst for EG electro-oxidation. Fe and Mn non-noble metals significantly decrease the onset potential and eliminate poisoning species through the so-called bi-functional

mechanism. According to a bi-functional mechanism, as stated before, the adsorption of oxygenous species such as hydroxyl ions occurs at a lower potential. Fe and Mn release it to oxidize CO_{ads} or adsorbed CO-like carbonaceous species on the Pd adjacent site [35]. Alloying Pd with Fe and Mn improves the oxidation of EG owing to a synergistic effect, making Pd sites accessible from carbonaceous species. By doing that, the stability and the activity are enhanced during the electro-oxidation of EG in an alkaline medium.

Previously, in the Tafel plot results, two mechanisms were observed, and this can be due to the presence of Fe and Mn in trimetallic and bimetallic Pd-based electrocatalysts. These findings foresee that Fe and Mn complement each other as they all serve an almost similar purpose on the catalysts' surface. Subsequently, Pd can dissociate EG into fragments and two parallel reaction pathways have been proposed [36, 43-45]: as shown in Scheme 9.1, the oxidation of EG is complex as it comprises a large variety of final reaction products. When EG interacts with the Pd surface, it oxidizes with one hydroxyl group to form glycolate and oxidizes to oxalate (non-poisoning path) and formate (poisoning route). The oxidation of oxalate, even though it is the formation of non-poisoning species, is not preferable to formate as it has the keen ability to break the C-C bond cleavage due to the more significant production of carbonate. Once the C-C bond's breakage is successful, the electrocatalysts are free from being attacked by poisonous species, and the electrocatalytic activity is ameliorated. The increase in current density proved this, the more favorable value of the ratio of the peak current density, and the onset potential is shifted negatively as well as high stability for electro-oxidation of PdFeMn/C in comparison to its bimetallic and monometallic counterparts.



Scheme 9.1 Schematic diagram for the illustration of reaction pathways for EG electro-oxidation in an alkaline medium [35]

9.2.3.6 Chronoamperometric analysis

A chronoamperometry test was conducted to investigate the stability factor and electrochemical activity of Pd/C, PdFe/C, PdMn/C, and PdFeMn/C in 0.5 M KOH and 0.5 M EG solutions at a constant potential of -0.2 V vs. Ag/AgCl, sat'd KCl, as shown in Figure. 9.11. A sharp descent in the current densities with time, notably for all the electrocatalysts, was observed at the initial stage, thus illustrating the poisoning of the electrocatalysts by chemisorbed carbonaceous species impeding the adsorption and oxidation of ethylene glycol [2, 20, 25, 26]. After this stage, all the electrocatalysts retained their current densities at a pseudo-steady state until the 1800s. In this stage, the adsorbed hydroxyl ions and oxygenated species sustain their relative balance by removing all the intermediate species on adjacent Pd sites. A higher current density of PdFeMn/C was depicted, demonstrating the best electro-catalytic durability towards the EG oxidation reaction compared to their counterparts. This is in accord with all the measurements performed on the electrocatalysts.

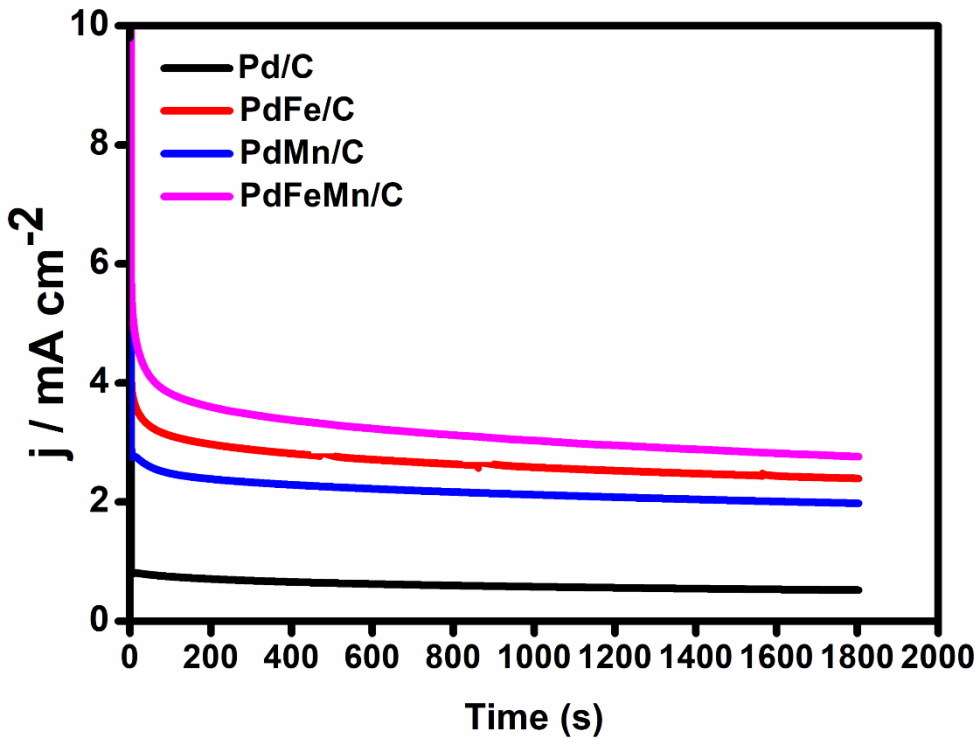


Figure 9.11: Chronoamperometric curves of Pd/C, PdFe/C, PdMn/C and PdFeMn/C in 0.5 M KOH / EG solutions at -0.2 V.

9.2.3.7 Electrochemical Impedance Measurements

EIS was used to elucidate the interfacial electrochemical response of the catalysts in a mixture of EG and supporting electrolytes in the Nyquist plots shown in (Figure. 9.12a). Figure. 9.12b shows the electrical equivalent circuit (EEC) used in fitting the impedance spectra (Nyquist plots) into appropriate parameters, where R_s is the electrolyte resistance, R_{ct} is the charge transfer resistance and CPE is the constant phase element, as illustrated by Ramulifho and co-workers 2012 [46].

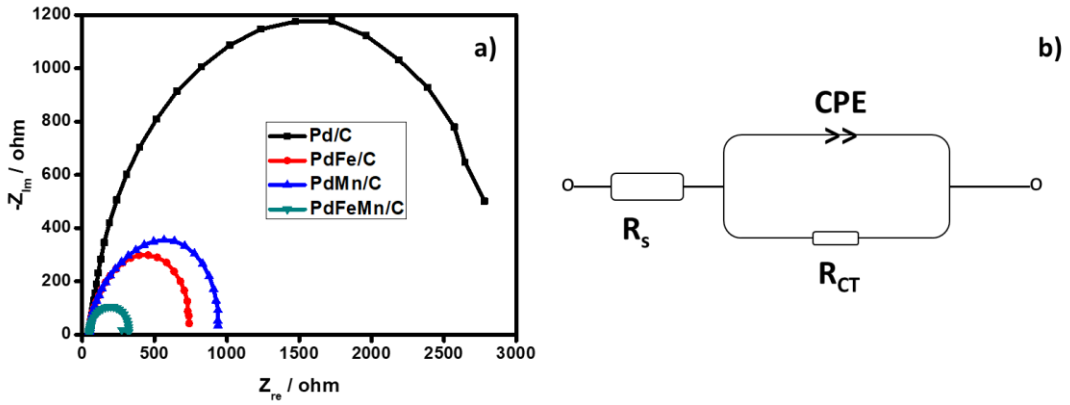


Figure 9.12: (a) Nyquist curves of electrocatalysts at -0.2 V, b) the EEC used in fitting the spectra.

Table 9.4 summarises the electrochemical impedance parameters, and the diameter of the semicircles corresponds to the value of the R_{ct}, which best explains the kinetics of the EGOR on the electrodes. As depicted, PdFeMn/C has a lower value of R_{ct}, indicating the rapid degree of ethylene glycol electro-oxidation and excellent electro-catalytic behaviour compared to its counterparts. These results can further exemplify the faster electron transfer of ethylene glycol oxidation on PdFeMn/C electrocatalysts. In addition, the PdFeMn/C has the lowest R_s value amongst the electrocatalysts in this work. This explains its improved ionic conductivity in the mixture of EG and supporting electrolytes, amongst other electrocatalysts. However, the PdFeMn/C exhibits a higher CPE value than the bimetallic and monometallic counterparts, revealing its ability to store more charges during the EGOR, and the ideality values (n < 1.0) for all the electrocatalysts confirm their pseudo-capacitive behaviour.

Table 9.4: Electrochemical Impedimetric data for EGOR on Pd/C, PdMn/C, PdFe/C and PdFeMn/C catalysts.

	EIS parameters			
	R_s (Ω)	R_{ct} (kΩ))	*N*	*CPE* (F.s$^{(1-n)}$) x 10^2
PdC	49.30 ± 0.55	2.92 ± 0.001	0.87	0.13 ± 0.001
PdFeC	46.10 ± 0.43	0.73 ± 0.001	0.88	0.28 ± 0.002
PdMnC	48.20 ± 0.69	0.92 ± 0.001	0.84	0.18 ± 0.003
PdFeMnC	45.33 ± 0.43	0.27 ± 0.001	0.87	0.43 ± 0.003

9.2.3.8 Linear sweep voltammograms: oxygen reduction reaction

Figure 9.13. Exhibits the LSV of Pd/C, PdFe/C, PdMn/C and PdFeMn/C electrocatalysts in (0.1 M KOH) electrolyte purged with O_2 at the scan rate of 10 mV/s with rotating speed varied from 400 to 4000 rpm. It is noticeable that the limiting current density at the diffusion-dominated potential range of all the as-prepared electrocatalysts appeared to increase as the rotating speed increased, indicating that a mass transport limit is occurring at the higher overpotential [47, 48].

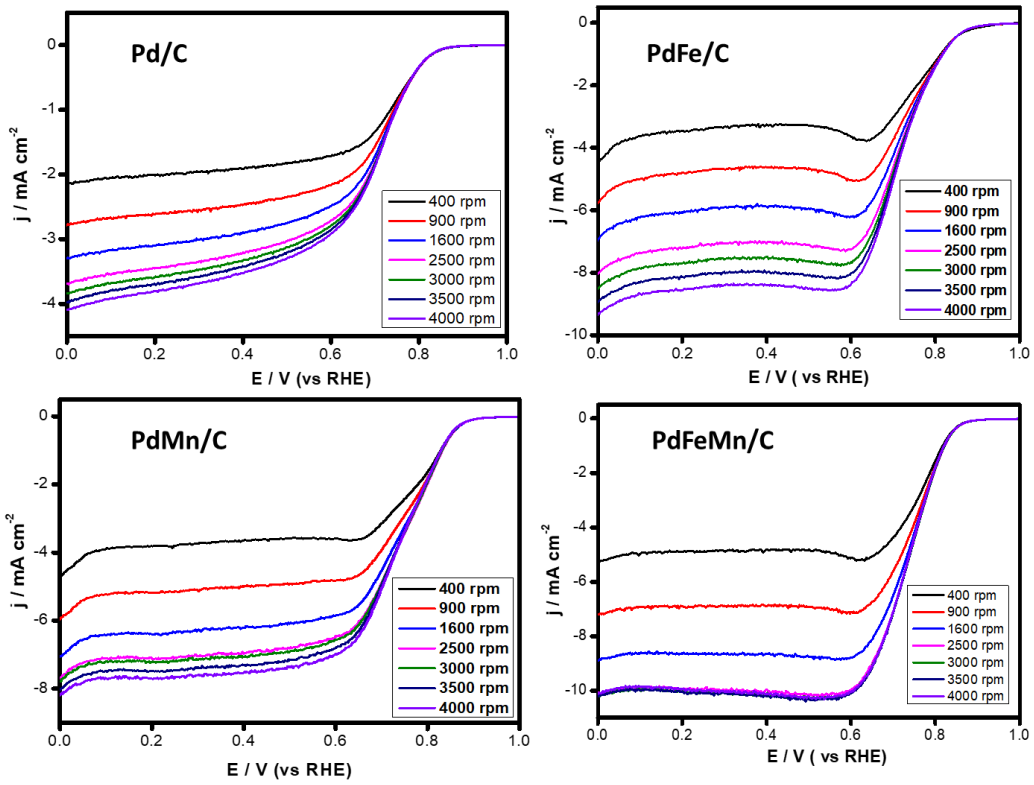


Figure 9.13: ORR polarisation curves of Pd/C, PdFe/C, PdMn/C and PdFeMn/C electrocatalysts in 0.1 M KOH electrolyte purged with O_2 at the scan rate 10 mV / s with rotating speeds from 400 to 4000 rpm.

Figure 9.14. Displayed the ORR polarisation curves for comparison purposes of Pd/C, PdFe/C, PdMn/C, and PdFeMn/C electrocatalysts measured at 1600 rpm in 0.1 M KOH solution, scan rate of 10 mV / s. It is seen from the curve that the onset potential of PdFeMn/C is higher than

that of its counterparts. The catalysts increasing trend of the onset potential is as follows: PdFeMn/C > PdFe/C > PdMn/C > Pd/C.

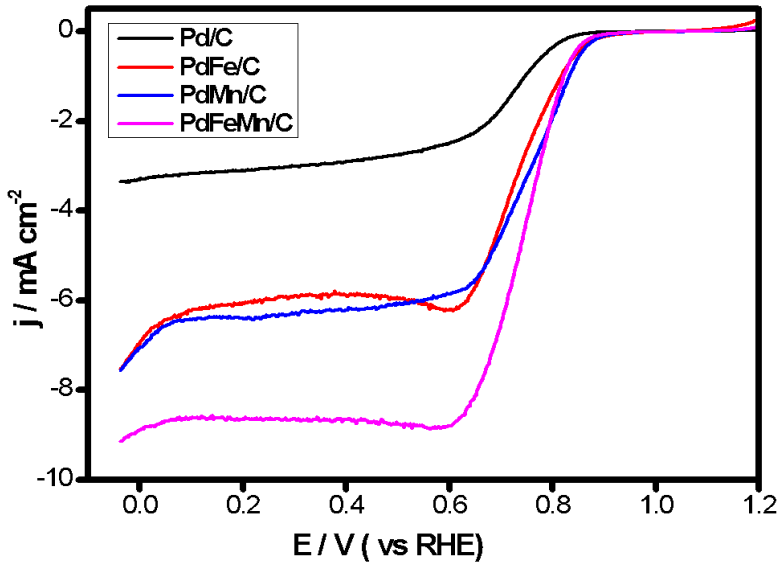


Figure 9.14: The ORR polarisation curves compare the electrocatalysts measured at 1600 rpm.

Figure 9.15. The ORR polarisation curves exhibited using Koutecky-Levich (K-L) at different potentials are analyzed. The K-L, in this instance, was utilised to obtain the number of electrons transferred per O_2 molecule determined during the ORR process [49, 50]. The number of electrons was estimated using the following K-L Equation 9.5:

$$\frac{1}{j} = \frac{1}{j_k} + \frac{1}{j_d} = -\frac{1}{nFkC_{O2}} - \frac{1}{0.62nFD_{O2}^{\frac{2}{3}}\upsilon^{-1/6}C_{O2}\omega^{1/2}} \qquad (9.5)$$

Where j, j_k, and j_d measured the current density, kinetics and diffusion-limited current densities, respectively, n is the number of electrons transferred per O_2 molecule, F is the Faraday constant of 96,485 C mol^{-1}, k is the rate constant for O_2 reduction, D_{O2} is the diffusion coefficient of O_2 (1.93 x 10-5 cm^2 s^{-1}), υ is the kinematic viscosity of the solution (0.01 cm^2 s^{-1}), and ω is the electrode rotation rate (rad s^{-1}) [49, 51]. The overall n value of Pd/C, PdFe/C, PdMn/C and PdFeMn/C electrocatalysts were calculated to be 3.15, 3.36, 3.66, and 3.28, correspondingly. The bimetallic and trimetallic electrocatalysts were observed to have a superior value of n over Pd/C, indicating the 4-electron transfer is more favored towards ORR

over Pd/C. Therefore, it can be deduced that adding one or two co-metals severely influences the number of electrons towards ORR [52].

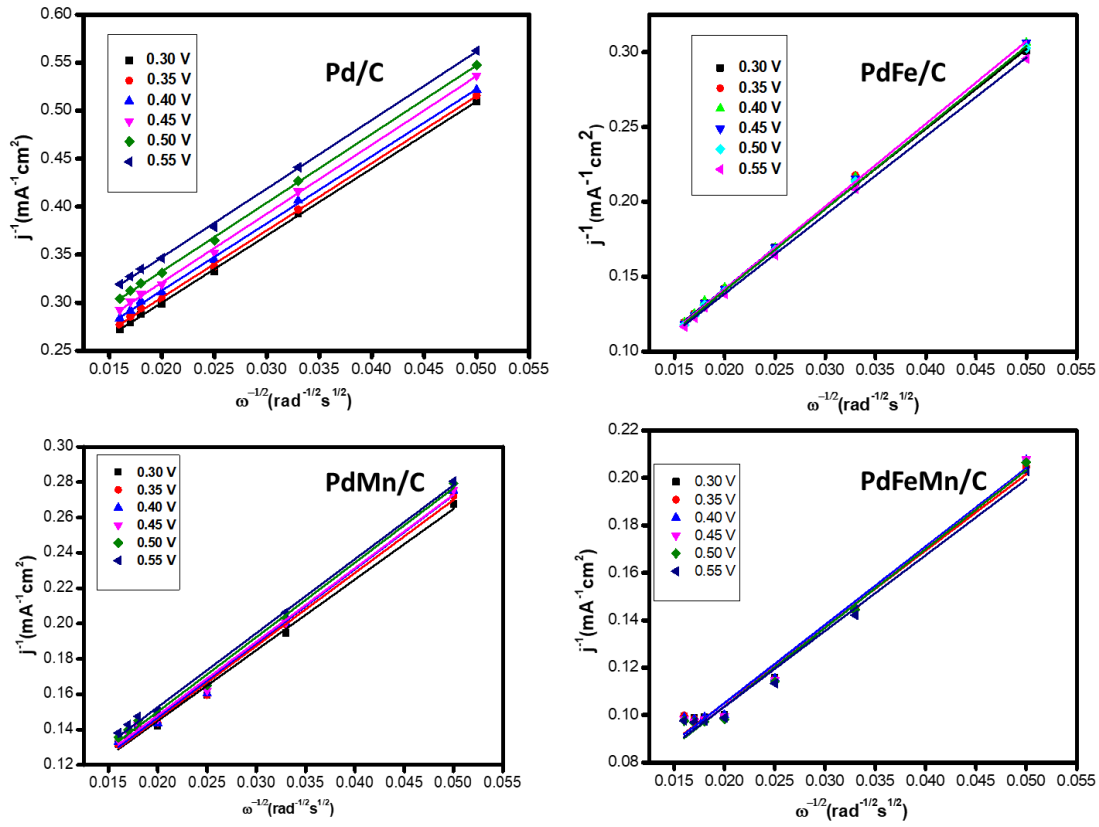


Figure 9.15: Koutecky-Levich Plots of ORR polarisation curves of electrocatalysts taken at varied potentials (0.3, 0.35, 0.40, 0.45. 0.50, 0.55 V vs RHE).

9.3 Conclusions

In this research work, carbon-supported trimetallic ferromanganese alloys, bimetallic and monometallic Pd-based electrocatalysts (PdFeMn/C, PdFeC, PdMn/C, and Pd/C) were synthesised via a facile two-step MW method. The adopted synthetic approach on all the electrocatalysts yielded a uniform homogeneous distribution on the support material, displayed a polycrystalline nature, and a small particle size distribution of about 5 nm. The electrocatalytic performance was examined for EGOR in the basic medium using CV, LSV, CA, and EIS. The PdFeMn/C electrocatalyst exhibited high activity and excellent stability towards the oxidation of EG due to the electronic structure and bi-functional mechanism upon the insertion of Fe-Mn unto Pd/C, amongst other electrocatalysts. The effect of EG

concentration ranges from 0.1 M to 3.0 M at fixed hydroxyl (OH^-) ion concentration shows the decrease in current density when the concentration is increased to 3.0 M and when the OH^- ion is varied at fixed EG concentration.

These results reveal that the EG oxidation reaction is of first order to both OH^- and EG. After that, the best two electrocatalysts (PdFe/C and PdFeMn/C) were explored as anode materials and tested for the proof-of-concept in the two-electrode configuration with the micro-3D printed cell, where the PdFeMn/C delivered improved micro-ethylene glycol fuel cell activity with respective to high power density and galvanostatic stability. The ORR studies for Pd/C, PdFe/C, PdMn/C and PdFeMn/C electrocatalysts were investigated in alkaline medium. The electrocatalytic activity of Pd/C was improved by adding co-metals, resulting in a higher onset potential and higher n value. The satisfactory results show how exploiting PdFeMn/C electrocatalyst is a promising candidate for developing high-performance direct ethylene glycol fuel cells and ORR performance.

9.4 References

[1] J.M. Sieben, M.M.E. Duarte, International Journal of Hydrogen Energy. 36 (2011) 3313-3321.

[2] O.O. Fashedemi, K.I. Ozoemena, Electrochimica Acta. 128 (2014) 279-286.

[3] A. Falase, M. Main, K. Garcia, A. Serov, C. Lau, P. Atanassov, Electrochimica Acta. 66 (2012) 295 - 301.

[4] C. Wen, Y. Wei, D. Tang, B. Sa, T. Zhang, C. Chen, Scientific reports. 7 (2017) 4907.

[5] T. Ramulifho, K.I. Ozoemena, R.M. Modibedi, C.J. Jafta, M.K. Mathe, Electrochimica Acta. 59 (2012) 310 - 320.

[6] C. Bianchini, P.K. Shen, Chem. Rev. 109 (2009) 4183.

[7] L. Xin, Z. Zhang, J. Qi, D. Chadderdon, W. Li, Applied Catalysis B: Environmental. 125 (2012) 85 - 94.

[8] S. Beyhan, K. Uosaki, J.M. Feliu, E. Herrero, Journal of Electroanalytical Chemistry. 707 (2013) 89 - 94.

[9] R.S. Amin, R.M. Abdel Hameed, K.M. El-Khatib, M. Elsayed Youssef, International Journal of Hydrogen Energy. 39 (2014) 2026 - 2041.

[10] A.K. Ipadeola, N.Z. Lisa Mathebula, M.V. Pagliaro, H.A. Miller, F. Vizza, V. Davies, Q. Jia, F. Marken, K.I. Ozoemena, ACS Applied Energy Materials. 3 (2020) 8786 - 8802.

[11] H. Rostami, A. Omrani, A.A. Rostami, International Journal of Hydrogen Energy. 40 (2015) 9444 - 9451.

[12] F. Fathirad, A. Mostafavi, D. Afzali, International Journal of Hydrogen Energy. 42 (2017) 3215 - 3221.

[13] R.M. Modibedi, T. Masombuka, M.K. Mathe, International Journal of Hydrogen Energy. 36 (2011) 4664 - 4672.

[14] F. Zhu, G. Ma, Z. Bai, R. Hang, B. Tang, Z. Zhang, X. Wang, Journal of Power Sources. 242 (2013) 610 - 620.

[15] Y. Huang, Y. Guo, Y. Wang, J. Yao, International Journal of Hydrogen Energy. 39 (2014) 4274 - 4281.

[16] W. Wang, D. Chai, Y. Yang, Y. Liu, Y. Kang, Z. Lei, International Journal of Hydrogen Energy. 40 (2015) 10041-10048.

[17] H. Xu, B. Yan, K. Zhang, J. Wang, S. Li, C. Wang, Y. Du, P. Yang, Electrochimica Acta. 261 (2018) 521- 529.

[18] A. Chen, C. Ostrom, Chemical Reviews 115 (2015) 11999 - 12044.

[19] L. Demarconnay, S. Brimaud, C. Coutanceau, J.M. Léger, Journal of Electroanalytical Chemistry. 601 (2007) 169-180.

[20] T. Li, Y. Huang, K. Ding, P. Wu, S.C. Abbas, M.A. Ghausi, T. Zhang, Y. Wang, Electrochimica Acta. 191 (2016) 940-945.

[21] A. Marchionni, M. Bevilacqua, C. Bianchini, Y. Chen, J. Filippi, P. Fornasiero, A. Lavacchi, H. Miller, L. Wang, F. Vizza, ChemSusChem. 6 (2013) 518-528.

[22] S. Song, Y. Wang, P. Tsiakaras, P.K. Shen, Applied Catalysis B: Environmental. 78 (2008) 381-387.

[23] C. Venkateswara Rao, B. Viswanathan, The Journal of Physical Chemistry C. 113 (2009) 18907-18913.

[24] M.A. Matin, J. Jang, Y. Kwon, Journal of Power Sources. 262 (2014) 356-363.

[25] K. Mohanraju, L. Cindrella, International Journal of Hydrogen Energy. 41 (2016) 9320-9331.

[26] M. Rethinasabapathy, S. Kang, Y. Haldorai, M. Jankiraman, N. Jonna, S.R. Choe, Y.S. Huh, B. Natesan, International Journal of Hydrogen Energy. 42 (2017) 30738-30749.

[27] J.A. Gerbec, D. Magana, A. Washington, G.F. Strouse, Journal of the American Chemical Society. 127 (2005) 15791-15800.

[28] Z. Moorhead-Rosenberg, K.L. Harrison, T. Turner, A. Manthiram, Inorganic Chemistry.52 (2013) 13087-13093.

[29] R. Wang, S. Liao, H. Liu, H. Meng, Journal of Power Sources. 171 (2007) 471-476.

[30] J. Goel, S. Basu, International Journal of Hydrogen Energy. 39 (2014) 15956-15966.

[31] R. Ahmadi, M.K. Amini, J.C. Bennett, Journal of Catalysis. 292 (2012) 81-89.

[32] S. Hu, F. Munoz, J. Noborikawa, J. Haan, L. Scudiero, S. Ha, Applied Catalysis B: Environmental. 180 (2016) 758-765.

[33] H. Lv, H. Zhao, T. Cao, L. Qian, Y. Wang, G. Zhao, Journal of Molecular Catalysis A: Chemical. 400 (2015) 81-89.

[34] S. Yang, J. Dong, Z. Yao, C. Shen, X. Shi, Y. Tian, S. Lin, X. Zhang, Scientific reports. 4 (2014) 4501.

[35] E.H. Yu, U. Krewer, K. Scott, Energies. 3 (2010) 1499-1528.

[36] K. Matsuoka, Y. Iriyama, T. Abe, M. Matsuoka, Z. Ogumi, Electrochimica Acta. 51 (2005) 1085-1090.

[37] A.K. Ipadeola, R. Barik, S.C. Ray, K.I. Ozoemena, Electrocatalysis (2019) 1-15.

[38] H. Huang, X. Hu, J. Zhang, N. Su, J. Cheng, Scientific reports. 7 (2017) 45555.

[39] Z.X. Liang, T.S. Zhao, J.B. Xu, L.D. Zhu, Electrochimica Acta. 54 (2009) 2203-2208.

[40] M. Zhang, Z. Yan, J. Xie, Electrochimica Acta. 77 (2012) 237-243.

[41] W. Du, K.E. Mackenzie, D.F. Milano, N.A. Deskins, D. Su, X. Teng, Acs Catalysis. 2 (2012) 287-297.

[42] L. An, T.S. Zhao, S.Y. Shen, Q.X. Wu, R. Chen, International Journal of Hydrogen Energy. 35 (2010) 4329-4335.

[43] O.O. Fashedemi, H.A. Miller, A. Marchionni, F. Vizza, K.I. Ozoemena, Journal of Materials Chemistry A. 3 (2015) 7145-7156.

[44] Z. Guo, X. Kang, X. Zheng, J. Huang, S. Chen, Journal of Catalysis. 374 (2019) 101-109.

[45] Y. Chen, X. Zheng, X. Huang, A. Wang, Q. Zhang, H. Huang, J. Feng, Journal of Colloid and Interface Science. 559 (2020) 206-214.

[46] T. Ramulifho, K.I. Ozoemena, R.M. Modibedi, C.J. Jafta, M.K. Mathe, Electrochimica Acta. 59 (2012) 310-320.

[47] J. Qiao, L. Xu, L. Ding, P. Shi, L. Zhang, R. Baker, J. Zhang, International Journal of Electrochemical Science 8 (2013) 1189.

[48] A.C. Queiroz, Lima, Fabio Henrique Barros de, Journal of Electroanalytical Chemistry. 707 (2013) 142-150.

[49] M.S. Matseke, T.S. Munonde, K. Mallick, H. Zheng, Electrocatalysis. 10 (2019) 436-444

[50] Y.H. Xue, L. Zhang, W.J. Zhou, S.H. Chan, International Journal of Hydrogen Energy. 39 (2014) 8449-8456.

[51] J. Kim, T. Momma, T. Osaka, Journal of Power Sources. 189 (2009) 909-915

CHAPTER 10

CONCLUSIONS AND RECOMMENDATIONS

10.1 Introduction

This chapter describes the overall conclusions of all the results obtained during the study and recommends future work.

10.2 Conclusions

Microwave-induced defective PdFe/C nano-electrocatalyst for highly efficient alkaline glycerol oxidation reactions.

- Pd-based mono- and bi-metallic nano-electrocatalysts were successfully synthesised using two methods for comparison study: microwave solvothermal method and conventional sodium borohydride process.
- During the comparative study of two different methods, the microwaved synthetic method proved highly effective for synthesizing Pd/C and PdFe/C nano-electrocatalysts. This was confirmed by physicochemical analysis, high crystalline structure, and superior electrochemical behaviour of both nano-electrocatalysts.
- The importance of the co-metal in Pd/C was investigated via GOR in an alkaline medium. It was confirmed by DFT simulation that the bimetallic nano-electrocatalysts increased the electron density over pure Pd. Even the electrochemical study showed that incorporating Fe into Pd/C led to a high-density response, less susceptibility to poisoning, and higher conductivity.

Interrogating the effect of microwave irradiation for the synthesis of bi-metallics nano-electrocatalysts towards EOR

- The effect of microwave irradiation on Pd/C, PdFe/C, PdMn/C, and PdCo/C nano-electrocatalysts were investigated at different ratio studies (Pd_2M/C and PdM/C).
- The effect was observed during the increase in the crystalline nature of the nano-electrocatalysts and the smaller particle sizes of the catalysts after treatment with a microwave.
- Albeit all the bi-metallics gave powerful electrochemical responses to EOR. However, the importance of the ratio was taken into consideration. The bi-metallics nano-electrocatalysts treated at Pd_2M/C ratio have confirmed their superior electrocatalytic response as opposed to PdM/C bimetallics.

Electrochemical activities of Palladium-based bi-metallic nano-electrocatalysts towards ethylene glycol oxidation in alkaline medium

- The influence of the co-metals on Pd/C was probed for ethylene glycol electrooxidation in an alkaline medium.
- It was observed that Pd_2M/C of PdFe/C PdMn/C and PdCo/C nano-electrocatalysts have greatly improved the electrocatalytic response towards EGOR in alkaline medium over PdM/C.
- The DFT simulation predicted that PdMn would be the best electrocatalyst for EG. It should be noted that the performance of the electrocatalysts depends on several factors (such as particle size, ECSA, mA, SA morphology, porosity, etc.), and DFT calculations in this work did not consider any of these factors. Thus, this discrepancy may be related to the poor ECSA of the PdMn (~ 17 $m^2 g^{-1}$) compared to the PdFe (> 30 $m^2 g^{-1}$).

The electrochemical activity of trimetallic palladium-based electrocatalysts towards ethanol, ethylene glycol, and glycerol in an alkaline medium.

- The trimetallic palladium-based electrocatalysts were investigated towards ethanol, ethylene glycol, and glycerol in an alkaline medium. The electrochemistry was

conducted and confirmed that the trimetallic electrocatalysts exhibit excellent electrocatalytic activity in all the alcohols compared to PdFe/C and Pd/C electrocatalysts.

- The electrochemical impedance performance revealed that all the trimetallic electrocatalysts possess the smallest R_{ct} value towards ethylene glycol electro-oxidation amongst ethanol and glycerol, indicating the faster electrode kinetics.
- After that, the best two electrocatalysts (PdFe/C and PdFeMn/C) were explored as anode materials and tested for the proof-of-concept in the two-electrode configuration with the micro-3D printed cell towards all the alcohols in alkaline medium. The PdFeMn/C and PdFe/C delivered improved micro-ethylene glycol fuel cell activity with respective to high power density and galvanostatic stability relative to micro-ethanol and micro-glycerol fuel cells.
- In conclusion, the PdFeMn/C electrocatalyst showed the best performance for EGOR compared to EOR and GOR, especially by giving the highest specific current density and lowest binding energy (observed from DFT calculation).

Facile synthesis of Palladium-based ferromanganese alloy supported on carbon as an Excellent Anode for Direct Ethylene Glycol Fuel Cell.

- A facile two-step microwave-assisted synthetic technique was used to synthesise a carbon-supported palladium-based ferromanganese alloy. The adopted synthetic approach in all the electrocatalysts yielded a uniform homogeneous distribution on the carbon support, polycrystalline nature, and small particle size distribution of about 5 nm.
- The electrocatalytic performance of PdFeMn/C electrocatalysts offered higher activity and better stability over Pd/C, PdFe/C, PdMn/C towards EGOR in basic medium. The good performance of PdFeMn/C nano-electrocatalyst towards EGOR arises due to the synergistic effect caused by the two co-metals embedded in the surface of the Pd electrode.
- The effect of EG and alkaline concentration were investigated for PdFeMn/C, and it was noticeable that at the fixed OH^-, there was a decrease in current density at 3.0 M EG due to the plethora of EG species overpowering the OH^- species. On the other hand, at the fixed EG, it was observed that there was a rise in current density as the OH- concentration increases occurred due to the surplus amount of OH^- coverage on the surface of the

electrode. This remarkable excess of OH^- enhanced the kinetics and facilitated the removal of carbonaceous species on the electrode surface.

- The proof-of-concept in the two-electrode configuration with the micro-3D printed cell was explored with two best-performing electrocatalysts. The results revealed that PdFeMn/C improved micro-ethylene glycol fuel cell activity with high power density and galvanostatic stability.
- We noted that alloying Pd/C electrocatalysts with co-metals gave excellent activity towards ORR in an alkaline medium.

10.3 Recommendations

Future work will test the performance of all the promising prepared electrocatalysts in direct alcohol fuel cells. This will help fully understand the electrocatalyst's electrochemical behaviour in a proof of concept. Thus far, the PdFeMn/C electrocatalyst has been tested, and the results were appealing. Therefore, it is recommended to conduct further analysis of other electrocatalysts to conclude this work.

Pd-based electrocatalysts have shown significant interest in the ORR application. Therefore, PdFeCo/C and PdCo/C electrocatalysts will be tested for the ORR application and compared with the performance obtained from PdFeMn/C and PdMn/C electrocatalysts. This will allow an overall conclusion on the ORR work on both the trimetallic electrocatalysts studied in this thesis.

Secondly, we plan to commercialise this catalyst in the near future. However, the precursors to making this material are expensive. Therefore, we are approaching South African mines, precious metals, and small, medium, and micro enterprise (SMME) companies to work with them to outsource the precursors instead of procuring them from the chemical manufacturing industry. This will also promote the beneficiation of minerals (Pd, Fe, Mn, etc.) available in SA. Several proposals have been submitted to collaborate with one or all sectors to enhance mass production for further development in portable devices.

Lastly, the advancement of electrolyzer technology for hydrogen production is thriving worldwide. Therefore, it will be interesting to pursue the use of Pd-based ferroalloy electrocatalysts within this technology and observe their performance. Even though it is a

bit out of scope regarding the application, investigating their performance will contribute to the Fuel cell value chain (as a whole).